Dissertation
submitted to the
Combined Faculties of the Natural Sciences and Mathematics
of the Ruperto-Carola-University of Heidelberg, Germany
for the degree of
Doctor of Natural Sciences

Put forward by
Niklas Müller
born in: Gießen
Oral examination: 21.06.2017

Strong magnetic fields and non equilibrium dynamics in QCD

Referees: Prof. Dr. Jan M. Pawlowski
Prof. Dr. Tilman Plehn

Abstract The concept of symmetry is without doubt the most significant centerpiece of modern science. Our current understanding of the visible universe is phrased into a basic set of equations describing what we call 'gauge theories'. The laws governing the dynamics of nature have been derived studying the symmetry properties of these equations, that is their invariance or non-invariance under certain symmetry 'transformations'. Because of their grand success and while seeming omnipotent, it came as a sensational surprise, that nature mysteriously does not obey some of the above symmetry principles by mechanisms that are elusive: Quantum Anomalies. The intriguing feature of the anomalous violation of symmetries is that it cannot be understood by the defining set of equations that were postulated to comprise the physical content of nature, but rather from the structures of quantum theories itself. Quantum anomalies emerge from the transition from the classical to the quantum level of nature, and researchers have realized that the properties of the physical vacuum (that is the quantum equivalent of 'nothing') are very non-trivial.

Symmetries are the cornerstones of gauge theories and the fundamental forces they describe. The vast majority of visible matter is governed by the strong interactions, formulated through the theory of Quantum Chromodynamics (QCD). In this context, symmetry principles also dictate the existence of another mysterious concept: topology. Topology is the principle used to describe the fundamental structure of an object, invariant under a certain transformation. In physics it describes the invariance of the aforementioned basic set of equations under continuous and hence structure-preserving manipulations. It is very suggestive that quantum anomalies and the concept of topology should be intimately related and in fact this assertion is most famously confirmed by the so-called axial anomaly.

The physics of quantum anomalies and topology is intriguing and often mysterious, yet central to many of the fundamental mechanisms of nature. As the anomalous violation of classical symmetries in the earliest stages of the universe is conjectured to be responsible for the dominance of matter over anti-matter, researchers attempt to recreate the dynamics of matter under extreme conditions at heavy ion collider experiments and thus understand these challenging

mechanisms. In the early universe as well as in present day experiments the emergence of quantum anomalies is tied to *out-of-equilibrium* systems.

In this thesis we focus on a comprehensive attempt at establishing the theoretical foundations of the non-equilibrium description of anomalous and topological dynamics. To this end we present a selection of different techniques and approximation schemes, which are motivated by the properties of the space-time evolution of QCD matter in ultra-relativistic heavy ion collisions. Most importantly we aim to illustrate that the techniques, which are presented here, are applicable to a number of systems in nature, starting from strong-field laser physics to cosmology. The nature of topological effects is much richer in out-of-equilibrium systems and in accord with present progress in the experimental study of anomalous effects, we hope to contribute to the establishment of a novel view on anomalies and topology beyond the previous equilibrium paradigm.

Zusammenfassung Die Erkenntnis der fundamentalen Bedeutung von Symmetrien ist prägend für die Entwicklung der modernen Physik. In diesem Zusammenhang kann unser momentanes Verständnis des sichtbaren Universums durch einige grundlegende Gleichungen, welche mittels so genannten 'Eichtheorien' ausgdrückt werden, beschrieben werden. Die Gesetzmässigkeiten der Physik können dann von den Symmetrieeigenschaften eben dieser Gleichungen abgeleitet werden. Beginnend in der Mitte des 19. Jahrhundert hat sich diese Sichtweise als extrem erfolgreich und doch nicht allmächtig erwiesen. In der letzten Hälfte des 20. Jahrhunderts haben Forscher symmetrieverletzende Phänomene entdeckt, die sich nicht durch oben genannte Gleichungen beschreiben lassen: Quantenanomalien. Die mysteriöse Eigenschaft dieser anomalen Verletzungen von Symmetrien ist, dass deren Ursprung im Übergang von klassischen hin zu quantenmechanischen Beschreibungen zu finden ist. Mit diesem Übergang verbunden ist die Erkenntnis, dass die Struktur des Vakuums (also des 'Nichts') auf der Quantenebene nicht trivial ist.

Symmetrien sind die den Eichtheorien zugrundeliegenden Bausteine und beschreiben somit die uns umgebende Materie und deren fundamentale Wechselwirkungen. Dabei kann der größte Teil des sichtbaren Universums mittels der Theorie der Quantenchromodynamik verstanden werden, welche auf nicht-Abelschen kontinuuierlichen Symmetriegruppen basiert. In diesem Zusammenhang bestimmen Symmetrien auch die Eigenschaften eines weiteren wichtigen Konzepts: der Topologie. Topologie ist das Prinzip, welches den Zusammenhang zwischen der Struktur des 'Raumes' der Objekte, der durch obige Gleichungen beschrieben wird, mit den Eigenschaften der Lösungen der eben dieser Grundgleichungen verknüpft. In der Tat sind Quantenanomalien und Topologie eng verwandt.

Die Physik der Quantenanomalien und der Topologie ist faszinierend und oft rätselhaft, gleichzeitig sind diese Konzepte von entscheidender Bedeutung für einige der fundamentalsten Aspekte der Natur. Die anomale Verletzung von klassischen Symmetrien im frühen Universum ist vermutlich verantwortlich für die heutige Existenz der Materie und des Verhältnis von Materie zu Antimaterie. Aus diesem Grund ist es ein wichtiges Bestreben aktueller Forschung die Mechanismen von Materie unter extremen Bedingungen, wie diese im frühesten Universum herrschten, im Experiment zu erzeugen und zu verstehen. Dabei ist zu bemerken, dass die Dynamik der Quantenanomalien im frühen Universum, wie in modernen Schwerionenexperimenten, mit dem Verhalten der Materie fernab des thermischen Gleichgewichts zusammen hängt. Aus diesem Grund ist ein zentraler Aspekt dieses Dissertationsvorhabens die Grundlagen von theoretischen Beschreibungen der Nicht-Gleichgewichts-Dynamik von anomalen und topologischen Effekten zu etablieren. In dieser Arbeit präsentieren wir eine umfassende Auswahl von Methoden und Techniken, welche durch die Herausforderungen der quantitativen Beschreibung einer Schwerionenkollision motiviert sind, deren Anwendungen aber wesentlich universeller ist. Die Methoden, die in dieser Thesis angewandt werden, sind auf eine Reihe von physikalischen Systemen übertragbar – beginnend mit zukünftigen Starkfeld-Laserexperimenten bis hin zu kosmologischen und astrophysikalischen Fragestellungen. Dabei ist es ein zen-

trales Resultat dieser Arbeit, dass die Dynamik von topologischen Effekten in Nicht-Gleichgewichtssituationen wesentlich umfassender und vielseitiger ist, als dies mittels gegenwärtigen Gleichgewichtstechniken hätte vorhergesehen werden können. Diese Einsicht ist im Einklang mit den spektakulären Fortschritten in experimentellen Studien von anomalen Effekten an Schwerionenexperimenten wie RHIC und LHC und daher hoffen wir, dass die vorliegende Arbeit einen wichtigen Beitrag zum modernen Verständnis von Anomalien und Topologie leisten kann.

Contents

Unless stated otherwise, in this manuscript we will use units in which $\hbar = c = k_B = 1$.

Chapter 1

Introduction

1.1 Goal of this thesis

This thesis is an attempt to elucidate the importance of a thorough understanding for the *non-equilibrium dynamics* of topological and anomalous effects in relativistic gauge theories. The connection between topological gauge field configurations [1–5] and the anomalous violation of symmetries associated with fermionic currents has long been known [6, 7]. While the subject has received considerable attention in the context of equilibrium or vacuum physics, such as in S-matrix scattering experiments [8], the non-equilibrium dynamics of the aforementioned effects have remained elusive. A striking example of the importance of the non-equilibrium dynamics of anomalous effects is electroweak-baryogenesis [9–12]: under sufficient out-of-equilibrium conditions the observed matter/anti-matter asymmetry of the present-day universe is conjectured to be caused by the combination of anomalous baryon- plus lepton-number and C (charge conjugation) and CP (charge and parity conjugation) non-conservation. Moreover quantum anomalies are also understood to play an important role in the electronic properties of strongly correlated condensed matter systems [13].

Recently the possibility of direct experimental access to the non-equilibrium dynamics of anomalous effects has been conjectured. By means of the Chiral Magnetic Effect (CME) [14–16] local $P-$ and $CP-$ odd fluctuations in Quantum Chromodynamics (QCD) manifest themselves via experimentally observable correlations of electric charges. The CME in practice converts fluctuations of axial charge imbalances in the strongly correlated quark-gluon plasma (QGP) into electric currents along the direction of the Abelian magnetic fields that are created by the spectators in an off-central collision of heavy nuclei [17, 18].

While the CME has been observed in condensed matter systems [19], its experimental realization in the context of heavy ion collisions is still unclear [20]. It is generally agreed upon that there exist significant background contributions to the CME signal, such as for example from local charge conservation [21–27], that generate correlations between charged particles mimicking the effects

of the CME. Unfortunately there is neither an understanding of the relative magnitude between CME signal and its background nor of their systematics, for example such as the dependence of these signatures on the centrality or $\sqrt{s}$ of a collision. While early on intriguing hints of the CME have been seen at RHIC and LHC [28–30], recent experimental searches at the CME experiment [27] have come up with controversial results: by comparing correlations of charged particles in both Proton-Nucleus as well as Nucleus-Nucleus collisions it was found that centrality dependence of these correlations in nearly identical for both systems[1]. While this finding put pressure on the CME interpretation of charge correlations in heavy ion collisions, these current studies have fairly limited evidential value as they have only been performed for a restricted choice of oberservables. In comparison some recent results of the RHIC experiments are discussed in [31, 32].

The latest controversy puts a heavy burden on theorists: While researchers have proposed the existence of a variety of novel transport phenomena, the understanding of experimental manifestations of these effects is very limited. This is mainly due to the fact that the most important contributions to anomalous transport originate in the earliest moments of a heavy ion collision, since the lifetime of the external Abelian magnetic fields in non-central heavy ion collisions is extremely short and is expected to decay well before $t = 1fm/c$ [17, 18]. The dynamics of a heavy ion collision during these early times represents a challenging far-from-equilibrium situation and calls for very advanced theoretical descriptions. Weak-coupling frameworks applicable at high energies indicate that, at these early times, the strongly correlated quark and gluon matter is far off-equilibrium in a highly overoccupied plasma state [33–35], which subsequently evolves to a QGP state of matter. The question of thermalization in this context is still unresolved [36].

Classical-statistical simulations, that have been used to study the initial state particle production [37–40] and to investigate aspects of thermalization [41–44], have proven to be a very suitable ab-initio approach that allows quantitative understanding of the non-equilibrium dynamics of a heavy ion collision at early time. They have been very successfully employed to study the dynamics of highly occupied non-Abelian plasmas in expanding geometries and most famously have identified the so called 'Bottom-up' scenario [45] as the relevant effective description of weak-coupling thermalization [46].

In this thesis we present first attempts at including the dynamics of fermions into these powerful simulation techniques [47–52]. The far-from equilibrium dynamics of fermions in ultra-relativistic heavy ion collisions is of crucial importance for the understanding of anomalous chiral transport. Fermions are the carriers of the electromagnetic properties of QCD matter and as such are responsible for the polarization dynamics of the CME in peripheral heavy ion collisions. Apart from the physics of strong magnetic fields, electro-magnetic probes, such as photons, are of great importance for the comprehension of the spacetime evolution of heavy ion collisions [53–58]. This is because of the fact

[1] We note that the magnetic fields created in $p - Pb$ are either zero or at least very small.

that their mean free path is much larger than typical system sizes [59] and they leave the medium essentially unscathed. Photons provide excellent probes for the dynamics of the space-time evolution of the fireball created, as they are produced throughout every stage of the collision.

Somewhat surprisingly the production of electromagnetic probes during a heavy ion collision is not yet well-understood, as there is still significant discrepancy between theoretical predictions and experimental results [60–62]. Specifically when contrasted with theoretical predictions, direct photon spectra exhibit a substantial excess at low $p_\perp$, while also showing greater azimuthal anisotropy than predicted by thermal production models [63]. These two effects comprise the so-called *direct photon puzzle*. While in this study no computations of non-equilibrium photon production are presented, the techniques developed and presented here serve as the basis for future studies [64].

The interplay of the axial anomaly and Abelian magnetic fields, leading to the emergence of anomaluous vector and axial-currents, is by no means unique to heavy ion collisions. In section 3 we propose to study the Chiral Magnetic Effect and anomalous transport using high intensity laser beam experiments [65, 66]. The creation of electromagnetic fields beyond the famous Schwinger limit [67–69] is within reach of experiments that are expected to be available within the next two decades [70–75] and the non-linear regime of Quantum Electrodynamics (QED) offers a prime opportunity to investigate the non-equilibrium dynamics of anomalous effects. In this thesis we will show that the Abelian equivalent of the chiral magnetic effect leads to novel polarization effects, which we call 'dynamical anomalous refringence' and which have not been considered before [76]. In this context we find interesting tracking behavior of electromagnetic fields, which are due to non-linear effects and the creation of anomalous electric currents. Unlike ultra-relativistic heavy ion collisions, future laser beam experiments provide an almost background-free test ground for the investigation of the aforementioned effects.

Moreover the effects of the Abelian anomaly in far-from equilibrium situations is conjectured to be important in an astrophysical context [77–80]: the transfer between fermionic chirality and magnetic helicity exhibits non-trivial dynamics in out-of-equilibrium situations, by possibly leading to chiral instabilities. In this context the role of the fermion mass is conjectured to be responsible for the reduction of chirality and thus might dampen the aforementioned instabilities [81, 82]. Therefore in this thesis we will investigate the role of the fermion mass in the anomalous dynamics of both Abelian and non-Abelian gauge theories quantitatively.

We note that the non-equilibrium dynamics of anomalous and topological effects in Abelian and non-Abelian gauge theories is ideally suited to be studies using analogue quantum simulators [83–85]. Systems of ultra-cold atoms might be used to perform quantum simulations of gauge theories and experiments non-equilibrium dynamics of Quantum-Electrodynamics in lower dimensions have been proposed [86]. Remarkably these experiments could contribute to the understanding of gauge theories and matter beyond the approximations that are employed in this thesis and consequently might give insights into the mechanisms

of thermalization in gauge theories. While ultra-relativistic heavy ion collisions, strong-field QED and ultra-cold quantum gases represent very different physical systems on vastly different scales, these fields share many common features [87] and might be addressed from a more 'universal' perspective.

Moreover in this thesis we hope to convince the reader that topological and anomalous effects far-from-equilibrium comprise a very rich field of research and the techniques that we outline here, might open new perspectives – beyond the conventional mindset about anomalous effects, that is by now well established.

1.2 Outline of this work

The following manuscript is organized as follows: in subsection 1.3 we give a general introduction into the physics questions that are addressed in this work. To provide some context we give a rough overview over the current understanding of the dynamics of a heavy ion collision and we point out important shortcomings of current theoretical descriptions and associated challenges for researchers in section 1.3.1. Further in section 1.3.2 we will outline the physics behind the Chiral Magnetic Effect and anomalous and topological phenomena in heavy ion collisions and other fields.

An introduction into the technical and conceptual basics that are employed in this thesis is given in section 2. There we will first outline the ideas and concepts between the path integral formalization of non-equilibrium many body systems, via the Schwinger-Keldysh closed time path and its equivalent Hamiltonian formulation. Furthermore we will give an introduction into the lattice formulation of quantum field theories with a special emphasize on Abelian and non-Abelian gauge theories in section 2.2. Based on this we will proceed to discuss the classical-statistical approximation, as it is used in many subsequent chapters of this thesis to address various problems in different fields of physics, starting with strong field laser experiments and continuing with the physics of the Chiral Magnetic Effect in ultra-relativistic heavy ion collisions.

Based on the introductory chapters we will then proceed to present the various aspects of the research that we have performed during my doctoral studies. The common 'theme' of the subsequent chapters is the non-equilibrium dynamics of anomalous and topological effects. In chapter 3, we will investigate the non-linear regime of QED beyond the Schwinger limit, which can be reached with next generation laser beam experiments. These systems are expected to represent challenging non-equilibrium systems, which provide intriguing novel effects: as such the Abelian axial anomaly has been rarely discussed in this context. In section 3 we show explicitly that future experiments might provide an unique chance to study novel experimental realizations of the Abelian axial anomaly, and thus give an insight into many other fields. Subsequently in section 4, we will present a study of anomalous fermion production from non-Abelian gauge field configurations, which are typical for the early time regime of a heavy ion collision. This chapter provides an interesting perspective on the investigation of the far-from-equilibrium dynamics of the axial anomaly using

real-time lattice techniques.

In section 5 we will present the most advanced ab-initio study to this day of the CME in the earliest time regimes of a heavy ion collision. By implementing the dynamics of Abelian and non-Abelian gauge fields and simulating non-equilibrium fermion production during topological transitions, we can investigate anomalous transport quantitatively. The results that are presented in this chapter have only become possible because of advanced algorithmic techniques that we have developed.

Section 6 is not only an attempt to put the results of our real-time lattice simulations into the bigger context of the space-time history of an ultra-relativistic heavy ion collisions, it furthermore provides new insights into the structure of quantum anomalies and how they arise from quantum field theory. In this section we develop a Lorentz-covariant and consistent chiral kinetic theory using the string-inspired world-line framework. Our results put pressure on recent attempts at relating the topology of quantum anomalies with that of Berry's phase.

Section 7 completes the work presented in this thesis. Here we present results that have been obtained studying chiral symmetry breaking in the presence of strong magnetic fields in the strongly coupled regime of QCD. To this end we resolve the previous discrepancy between various model and lattice computations regarding the dynamics of inverse magnetic catalysis.

1.3 Anomalous Effects and far-from equilibrium dynamics

In this section we provide an overview of the current status of the searches for anomalous and topological phenomena in ultra-relativistic heavy ion collisions. In order to be able to put the results presented in this thesis into perspective with the enormous challenges associated with current experimental and theoretical efforts, in section 1.3.1 we begin by giving a short introduction of the status of understanding of the dynamics of a heavy ion collision. Subsequently we will focus on the physics of the Chiral Magnetic Effect and we will present the basics of anomalous transport phenomena in Quantum Chromodynamics (QCD) in section 1.3.2.

1.3.1 Current challenges in heavy ion physics

Ultra-relativistic heavy ion collisions are a prime testing ground for the questions associated with many properties of QCD matter. By colliding heavy nuclei at collision energies of a few hundreds of GeV to several TeV per nucleon, experiments at both Brookhaven National Lab and CERN provide thereby direct experimental access to novel states of matter. Most intriguing are two specific states of matter, created under these extreme conditions, that are of importance for the investigations presented in this manuscript and which we shall discuss in more detail therefore. These are the Quark Gluon Plasma and the Color Glas Condensate [33–35], which we illustrate by roughly following the approach of [88, 89]. After having clarified the relevant concepts that are required to understand the properties of these intriguing states of matter, we will proceed to illustrate how these states of matter arise in the spacetime evolution of ultra-relativistic heavy ion collisions.

Nuclear matter under normal conditions consist of protons and neutrons, while the more fundamental constituents – quarks and gluons – are confined and not directly accessible by experiment. Nuclear systems at very high energy densities however look fundamentally different: in this case protons and neutrons overlap and their fundamental constituents can move freely. This process, called deconfinement, is a necessary condition for matter to exist in the form of what is called a *quark-gluon plasma*. An important feature of QCD matter at high energies is the weak coupling due to asymptotic freedom, which as we shall show below, allows perturbative approaches in certain kinematic regimes – and classical methods in others. We note that typical energy densities that are sufficient to produce a quark-gluon plasma, are of the order of 1 $\mathrm{GeV}/(\mathrm{fm})^3$. Often the physics of the quark gluon plasma is described in thermal equilibrium, but recent investigations suggest that the plasma created in ultra-relativistic heavy ion collisions might not be in equilibrium at any time [36].

The Color Glass Condensate The initial condition of a hadron in the high energy limit can be understood from the weakly-coupled regime of QCD. The ini-

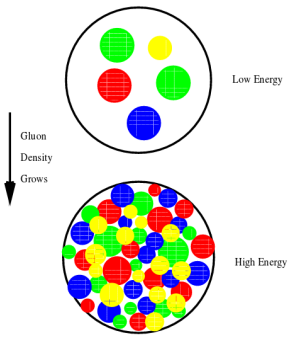

Figure 1.1: Saturation of gluons – the consituents that are probed as the kinematic variable x decreases. Figure taken from [88].

tial condition is tied to the many-body wave-function of a heavy ion in the high energy limit of QCD and receives contributions from gluons and (anti-)quarks on all scales and for every value of the momentum fraction $x = E_{constit}/E_{had}$. Kinematical variables are usually defined in the infinite-momentum frame of a Lorentz contracted hadron. Another important kinematic variable is the resolution scale Q^2 of the probe (the four-momentum transfer).

In the context of Deep Inelastic Scattering (DIS) [90, 91] the evolution of the distribution of the constituents comprising the wave function of a hadron as a function of x and Q^2 is well understood from perturbative QCD. The DGLAP (Dokshitzer-Gribov-Lipatov-Altaralli-Parisi) [92–94] evolution equations realize the Q^2 evolution of fermion and gluon distribution functions by resumming leading logarithms of $\alpha_s \log Q^2$, where α_s is the perturbative QCD coupling, while the evolution in x is considered sub-leading. Similarly the evolution in x is understood via the BFKL (Balitsky-Fadin-Kuraev-Lipatov) equations [95–97] (c.f. Fig. (1.2)). In the regime of extremely small x this perturbative understanding however is challenged, as we shall show below. To understand the Q^2 and x evolution of the participants of a heavy ion, we note that, in units of the rapidity y, the density of small x partons (which are mostly gluons) is given by

$$\frac{dN}{dy} = xG(x, Q^2)\,, \tag{1.1}$$

Here y is the momentum space rapidity. The gluon distribution $G(x, Q^2$ in Eq.(1.1)[2] has been measured for protons at HERA [98] with high precision and was shown to rise for small x and fixed Q^2 (see Fig. (1.2)). A similar behavior is predicted from the aforementioned evolution equations.

As the density of low-momentum gluons grows, a rapidly rising cross-section could violate unitarity and thus the naive evolution must break down at some

[2]A parton distribution function is defined as the probability of testing a parton with given momentum fraction x and at four momentum transfer Q^2.

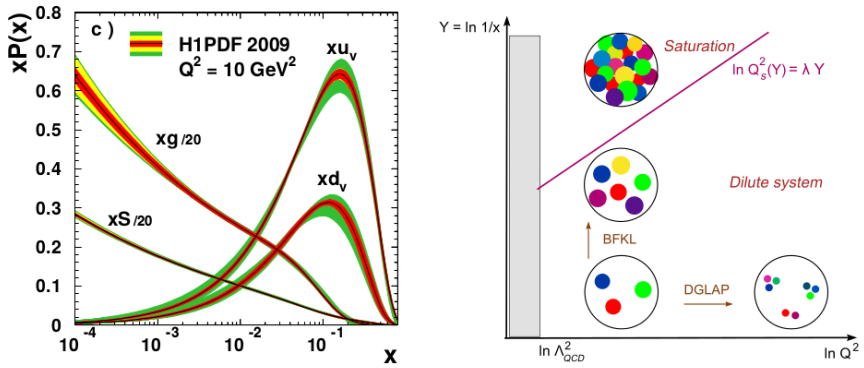

Figure 1.2: Left: The x-evolution of gluon and quark distributions for $Q^2 = 10$ GeV measured at HERA. Right: A pictographic representation of the evolution of the gluon distribution in x and Q^2. Figure taken from [35].

point. The conventional BFKL evolution assumes a linear superposition of gluons, however as one goes to very small x QCD becomes very dense and gluons start to overlap, as is sketched in Fig. (1.1). Thus at some point the linear DGLAP and BFKL evolution equations must break down and the non-linear evolution of the parton distributions must be taken into account. The aforementioned overlap marks the onset of the so-called *saturation regime*, where the gluon phase space density $\rho \propto 1/\pi R^2\, dN/d^2p_T$ becomes of order $1/\alpha_s$ [89, 99].

This special state of matter is called a *Color Glass Condensate* (CGC). The term 'glass' is used because of the typical evolution time scale of those constituents. This time scale is inherited from the constituents with higher momentum fraction and is considerably longer than one naturally expects. The non-linear saturation effects are characterized by a typical saturation scale $Q_s = Q_s(x)$, where for momenta with $Q < Q_s$ gluon saturation dominates (see the op left corner of the plot on the right of Fig. (1.2)). The saturation scale typically is $Q_s^2 \propto \alpha_s N_c\, dN/dy/\pi R^2$. Typical values for Q_s are of the order of a few GeV for present day experiments at RHIC and LHC [89, 99]. Below we will find that the physics of saturation in ultra-relativistic heavy ion collisions can be efficiently described by the use of classical fields.

Heavy Ion Collisions While the physics of the Color Glass Condensate gives a very good picture of the initial conditions for an ultra-relativistic heavy ion collision, the space-time evolution of the latter is more complicated and not yet understood entirely. From the CGC perspective heavy ion collisions can be imagined by the collision of two two-dimensional[3] sheets of colored glass. As

[3]We note that at ultra-relativistic energies heavy ions are Lorentz contracted in the longitudinal direction and might be treated sheet-like. Upon closer inspection this is equivalent to the the kinematic limit utilized in the saturation picture, which is essentially two-dimensional

these sheets smash into each other, they trail behind 'melted glass' from which quark and gluons are produced. Below we attempt to illustrate this somewhat prosaic picture explicitly. To this end we introduce appropriate kinematic variables in light-cone coordinates and using light-cone gauge $A^+ \equiv A^0 + A^3 = 0$

$$P^{\pm} = \frac{E \pm p_z}{\sqrt{2}}, \tag{1.2}$$

$$X^{\pm} = \frac{t \pm z}{\sqrt{2}}\,. \tag{1.3}$$

Furthermore we make use of the position space rapidity and proper time variables

$$\eta \equiv \tanh^{-1}\frac{z}{t} = \frac{1}{2}\ln\left(\frac{X^-}{X^+}\right), \qquad \tau \equiv \sqrt{t^2 - z^2}\,, \tag{1.4}$$

as well as the momentum space rapidity

$$y = \frac{1}{2}\ln\left(\frac{P^-}{P^+}\right). \tag{1.5}$$

Fig. (1.3) gives an illustration over these kinematic variables. As the heavy ions travel approximately on the light cone, we have $P^+ \neq 0$ and $P^- = 0$ for the rightmoving hadron and vice versa for the leftmoving one. Particles which carry only a fraction of the respective projectiles, and the particles produced from the medium, are confined inside the causal light cone region. Consequently the rapidity range of any particle produced in experiment is restricted by the hadron rapidities.

An important feature of the parton distribution functions is that the valence and gluon degrees of freedom are well separated in x, as is evident from Fig. (1.2). Thus at small x we aim to describe a theory of gluons only, which we shall call 'wee' gluons due to the small momentum fraction they are carrying. The valence partons act as *static* sources for the wee gluons, as can be seen from simple estimates of the characteristic time scales (hence the name 'glass', c.f. [99]). The interactions between valence and wee partons can be described using an effective action[4], which was first established in [89, 99] (here for one of the two nuclei)

$$Z[j] = \int [d\rho]\, W_{\Lambda^+}[\rho] \left[\frac{\int^{\Lambda^+} [dA]\, \delta(A^+) \exp\left(iS[A,\rho] - \int j\cdot A\right)}{\int^{\Lambda^+} [dA]\, \delta(A^+) \exp\left(iS[A,\rho]\right)} \right], \tag{1.6}$$

where Λ^+ is a typical longitudinal momentum scale, separating sources and fields and the small x effective action is given as

$$S[A,\rho] = \frac{1}{4}\int_x F^a_{\mu\nu}F^{\mu\nu,a} + \frac{i}{N_c}\int d^2X_\perp dX^-\,\delta(X^-)\mathrm{Tr}\left(\rho\, U_{\infty,-\infty}[A^-]\right)) \tag{1.7}$$

[4]We note that this form of effective action looks suspiciously similar to something we will discover in section 6 in a very different context.

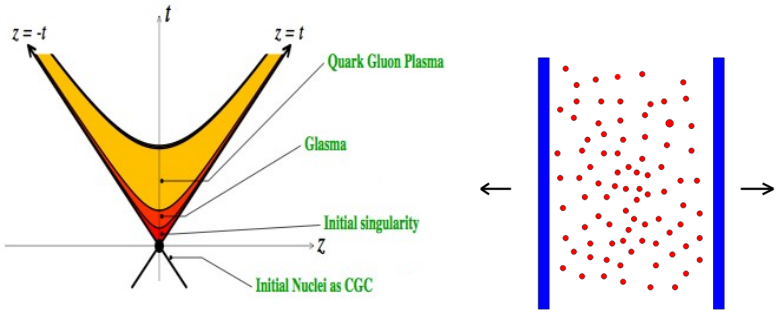

Figure 1.3: Left: Lightcone diagram of a heavy ion collision as an illustration of the kinematic variables used. Right: Schematic view of a heavy ion collision through two Lorentz-contracted sheets of Color Glass. The constituents that carry a large momentum fraction of the projectile suffer only small momentum losses and essentially continue as part of the colliding 'discs'. Behind them they trail the 'wee' partons at smaller momentum space rapidity y, which later make up the medium, from which more particles are produced. Figures taken from [88].

with

$$U_{\infty,-\infty} \equiv \mathcal{P} \exp\left(ig \int dX^+ \, A^{-,a} t^a \right), \tag{1.8}$$

where t^a are the generators of $SU(3)$. Eq.(1.7) can be understood as a the action of 'classical' soft gauge fields, interacting with random color sources at larger x. The weight $W[\rho]$ in Eq.(1.6), which represents the distribution of color sources, might be described by a Gaussian distribution, but does not reproduce many important features in this case. In order to include generic quantum fluctuations, $W[\rho]$ must necessarily be a non-Gaussian distribution. To this end the JIMWLK (Jalilian-Marian, Iancu, McLerran, Weigert, Leonidov, Kovner) [100–106] evolution framework allows to systematically incorporate quantum fluctuations into the source functionals by means of a Wilson renormalization group evolution.

In practice, solving the dynamics of the wee partons described by the effective action Eq.(1.6) for a fixed configuration of sources is equivalent to solving

$$[D_\mu F^{\mu\nu}]^a = \delta^{\nu+} \delta(X^-) \rho^a(X^+) \, . \tag{1.9}$$

Moreover from the CGC-effective action observables can be calculated as

$$\langle \mathcal{O} \rangle_Y = \int [d\rho_1][d\rho_2] \, W_{x_1}[\rho_1] W_{x_2}[\rho_2] \, \mathcal{O}[\rho_1, \rho_2] \, , \tag{1.10}$$

where $Y \equiv \log 1/x_F$, $x_F = x_1 - x_2$ is the difference of the parton fractions of each nuclei. Explicit solutions of Eq.(1.9) are discussed in great detail in [99], but we note that typical solutions to Eq.(1.9) for fixed source terms are given

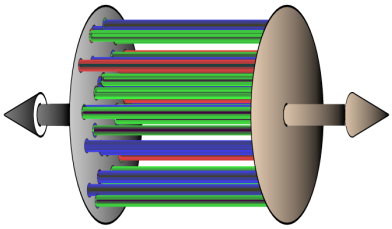

Figure 1.4: Schematic representation of typical solutions for the 'wee' gluon fields from the CGC framework. This picture should be understood in $\eta - \tau$ coordinates, with the longitudinal direction being η. Figure taken from [35]

by *longitudinal color-electric and color-magnetic fields*, which are screened on typical transverse scales of $1/Q_s$, where Q_s is the gluon saturation scale. These field configurations are called color flux-tubes and should not be confused with a similar notion in the context QCD-strings and confinement. A sketch of these so-called 'glasma flux tubes' is given in Fig. (1.4). Characteristic field amplitudes in the flux-tube regime are of order $A \propto 1/g$ [107–110].

The emergence of these characteristic configurations of large coherent fields is central to the understanding of many properties of a heavy ion collision and justifies the use of *classical-statistical simulations*. Upon closer inspection, it is found that the flux-tubes are roughly boost-invariant (that is independent of η) and generate long range rapidity correlations [111] between created particles that can be measured in experiment.

The significance of these initial conditions for the effects discussed in this section is drastic: Flux tubes carry non-zero 'topological' density $\mathbf{E}^a \cdot \mathbf{B}^a$, which however is not related to the vacuum structure of QCD as we will shown in section 4[5]. Naturally flux-tube initial conditions lead to significant anomalous fermion production as we shall explicitly compute.

The spacetime evolution of a heavy ion collision Starting from the CGC/Glasma effective framework, we proceed to illustrate the subsequent stages of a heavy ion collision. Due to instabilities induce by fluctuations, the initial fields decohere on typical time scales $1/Q_s$, and form a boost invariant state with large occupancies along the transverse directions. This Glasma is characterized by a large anisotropy and thus exhibits Weibel instabilities [112–115]. In turn this leads to an exponential growth of quantum fluctuations and a quick break-up of boost invariance [116–118]. Eventually energy conservation causes a saturation of the instabilities, producing a state, which is best described as an overoccupied non-Abelian plasma.

[5] We emphasize that the flux tube contributions are clearly distinct from 'purely' topological contributions such as sphalerons, that are investigated in section 5. We point out that the relevance of this distinction between vacuum contributions and effects of the initial conditions is only transparent in out-of-equilibrium situations.

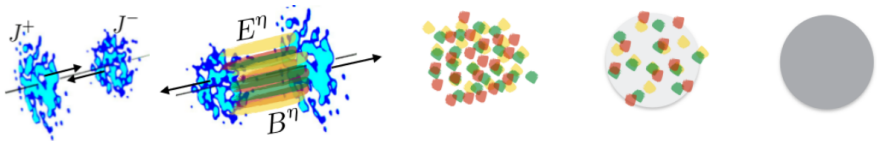

Figure 1.5: Schematic view of the space time evolution of a heavy ion collision: (a) CGC picture of the initial condition in the high energy saturation regime. (b) & (c) Flux tube and glasma regime. (d) Kinetic regime. (e) Hydrodynamic regime. This figure is courtesy of Soeren Schlichting, Univ. of Washington and used with his generous permission.

While instabilities lead to an isotropization of the system, the longitudinal expansion of the fireball still dominates its evolution and as a result the (momentum-)anisotropy increases slowly. Ultimately the dynamics becomes independent of the initial conditions and approaches an universal attractor solution [46, 119, 120][6]. This solution is in concord with the BMSS (Baier-Mueller-Schiff-Son) 'bottom-up' scenario [45]. The latter agreement is rather unexpected because of the absence of late-time plasma instabilities that should be present in weak-coupling kinetic formulations. The most convincing interpretation of this 'unreasonable' agreement is that the BMSS scenario reproduces the correct 'universal' features of the theory, while the details of the microscopic formulation do not seem to matter for many observables out-of-equilibrium. At time $Q_s\tau \propto \alpha^{-3/2}$ the characteristic occupancy of the plasma drops to 1 and classical-statistical simulations break down. In this regime the system is believed to be still weakly coupled and kinetic descriptions have been put forward. In the BMSS scenario inelastic processes are suggested to lead to thermalization. This picture however is highly controversial: eventually the system must become strongly coupled and transition to a hydrodynamic stage. Hydrodynamics is a macroscopic formulation of the late time stages of a collision and has predicted many observables such as particle rates and azimuthal asymmetries with great accuracy. Nevertheless despite encouraging agreement between different theoretical approaches the question of thermalization even in central $A+A$ collisions is controversial and the success of hydrodynamics is under debate [36]. We note that hydrodynamics neither needs thermalization [113] nor isotropization [36] to work. We further point out that thermalization has been addressed by comparing weak coupling scenarios and AdS/CFT computations [121] with good agreement. The apparent puzzle of thermalization and the success of hydrodynamics is a prime motivation to study more detailed aspects of the dynamics of ultra-relativistic heavy ion collisions: as already discussed in the introduction, photons are produced at all stages of a heavy ion collision and given the fact that experimental and theoretical descriptions of both photon rates and flow do not match, more work has to be done. The chiral magnetic effect and anomalous hydrodynamics are yet another important test of the hydrodynamic

[6] We emphasize that this famous insight is due to classical-statistical simulations.

paradigm: while hydrodynamics so far has been ignorant about spin dynamics, CME physics requires a precise understanding of the latter far from equilibrium. It is thus an interesting question, whether hydrodynamics will continue to successfully predict spin-related observables. In the following section 1.3.2 we will give a detailed introduction into the physics of the Chiral Magnetic Effect and we will highlight the challenges that it poses for theory. We note that, due to its importance in present day research, many contributions from various perspectives can be found in the literature and the introduction presented here is by no means exhaustive. In this thesis we will omit discussion of the hadronic and freezeout stage of a collision. More details can be found in [14–16, 20]

1.3.2 Anomalous Effects

The combination of quantum anomalies with magnetic fields and vorticity has been speculated to result in a new class of transport phenomena [14–16] observable in heavy ion experiments. The important difference of the phenomena that we will introduce in this section, when compared to 'conventional' transport mechanisms is that their origin is (in part) topological and thus *non-dissipative*. The deconfied quark-gluon plasma has been identified as a prime candidate for supporting chiral/anomalous transport phenomena due to the appearance of near-chiral fermions. In this section we give an introduction into anomalous effects in QCD and we will discuss their importance during various stages of a heavy ion collision.

Central to our work are the fermionic vector- and axial current densities

$$j^\mu = \langle \bar{\psi}\gamma^\mu\psi\rangle, \qquad j_5^\mu = \langle \bar{\psi}\gamma^\mu\gamma_5\psi\rangle\,, \tag{1.11}$$

which can be separated in currents of left and right handed particles, that in a theory with chiral fermions are separately conserved. While axial currents are hard to probe in experiment, vector currents are typically related to global quantities, such as electric charge. Therefore they can be tested by studying the electromagnetic properties of the medium. The emergence of anomalous vector currents can be understood as follows: conventionally an electrically conducting medium supports ohmic currents relating P-odd electric fields with P-odd currents

$$\mathbf{j} = \sigma\mathbf{E}\,. \tag{1.12}$$

Eq.(1.12) is obtained when assuming that the carriers of electric charge are point-like (scalars, electric charge density being P-even), i.e. not taking into account the spin of particles. Particles with spin however can support of types of vector-currents by means of Eq.(1.11). As we will show below, the Chiral Magnetic Effect predicts the generation of a vector in the form

$$\mathbf{j} = \sigma_5\mathbf{B}\,, \tag{1.13}$$

and as is fixed by discrete symmetries σ_5 must be CP-odd. From Eq.(1.11) one identifies the zeroth component of the axial current, which is the axial density

as having the correct parity to provide the origin of the anomalous conductivity $\sigma_5 \propto j_5^0$ [14–16].

The axial anomaly In quantum field theory the source of axial charge creation is the axial anomaly, which relates topological non-trivial gauge field configurations with the creation of a chiral imbalance. While the axial current defined in Eq.(1.11) is naively conserved in a classical theory, quantum fluctuations lead to its non-conservation upon quantization. The later is expressed in the famous *local* non-conservation equation

$$\partial_\mu j_5^\mu = 2m\langle\bar{\psi} i\gamma_5\psi\rangle - \frac{g^2}{16\pi^2} F^a_{\mu\nu}\tilde{F}^{\mu\nu,a}\,. \tag{1.14}$$

Here the first term on the r.h.s is the pseudoscalar condensate, which is a classical contribution due to the finite fermion mass. The term $\propto F\tilde{F}$ is the contribution of the anomaly. It can be understood from the inability of regularizing the theory while maintaining chiral symmetry at the same time [6, 7]. The derivation of Eq.(1.14) can be found in many textbooks, mostly following the path integral formulation of Fujikawa [122, 123], which nicely illustrates that it is the fermionic measure that is responsible for the non-conservation, or by using Hamiltonian techniques [124].

Eq.(1.14) describes the *local* violation of the axial current (density) and in order to perform it into an equation containing global quantities, it might be integrated over space and time with suitable boundary conditions. Neglecting the fermion mass and performing the integral of the spatial volume with trivial boundary conditions at infinity, followed by the integration over time yields

$$\Delta J_R^0 - \Delta J_L^0 = 2\,Q_w\,, \tag{1.15}$$

Here Δ denotes the difference of a quantity between the final and initial time, $\Delta X \equiv X(t_f) - X(t_i)$, and

$$J_R^0 - J_L^0 = \int d^3x\, j_5^0\,. \tag{1.16}$$

The space-time integral over the anomaly term gives $Q_w = \int_V \Delta K^0$, which is the Chern-Simmons topological charge. It is obtained by writing the anomaly term as the divergence of a four-current $F\tilde{F} \propto \partial_\mu K^\mu$. The Chern-Simmons four current can be identified as

$$K^\mu = 2\epsilon^{\mu\nu\alpha\beta}\mathrm{tr}\left(A_\nu F_{\alpha\beta} + \frac{2}{3} ihA_\nu A_\alpha A_\beta\right) \tag{1.17}$$

which is related to the topological charge as

$$Q_w = \frac{g^2}{32\pi^2}\int d^4x\,\partial_\mu K^\mu\,. \tag{1.18}$$

For vacuum boundary conditions (or for periodic conditions), which is the case when we integrate over all space-time, Q_w is integer valued and of topological nature. Moreover it is related to the non-trivial vacuum structure of $SU(N_c)$ gauge theories. In this case Eq.(1.15) is an example of a so-called *index theorem*, relating the analytical index of the Dirac operator (which is the difference of eigenvalues with left/right chirality) to the topological index of the gauge sector. This perspective, which evolves around the structure of the QCD vacuum, is widely assumed; unfortunately it is not very relevant for heavy ion collisions: as in ultra-relativistic heavy ion collisions the space and time resolved (local) dynamics of fundamental matter is tested, as opposed to the vacuum-to-vacuum nature of S-matrix scattering. Therefore the local version of the anomaly equation Eq.(1.14) is of relevance for experiment and the topological content given in Eq.(1.15) must be extracted.

Topological transitions play a role for the physics of the axial anomaly in heavy ion collisions. Real-time transitions between field configurations with different topological invariant are called sphalerons. It has been found that sphaleron transitions occur far more frequently in the non-equilibrium glasma [125], than in thermal situations [126] and thus it is an interesting challenge for future studies to investigate the relative importance of non-topological field configurations and manifest topological transitions for the physics of the CME. Interestingly however, generic initial conditions for heavy ion collisions obtained from the CGC picture provide $F\tilde{F} \propto \mathbf{E} \cdot \mathbf{B}$, that is parallel color-electric and magnetic field configurations – which are not topological. Therefore the CGC naturally results in an important contribution to the axial anomaly of non-topological origin. Yet again this fact is easily overlooked, when treating the problem using equilibrium techniques, and it highlights the rich phenomemnology related to out-of-equilibrium situations.

The Chiral Magnetic Effect It has been found that sphaleron transitions occur far more frequently in the non-equilibrium glasma [125], than in thermal situations [126] and thus it is an interesting challenge for future studies to investigate the relative importance of non-topological field configurations and manifest topological transitions for the physics of the CME. To explicitly understand the mechanism behind the CME, let us assume a system of chiral fermions in a background magnetic field. For chiral fermions the momentum direction of a particle and its spin are necessarily identified. Provided the magnetic field is strong enough, the particles tend to align their spin with or opposite to the external field lines as is shown in the left side of Fig. (1.6). Due to the identification of spin and momentum for chiral fermions positively charged right-handed fermions will move along the field lines, while negatively charged right-handed particles move in the opposite direction. Thus a current is generated along this direction, which however is exactly canceled by the inverse mechanism of left-handed particles. However if there exists an imbalance between left and right handed particles, as it is created through the axial anomaly, the currents of left and right handed particles do not cancel exactly and a net current survives.

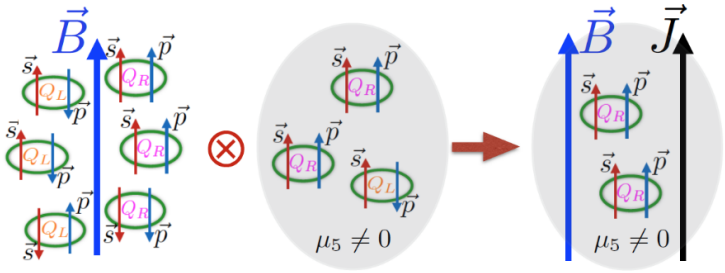

Figure 1.6: Schematic representation of the Chiral Magnetic Effect. Left: in the presence of an equal number of left and right handed fermions no net polarization current is induced by magnetic fields. Center and right: Due to the axial anomaly an imbalance of axial charge can be generated, which in turn yields an electromagnetic current along **B**. Figure taken from [16]

In the hot medium created during an ultra-relativistic heavy ion collision, local domains of non-zero $F\tilde{F}$ will exist. Consequently these domains will result in local violation of axial symmetry and axial charge is produced. As QCD conserves P- and CP-globally the effect of these local domains is on average zero: no net axial charge is produced and thus no net electromagnetic current can be created via the CME. Nevertheless the Chiral Magnetic Effect will result in a non-trivial behavior of *correlations* of electric charges as a function of the magnetic field, since non-trivial correlations of $F\tilde{F}$ are induced. As the resulting electric charge correlations dependent on the strength of the background magnetic field, they can be tested studying the centrality dependence of the correlations of charged particles on an event-by-event basis.

Anomalous Transport While the Chiral Magnetic Effect is the perhaps best known of a series of effects that related anomalous dynamics with the existence of magnetic fields or vorticity it is not exceptional: the inverse of the CME is the Chiral Separation Effect (CSE), which describes the creation of an axial current in the presence of a non-zero vector density

$$\mathbf{J}_5 = \sigma_v \mathbf{B}\,, \tag{1.19}$$

and we note that similar dynamics is induced by the so called Chiral Vortical Effect (CVE), which couples a vorticity $\boldsymbol{\omega} = \boldsymbol{\nabla} \times \boldsymbol{v}/2$, where $\boldsymbol{v}$ is the flow velocity field. In the latter case, analogous to the Chiral Magnetic Effect, a current is generated along a given vorticity $\boldsymbol{\omega}$ in the presence of an axial density. The chiral vortical effect is the exact equivalent of the CME with the magnetic field replaced by $\boldsymbol{\omega}$.

The interplay between the CME and the CSE can be easily understood to create new types of collective excitations. While for our previous discussion we have made use of a single particle picture, the emergent anomalous transport phenomena are best described by continuous currents and densities. The

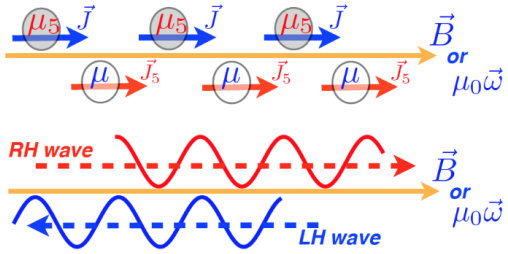

Figure 1.7: Pictographic representation of the Chiral Magnetic Wave, which is actually a chiral density wave. In analogy with the nature of Maxwell's equation, an interplay of the CME and CSE in connection with anomalous conductivities leads to the emergence of a (hydrodynamic) gap-less mode, which is non-dissipative. Figure taken from [16]

physics of the *Chiral Magnetic Wave* (and the Chiral Vortical Wave) has first been discussed within the framework of anomalous hydrodynamics: by plugging the constituent relations of vector and axial currents, which contain anomalous conductivities, into the (non-conservation) equations of vector and axial currents, one obtains a system of coupled equations for vector and axial charge densities. Then it can be shown that the system contains propagating modes (whereas in the absence of the anomalous conductivities only dissipative modes can exist). Moreover the collective excitations are found to be gap-less in the idealized limit of large magnetic fields and simple estimates predict a linear dispersion relation of these *chiral density waves*. Analogous the Chiral Vortical Wave is a similar excitation with the role of the magnetic field provided by a fluid vorticity. A schematic representation of the mechanisms behind chiral density waves is given in Fig. (1.7)

Experimental Status The current experimental status of the Chiral Magnetic and related effects in QCD is controversial (see [20]). The history of CME searches began in 2009 with the STAR collaboration presenting first results of the observation of azimuthal correlation between charged particles[28, 127]. As the CME is conjectured to induce charge separation along magnetic fields, which are usually perpendicular to the reaction plane of the collision Ψ_{RP}, the azimuthal distribution of particles (all particles, charged or identified) is written in the most general form as [20]

$$\frac{dN}{d\phi} \propto 1 + 2v_1 \cos(\phi - \Psi_{RP}) + 2v_2 \cos 2(\phi - \Psi_{RP}) + \cdots + 2a_{\pm} \sin(\phi - \Psi_{RP})\,. \tag{1.20}$$

Here ϕ is the angle in the azimuthal plane and Ψ_{RP} is the angle of the reaction plane in the lab frame. Further the v_n are the conventional flow coefficients and $a_+ = -a_- \propto \mu_5 B$ account for the effects of anomalous transport. Obviously Eq.(1.20) is a somewhat naive expression and needs further discussion.

As discussed above, QCD does not violate CP and P globally and thus the event average $\langle a_\pm \rangle = 0$, which is in agreement with experimental results. The signature of *local* $CP-$ and $P-$ violation in turn is a non-vanishing of the correlations of the azimuthal coefficients, $\langle a_\pm a_\pm \rangle \neq 0$. However since $\langle a_a a_b \rangle$ can only be measured with difficulties, equivalent observables have been proposed

$$\begin{aligned}\gamma &\equiv \langle \cos(\phi_a + \phi_b - 2\Psi_{RP}) \rangle = \langle \cos \Delta\phi_a \cos \Delta\phi_b \rangle - \langle \sin \Delta\phi_a \sin \Delta\phi_b \rangle \\ &= (\langle v_{1,a} v_{1,b} \rangle - \langle a_a a_b \rangle) + B_{in} - B_{out} \approx -\langle a_a a_b \rangle + B_{in} - B_{out} \,, \end{aligned} \tag{1.21}$$

where $B_{in,out}$ represents $P-even$ in- and out-of-plane background contributions and $\Delta\phi = \phi - \Psi_{RP}$. The Chiral Magnetic Effect predicts the observable γ to scale with the magnetic field, rising for more off-central collisions and moreover it is expected to be greater than zero for both same and opposite charge correlations. The effect was initially studied using $Au + Au$ and $Cu + Cu$ collisions at 62.4 GeV and 200 GeV. While the opposite charge correlations were shown to agree with qualitative expectations, the same charge correlations were found to even be negative for certain energies, which was later confirmed by LHC experiments [128].

It should be noted however that there is no prediction yet of the absolute magnitude of the γ correlator or similar observables and their respective backgrounds. A major source of uncertainty is background from elliptic flow from 'conventional' two-particle correlations. Accordingly, an improved correlation observable has been proposed, where reaction plane independent correlations are subtracted [129]. Recently the comparison of the γ correlator in $p + Pb$ and $Pb + Pb$ from the CMS experiment has put pressure on the CME interpretation, as the centrality/number of participants dependence of γ has been shown to be nearly identical in both systems, despite the fact the magnetic fields in $p + Pb$ are much smaller.

Apart from defining appropriate observables, which necessarily are P- and CP-even to understand phenomena with P- and CP-odd origins, large uncertainties arise from the incomplete understanding of the space-time evolution of heavy ion collisions. Fig. (1.8) serves as an illustration of the challenges associated with the quantitative understanding of the CME, as it puts anomalous and topological transport phenomena in context with the temporal stages of a heavy ion collision which we had outlined in section 1.3.1. Here the different regimes are illustrated, starting from the CGC/glasma initial conditions (a)-(b), continuing with the regime of instabilities and turbulence in a highly occupied plasma (c) towards the kinetic (d) and finally hydrodynamic regime (e). Classical statistical simulations [41–44, 46] are by now a widely used tool in quantum many-body systems far from equilibrium. As such they fit well to yield an accurate description of the early time regimes (a)-(c) depicted in Fig. (1.8): While the gluonic dynamics is dominated by coherent and highly occupied fields, the fermionic contribution to the initial state is negligible. However as field amplitudes are of order $1/g$, every process producing fermions is parametrically order one [52]. Thus fermion production is large and important at early times. Nevertheless, due to the Pauli principle, fermions are at most unit-

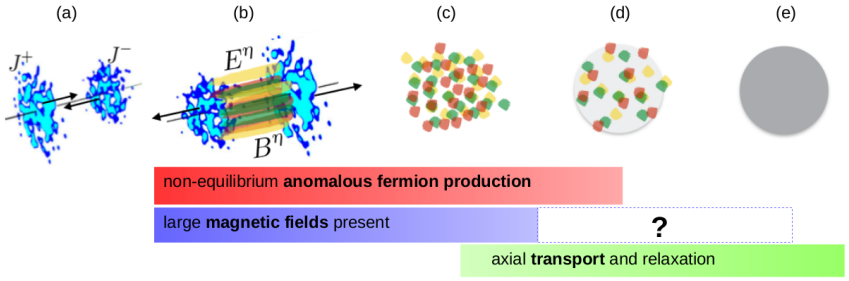

Figure 1.8: Schematic representation of the different stages of a heavy ion collision and the relevant regimes for the Chiral Magnetic Effect. Part of this figure is courtesy of Soeren Schlichting, Univ. of Washington and used with generous permission.

occupied and the gluons dominate the energy density at these stages. Quark production from large coherent color field configurations is studied in section 4. While flux tubes naturally provide large contributions to the anomaly via longitudinal field configurations $\propto \mathbf{E}^a \cdot \mathbf{B}^a$, it should be noted that topological transitions, such as sphalerons, exceed thermal rates by far for comparable energy densities in the far-from equilibrium glasma. Thus, the effects of the axial anomaly are extremely relevant at early times and the medium supporting anomalous transport is formed very quickly.

Theoretical approaches The lifetime of the magnetic field is typically very short [130–134] and while it has been speculated that, due to an anomalous conductivity induced quickly in the plasma, the duration of the magnetic field might be sustained longer [135–140], it is more likely that the magnetic field dies quickly and well before $t \approx 1\, fm/c$. Thus the early time regime, well captured by classical-statistical simulations, is the most crucial one for the phenomena of anomalous and topological transport effects.

As occupancies fall and the mean free path of quasi-particle excitations becomes large, the system enters a kinetic phase. Over the past years, kinetic descriptions of fermions have been developed, drawing a connection between the geometry of Berry phases [141], tied to the adiabatic approximation, and that of the anomaly [142–154]. These descriptions are so far only available for non-relativistic systems and the applicability to heavy ion collisions is under debate. In the kinetic regime the magnetic field has most likely fallen off. Nevertheless the axial- and vector- currents that were anomalously produced at earlier stages undergo transport and dissipation through the medium. As such they are exposed to local domains of topological charge of typical size Q_s^{-1} and – in the massive case – they undergo chirality changing scatterings with each other. This regime is subject to section 6, where we systematically develop a Lorentz covariant chiral kinetic theory. Moreover, we point out some shortcomings of previous approaches.

The perhaps most studied regime of the space-time evolution of a heavy ion collision is the strongly correlated stage in which hydrodynamics becomes applicable. Anomalous hydrodynamics [137, 155–159] is a very efficient tool to study the transport of axial and vector charges through the medium, but owing to its macroscopic nature, it requires input from the underlying microscopic theory. Utilizing transport coefficients as input from lattice computations, 'conventional' hydrodynamics has proven very successful in describing many observables such as flow. In regards to anomalous and topological properties this might prove difficult: as we hope to illustrate in this manuscript, the nature of anomalous transport out-of-equilibrium differ drastically from thermal predictions. Moreover, due to its topological nature, anomalous transport is dissipation-free and thus signatures produced at early times might survive the subsequent transport through the medium. Therefore it is of utmost importance to understand the initial conditions that go into anomalous hydrodynamic simulations from the far-from-equilibrium early time perspective.

Chapter 2

Basics

2.1 Non-equilibrium Quantum Field Theory

Time evolution in the context of modern quantum field theory can be understood by a two-fold approach – via the Hamiltonian operator formalism and by the formulation through the Schwinger-Keldysh contour. Not surprisingly both are fundamentally related. In this section we will give an introduction into real-time evolution in a quantum many-body context. The basics of this field have been long established [160–163] and can be found in many excellent textbooks [164–167]. This compact introduction is based on the book by Kamenev [166] and lecture notes by Berges [164, 165].

The perhaps more fundamental approach to time evolution is via Hamiltonian dynamics: Given a quantum many-body Hamiltonian operator $\hat{H}$ and a set of quantization rules, elevating the classical structure of phase space to the quantum equivalent of a many-body Hilbert space. The dynamics of an operator is then encoded in the Heisenberg equation of motion

$$\partial_t \mathcal{O} = i[\hat{H}, \mathcal{O}]. \tag{2.1}$$

As is evident from Eq.(2.1), and given $\hat{H}$ is defined from some quantum many-body theory, we see that for many cases time evolution in quantum field theory is analogous to what is already familiar from quantum mechanics – the difference being the many (most likely *infinitely* many) degrees of freedom. Nevertheless Eq.(2.1) is of little use in many situations: In the Hamiltonian approach (both in the Heisenberg and the Schrödinger picture) the dynamics of a system is encoded in terms of abstract *operators* and their corresponding Hilbert-space structures. Only in a very restricted set of situations an explicit representation of the latter two can be found (usually only for systems with very few degrees of freedom). An alternative approach to Eq.(2.1) is thus desirable and is given in terms of the Schwinger-Keldysh formulation of real-time path integrals.

To illustrate the latter approach we let the system of interest be specified by a time-dependent Hamiltonian and a density matrix (operator) $\hat{\rho}$ defined in

the infinite past. The density operator obeys the von-Neumann equation and its time dependence is given by

$$\hat{\rho}(t) = \hat{U}_{t,-\infty}\hat{\rho}(-\infty)\hat{U}_{-\infty,t}, \tag{2.2}$$

where $\hat{U}_{t,t'} = \mathcal{T}\exp -i\int_{t'}^{t} dt\,\hat{H}$ is the time-ordered time evolution operator. Accordingly the expectation value of some operator at given time is

$$\langle\mathcal{O}\rangle(t) = \frac{\mathrm{Tr}(\mathcal{O}\hat{\rho}(t))}{\mathrm{Tr}(\hat{\rho}(t))} = \frac{\mathrm{Tr}(\hat{U}_{-\infty,t}\,\mathcal{O}\,\hat{U}_{t,-\infty}\hat{\rho}(-\infty))}{\mathrm{Tr}(\hat{\rho}(t))}. \tag{2.3}$$

The rightmost trace, when read from right to left, can be understood in a pictorial way as comprising a two-way contour, which begins with $\hat{\rho}$ at $t = -\infty$ and is the continued to the insertion of $\mathcal{O}$ at finite time t and then winding back to $-\infty$, as is shown in Fig. (2.1). In the second equality of Eq.(2.3) we have used the cyclicity of the trace. We note that without loss of generality the

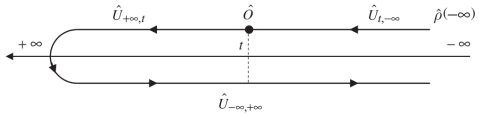

Figure 2.1: Pictographic representation of the trace of the density matrix in terms of the Schwinger-Keldysh contour. Figure taken from [166].

contour might start at finite time t_0; it furthermore can be extended to the future arbitrarily as forward and backward contours cancel if there is no insertion of an operator. The whole idea behind the Schwinger-Keldysh approach is to find a path integral representation of this contour.

Before we will proceed with the construction of the latter, we will try and connect the picture encoded in Fig. (2.1) to the 'usual' vacuum-to-vacuum' (in-out) approach to *time-independent* problems in quantum field theory. In such a case the initial density matrix describes either a thermal or a vacuum state and the time dependence is trivial. If $\hat{\rho} = |0\rangle\langle 0|$ and the initial vacuum is stable (i.e. evolves unitarily), the above closed time contour can be extended to $t = +\infty$ and the backward might be dropped. This can be understood as in this case the in-vacuum and the out-vacuum are simply related

$$|0\rangle_{in} = e^{i\theta}|0\rangle_{out}, \tag{2.4}$$

with θ being some phase that can be eliminated by proper normalization. We will now proceed with the more interesting case of an explicit time-dependent problem. From Eq.(2.3) such can be understood by finding a representation for

$$\mathrm{Tr}\left(\hat{U}_{\mathcal{C}}\hat{\rho}_0\right), \tag{2.5}$$

where we now have written $\hat{\rho}_0$ for the initial state density matrix at t_0 and $\hat{U}_{\mathcal{C}}$ is the evolution operator on the closed time contour. We illustrate this

construction using the simplest example of a scalar field theory, specified by the Hamiltonian (the exact form of this Hamiltonian matters only at the very end)

$$\hat{\mathcal{H}} = \frac{\hat{\pi}^2}{2} + \frac{(\nabla\hat{\phi})^2}{2} + \frac{m^2}{2}\hat{\phi}^2, \tag{2.6}$$

and $\hat{H} \equiv \int_{\boldsymbol{x}} \hat{\mathcal{H}}$. The trace in Eq.(2.5) can be represented by a complete set of states $|\phi^{\pm}\rangle$ with eigenvalues $\phi^{\pm}$ of the field operator acting on eigenstates at time t_0,

$$\mathrm{Tr}\left(\hat{U}_{\mathcal{C}}\hat{\rho}_0\right) = \int [d\phi^-]\langle\phi^-|\hat{U}_{\mathcal{C}}\hat{\rho}_0|\phi^-\rangle = \int [d\phi^-][d\phi^+]\langle\phi^-|\hat{U}_{\mathcal{C}}|\phi^+\rangle\langle\phi^+|\hat{\rho}_0|\phi^-\rangle\,, \tag{2.7}$$

where $[d\phi^{\pm}] = \prod_{\mathbf{x}} d\phi^{\pm}(\mathbf{x})$. This expression contains two parts: while $\langle\phi^+|\hat{\rho}_0|\phi^-\rangle$ is a matrix representation of the initial state, $\langle\phi^-|\hat{U}_{\mathcal{C}}|\phi^+\rangle$ is the forward and backward evolution of the system on the Schwinger-Keldysh contour. With some hindsight in notation we can write

$$\begin{aligned}\langle\phi^-|\hat{U}_{\mathcal{C}}|\phi^+\rangle &= \langle\phi^-|e^{-i\int_{t_f}^{t_i}\hat{H}dt}e^{-i\int_{t_i}^{t_f}\hat{H}dt}|\phi^+\rangle \\ &= \int [d\phi^N][d\phi^{N+1}]\langle\phi^-|e^{-i\int_{t_f}^{t_i}\hat{H}dt}|\phi^{N+1}\rangle\langle\phi^{N+1}|1|\phi^N\rangle\langle\phi^N|e^{-i\int_{t_i}^{t_f}\hat{H}dt}|\phi^+\rangle\,.\end{aligned} \tag{2.8}$$

Eq.(2.8) illustrates that the Schwinger-Keldysh construction actually comprises *two* path integrals, whose boundary conditions are identified at t_f and whose initial conditions are distributed according to the density matrix specified in Eq.(2.7). For both legs of the contour the path integral can be constructed using standard techniques: by discretization $t \to t_k$, $\delta t_k \equiv (t_k - t_{k-1})/N$ $(N \to \infty)$ and by insertion of conjugate momentum eigenstates $1 = \int [d\pi^{k,k-1}]\,|\pi^{k,k-1}\rangle\langle\pi^{k,k-1}|$, the following expression is found

$$\begin{aligned}\langle\phi^-|\hat{U}_{\mathcal{C}}|\phi^+\rangle = \int \Big(\prod_{k=1}^{2N-1}[d\phi^k]\Big)\Big(\prod_{\substack{k=1\\k\neq N+1}}^{2N}[d\pi^{k,k-1}]\Big)\delta[\phi^{N+1}-\phi^{N+1}] \\ \times \exp i\sum_{k=2}^{2N}\delta_k\int_{\boldsymbol{x}}\left(\pi_\mu^{k,k-1}\frac{\left[\phi^{k,\mu}-\phi^{k-1,\mu}\right]}{\delta_k} - \mathcal{H}(\pi^{k,k-1},\phi^k)\right),\end{aligned} \tag{2.9}$$

where it is understood that $\phi^0 = \phi^-$ and $\phi^{2N} = \phi^+$. As π appears at most quadratic in this expression, it might be integrated out. Taking the continuum limit we can then write

$$\mathrm{Tr}\left(\hat{U}_{\mathcal{C}}\hat{\rho}_0\right) = \int [d\phi^-][d\phi^+]\rho[\phi^-,\phi^+]\int_{\phi^-}^{\phi^+}\mathcal{D}\phi\,\exp\left(i\int_{\mathcal{C}} d^4x\,\mathcal{L}\right), \tag{2.10}$$

We have accounted for the orientation of the time integration by using the compact notation $\int_{\mathcal{C}} d^4x = \int_{\mathcal{C}} d^0x \int d^3x$, the $\mathcal{C}$ indicating contour integration as in Fig. (2.1). Here

$$\int_{\mathcal{C}} = \int_{t_0}^{t_f} dt - \int_{t_f}^{t_0} dt \,. \tag{2.11}$$

Eq.(2.10) is the central result of this section. While using a double time-contour might have seemed odd before going through the above construction, its interpretation is clear: The structure of the closed time contour accounts for *time ordering* which is equivalent with *operator ordering* in the Hamiltonian approach. With this interpretation in mind, Eq.(2.10) can be made more transparent. Provided we use the notation $\phi(t) \to \phi(t)^{\pm}$, with ϕ^+ (ϕ^-) having support only on the upper (lower) contour, we find that four combinations of two-point functions can be constructed, $\langle \phi^{\pm}(x), \phi^{\pm}(y) \rangle$, the propagator thus having a 2×2 matrix structure. By going to the Keldysh basis, we find an illustrative interpretation of the field components and their related propagators

$$\tilde{\phi} = \phi^+ - \phi^- \tag{2.12}$$

$$\bar{\phi} = \frac{\phi^+ + \phi^-}{2}. \tag{2.13}$$

Setting $\tilde{\phi} = 0$ in Eq.(2.10) corresponds to a saddle-point of the action, thus $\bar{\phi}$ is denoted the classical and $\tilde{\phi}$ the quantum field. This identification is the basis for the classical-statistical approximation discussed in section 2.3. In the Schwinger-Keldysh basis the matrix propagator is

$$G(x,y) = \begin{pmatrix} F(x,y) & -iG^R(x,y) \\ -iG^A & 0 \end{pmatrix}, \tag{2.14}$$

where F is the statistical propagator and $G^{A/R}$ are the advanced/retarded two-point functions. The spectral function is defined as $\rho(x,y) = G^R(x,y) - G^A(x,y)$. The explict expressions for the latter objects is

$$F(x,y) = \frac{1}{2}\langle \{\hat{\phi}(x), \hat{\phi}(y)\} \rangle - \langle \hat{\phi}(x) \rangle \langle \hat{\phi}(y) \rangle \tag{2.15}$$

$$\rho(x,y) = i\langle [\hat{\phi}(x), \hat{\phi}(y)] \rangle \tag{2.16}$$

$$G^R(x,y) = i\langle [\hat{\phi}(x), \hat{\phi}(y)] \rangle \theta(x^0 - y^0) \tag{2.17}$$

$$G^A(x,y) = -i\langle [\hat{\phi}(x), \hat{\phi}(y)] \rangle \theta(y^0 - x^0) \,, \tag{2.18}$$

and in the last two lines the theta function is understood in 'physical' time and *not* on the Schwinger-Keldysh contour. The technical details of specifying fields and correlation functions on the Schwinger-Keldysh contour is not the goal of this work and thus we refer the reader to [164, 165] for a very comprehensive overview. In the following section 2.3 we will make use of the closed path construction for gauge theories with fermions and we will derive what is known as the classical-statistical or truncated-Wigner approximation to the non-equilibrium path integral.

2.2 Lattice Gauge Theory

Quantum field theory has proven to be extremely successful in describing many-body systems, but comes with many caveats in its continuum formulation: regularization and renormalization are necessary but often tedious ingredients in tackling the emerging divergences in continuum quantum field theory. Many descriptions of how to regularize these divergences have been put forward, which have shown to be successful mostly in the context of perturbation theory. Most of these techniques follow the approach to regularize the theory by explicitly removing divergences from single diagrammatic computations – instead of regularizing the theory itself on the basis of the path integral. One such – more universal – approach to renormalization is the renormalization group [168] and more specifically the function renormalization group framework (FRG) [169–171]. This very powerful technique has shown to be highly successful and accurate in describing quantum many-body systems at arbitrary coupling.

In this thesis we will be concerned with the dynamics of *gauge theories*, so that any regularization procedure that we will employ must respect the demands of *gauge symmetry*. Any regularization must obey the *Ward-identities* related to the gauge symmetry under consideration. A very powerful and natural regularization description that is applicable for gauge theories are *lattice gauge theories* [172–175]. As the center of this work is on real-time dynamics, we will in the following focus on the Hamiltonian formulation of lattice gauge theory [176], which we will outline below in detail and we will connect to the Schwinger-Keldsyh path integral formalism as well .

The basic idea behind the Hamiltonian formulation of lattice gauge theory in 3+1 dimensions is to discretize space on a hyper-cubic lattice of N_i lattice sites for each dimension $i = x, y, z$

$$\mathbf{x} = (x^1, x^2, x^3) \to (n^1 a_1, n^2 a_2, n^3 a_3), \qquad n^i \in 0, \dots, N_i - 1, \tag{2.19}$$

while time is left continuous (but can be discretized as well for the closed time contour construction). The inverse distance a_i^{-1} plays the role of a UV cutoff of the theory, as excitations with a shorter wave length obviously cannot be described. In the following we assume temporal-axial gauge $A^0 = 0$, which is beneficial in our case. Matter field are accordingly defined on the sites of the lattice $\phi(\mathbf{x}) \to \phi(\mathbf{n})$ with spatial derivatives discretized accordingly

$$\nabla^i \phi(\mathbf{n}) \equiv \frac{\phi(\mathbf{n} + \hat{\mathbf{i}}) - \phi(\mathbf{n} - \hat{\mathbf{i}})}{2\, a_i} \,. \tag{2.20}$$

Gauge theories The lattice now allows for a very illustrative understanding of what a gauge theory is [177]: We note that in the continuum the gauge covariant derivative is given by

$$D_\mu \phi = \partial_\mu \phi + igA\phi, \tag{2.21}$$

where A can be Lie-group valued. Now let P be a finite path going from one space point $\mathbf{x}_0$ to another $\mathbf{x}_1$. Let us require that the covariant derivative of

the scalar field vanishes along that path (parallel transport), parametrized by $s \in [0,1]$

$$\frac{dx^\mu}{ds} D_\mu \phi = 0 \qquad \equiv \qquad \frac{d\phi}{ds} = -ig \frac{dx^\mu}{ds} A\phi \tag{2.22}$$

The solution of this equation is given by

$$\phi(\mathbf{x}_1) = g(P)\phi(\mathbf{x}_0), \qquad g(P) \equiv \mathcal{P} \exp\left(-ig \int_0^1 ds \frac{dx^i}{ds} A_i\right). \tag{2.23}$$

Now imagine that the path P would start at one lattice site $\mathbf{n}_0$ and ends at another $\mathbf{n}_1$: if we assume a_i to be small, then A_i is approximately constant on every path. Thus knowing $g(P)$ for every connection between two lattice sites is equivalent to knowledge of A_i everywhere on the lattice. Thus we define the fundamental object describing gauge fields on a lattice, which we call a gauge link as

$$U_{i,\mathbf{n}} \equiv \exp\left(iga_i A_i(\mathbf{n})\right). \tag{2.24}$$

Formulating gauge theories on a lattice using Eq.(2.24) results in defining a regularized theory that maintains gauge co-/invariance. Accordingly we can formulate the Hamiltonian of a $SU(N_c)$ gauge theory on the lattice (in temporal-axial gauge)

$$H = \frac{a^3}{2} \sum_{\mathbf{n},i,a} E^a_{i,\mathbf{n}} E^a_{i,\mathbf{n}} + \frac{2N_c}{g^2 a} \sum_{\mathbf{n},i<j} \left(1 - \frac{1}{2\,N_c} \mathrm{tr}[U_{ij,\mathbf{n}} + h.c.]\right). \tag{2.25}$$

Here we have defined the gauge covariant plaquette variable

$$U_{ij,\mathbf{n}} \equiv U_{i,\mathbf{n}} U_{j,\mathbf{n}+\hat{\mathbf{i}}} U^\dagger_{i,\mathbf{n}+\hat{\mathbf{j}}} U^\dagger_{i,\mathbf{n}}\,, \tag{2.26}$$

which in the limit of small lattice spacing a is related to the field strength tensor $F_{n,ij} = F^a_{n,ij} t^a$, where t^a are the generators of $SU(N_c)$ in the fundamental representation,

$$U_{ij,\mathbf{n}} \approx 1 + iga_i a_j F_{n,ij} + \mathcal{O}(a^4 F^2)\,. \tag{2.27}$$

Further we have introduced the conjugate momentum variable $\mathbf{E}^a_n$ (the electric field). Using Eq.(2.27) and the (unimproved) definition of the magnetic field $B_{i,\mathbf{n}} = B^a_{i,\mathbf{n}} t^a$

$$B^a_{i,\mathbf{n}} = -\frac{1}{2}\epsilon^{ijk} F^{jk}_n \approx \frac{i}{g a_j a_k} \epsilon^{ijk} \mathrm{Tr}\; t^a U_{jk,\mathbf{n}} \tag{2.28}$$

it can be shown that in the continuum limit $a \to 0$, $a^3 \sum_n \to \int d^3x$ the well-known result for the Hamiltonian is recovered

$$H = \frac{1}{2} \int d^3x\, \mathrm{Tr}\left(\mathbf{E}^2 + \mathbf{B}^2\right). \tag{2.29}$$

Similarly the Hamiltonian definition of lattice gauge theory can be extended to an action formalism. To this end, we introduce discretized time $t \to t_k = n_k^t a_t$, where $a_t \ll a_i$ is the lattice spacing in the time direction. We emphasize however that in practice there is no need to treat the time direction via a lattice description; when solving time evolution equations on a computer we necessarily need to discretize time. This is a technical requirement and should not be seen as a fundamental property of our description. The lattice *action* is given as

$$S = \frac{2N_c}{g^2} \sum_{\mathbf{n}} \left\{ \sum_i \frac{a_i}{a_t} \left(1 - \mathrm{Tr}[U_{0i,\mathbf{n}} + h.c.]\right) - \sum_{i<j} \frac{a_t}{a_i} \left(1 - \frac{1}{2N_c} \mathrm{Tr}[U_{ij,\mathbf{n}} + h.c.]\right) \right\} \tag{2.30}$$

where the electric field can be related to the temporal plaquette

$$E^a_{i,\mathbf{n}} = -\frac{i}{2g a_i a_t} \mathrm{Tr}\ t^a U_{0i,\mathbf{n}}. \tag{2.31}$$

We note that while we have written all fields with spatial subscript $\mathbf{n}$, in the continuous time formulation they are to be understood as functions of t, whereas the electric field in the case of a discretized temporal direction is defined at the center between two time steps $(t_k + t_{k+1})/2$. Similarly spatial links $U_{i,\mathbf{n}}$ are defined at $\mathbf{n} + \hat{i}/2$. Magnetic fields are defined at the center of the plaquette from which they are defined (see Eq.(2.28)). We note that the definition of the gauge Hamiltonian Eq.(2.25) and the corresponding electric and magnetic fields is the simplest possible. Accordingly improved gauge Hamiltonians are possible, but shall not be discussed in this thesis for the gauge sector [178].

Lattice Fermions We now proceed to the definition of a fermion Hamiltonian on the lattice, which is a complicated issue when compared to the gauge sector. The naive discretization of the well known Dirac-Hamiltonian introduces spurious artificial degrees of freedom on the lattice: *fermion doublers*. The emergence of so-called fermion doublers can be understood from the lattice-dispersion relation of fermions and, while it might seem as a defect of our formulation, fermion doublers are related to profound mechanisms. In this section we give an introduction into the simplest formulation of lattice fermions using both massive Wilson fermions as well as massless lattice fermions by means of the overlap discretization description. The following two subsections contain material that might also be found in various textbooks [173–175]. In section 5 we present for the first time how operator improvements for Wilson fermions can be introduced in the context of real-time evolution and moreover we present the (to our knowledge) first ever real-time simulation of chiral lattice fermions.

The appearance of lattice doublers, when defining fermions on the lattice can be understood as follows: The naive lattice Hamiltonian (in the absence of gauge fields) is given by

$$H_{naive} = \frac{a^3}{2} \sum_{\mathbf{x}} [\hat{\psi}^\dagger_{\mathbf{x}}, \gamma^0 \left(-i \not{D} + m\right) \hat{\psi}_{\mathbf{x}}], \tag{2.32}$$

where $\sum_{\mathbf{x}} \equiv a^3 \sum_{\mathbf{n}}$ the discretized Dirac operator is given as follows

$$-i\not{D}\hat{\psi}_{\mathbf{x}} = \frac{-i}{2a}\sum_i \left(\gamma^i[\hat{\psi}_{\mathbf{x}+\hat{i}} - \hat{\psi}_{\mathbf{x}-\hat{i}}]\right) \tag{2.33}$$

The eigenvectors and eigenfunctions to Eq.(2.32) can be easily found. As in the continuum formulation, particle and anti-particle solutions are found which read

$$\begin{aligned}\phi^u_{\lambda,\tilde{\mathbf{p}}}(\mathbf{x}) &= u_{\mathbf{p},\lambda} e^{-i\mathbf{p}\cdot\mathbf{x}+i\omega_{\tilde{p}}}\,,\\ \phi^v_{\lambda,\tilde{\mathbf{p}}}(\mathbf{x}) &= v_{\mathbf{p},\lambda} e^{+i\mathbf{p}\cdot\mathbf{x}-i\omega_{\tilde{p}}}\,,\end{aligned} \tag{2.34}$$

where u/v are (anti-)particle spinors that we shall leave unspecified for now. In our notation $\lambda = \pm$ denotes different chirality/helicity- components. The eigenfunctions of the Hamiltonian Eq.(2.32) are specified on the conjugate lattice $\tilde{\Lambda}$ with

$$\tilde{\Lambda} = \{\mathbf{q} | q_i \in -N_i/2, \ldots, N_i/2 - 1\}, \qquad p_i \equiv \frac{2\pi}{N_i\, a_i} q_i\,. \tag{2.35}$$

The corresponding momentum eigenvalue to a point on the conjugate lattice is given as

$$\tilde{\mathbf{p}} \equiv (\tilde{p}^1, \tilde{p}^2, \tilde{p}^3), \qquad \tilde{p}^i = \frac{1}{a_i}\sin\left(2\pi\frac{q_i}{N_i}\right) = \frac{1}{a_i}\sin\left(p_i a_i\right) \tag{2.36}$$

which is found by plugging Eq.(2.34) into Eq.(2.32) and is depicted in Fig. (2.2). The corresponding energy eigenvalue is

$$\omega = \sqrt{m^2 + \sum_i \tilde{p}_i^2}\,. \tag{2.37}$$

The continuum limit of Eq.(2.36) is found for $a \to 0$. As can be seen from Fig. (2.2) this limit is obtained not only at $p_i = 0$, but also at $p_i = \pm\pi/a_i$, the latter being nonphysical: the naive discretization of the Dirac Hamiltonian produces $2^d - 1$ unphysical degrees of freedom called *doublers* (where d is the spatial dimension)[1] Lattice doublers have been found in earliest attempts at discretizing fermionic actions and to this end many possible approaches have been proposed. In the following section we follow an idea due to Wilson [172] to remove fermion doubler from the spectrum. We will modify the dispersion relation of lattice fermions by introduction of irrelevant operators into the Hamiltonian Eq.(2.32). These will cause the fermion doublers to be very massive, so that they cannot be excited. This modification comes at the price of being unable to define *chiral* lattice fermions. This 'trade-off' has been understood as being part of a very general theorem due to [179–181]. In lattice simulation of fermions one can only achieve two off the following properties, but never all three at the same time:

[1] We note that in principle temporal doublers might be excited as well, if time is discretized in order to solve the dynamics of a system specified by Eq.(2.32) numerically. In practice this problem is of no relevance, provided the time-discretization is fine enough.

1. chiral symmetry

2. anomalies

3. locality

The appearance of the anomaly in this list is very intriguing and a crucial component of this thesis, which discuss in more detail in section 5. The above list can understood as follows: Lattice regularization is regularization on the basis of the path integral and not on the basis a-posteriori regularization of emerging diagrams and n-point functions, thus it is a 'perfect' regularization in the sense that it cannot have anomalies. We know however that anomalies are physical and hence in a naive lattice discretization anomalies must be canceled by additional degrees of freedom. This role is played by the doublers as has been proven by [179, 182]. Wilson fermions break chirality explicitly and the axial anomaly is recovered from the regulator terms in the continuum limit. We will discuss them in the following section 2.2.1. A further, perhaps more exotic approach, is to give up locality. In this case we can have a chiral theory with anomalies, but the theory becomes non-local. In section 2.2.2 we will discuss the concept of so-called overlap-fermions as an example of such a non-local formulation of lattice fermions.

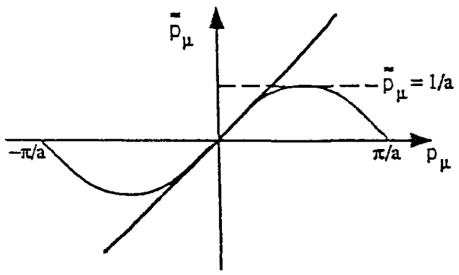

Figure 2.2: Plot of the fermion dispersion relation versus the Brioullin zone. Figure taken from [173].

2.2.1 Wilson Fermions

Wilson fermions [172] are as simple attempt to overcome the fermion doubling problem. The Wilson-Dirac Hamiltonian, including interactions with gauge fields, is given by

$$H_W = \frac{a^3}{2} \sum_{\mathbf{x}} [\hat{\psi}^\dagger_{\mathbf{x}}, \gamma^0 \left(-i \not{D}_W + m\right) \hat{\psi}_{\mathbf{x}}] \,, \tag{2.38}$$

where the action of the Wilson-Dirac operator simply is

$$-i\not{D}_W\hat{\psi}_{\mathbf{x}} = \frac{1}{2}\sum_i \left[\left(-i\gamma^i - r_W\right) U_{\mathbf{x},i}\hat{\psi}_{\mathbf{x}+\hat{i}} + 2r_w\hat{\psi}_{\mathbf{x}} + \left(i\gamma^i - r_W\right) U_{\mathbf{x},-i}\hat{\psi}_{\mathbf{x}-\hat{i}}\right] \tag{2.39}$$

where $U_{\mathbf{x},-i} \equiv U^{\dagger}{}_{\mathbf{x}-\hat{i},i}$. The fermion operators obey the usual anti-commutation relations

$$\{\hat{\psi}_{\mathbf{x},a}, \hat{\psi}^{\dagger}_{\mathbf{y},b}\} = V\delta_{\mathbf{x},\mathbf{y}}\delta_{a,b}\,, \tag{2.40}$$

where a, b stand for both spinor and any other internal degrees of freedom and $V = \prod_i N_i a_i$ is the lattice volume. Here $U_{\mathbf{x},i}$ stand for the link operators defined above. The dispersion relation of Wilson fermions is now given as

$$\omega = \sqrt{\tilde{m}^2_{\mathbf{q}} + \sum_i \tilde{p}_i^2}\,, \tag{2.41}$$

where $\tilde{p}_i$ is given in Eq.(2.36) and

$$\tilde{m}^2_{\mathbf{q}} = m^2 + r_w \sum_i \frac{2}{a_i}\sin^2\left(\pi\frac{q_i}{N_i}\right)\,. \tag{2.42}$$

As can be understood from Fig. (2.2) the degeneracy between the continuum modes and the doublers is lifted by the momentum dependent mass term Eq.(2.42). The fermion doublers are supressed from the spectrum of the theory. In section 4 we discuss the role of Wilson fermions in the realization of the axial anomaly explicitly. In section 5 we introduce *operator improvements* to systematically remove lattice discretization errors and to improve their convergence towards the continuum limit.

2.2.2 Overlap Fermions

In this section we give a short introduction into the concept of overlap fermions [183–185] in a Hamiltonian formulation [186]. This has been worked out in detail in [187], which is presented in section 5 of this thesis. Overlap fermions are an explicit realization of domain-wall fermions, which have been introduced by Kaplan [188]. The idea behind domain-wall fermions is to introduce an artificial fifth dimension with a background potential (a mass term) for the fermions that is given by a domain wall at the origin of that dimension. Rather than discussing the details of this idea, which are nicely illustrated in [189], we here focus on the explicit realization on the lattice. The Hamiltonian operator for massless overlap fermions is

$$H_{ov} = \frac{1}{2}\sum_{\mathbf{x}}[\hat{\psi}^{\dagger}_{\mathbf{x}}, \gamma^0(-i\not{D}_{ov})\hat{\psi}_{\mathbf{x}}]\,, \tag{2.43}$$

where the 3D spatial Dirac operator is now given as

$$-i\not{D}_{ov} = M\left(\mathbb{I} + \frac{\gamma^0 H_W(M)}{\sqrt{H_W^2(M)}}\right) \tag{2.44}$$

where $H_W(M)$ is the original Wilson Hamiltonian operator kernel defined in section 2.2.1, but with the mass m being replaced by the negative of the parameter M, which represents the domain wall height that localizes chiral fermions on 4D Euclidean spacetime, starting from a 5D domain-wall formalism [188].

$$H_W = \gamma^0(-i\not{D}_W - M) \tag{2.45}$$

For all practical purposes we can treat M as a free parameter, for which we need to find an optimal value to guarantee best convergence to the continuum. The domain wall height takes values $M \in (0, 2]$ in units of the inverse lattice spacing. The overlap Dirac operator for massless quarks in three spatial dimensions fulfill the lattice chirality condition, which is given by the Ginsparg-Wilson relation [190],

$$\{\not{D}_{ov}, \gamma_5\} = -i\not{D}_{ov}\gamma_5\not{D}_{ov}\,. \tag{2.46}$$

In addition the overlap Dirac operator is γ_0-Hermitian and thus satisfies

$$\{\not{D}_{ov}, \gamma_0\} = -i\not{D}_{ov}\gamma_0\not{D}_{ov}\,. \tag{2.47}$$

Accordingly, we define the axial charge operator as

$$Q_5 = \frac{1}{2}\sum_{\mathbf{x}}\left[\hat{\psi}^\dagger_{\mathbf{x}}, \gamma_5\left(1 - \frac{-i\not{D}_{ov}}{2}\right)\hat{\psi}\right]\,, \tag{2.48}$$

and it can be shown (see [187] and references therein) that $[H, Q_5] = 0$. Therefore we can write

$$\frac{dQ_5}{dt} = \frac{\partial Q_5}{\partial t}\,. \tag{2.49}$$

The time dependence of the axial density operator Q_5 is thus solely due to the explicit time evolution of the field operators contained in Eq.(2.48). In the overlap formulation axial charge is generated in exactly the same way as in the continuum. More general, in the overlap formulation we can define axial- and vector-currents by the use of chiral projectors. Left- and right-handed fermion fields can be defined in terms of the lattice projection operators $\hat{P}_\pm$ as

$$\hat{\psi}_{R/L} = \frac{1}{2}(\mathbb{I} \pm \hat{\gamma}_5)\hat{\psi} \equiv \hat{P}_\pm\hat{\psi}\,, \quad \hat{\gamma}_5 = \gamma_5(1 + i\not{D}_{ov})\,. \tag{2.50}$$

In contrast, projection operators for the conjugate fields are defined as

$$\hat{\psi}^\dagger_{R/L} = \hat{\psi}^\dagger\frac{1}{2}(1 \pm \gamma_5) \equiv \hat{\psi}^\dagger P_\pm \tag{2.51}$$

Currents might be defined from the variation of the Hamiltonian, or in analogy to the continuum by constructing these quantities in terms of the physical left and right-handed fermion modes [191, 192]. Based on this approach, the vector current for overlap fermions in real-time is constructed as

$$\begin{aligned} j_v^\mu &= \frac{1}{2}\langle[\hat{\psi}_R^\dagger, \gamma_0\gamma^\mu\hat{\psi}_R]\rangle + \frac{1}{2}\langle[\hat{\psi}_L^\dagger, \gamma_0\gamma^\mu\hat{\psi}_L]\rangle \\ &= \frac{1}{2}\langle[\hat{\psi}^\dagger, \gamma_0\gamma^\mu\Big(\mathbf{1} - \frac{-i\not{D}_{ov}^s}{2}\Big)\hat{\psi}]\rangle; \end{aligned} \tag{2.52}$$

similarly the axial current is

$$\begin{aligned} j_a^\mu &= \frac{1}{2}\langle[\hat{\psi}_R^\dagger, \gamma_0\gamma^\mu\hat{\psi}_R]\rangle - \frac{1}{2}\langle[\hat{\psi}_L^\dagger, \gamma_0\gamma^\mu\hat{\psi}_L]\rangle \\ &= \frac{1}{2}\langle[\hat{\psi}^\dagger, \gamma_0\gamma^\mu\gamma_5\Big(\mathbf{1} - \frac{-i\not{D}_{ov}^s}{2}\Big)\hat{\psi}]\rangle\ . \end{aligned} \tag{2.53}$$

We note that the Hamiltonian formulation of overlap fermions in Minkowskian metric is non-trivial and therefore we present some details in appendix B.3. Furthermore we give an illustration of the numerical implementation of overlap fermions there. We remark that our results for the Hamiltonian formulation agree with [186]. As part of section 5 we will extend our discussion of Wilson and overlap fermions by including operator improvements.

2.3 The classical statistical approximation

In this section we introduce the classcial-statistical approximation [48, 51, 52, 119, 193–197] used in far-from-equilibrium situations of various quantum many-body systems. The motivation for this approach is the following: often quantum-many-body systems behave quasi-classical if systems are highly occupied or dominated by large coherent fields, such that the correspondence principle becomes applicable. In concert with our general dual approach to non-equilibrium physics via both the Hamiltonian and the Schwinger-Keldysh construction, we will here give a short but hopefully instructive introduction into the subject and refer the reader to [196] for more details.

The Schwinger-Keldysh constructions allows to formulate the classical-statistical limit explicitly by means of a saddle-point expansion of the quantum fields around the classical fields defined in Eq.(2.12). To begin with the generating functional of non-equilibrium correlation functions is given as

$$\mathcal{Z} = \int \mathcal{D}A \int \mathcal{D}\bar{\psi}\mathcal{D}\psi\, \rho(t_0)\, \exp\left(iS_G + iS_F\right), \tag{2.54}$$

where the field space measure is defined on the Schwinger-Keldysh contour as

outlined in section 2.1. The different parts of the action are given by

$$S_G = -\frac{1}{4}\int_{\mathcal{C}} d^4x\, F^{\mu\nu}(x)F_{\mu\nu}(x)$$
$$S_F = \int_{\mathcal{C}} d^4x\, \bar{\psi}(x)\left(i\gamma^\mu\partial_\mu - e\gamma^\mu A_\mu - m\right)\psi(x) \tag{2.55}$$

and for simplicity we have restricted ourselves to Abelian gauge fields. We make the assumption that the initial density matrix ρ is separable into a fermionic and bosonic part and is at most quadratic in the fermion fields. The corresponding expression then reads

$$\rho(t_0) = \exp\left(-\int d^3x d^3y\, \bar{\psi}(\mathbf{x})\kappa^{-1}(\mathbf{x},\mathbf{y})\psi(\mathbf{y})\right)\rho(A(t_0))\,, \tag{2.56}$$

where the kernel κ^{-1} specifies the initial Gaussian state of the fermions. For all practical purposes we need not to specify what κ^{-1} is since, as we shall show, we will find a much simpler and more intuitive form for the fermion real time evolution and instead of defining the initial density matrix, we will set-up initial conditions for the fermionic one- and two-point correlations. In the following we will omit writing κ^{-1} explicitly therefore. We will now proceed to derive the classical statistical limit and to this end, we express the action defined in Eq.(2.55) in the Keldysh-basis for the gauge fields

$$A^+_\mu(x) = \bar{A}_\mu(x) + \frac{\tilde{A}_\mu(x)}{2}$$
$$A^-_\mu(x) = \bar{A}_\mu(x) - \frac{\tilde{A}_\mu(x)}{2} \tag{2.57}$$

In this basis the gauge part of the action can be written as

$$S_G = \int_{\mathcal{C}^+} d^4x\, \tilde{A}_\nu(x)\partial_\mu F^{\mu\nu}[\bar{A}(x)], \tag{2.58}$$

which is linear in $\tilde{A}$. In the case of non-Abelian gauge theories three- ($\propto \tilde{A}\bar{A}\bar{A}$, $\propto \tilde{A}\tilde{A}\tilde{A}$) and four-point vertices ($\propto \tilde{A}\bar{A}\bar{A}\bar{A}$, $\propto \tilde{A}\tilde{A}\tilde{A}\bar{A}$) will arise as well (c.f. [196]). The fermionic part of the action is treated as follows: by performing the Grassmanian integration the one-loop fermionic action is obtained

$$\int \mathcal{D}\bar{\psi}\mathcal{D}\psi\, \exp\left(i\int_{\mathcal{C}} d^4x\, \bar{\psi}[i\gamma^\mu\partial_\mu - e\gamma^\mu A_\mu - m]\psi\right) = \det i\Delta^{-1}\,, \tag{2.59}$$

where $\Delta^{-1} \equiv i\gamma^\mu\partial_\mu - e\gamma^\mu A_\mu - m$. From this the fermionic effective action is defined as

$$\det i\Delta^{-1} = \exp \mathrm{tr}\log(i\Delta^{-1}). \tag{2.60}$$

By means of the classical-statistical the effective action defined by Eq.(2.59) is expanded to linear order in the quantum field $\tilde{A}$. To this end we define

$$\begin{aligned}\Delta^{>}(x,y) &= \langle\psi(x)\bar{\psi}(y)\rangle_{\bar{A}} \\ \Delta^{<}(x,y) &= -\langle\bar{\psi}(y)\psi(x)\rangle_{\bar{A}}\end{aligned} \tag{2.61}$$

and $\langle\dots\rangle_{\bar{A}}$ denotes the operator expectation value in the background of the classical field $\bar{A}$. Thus the fermionic effective action in the classical statistical limit is written as

$$\mathrm{tr}\log\left(i\Delta\right) = -i\int\limits_{\mathcal{C}^+} d^4x\,\left[\Delta^{>}(x,x)+\Delta^{<}(x,x)\right]\frac{\tilde{\not{A}}}{2} \equiv -i\int\limits_{\mathcal{C}^+} d^4x\,\bar{j}^\mu\tilde{A}_\mu. \tag{2.62}$$

From this expression we can identify the fermionic current and define it in terms of the statistical propagator F

$$\bar{j}^\mu(x) = e\,\mathrm{tr}\left(\gamma^\mu F(x,x)\right), \qquad F(x,y) \equiv= \langle[\psi(x),\bar{\psi}(y)]\rangle_{\bar{A}} \tag{2.63}$$

The resulting Schwinger-Keldysh path integral is given as

$$\mathcal{Z} = \int\mathcal{D}\bar{A}\mathcal{D}\tilde{A}\,\rho(A)\exp i\int\limits_{\mathcal{C}^+} d^4x\,\tilde{A}_\nu(x)\left(\partial_\mu F^{\mu\nu}[\bar{A}(x)]-\bar{j}^\mu(x)\right), \tag{2.64}$$

and we note that the path integral integration can be split into a part at $t=t_0$, which comprises the initial conditions, and a part for $t>t_0$: $\mathcal{D}\tilde{A} = \mathcal{D}\tilde{A}_0\mathcal{D}\tilde{A}'$. We further write the initial density matrix as a Wigner transform, where E_0 is the conjugate field at t_0 (c.f. [196]) and $\rho_W(\bar{A}_0,\Pi_0)$ is the initial phase space density

$$\rho(A) = \int d\Pi_0\,\rho_W(\bar{A}_0,E_0)\,\exp\left(i\int d^3x\,E_0^\mu(\mathbf{x})A_{0,\mu}(\mathbf{x})\right). \tag{2.65}$$

The integral over $\mathcal{D}\tilde{A}_0$ then extracts ρ_W and the integral over $\mathcal{D}\tilde{A}'$ results in a functional delta function

$$\mathcal{Z} = \int\mathcal{D}\bar{A}_0\mathcal{D}\bar{A}'\int\mathcal{D}E_0\,\rho_W(\bar{A}_0,E_0)\,\delta\left(\partial_\mu F^{\mu\nu}[\bar{A}']-\bar{j}^\nu\right) \tag{2.66}$$

Eq.(2.66) is the central result of this section, it illustrates the meaning of the classical-statistical approximation nicely: The approximation amounts to solving the classical equations of motions for the c-number fields $\bar{A}$, whose initial conditions are sampled from an arbitrary phase-space distribution ρ_W. Observables are then calculated as ensemble averages with respect to these initial conditions. We further note that the current specified in Eq.(2.63) is obtained by inverting Δ^{-1}. This is equivalent to solving

$$\left(i\not{\partial}-e\not{A}-m\right)F(x,y) = 0\,. \tag{2.67}$$

The path integral formulation of gauge theories requires a careful treatment of gauge symmetry. Aiming at describing time dependent problems, we fix the axial-temporal gauge $A_0 = 0$. Variation of the gauge action Eq.(2.55) wrt. A_0 yields the well known (Abelian) Gauss constraint

$$\partial_i E^i = -\bar{j}^0 \,, \tag{2.68}$$

where $\bar{j}^0$ is the charge density and $\mathbf{E} = \partial_t \mathbf{A}$ is the electric field. Eq.(2.68) must be imposed on the initial conditions, specified by the initial density matrix and is guaranteed to be satisfied at any later time, as the equations of motion conserve the constraint.

We further note that the same limit could have been obtained in the Hamiltonian perspective by simply replacing the operators in the Heisenberg equation of motion by their expectation values. For comparison we will outline this approach as well – this time however in lattice formulation and for $SU(N_c)$ gauge fields for completeness. The Hamiltonian is defined as $H = H_f + H_G$, with H_G defined in Eq.(2.25) and H_f defined in Eq.(2.38), that is we outline the procedure for fermions using Wilson discretization. Furthermore we have the commutator rules for the field *operators*

$$\begin{aligned}
[E^a_{j,n}, A^b_{i,m}] &= i\delta_{ij}\delta_{nm}\delta^{ab}\frac{1}{a_1 a_2 a_3}, \\
[E^a_{j,n}, E^b_{i,m}] &= [A^a_{j,n}, A^b_{i,m}] = 0 \\
[E^a_{j,n}, U_{i,m}] &= -\frac{g a_i}{a_1 a_2 a_3}\delta_{ij}\delta_{nm} t^a U_{i,m} \\
[E^a_{j,n}, U^\dagger_{i,m}] &= \frac{g a_i}{a_1 a_2 a_3}\delta_{ij}\delta_{nm} U^\dagger_{i,m} t^a
\end{aligned} \tag{2.69}$$

Operator time evolution is then due to the Heisenberg equations Eq.(2.1), the result of which is

$$\frac{dE^a_{i,n}}{dt} = \frac{2}{ga^3}\sum_{j\neq i} \text{Im tr}\,(t^a[U_{ij,n} + W_{ij,n}]) + \frac{g}{2}\text{Re tr}\left([\psi_{n+1}, \bar{\psi}_n](\gamma^i - ir)t^a\right) \tag{2.70}$$

where $W_{ij,n} = U_{i,n}U^\dagger_{j,n-\hat{j}+\hat{i}}U^\dagger_{n-\hat{j}}U_{j,n-\hat{j}}$ and $U_{ij,n}$ is the plaquette defined in Eq.(2.26). The time evolution of the links is given by

$$\frac{dU_{i,n}}{dt} = iga_i t^a U_{i,n}\, E^a_{i,n} \,. \tag{2.71}$$

In accordance with the path integral approach outlined above, the Gauss law must be imposed for the initial conditions of the lattice gauge field evolution. In the Hamiltonian formulation there is no variational principle that might give the equivalent of Eq.(2.68). The Gauss constraint should rather be understood as an operator valued identity projecting out the physical part of the Hilbert

space. In lattice formulation the non-Abelian Gauss constraint reads

$$\sum_i \left[\mathrm{tr}\left((t^a U_{0i,n}\right) - \mathrm{tr}\left(t^a U^\dagger_{i,n-\hat{i}} U_{0j,n-\hat{i}} U_{i,n-\hat{i}} \right) \right] = -\frac{g}{2} \mathrm{Re\ tr}\left([\hat{\psi}_n, \hat{\bar{\psi}}_n] \gamma^0 t^a \right) \tag{2.72}$$

Eq.(2.72) commutes with the Hamiltonian and is thus conserved.

It should be noted that Eq.(2.70) and Eq.(2.71) are operator valued evolution equations. The classical statistical approximation now consists of the assumption that the gauge field operators can be replaced by their expectation value. In a slight abuse of notation we will use the same symbol for both the expectation value as well as the operator itself, as the difference should always be clear from the context. Time evolution in the fermion sector is obtained in a similar fashion. The canonical anti-commutation relations are given by

$$\{\psi^{\dagger,a}_n, \psi^b_m\} = \frac{1}{a^d} \delta_{nm} \delta_{ab} \mathbb{I}\,, \tag{2.73}$$

where $\mathbb{I}$ is a unit matrix in spinor space. Therefore the time evolution of the fermion field operator is given by

$$\frac{d\psi^a_n}{dt} = -i \left(m + r \sum_i \frac{1}{a_i} \right) \gamma^0 \psi^a_n + i \sum_{i,b} \frac{\gamma^0}{2a_i} \left([i\gamma^i + r] U^{ab}_{i,n} \psi^b - [i\gamma^i - r] U^{ab}_{-i,n} \psi^b \right) . \tag{2.74}$$

A crucial difference to the treatment of the gauge degrees of freedom is that a classical limit of Eq.(2.74) does not exist. Fermions are always 'quantum' and no correspondence principle can ever applied. Nevertheless despite being an operator equation, Eq.(2.74) can be solved on a computer by means of a mode function decomposition. Owing to the fact that the fermion action is quadratic, the Dirac equation is linear. In that case we can decompose

$$\psi_n(t) = \frac{1}{V} \sum_{\mathbf{q},\lambda} \left(b_{\mathbf{q},\lambda} \phi^u_{\mathbf{q},\lambda}(\mathbf{x},t) + d^\dagger_{\mathbf{q},\lambda} \phi^v_{\mathbf{q},\lambda}(\mathbf{x},t) \right) \tag{2.75}$$

and by plugging Eq.(2.75) into Eq.(2.74) we see that we actually need to evolve the c-numbered modefunctions $\phi^{u/v}$ in time. The creation and annihilation operators b and d are time independent and their one and two-point functions might be specified at initial time

$$\begin{aligned} \langle b^\dagger_{\mathbf{q},\lambda} b_{\mathbf{q}',\lambda'} \rangle &= V n^u_{\mathbf{q},\lambda}\, \delta_{\mathbf{q},\mathbf{q}'} \delta_{\lambda,\lambda'} \\ \langle d^\dagger_{\mathbf{q},\lambda} d_{\mathbf{q}',\lambda'} \rangle &= V n^v_{\mathbf{q},\lambda}\, \delta_{\mathbf{q},\mathbf{q}'} \delta_{\lambda,\lambda'}\,, \end{aligned} \tag{2.76}$$

where $n^{u,v}$ are the occupation numbers for particles/antiparticles. Using the canonical anti-commutation relations, that are specified in Eq.(2.73), any fermionic observable can be constructed. Further details and an explicit choice of initial conditions for the modefunctions are found in the latter section, too.

Chapter 3

Anomaly-induced dynamical refringence in strong-field QED

The following section is based on the manuscript '*Anomaly-induced dynamical refringence in strong-field QED*' (N.M., F. Hebenstreit, J. Berges), published in Phys. Rev. Lett. 117 (2016) no.6, 061601 [76].

In this section we investigate the possible effects of the Abelian axial anomaly, which might arise in future strong-field laser beam experiments beyond the Schwinger limit. At first sight the research direction presented in this section does not seem to match the general focus of this work, but closer examination highlights the fact that the dynamics of QED beyond the Schwinger limit and ultra-relativistic heavy ion collisions are directly related: both systems represent extreme far-from-equilibrium systems, which are described by Abelian and non-Abelian gauge theories. Moreover the early time dynamics of heavy ion collisions is dominated by large coherent gauge fields and over-occupied non-Abelian plasmas, as are QED laser fields.

The most important connection between the two research areas however is the fact that strong-field laser experiments offer the unique possibility to study the real-time dynamics of the chiral anomaly directly. Thereby the experimental background is negligible. In this section we will discuss the basics of the real-time dynamics of anomalous effects in QED and and we will show that the conventional view on Abelian anomalies from vacuum and equilibrium perspectives must be drastically changed in far-from-equilibrium situations: More specifically we will outline how anomalous effects in the non-linear, out-of-equilibrium regime of QED manifests itself in novel and directly observable effects in laser experiments.

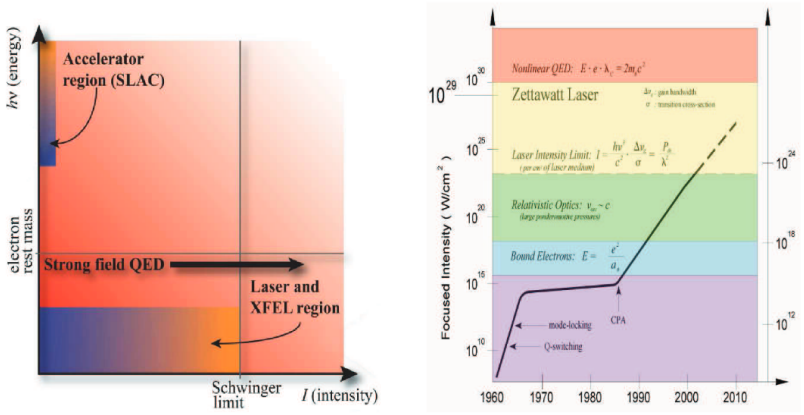

Figure 3.1: An overview on the current status of strong field laser physics. Left: Strong field laser experiments probe a yet unexplored regime of QED, opening new perspectives onto particle physics. Right: The time-line of the developement of laser technology. Provided previous groth rates hold, the non-linear regime of QED is reached in the near future. Figures taken from [65, 198].

3.1 Introduction

The quantum nature of the interactions of light with matter, described by the theory of Quantum Electrodynamics (QED) plays an important role in the regime of ultra-high intensity laser experiments. One of the most important processes, which has been predicted a long time ago, is electron-positron pair production from the QED vacuum in the presence of very strong electric fields beyond the famous Schwinger limit of roughly 10^{16} V/cm [67–69]. While particle particle pair production has been observed in the high energy regime of QED, tested at particle colliders, the non-linear regime of QED at high intensity is uncharted territory so far. Nevertheless the remarkable progress that has been achieved in the second half of the last century in laser-technology brings the realization of such non-perturbative dynamical phenomena into reach [65, 66, 198, 199]. Research facilties that are presently being constructed, such as ELI [200], as well as future projects allow for the possibility of performing particle physics using laser beams in the near future, as is compactly summarized in Fig. (3.1). This has triggered significant interest [70–75].

Remarkably, one of the centerpiecs of the intriguing transition from classical to quantum physics –the breaking of classical symmetries by radiative quantum corrections or so-called quantum anomalies – has not been in the focus of laser physics research yet. This is mainly due to two reasons: first, most of our understanding of the Abelian chiral anomaly originates from thermal equilibrium or vacuum physics, where no net anomalous effects can occur because of the trivial vacuum structure of Abelian gauge theories. Morevover the computational effort to investigate the real-time dynamics of anomalies in QED is tremendous.

In QED, the Adler-Bell-Jackiw axial anomaly [6, 7] involves the presence of a magnetic field and the relevant evolution of the quantum many-body system requires a full 3+1 dimensional treatment. Out of equilibrium conditions however can have dramatic consequences on the dynamics of the axial anomaly. Under suitable initial conditions net effects of the axial anomaly can be observed by measuring the polarization of electromagnetic fields in colliding laser-beams.

In this section we demonstrate that for large-electromagnetic fields the interplay between the Schwinger pair production and the Abelian anomaly yields a highly absorbtive medium, whose anomalous refrective properties are dynamically induced by the produced particles. By studing the non-linear interactions of the dynamically produced particles with the electromagnetic fields, we are able to predict macroscopically observable consequences, such as plasma oscillations and an anomalous rotation of the direction of the electric fields, which can be directly connected to the underlying quantum phenomema. We will show that these effects are caused by the Abelian version of the Chiral Magnetic Effect (CME), which relates the creation of anomalous electric currents and electric transport phenomena with anomalous particle production via the anomaly. Contrary to previous discussions of dispersive phenomena in QED, such as vacuum birefringence [201, 202], we emphasize that the effects discussed here are fundamentally different. Using classical-statistical lattice simulation techniques, our results are obtained from an *ab-initio* approach. In this non-perturbative ansatz the quantum nature of fermions is taken into account, while the bosonic gauge dynamics is accurately mapped onto the evolution of a statistical ensemble by making use of the correspondence principle.

Anomalies cause certain symmetries and related charges that have been conserved on the level of the classical theory to be no longer conserved, when quantum effects are being taken into account. In QED, the effects of the axial anomaly are the non-conservation of the axial-vector current $j_5^\mu = \langle \bar{\psi} \gamma^\mu \gamma_5 \psi \rangle$ involving the different chiral components of the Dirac gamma matrices γ^μ, where $\mu = 0, \ldots, 3$ and a fifth matrix $\gamma_5 = i\gamma^0\gamma^1\gamma^2\gamma^3$, which anti-commutes with all other matrices and whose existence is specific to even dimensions. In QED the four-divergence of the axial-vector current is given by

$$\partial_\mu j_5^\mu = 2m\langle \psi i\bar{\gamma}_5 \psi \rangle - \frac{e^2}{8\pi^2} F_{\mu\nu}\tilde{F}^{\mu\nu} \,, \tag{3.1}$$

which consist of two parts: the contribution proportial to the fermion mass m can be understood from the mixing of different chiral components, as chirality for a massive particle is a Lorentz-frame dependent quantity and not necessarily conserved. The corresponding axial charge is given as $Q_5 \equiv \int d^3x\, j_5^0 = \int d^3x\, \langle \bar{\psi}\gamma^0\gamma_5\psi \rangle$. We note however that – in the ficticious absence of the anomaly – and for suitable initial conditions chirality might be conserved in a given frame, even for a massive particle (but not in every frame)[1]. The second term

[1] This is equivalent to the pseudoscalar density being zero. We have tested such configurations explicitly: in a frame where electric and magnetic fields are homogenous and perpendicular, no axial charge is created at later time when one starts with the fermionic vaccum.

in Eq.(3.1) is the anomalous contribution to the axial non-conservation, which is given in terms of the electromagnetic field strength tensor $F_{\mu\nu} = \partial_\mu A_\nu - \partial_\nu A_\mu$ and its dual $\tilde{F}^{\mu\nu} \equiv \frac{1}{2}\epsilon^{\mu\nu\rho\sigma}F_{\rho\sigma}$. By introducing the Chern-Simmons current $K^\mu = 4\epsilon^{\mu\nu\rho\sigma}A_\nu\partial_\rho A_\sigma$, the anomalous term in Eq.(3.1) can be written as a total divergence

$$\partial_\mu K^\mu = F_{\mu\nu}\tilde{F}^{\mu\nu} = 4\,\mathbf{E}\cdot\mathbf{B}\,. \tag{3.2}$$

This fact emphasizes the importance of boundary conditions in the understanding of anomalies and their relation to the topology of gauge fields. As QED is topologically trivial, the space-time integral of Eq.(3.2) with boundaries at space-time infinity is zero[2] – unlike the case of non-Abelian theories (compare to Eq.(1.15)). In contrast, far-from-equilibrium situations in QED can have dramatic consequences for the effects of the anomaly. More specifically we demonstrate that Schwinger pair production in strong-field QED leads to non-equilibrium states for which the axial anomaly results in a very significant axial charge density with intriguing obersvable consequences. This is in accordance with our observations in section 2.1: the conventional 'in-out' picture of quantum field theory and its conventional path integral construction, employed for example in S-matrix experiments, breaks down in far-from-equilibrium situations: Schwinger pair production is a prime example of a situation requiring generalization on the Schwinger-Keldysh contour, as the intial vacuum is not necessarily stable against particle production and time-evolution must be seen from the 'in-in' perspective.

3.2 Non-equilibrium strong-field QED

Electron-positron pair production is a challenging non-perturbative and non-equilibrium phenomenon, which is induced by large coherent electric fields present at initial time. In this section we consider uniform electric and magnetic fields, as this is the most realistic situation on length scales relevant in laser-physics experiments. We will work in $g = \mathrm{diag}(+,-,-,-)$-metric. By means of the Schwinger-effect, matter is dynamically produced from the large coherent electric fields. Once produced, it will backreact on the applied fields, such that the total energy is conserved. Such a situation is not time translation invariant as eventually energy is transferred from the gauge sector to the fermion sector. The net axial charge produced at some later time $t_f > t_i$ is given by $Q(t_f) - Q(t_i)$, where typically neither t_i or t_f might be taken to the remote past or infinite future. This situation can be accurately simulated using the classical-statistical approximation and the Schwinger-Keldysh path integral formulation of quantum many body physics.

For our studies we choose initial conditions, which correspond to the fermionic vacuum, i.e. vanishing axial- and vector-currents, in the presence of a uniform

[2]This is understood as the finiteness of energy (the action) requires the field strength to be zero at spatial (space-time) infinity

magnetic field in the z-direction $\mathbf{B}_0 = B_0\mathbf{e}_z$. To this end we diagonalize the fermionic Hamiltonian in this background at intial time $t_i = 0$. We can neglect initial-state fluctuations in the gauge field sector, as previous studies have shown that they play a minor role for the dynamics of the system[3] Rather than starting with a constant electric field $\mathbf{E}_0 = E_0\mathbf{e}_\phi$, where $\mathbf{e}_\phi$ is a unit vector in the y-z plane with angle $\phi = (\mathbf{e}_z, \mathbf{e}_\phi)$, the initial condition for the electric field is given by an initial pulse $\mathbf{E}_0 = E_0(t)\mathbf{e}_\phi$, where the time profile is given by

$$E_0(t) = E_0 \mathrm{sech}^2(\omega(t - t_0)) \,. \tag{3.3}$$

This shape of initial condition is not drastically different to the case of a constant electric field, but allows comparision to earlier numerical studies without magnetic fields [19,37]. Furthermore the pulse Eq.(3.3) leads to very fast particle production, which reduces the numerical cost of our simulations and renders our numerical simulations possible. In order to resolve low momentum fermion and axial charge production, a large lattice volume $V = \prod_{i_1}^{3} a_i N_i$ is required in general. On the other hand the ultraviolet properties are probed during the time evolution, as the produced particle-anti-particle pairs are quickly accelerated. To this end we require a small lattice spacings a_i. Both those requirements present a serious challenge which we in practice could only overcome by the use of UV-improved operator definitions on moderatley sized lattices. As these techniques were developed in the context of the work presented in section 5, we will omit a detailed discussion at present and refer to the corresponding chapter. We perform our simulations on a $20 \times 20 \times 40$ grid with lattice spacings in units of the particle mass $ma_x = ma_y = 0.08$, $ma_z = 0.06$, which we have optimzed to suit the initial anisotropy of the system and to minimize lattice artifacts. As the system stays translation invariant in the $z-$direction at all times, we perform a Fourier transformation with respect to this coordinate to reduce the cost. The presented results are for initial conditions with $E_0 = 20E_c$, $\omega = 1.2m$ and $mt_0 = 2.5$ with an initial angle $\phi(0) = 25^\circ$ in the presence of a magnetic field $B_0 = 4.9\, B_c$, where

$$\begin{aligned} E_c &= \frac{m^2}{e} \approx 1.3 \times 10^{16} \text{ V/m}, \\ B_c &= \frac{m^2}{e} \approx 4.4 \times 10^{13} \text{ G}, \end{aligned} \tag{3.4}$$

and we followed particle physics convetions by setting $\hbar = c = 1$. The coupling e is chosen to approximately match the electromagnetic coupling α_{EM}. Typical field configuration at initial times are depicted in Fig. (3.2). As has been argued in [203] these kind of configurations with non-parallel electric and magnetic fields cause the Abelian version of the Chiral Magnetic Effect.

In section 1.3.2 we have discussed the dynamics of the chiral magnetic effects in QCD. Similarly in QED electromagnetic field configuration with $\mathbf{E} \cdot \mathbf{B}$ create

[3] This is very much unlike in the case of QCD, where gauge field fluctuations are known to trigger instabilities. This assumption however must be carefully studied in future work, as the transfer between fermionic and magnetic helicity via the anomaly might trigger novel types of instable behaviour far from equilibrium.

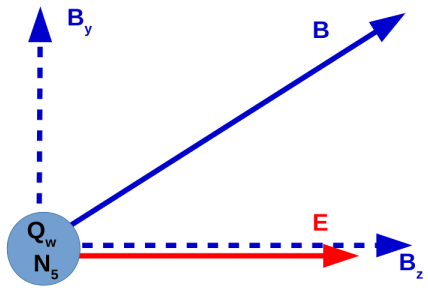

Figure 3.2: Typical initial condition leading to the Abelian version of the Chiral Magnetic Effect [203]. In practice we choose our coordinate systems such that the magnetic field points along the z-axis, while the electric field is rotated in the $y-z$-plane.

non-zero axial charge densities. At the same time the magnetic field induces a polarization in the produced fermionic matter and thus a contribution to the electric current. In the lowest-Landau-level approximation, wherer $\mathbf{B}$ is strong enough such that the dynamically produced matter is fully polarized the emergent current equals (c.f. [203])

$$\mathbf{J} = |e|N_5 \frac{\mathbf{B}}{|\mathbf{B}|} = -2|e|Q\frac{\mathbf{B}}{|\mathbf{B}|}\,, \tag{3.5}$$

where Q is the time integral of the total helicity of the gauge fields $Q \propto \int d^4x\, \mathbf{E}\cdot\mathbf{B}$. From Eq.(3.5) we directly see the anomalous transport coefficients (the conductivity) that comprise the response of the electric current to an external magnetic field. We note that for the case of QCD this conductivity is unknown and the relation between axial charge generation (which in this case is due to *non-Abelian* gauge fields) and the resulting anomalous currents is more complicated. QED offers a very simple testing ground for the study of the Chiral Magnetic Effect. In practice we utilize the non-equilibrium evolution equations, that have been outlined in section 2.3. Implementing constant Abelian magnetic fields on the lattice however requires some additional effort, as we will illustrate in the following section, before presenting the results of our simulations.

3.3 Abelian magnetic fields on the lattice

We have chosen to implement a homogenous magnetic field $\vec{B} = B\hat{z}$ along the z-direction of the lattice. Since on a periodic lattice the magnetic flux $qa_s^2 B N_x N_y$ is quantized in units of 2π [204], a spatially homogenous magnetic field cannot be varied continuously. Nevertheless our gauge fields will be fully dynamical in the following. We work in temporal-axial gauge, $U_=1$ and we choose the $U(1)$

components of the gauge links according to [205],

$$U_{n,1}^{\mathrm{U}(1)} = \begin{cases} e^{ia_s^2 qBN_1 n_2} & , \quad n_1 = N_1 - 1 \\ 1 & , \quad \text{otherwise} \end{cases} \tag{3.6}$$

$$U_{n,2}^{\mathrm{U}(1)} = e^{-ia_s^2 qBn_1} \tag{3.7}$$

with $U_{n,3} = 1$ and $a_s^2 qB = \frac{2\pi m_B}{N_1 N_2}$ we can then realize different magnetic field strength by varying the magnetic flux quantum number m_B.

The implementation of magnetic fields on the lattice via Eq.(5.36) seems confusing at first sight and therefore we will outline the construction this expression in detail. Naively, the gauge potential describing a magnetic field along the z-direction might be chosen

$$A^\mu = (0, 0, -B_0 x, 0)\,, . \tag{3.8}$$

but in fact will prove more complicated. This can be understood as follows: imagine a testparticle traveling the $x^1 - x^2$ plane from the origin $(0, 0)$ to the opposite corner $(L_1, L_2) = (N_1 a_1, N_2 a_2)$ of the lattice on two different paths

$$\mathcal{C}_1 : \qquad (0,0) \quad \to \qquad (L_1, 0) \quad \to \quad (L_1, L_2) \tag{3.9}$$

$$\mathcal{C}_2 : \qquad (0,0) \quad \to \qquad (0, L_2) \quad \to \quad (L_1, L_2). \tag{3.10}$$

The phases picked up along these curves are given by the corresponding Wilson lines

$$\Phi(\mathcal{C}) = \exp\left(ie \int\limits_{\mathcal{C}} A_\mu(x)\ \mathrm{d}x^\mu \right), \tag{3.11}$$

from which it follows that the difference in phase along these two lines is

$$\Delta\Phi = \exp(ieB_0 L_1 L_2). \tag{3.12}$$

As the wavefunction must be single valued, the vanishing of the phase difference Eq.(3.12) yields a quantization condition for the magnetic field:

$$eB_0 = \frac{2\pi m_B}{L_1 L_2} \quad m_B \in \mathbb{Z}.. \tag{3.13}$$

The magnetic flux is quantized due to the non-trivial boundary conditions of the torus. We define the unit flux through per plaquette as $\phi = eB_0 a_s^2 = 2\pi m_B / N_1 N_2$. Consequently a naive generalization of Eq.(3.8) would be

$$U_{n,2} = \exp(ia_s^2 eB_0 n_1) \tag{3.14}$$

$$U_{n,1} = U_{n,3} = 1, \tag{3.15}$$

with eB_0 quantized as in Eq.(3.13). We note that m_B is periodic with period $[0, N_1 N_2]$. In the limit of small lattice spacings we recover the continuum result, provided m_B is much smaller than $N_1 N_2$.

$$U_{n,2} \to 1 + i2\pi \frac{n_1 m_B}{N_1 N_2} + \ldots. \tag{3.16}$$

In this limit with $n_1 \leq N_1$ the next term in the series is of order $1/N^2$ and vanishes as $N \to \infty$. In [205] an upper bound was given by $m_B \in [0, N_1 N_2/4]$, which restricts the range of magnetic fields that can be simulated.
Remebering the discussion about boundary conditions on the lattice, which is homotopic to a torus, we encounter a contradiction, as the gauge links defined in Eq.(3.15) do not fullfill the required periodicty,

$$U_{n+N_1\hat{\mathbf{1}},2} = \exp(ia_s^2 eB_0 N_1)\, U_{n,2}. \tag{3.17}$$

This nontrivial phase, picked up winding once around the torus in the $1-$direction can be easily compensated by a corresponding transition function at the overlap of two coordinate sets (i.e. between two lattice copies). Using the gauge freedom we require a transformation for all gauge fields living on the next lattice copy in the 1-direction, which has the following effect:

$$U_{n,2} \to U'_{n,2} = U_{n,2} \exp(-ia_s^2 eB_0 N_1). \tag{3.18}$$

As can be easily seen, this is accomplished by

$$U_{n+N_1\hat{\mathbf{2}},2} \to U'_{n,2} = G_n U_{n+N_1\hat{\mathbf{2}},2} G^{-1}_{n+\hat{\mathbf{2}}} \tag{3.19}$$

with $G(\boldsymbol{x}) = \exp(ia_s^2 eB_0 N_1 n_2)$. This gauge transformation has a nontrivial consequence for the gauge links in the 1-direction as well. We note that the links on the very last slice at $n_1 = N_1 - 1$ transform as

$$U_{n,1}\big|_{n_1=N_1-1} \to \exp(-ia_s^2 eB_0 N_1 n_2) \tag{3.20}$$

It is straightforward to check that the links with twisted boundary conditions defined here, reproduce the correct periodicity. Our findings result in the Abelian gauge links specified as in Eq.(5.36).

3.4 Anomaly induced dynamical refringence

Starting from the initial conditions specified in section 3.2, we perform real-time lattice simulations according to the description given in section 2 for QED. As the field strength that we are simulating, exceeds the critical field strength E_c, virtual electron-positron pairs are separated and become on-shell particles [67–69]. Although magnetic fields cannot create particles directly, they do have an important influence on the dispersion relation of fermions, as they introduce *discrete* energy levels (Landau-quantization), as has already been pointed out for collinear electric and magnetic fields with $\phi = \angle(\mathbf{E}, \mathbf{B}) = 0$ [206–209]. Due to the chiral magnetic effect, an anomalous electric current is produced along the magnetic field. The latter is a polarization current and, as explained in the introduction, is due to spin orientation. The case of parallel fields is special since the induced current from produced particles always parallels the applied electric field, as is the case also for $\mathbf{E}$ and $\mathbf{B}$ perpendicular to each other (cf. Fig. 3.3). In the latter case this is due to the fact that no anomalous current is produced. As

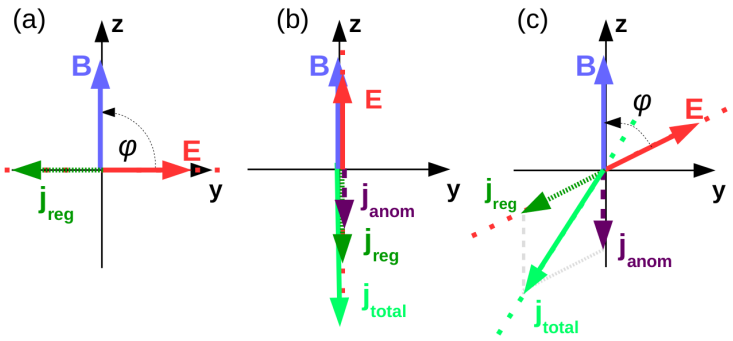

Figure 3.3: Schematic current generation for different values of the angle φ between the magnetic and electric field directions. (a) For $\varphi = \pi/2$, only a regular current j_{reg} is generated parallel to the electric field. (b) For $\varphi = 0$, an anomalous current j_{anom} is induced in addition to j_{reg}. Both of them point in the same direction. (c) For arbitrary values of the angle, j_{reg} and j_{anom} point in different directions. Accordingly, the total current j_{tot} is not parallel to the electric field direction. Figure taken from [76].

can be seen from Fig. (3.3), any other value of φ than parallel or perpendicular produces a net vector current that is not (anti-)parallel to the electric field, leads, since in addition to a regular current j_{reg} parallel to $\mathbf{E}$, to the generation of an anomalous current component j_{anom} parallel to $\mathbf{B}$ is induced by the chiral magnetic effect. However if the axial anomaly did not exist, the induced current and the electric field would be also be collinear for any other values of the angle between $\mathbf{E}$ and $\mathbf{B}$. Consequently, for general $\varphi = \measuredangle(\mathbf{E}, \mathbf{B})$ the presence of the quantum anomaly manifests itself in a distinctive macroscopic property of the total induced current. As our simulations include the backcoupling of the created currents on the dynamical electromagnetic fields, we can investigate the properties of the Abelian chiral magnetic effect in the non-linear regime of QED.

In Fig. 3.4 and 3.5 , we show the time dependence of the y– and z–components of the electric currents $j^i = e\langle\bar{\psi}\gamma^i\psi\rangle$ as well as the corresponding electric field components as a function of time. Since $\nabla \times \mathbf{E}(t) = 0$, the magnetic field of the system remains constant. Similar to a purely electric configuration, the interplay between particle production and subsequent screening of the electric field results in plasma oscillations [48, 196, 210]. By comparing Fig. 3.4 and 3.5, the zero crossings of each current component are seen to occur around the same time as the extremum of the respective electric field component and vice versa. However, in contrast to the Schwinger effect in a purely electric configuration, for which the electric current is always anti-parallel to the electric field so that all field components oscillate with the same plasma frequency, we now observe that the oscillations of the y– and z–components are *out of phase*. The intriguing behaviour is caused by the anomalous electric current produced via the chiral magnetic effect. [14, 15]: In magnetic fields the spin of particles aligns

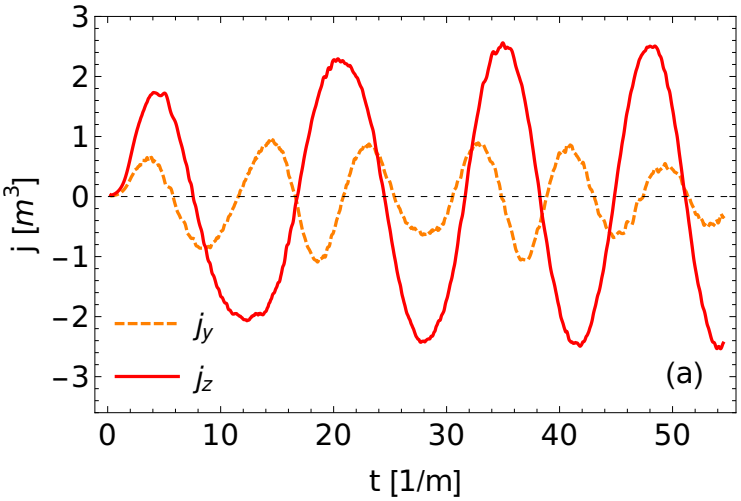

Figure 3.4: Time-evolution of the non-vanishing electric current which results from a regular and an anomalous contribution. Accordingly, the y– and z–components oscillate out of phase. Figure taken from [76].

with the external field and thus results in a correlation between electric charge, chirality and momentum. Positively charged, right-handed particles move along the magnetic field lines while negatively charged right-handed particles move in the opposite direction. This effect is usually cancelled by the inverse behavior of the left-handed particles. In the presence of an anomaly $\mathbf{E} \cdot \mathbf{B} \neq 0$, however, an imbalance between right- and left-handed particles is produced such that an anomalous electric current along the magnetic field direction is generated,

$$\vec{j}_{anom} = \sigma_5(q_5(t))\vec{B}, \tag{3.21}$$

where $\sigma_5(q_5(t)) \propto q_5 \propto \mathbf{E} \cdot \mathbf{B}$ is the dynamical anomalous conductivity. Unlike in simplified set-ups, such as discussed in [14, 15], σ_5 is a dynamical quantity and the chiral medium is time-dependent. Thus static calculations, where σ_5 is treated as a fixed transport coefficent, are insufficient to describe anomalous effects beyond the Schwinger limit. In Fig. 3.6 the time evolution of the angle between the magnetic and electric field is displayed. Remarkably, a rotation of the electric field relative to the magnetic field is observed, which is a direct important consequence of the anomaly. It stems from the non-alignment of electric field and currents and the field components being out-of-phase as a result. Only for the specific initial values $\varphi(0) = 0, \pi$ (parallel) and $\varphi(0) = \pm\pi/2$ (perpendicular) no anomalous rotation occurs (cf. Fig. 3.3). Most remarkably, we find that for general initial configurations the evolution of the angle φ is not monotonic, instead it exhibits a tracking behavior: Irrespective of the initial condition details, the system spends longest times near collinear field configurations with maximum quantum current, while disfavoring orthogonal fields with no anoma-

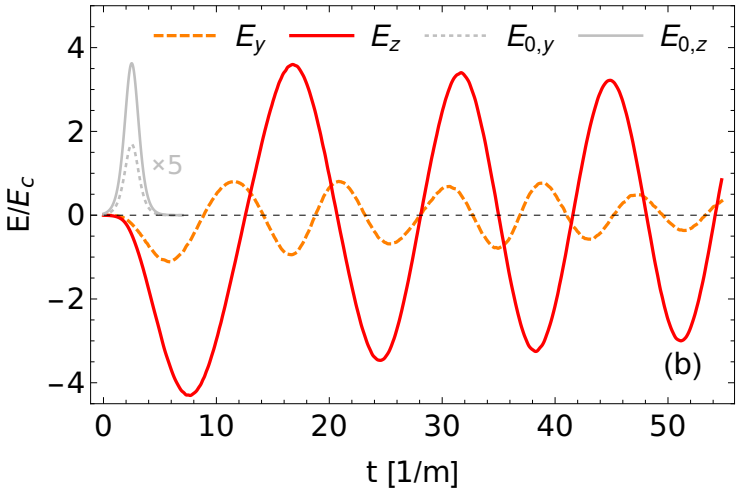

Figure 3.5: Time-evolution of the non-vanishing electric field components. Similar to the current, the y– and z–components of the electric field are also out of phase. As a consequence, $\mathbf{E}$ rotates relative to $\mathbf{B}$, cf. Fig. 3.6. Shown is also the initial pulse whose amplitude is rescaled by a factor of five for better visualization. Figure taken from [76].

lous current generation. In fact, $\varphi = \pm\pi/2$ turn out to be unstable stationary points (u), where even arbitrarily small deviations lead to the generation of axial charges and, accordingly, to an anomalous rotation of the electric field direction. The collinear tracking solutions (s) represent an important self-focusing mechanism, which makes our phenomenon of anomaly-induced dynamical refringence very robust and different from conventional dispersive phenomena described in terms of material constants. This intriguing dynamics points to the possibilty of using the axial anomaly as a focussing device for beyond the Schwinger-limit optics. Moreover this dynamics highlights the role of the fermion mass for the dynamics of the chiral magnetic and chiral separation effect: the explict violation of axial symmetry via the pseudoscalar condensate might be understood as kind of a damping term in the anomalous axial-non-conservation equations; it acts to reduce the amount of axial charge produced and thus ultimately dampens the chiral plasma oscillations observed here.

3.5 Axial charge production

Using our simulations we can check the realization of the Abelian anomaly equation (3.1) out of equilibrium explicitly. To this end we compute the different components of the Abelian anomaly equation (3.1). This allows us to judge the precision of our lattice simulations. Furthermore by investigating the anomaly budget, we can study the mass-dependence of the non-linear anomalous dynam-

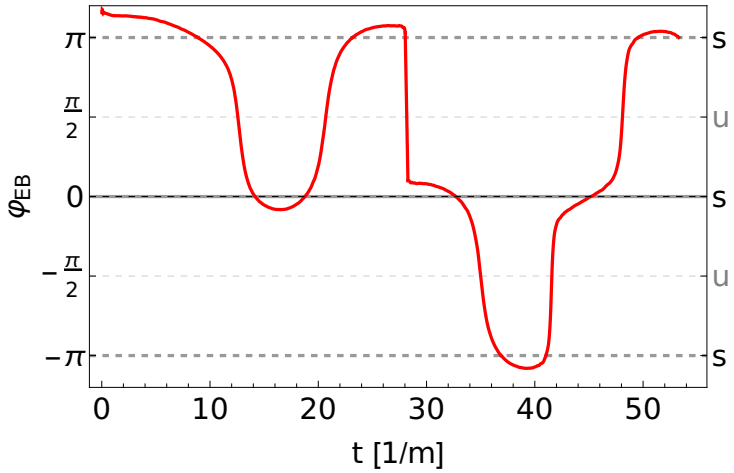

Figure 3.6: Anomalous rotation of the dynamical electric field as described by the time-dependent angle $\varphi(t) = \measuredangle(\mathbf{E}(t), \mathbf{B})$. The evolution exhibits tracking behavior, where the system spends longest times near collinear field configurations with maximum quantum current. Figure taken from [76].

ics. Here we study the time-integrated and volume-averaged anomaly equation:

$$q_5(t) = 2im \int_0^t \langle \bar{\psi}\gamma_5\psi \rangle dt' - \frac{e^2}{2\pi^2} \int_0^t \mathbf{E}\cdot\mathbf{B}\, dt' \,. \tag{3.22}$$

This equation consists of several contributions and we first compute the axial charge density $q_5(t)$ directly. The solid (blue) line of Fig. 3.7 clearly demonstrates that there is a non-zero generation of axial charge density, as electromagnetic helicity is transered to chirality via the anomaly equation. Subsequently we observe the nonequilibrium time evolution of the interplay between helicity and chirality. Moreover we display the individual contributions appearing on the r.h.s. of (3.22) with the time-integrated pseudoscalar condensate (first term/dotted orange curve) and anomaly term (second term/dashed-dotted red curve). The dashed (black) curve represents their sum and the agreement with q_5 within numerical errors reflects the underlying quantum anomaly and the ability of our methods to capture the intriguing phenomena associated with it. In fact, the exact reproduction of the anomaly equation is only expected in the continuum limit [179, 211]. While lattice artifacts from the Wilson term are negligible, the dominant error in our numerical results is due to the finite system size V and lattice spacings a_i. Based on restricted variations thereof, we estimate the total numerical error for the quantities considered to be of the order of a few percent, in overall agreement with the above consistency check of the anomaly equation. The dynamics that is depicted in Fig. (3.7) shows chiral plasma oscillations for several periods. We note while there is a continuous transfer of chirality between the gauge and fermion sectors, this transfer will

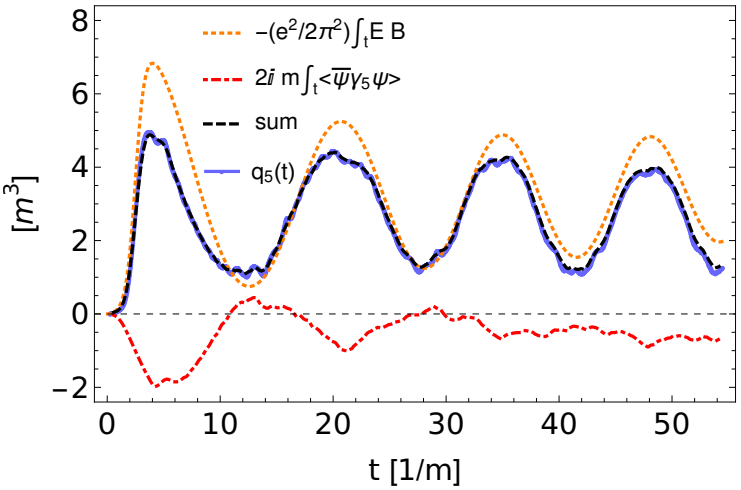

Figure 3.7: Generation of the axial charge density q_5 as a function of time. In addition, the different contributions on the r.h.s. of the space-time integrated anomaly equation (3.22) are shown. We note that in supercritical fields (as present in this case, cf. Fig.3.5) the recreation of axial charge via particle production dominates over the damping due to the finite fermion mass[81, 82], which is marked by the presence of the pseudoscalar condensate. Figure taken from [76].

ultimately be damped away, as the explicit violation of chiral symmetry via the finite quark mass tends to reduce the overall difference between left- and right handed particles. For early times the axial charge recreation via super-critical electromagnetic fields however dominates over damping processes. This relation might be very different in situations where the electromagnetic fields are considerably smaller than the Schwinger limit, as is of relevance in many astrophysical systems [81, 82]. We note that the realization of the non-equilibrium axial anomaly has been investigated for non-Abelian theories in Refs. [52, 212] and is subject to section 5.

3.6 Outlook and experimental applications

The simulations of strong-field QED beyond the Schwinger limit have shown that the Adler-Bell-Jackiw anomaly, which does not contribute to vacuum-to-vacuum transitions in QED, has dramatic consequences out of equilibrium. By using real-time lattice simulation of QED in the classical-statistical limit, we have shown that net axial charge is produced under suitable initial conditions in the presence of an unstable QED vacuum. The later situation is realized in the regime of electromagnetic fields exceeding the Schwinger limit. We have investigated the non-linear transfer of chirality/helicity from the gauge to the

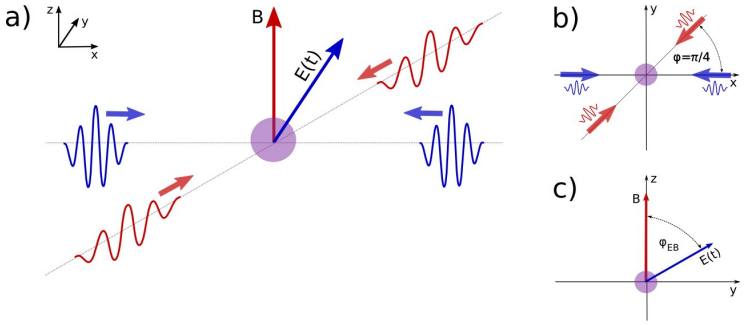

Figure 3.8: A schematic representation of a possible experimental set-up, that allows to create electromagnetic laser fields with large electric and magnetic fields in the focal region at an arbitrary initial angle. A minimum of four lasers is required as otherwise the Lorentz-invariant $\mathbf{E} \cdot \mathbf{B}$ cannot be generated. (a) 3-dimensional view. (b) The laser beams are collided at an angle of $\pi/4$ in the $x-y$-plane. (c) resulting electric and magnetic fields. This figure is courtesy of Florian Hebenstreit, Univ. Bern and is used with his generous permission.

fermion sector. To this end we have found that the Abelian version of the Chiral Magnetic Effects causes the emergence of anomalous electric currents for general electromagnetic field configurations. For non-parallel electric and magnetic fields with $\mathbf{E} \cdot \mathbf{B} \neq 0$ we find that the CME induces dynamical polarization effects and we find that the systems exhibits an intriguing tracking behaviour that tries to maximize the effects of the anomaly.

The existence of this very non-trivial medium has important consequences for future experiments: it could be tested directly by simple setups, e.g. by utilizing two counter-propagating optical laser pulses, producing a slowly varying standing-wave magnetic field which is superimposed by a single attosecond pulse in the focal region [213]. We depict such a possible experimental situation in Fig. (3.8). The intriguing dynamics of Fig. 3.5 leads to an anomalous rotation of the fermionic current and of the electric field, which can be observed by spectrometric measurements.

The study presented here is naturally extended to similar systems in a different context: the Abelian version of the Chiral Magnetic Effect has already been oberserved experimentally in Dirac semimetals [19, 214]. As the quantum-simulation of QED is becoming reality, using ultracold quantum gases [86], the dynamics of the axial anomaly in QED might be investigated further. Moreover the dynamics of the anomaly in an astro-physical context has received considerable attention in recent years: most importantly the role of the fermion mass in this context is poorly understood. As many of these systems involve the chiral dynamics of very light degrees of freedom, such as neutrinos, it is of utmost importance to being able to simulate systems with a wide range of quark masses.

Chapter 4

Transient anomalous charge production in strong-field QCD

This section is based on the publication 'Transient anomalous charge production in strong-field QCD' (N. Tanji, N.M. J. Berges), which is published in Phys. Rev D93 (2016) no.7, 074507 [arXiv:1603.03331] [52]. In the following we investigate the anomalous axial production from coherent color gauge fields. We compute the real-time evolution, starting with spatially homogeneous strong gauge fields, while the fermions are in vacuum. The idealized class of initial conditions is motivated by Glasma flux tubes in the context of heavy-ion collisions. We focus on axial charge production at early times, where important aspects of the anomalous dynamics can be derived analytically. This is compared to real-time lattice simulations. Quark production at early times leading to anomalous charge generation is investigated using Wilson fermions. Our results indicate that coherent gauge fields can transiently produce significant amounts of axial charge density, while part of the induced charges persist to be present even well beyond characteristic decoherence times. The comparisons to analytic results provide stringent tests of real-time representations of the axial anomaly on the lattice.

4.1 Transient anomalous charge production: gauge sector

4.1.1 Analytic discussion

We consider a non-Abelian gauge theory with $SU(2)$ color gauge group. Taking two colors simplifies the analysis as compared to the $SU(3)$ gauge group of QCD, while for our aims the difference is of minor relevance. We do not

consider longitudinally expanding systems, such as addressed in Ref. [215]. We concentrate on the nonequilibrium dynamics, starting from an initial state characterized by macroscopic color-electric fields of order $\langle E(0)\rangle \sim Q^2/g$ in the weak gauge coupling $g \ll 1$ relevant at a sufficiently high energy scale Q. All other gauge field modes, as well as the fermion sector, are taken to be in (free) vacuum initially. The early-time behavior for this problem can be solved analytically in an expansion in powers of the gauge coupling g following along the lines of Ref. [216], where simpler initial conditions have been considered in the absence of anomalous corrections. In particular, at leading order in g there is no back-reaction of the fermion sector on the gauge field dynamics at early times (see e.g. [196]).

In this section, we investigate transient anomalous effects in quantum chromodynamics (QCD) with two colors. The aim is to gain (semi-)analytical insights into axial charge generation due to the Adler–Bell– Jackiw anomaly equation [6, 7]

$$\partial_\mu j_5^\mu = 2m\overline{\psi} i\gamma_5 \psi + \frac{g^2}{4\pi^2}\mathbf{E}^a \cdot \mathbf{B}^a \tag{4.1}$$

out of equilibrium. It relates the four-divergence of the axial current $j_5^\mu = \overline{\psi}\gamma^\mu\gamma_5\psi$ ($\mu = 0, 1, 2, 3$ with Dirac matrices γ^μ and $\gamma_5 = i\gamma^0\gamma^1\gamma^2\gamma^3$) to the mixing of the different chiral components of the fermion fields ψ of mass m, and to the anomaly term $\sim \mathbf{E}^a \cdot \mathbf{B}^a$ involving the color electric fields $\mathbf{E}^a$ and magnetic fields $\mathbf{B}^a$ ($a = 1, 2, 3$).

To this end, we consider the real-time evolution starting with spatially homogeneous gauge fields. The field configuration is motivated by the Glasma flux-tube scenario, where the gluonic gauge fields in the immediate aftermath of a heavy-ion collision are dominated by coherent longitudinal color-electric and magnetic fields [217]. For a sufficiently energetic collision, the relevant gauge coupling g is weak and we consider $g \ll 1$.

More precisely, we investigate an idealized class of initial conditions, where the expectation values at time $t = 0$ for color-electric fields $E_i^a(0)$ and magnetic fields $B_i^a(0)$ with spatial components $i = x, y, z$ in temporal gauge are given by

$$\begin{aligned} \langle E_x^1(0)\rangle = \langle E_y^2(0)\rangle = \langle E_z^3(0)\rangle \sim \frac{Q^2}{g}, \\ \langle B_x^1(0)\rangle = \langle B_y^2(0)\rangle = \langle B_z^3(0)\rangle = 0, \end{aligned} \tag{4.2}$$

corresponding to an energy density $\sim Q^4/g^2$ parametrized in terms of the characteristic scale Q. All other modes, as well as the fermion sector, are taken to be in (free) vacuum initially. While we start with zero macroscopic color-magnetic field such that the anomalous contribution vanishes initially, it is generated during subsequent times. The nonequilibrium classical time evolution of the Yang–Mills fields can be solved analytically [218–220]. By taking into account quantum fluctuations, one observes that the solution represents the leading contribution for the corresponding quantum dynamics on a time scale shorter than

$t_\Theta \sim Q^{-1} \ln g^{-2}$. This allows us to derive a closed-form expression for the early-time behavior of axial charge generation from the anomaly equation.

The times beyond t_Θ, after which fluctuations cause decoherence of the initially uniform fields, are no longer described by our analytical treatment linearizing in fluctuations. Using real-time lattice simulation techniques, we verify that the early-time lattice dynamics indeed accurately reproduces our analytical results. Furthermore we find that transient homogeneous fields can lead to nonzero axial charge density even beyond the characteristic decoherence time.

While in general the investigation of more realistic field configurations and later times cannot be based on analytic solutions and requires non-perturbative real-time lattice simulation techniques [48–50, 193, 194, 196], our analytical expressions provide a stringent precision test for the numerical approaches. On a lattice, the axial anomaly is deeply connected to the fermion doubling problem and its regularization, which is well understood in Euclidean or 'imaginary-time' lattice field theory [179–181]. In particular, for Euclidean Wilson fermions all doublers can be regularized using a spatiotemporal Wilson term. In contrast, real-time simulations typically employ a combination of a spatial Wilson term together with a suppression of possible temporal doublers using suitable initial conditions [195, 212]. Employing real-time lattice simulations for two-color QCD, we analyze in detail the validity of the axial anomaly equation on the lattice by explicitly computing the nonequilibrium axial charge density from the underlying fermion current.

The chapter is organized as follows. In section 4.1, we investigate the real-time evolution of the gauge field sector. We derive an analytic expression for the production of the axial charge and compare it to real-time lattice simulations in pure gauge theory. In section 4.2, we investigate the fermion sector and perform real-time lattice simulations with Wilson fermions. We analyze the axial anomaly out of equilibrium and demonstrate that it can be accurately computed using a spatial Wilson term. Section 5.4 is devoted to concluding remarks. In an appendix, we show an alternative verification of the chiral anomaly with a cutoff regularization method.

It is convenient to formulate the gauge field dynamics in terms of gauge potentials $A^a_\mu(x)$ with $x = (x^0, \mathbf{x})$ in temporal gauge, where $A^a_0(x) = 0$, and to split the field into a time-dependent expectation value $\langle A^a_i(x)\rangle = \bar{A}^a_i(x^0)/g$ and a quantum fluctuation according to

$$A^a_i(x) \;=\; g^{-1}\bar{A}^a_i(x^0) + \delta A^a_i(x)\,. \tag{4.3}$$

Introducing the rescaled macroscopic field $\bar{A}$ simplifies the power-counting in g. Starting from the spatially homogeneous macroscopic field configuration, we may linearize the dynamics in δA for sufficiently early times. The range of times, for which the linearized description is valid, is determined below.

At zeroth order in the fluctuations, we obtain the field equation for the macroscopic field

$$\big(D_\mu[\bar{A}]F^{\mu\nu}[\bar{A}]\big)^a \;=\; 0\,, \tag{4.4}$$

which corresponds to the classical Yang–Mills equation with field strength tensor

$$F^a_{\mu\nu}[\bar{A}] \;=\; \partial_\mu \bar{A}^a_\nu - \partial_\nu \bar{A}^a_\mu - \epsilon^{abc} \bar{A}^b_\mu \bar{A}^c_\nu \tag{4.5}$$

and covariant derivative

$$D^{ab}_\mu[\bar{A}] \;=\; \partial_\mu \delta^{ab} - \epsilon^{acb} \bar{A}^c_\mu \,. \tag{4.6}$$

One observes that the classical equation (4.4) for the rescaled macroscopic field $\bar{A}$ does not depend on the coupling g. Moreover, all spatial derivatives of $\bar{A}$ actually vanish. The next order corresponds to the linearized equation for the fluctuations [221],

$$\big(D_\mu[\bar{A}] D^\mu[\bar{A}] \delta A^\nu\big)^a - \big(D_\mu[\bar{A}] D^\nu[\bar{A}] \delta A^\mu\big)^a - \epsilon^{abc} \delta A^b_\mu F^{c\mu\nu}[\bar{A}] \;=\; 0 \,. \tag{4.7}$$

Equations (4.4) and (4.7) describe the gauge dynamics up to corrections of order $(\delta A)^2$ in the fluctuations and to leading order in the coupling g.

Writing $t \equiv x^0$, we consider the time-dependent field configuration [218, 219]

$$\bar{A}^a_i(t) = \mathcal{A}(t) \left(\delta^{a1}\delta_{ix} + \delta^{a2}\delta_{iy} + \delta^{a3}\delta_{iz}\right). \tag{4.8}$$

The corresponding chromo-electric and magnetic field components are

$$\langle E^1_x\rangle(t) = \langle E^2_y\rangle(t) = \langle E^3_z\rangle(t) = g^{-1}\partial_t \mathcal{A}(t) \,, \tag{4.9}$$

$$\langle B^1_x\rangle(t) = \langle B^2_y\rangle(t) = \langle B^3_z\rangle(t) = g^{-1}\mathcal{A}^2(t) \,, \tag{4.10}$$

from which we recover the initial conditions (4.2) by choosing

$$\mathcal{A}(0) = 0 \,, \qquad \partial_t \mathcal{A}(0) = \frac{Q^2}{\sqrt{3}} \,. \tag{4.11}$$

With the employed normalization the energy density is given by $Q^4/2g^2$.

For the configuration (4.8), the macroscopic field equation (4.4) reads

$$\partial_t^2 \mathcal{A}(t) + 2\mathcal{A}^3(t) = 0 \,. \tag{4.12}$$

With the initial conditions (4.11), the solutions of this equation can be expressed in terms of Jacobi elliptic functions as

$$\mathcal{A}(t) = \frac{Q}{3^{1/4}} \,\mathrm{cn}\left(\sqrt{\frac{2}{\sqrt{3}}}\, Qt - K(1/2),\; \frac{1}{2}\right), \tag{4.13}$$

where $K(1/2)$ denotes the complete elliptic integral of the first kind [222]. The nonzero components of the color-electromagnetic fields then read

$$\begin{aligned}\langle E^a_i\rangle(t) = -\sqrt{\frac{2}{3}}\frac{Q^2}{g}\,\mathrm{sn}&\left(\sqrt{\frac{2}{\sqrt{3}}}\, Qt - K(1/2), \frac{1}{2}\right) \\ &\times \mathrm{dn}\left(\sqrt{\frac{2}{\sqrt{3}}}\, Qt - K(1/2), \frac{1}{2}\right),\end{aligned} \tag{4.14}$$

$$\langle B^a_i\rangle(t) = \frac{1}{\sqrt{3}}\frac{Q^2}{g}\,\mathrm{cn}^2\left(\sqrt{\frac{2}{\sqrt{3}}}\, Qt - K(1/2), \frac{1}{2}\right). \tag{4.15}$$

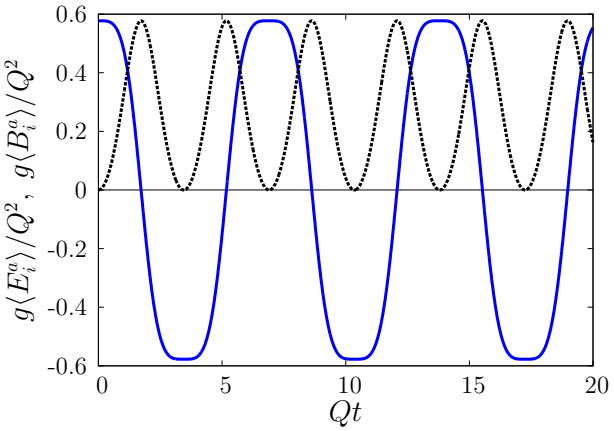

Figure 4.1: Evolution of the rescaled nonzero components of the color-electric field (solid line) and magnetic field (dashed line) in the linear regime, where they are described by the analytic solutions (4.14) and (4.15). Figure taken from [52].

In Fig. 4.1, these fields are plotted as a function of time. They oscillate in time with a characteristic frequency $\sim Q$. By multiplying with g/Q^2, the quantities become dimensionless and independent of the value of g.

Starting from the configuration with a strong color-electric field and vanishing magnetic field, one observes that the latter is subsequently generated. The build-up of the chromo-magnetic fields is possible because of the non-linear gauge dynamics, which is uniquely due to the non-Abelian nature of the theory. In general, one can write

$$\mathbf{E}^a \cdot \mathbf{B}^a = -\epsilon^{\mu\nu\rho\sigma}\partial_\mu \,\mathrm{tr}\left(A_\nu \partial_\rho A_\sigma + \frac{2}{3} i g A_\nu A_\rho A_\sigma\right). \tag{4.16}$$

Therefore, a nonzero $\mathbf{E}^a \cdot \mathbf{B}^a$ may be obtained even for spatially homogeneous gauge potentials in a non-Abelian theory.

The anomaly equation (4.1) relates $\mathbf{E}^a \cdot \mathbf{B}^a$ to the four-divergence of the axial fermion current j_5^μ. For the homogeneous system, the spatial divergence drops out for the evaluation of the expectation value of this current. The axial charge density $n_5(t) = \langle j_5^0(x)\rangle$ is then obtained by integrating over time:

$$n_5(t) = 2m \int_0^t dt' \,\langle \overline{\psi} i\gamma_5 \psi\rangle(t') + \frac{g^2}{4\pi^2}\int_0^t dt' \,\langle \mathbf{E}^a \cdot \mathbf{B}^a\rangle(t') \tag{4.17}$$

for zero initial axial charge. The first term on the right hand side arises from the mixing of the different chiral field components in the presence of a mass. Therefore, in a massless theory the axial charge density is entirely determined by the anomalous second term. In particular, to lowest order in the fluctuations

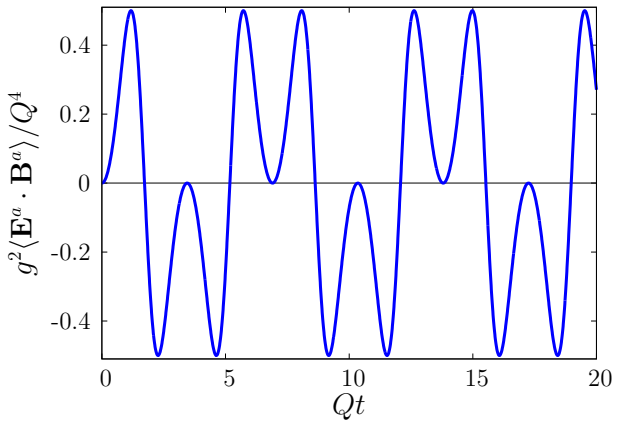

Figure 4.2: Time-dependence of the anomalous contribution $\sim \langle \mathbf{E}^a \cdot \mathbf{B}^a \rangle$ in the linear regime. Figure taken from [52].

we have $\langle \mathbf{E}^a \cdot \mathbf{B}^a \rangle = \langle \mathbf{E}^a \rangle \cdot \langle \mathbf{B}^a \rangle$, and the time evolution of this term is plotted in Fig. 4.2. Therefore, in this approximation our solutions (4.14) and (4.15) determine the dynamics of the axial charge generation, and in the massless limit we find from integration:

$$n_5(t) = \frac{Q^3}{3^{3/4} 4\pi^2} \, \mathrm{cn}^3 \left(\sqrt{\frac{2}{\sqrt{3}}} \, Qt - K(1/2), \frac{1}{2} \right) , \tag{4.18}$$

as plotted in Fig. 4.3. We further find that only the second term $\sim A^3$ on the right hand side of (4.16) contributes to the anomaly for the initial conditions considered, such that (4.18) can also be written as

$$n_5(t) = \frac{1}{4\pi^2} \mathcal{A}^3(t) \, . \tag{4.19}$$

Equation (4.18) is the central result of this section, which will be further discussed and used in section 4.2 to verify implementations of the axial anomaly in real-time lattice simulations. However, before doing so we have to establish the solution's range of validity in time. In the quantum theory, the fluctuations $\delta A_i^a(x)$ cannot be neglected in general: While the expectation value $\langle \delta A_i^a(x) \rangle \equiv 0$ by definition, the correlation $\langle \delta A_i^a(x) \delta A_j^b(y) \rangle$ cannot vanish identically because of the uncertainty relation. Starting with large macroscopic fields and all other modes in vacuum, where $Q^2/g^2 \sim \langle A_i^a(x) \rangle \langle A_j^b(x) \rangle \gg \langle \delta A_i^a(x) \delta A_j^b(y) \rangle \sim Q^2$ at initial times $x^0 = y^0 = 0$, we have to investigate on which time scale fluctuations grow to become large enough such that they modify our result (4.18).

The initial growth of fluctuations is described by (4.7), evaluated for the macroscopic field configuration (4.8). Again carrying over the analysis of Ref. [216] to our problem, we consider a Fourier expansion of the fluctuations and analyze

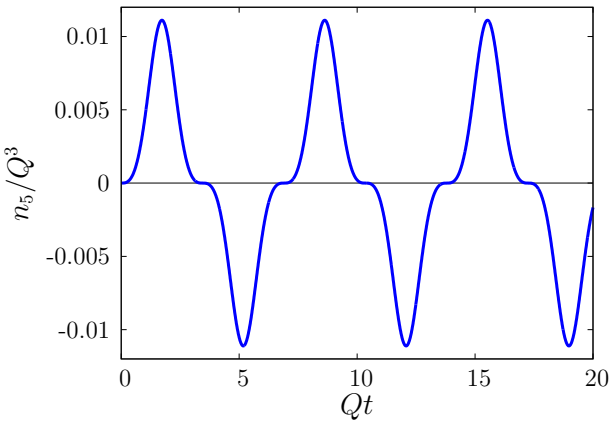

Figure 4.3: Time-dependence of the axial charge density in the massless limit, as described by the analytic result (4.18). Figure taken from [52].

which momentum modes dominate the growth of fluctuations. For the employed temporal gauge, the fluctuation equation can be written as a matrix equation of the form

$$\partial_t^2(\delta A) = -\Omega^2[\bar{A}] \cdot (\delta A)\,. \tag{4.20}$$

In fact, there are negative eigenvalues for Ω^2 related to Nielsen–Olsen type instabilities [223, 224]. In addition, there are parametric resonance instabilities arising from the oscillatory behavior of the macroscopic field $\bar{A}(t)$, which are expected to be sub-leading according to Ref. [216]. Therefore, we proceed by computing the most negative eigenvalues of Ω^2 for constant $\bar{A} \sim Q$ to determine the characteristic exponential growth rates for fluctuations.

From the three color times three spatial directions, $\Omega^2[\bar{A}]$ has a 9×9 matrix structure. In the spatial momentum space, its nine eigenvalues depend on momentum $\mathbf{p}$ only through its modulus $p = |\mathbf{p}|$, and they read:

$$\omega_{1/2}^2 = p^2 \pm 2|\mathcal{A}|\,p\,, \tag{4.21}$$

$$\omega_{3/4/5/6}^2 = \mathcal{A}^2 + \frac{1}{2}p^2 \pm \frac{1}{2}\sqrt{(2\mathcal{A}^2 + p^2)^2 \pm 8|\mathcal{A}|^3 p}\,, \tag{4.22}$$

while $\omega_{7/8/9}^2$ are given by the roots of

$$\begin{aligned} 0 = -4\mathcal{A}^4 p^2 + (12\mathcal{A}^4 + 4\mathcal{A}^2 p^2 + p^4)\,x \\ -(8\mathcal{A}^2 + 2p^2)\,x^2 + x^3\,, \end{aligned} \tag{4.23}$$

which are always non-negative. We find that (4.21) has negative eigenvalues for $0 < p < 2|\mathcal{A}|$, with the largest negative eigenvalue for $p_\star = |\mathcal{A}|$ given by $-\mathcal{A}^2$. Similarly (4.22) yields negative eigenvalues, with the largest for $p_\star =$

$(1+\sqrt{5})|\mathcal{A}|/2$ given by $-(\sqrt{5}-1)\mathcal{A}^2/2$. Since $\mathcal{A} \sim Q$, we conclude that the characteristic growth of fluctuations with momentum $p_\star \sim Q$ is described by an exponential behavior with rate $\gamma_\star \sim Q$. In spatial Fourier space, we therefore find for the fastest growing linear combination of fields the parametric behavior

$$\langle \delta A \delta A \rangle(t, p_\star) \sim Q^{-1}\, e^{\gamma_\star t}\,. \tag{4.24}$$

Next-to-leading order quantum corrections to the leading weak-coupling behavior of the fluctuation equation (4.7), both from gauge-field and fermion fluctuations, are proportional to g^2 (see e.g. [196]). Parametrically, these quantum corrections are expected to become relevant once they have grown enough such that they can compensate for the small factor of g^2. Stated differently, they become relevant at the time t_Θ at which the dimensionless product

$$g^2 Q\, \langle \delta A \delta A \rangle(t, p_\star) \;\sim\; g^2\, e^{\gamma_\star t} \tag{4.25}$$

is of order unity, i.e. at the time

$$t_\Theta \;\sim\; Q^{-1} \log(g^{-2})\,. \tag{4.26}$$

Before that time, the analytic estimate (4.18) for the anomalous charge generation dynamics may also be used to test real-time lattice simulation techniques that can be applied to more general out-of-equilibrium situations.

4.1.2 Real-time lattice gauge theory simulations

In this section, we go beyond the linear analysis by conducting classical-statistical lattice simulations for the pure gauge theory using standard procedures [41, 43, 44, 118, 225]. The system is defined by the lattice Hamiltonian for gauge fields

$$\begin{aligned} H_g = {} & \frac{a^3}{2} \sum_{\mathbf{x},i} E_i^a(x) E_i^a(x) \\ & + \frac{2N_c}{g^2 a} \sum_{\mathbf{x},i<j} \left(1 - \frac{1}{N_c} \mathrm{Re\ Tr}\, U_{ij}(x) \right), \end{aligned} \tag{4.27}$$

where a denotes the spacing of the isotropic spatial lattice, and $U_{ij}(x)$ is the spatial plaquette defined by

$$U_{ij}(x) = U_i(x) U_j(x+\hat{i}) U_i^\dagger(x+\hat{j}) U_j^\dagger(x). \tag{4.28}$$

Here $U_i(x) = \exp\{iga A_i(x)\}$ is the link variable describing the gauge degrees of freedom on the lattice. While we discretize the space coordinates, time is treated as a continuum variable in this formulation. We define the lattice magnetic field as

$$B_i^a(x) = -\frac{\epsilon_{ijk}}{ga^2} \mathrm{Im Tr}\left[T^a U_{jk}(x) \right]. \tag{4.29}$$

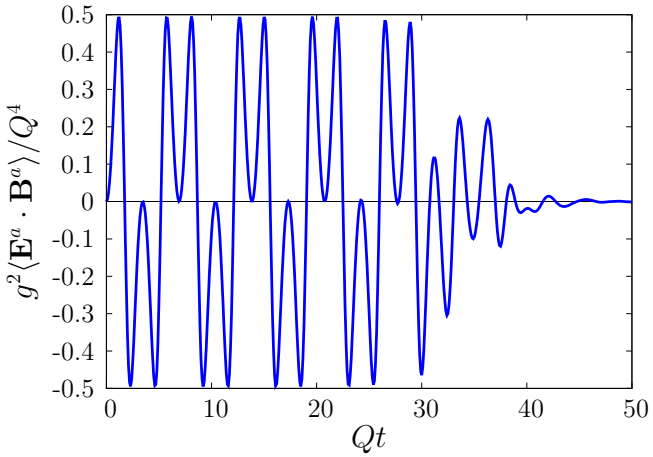

Figure 4.4: Time-dependence of $\langle \mathbf{E}^a \cdot \mathbf{B}^a \rangle$ from classical-statistical lattice simulations. Comparison to Fig. 4.2 shows very good agreement with the linear analysis at early times, while the growing fluctuations become relevant around t_Θ leading to the significant changes observed. Figure taken from [52].

This definition reduces to the continuum result $B_i = -\frac{1}{2}\epsilon_{ijk}F_{jk}$ as $a \to 0$.

To simulate the instability beyond the linear analysis, the following initial fluctuations are added to the coherent field initial conditions (4.11):

$$\delta A_i^a(0,\mathbf{x}) = \sum_{\lambda=1,2} \frac{1}{V} \sum_{\mathbf{k}} \frac{1}{\sqrt{2|\mathbf{k}|}} \left[\epsilon_{i,\mathbf{k}}^{(\lambda)} c_{\lambda,\mathbf{k}}^a e^{i\mathbf{k}\cdot\mathbf{x}} + \text{c.c} \right], \tag{4.30}$$

$$\delta E_i^a(0,\mathbf{x}) = -i \sum_{\lambda=1,2} \frac{1}{V} \sum_{\mathbf{k}} \sqrt{\frac{|\mathbf{k}|}{2}} \left[\epsilon_{i,\mathbf{k}}^{(\lambda)} c_{\lambda,\mathbf{k}}^a e^{i\mathbf{k}\cdot\mathbf{x}} - \text{c.c} \right], \tag{4.31}$$

where $\epsilon_{i,\mathbf{k}}^{(\lambda)}$ is the transverse polarization vector[1]. The ensemble average over random numbers $c_{\lambda,\mathbf{k}}^a$ is taken according to the variance

$$\langle c_{\lambda,\mathbf{k}}^a c_{\lambda',\mathbf{k}'}^b \rangle = \delta_{\lambda,\lambda'} \delta^{a,b} V \delta_{\mathbf{k},\mathbf{k}'}. \tag{4.32}$$

The non-perturbative lattice simulations take into account classical-statistical fluctuations up to arbitrary powers in $\delta A_i^a(t,\mathbf{x})$. As such, we expect agreement with the above analytic results for the linear approximation at early times, while deviations should occur around t_Θ, when higher powers of $\delta A_i^a(t,\mathbf{x})$ become relevant. In Fig. 4.4, we plot the time-dependence of $\langle \mathbf{E}^a \cdot \mathbf{B}^a \rangle$, which is averaged over space-coordinates as well as random initial configurations. At early times, the effects of the small fluctuations are invisible and the result are in very good agreement with the analytical solution that is plotted in Fig. 4.2. At later times

[1] We restore the Gauss law in this construction following Ref. [226].

around t_Θ, however, the exponentially growing fluctuations cause decoherence of the uniform fields, and thus the ensemble average of $\mathbf{E}^a \cdot \mathbf{B}^a$ is diminished significantly and approaches zero quickly afterwards as expected. The number of random initial configurations used in this computation is $N_{\text{conf}} = 128$, where we have checked that sufficient convergence is obtained. The other parameters used for this computation are $g = 10^{-3}$, $N_{\text{latt}} = 64^3$ and $Qa = 0.312$ for lattice spacing a.

When computing $\mathbf{E}^a \cdot \mathbf{B}^a$, one can use higher-order definitions of the electric field and the magnetic field with respect to lattice spacing; e.g. the forward-backward averaged definition of the electric field and the clover-averaged definition of the magnetic field [178]. We have numerically checked that for the configurations investigated in this work naive and higher order definitions of magnetic and electric fields agree, however we expect that for more inhomogeneous configurations higher order definitions are crucial for a thorough investigation of topology.

Figure 4.5 shows the axial charge density for the massless case, which is obtained by integrating the space and ensemble average of $\mathbf{E}^a \cdot \mathbf{B}^a$ over time. Again, the early time behavior agrees well with the analytical result (4.18). Although the macroscopic color-electric and magnetic fields approach zero quickly after a time around t_Θ, a non-vanishing axial charge density is seen to persist for a much longer time after t_Θ. This is possible because the axial charge density is determined by the integrated time history of $\langle \mathbf{E}^a \cdot \mathbf{B}^a \rangle$. This observation indicates that coherent gauge fields very efficiently produce an axial charge density at early times, while part of the induced density persist to be present even well beyond characteristic decoherence times.

4.2 Transient anomalous charge production: fermion sector

4.2.1 Axial anomaly with real-time Wilson fermions

In this section, we investigate axial charge generation by using real-time lattice simulations with Wilson fermions [48, 50, 51, 193–197, 212]. This approach allows us to directly compute quark production and anomalous charge generation at leading order in the small coupling $g \ll 1$ for strong gauge fields $A \sim Q/g$. Consequently, we can use the lattice results to test the anomaly equation (4.1) in this far-from-equilibrium situation by separately computing the fermion and gauge field terms on its left and right hand side.

Starting from a homogeneous field configuration according to (4.2), for early times before t_Θ the gauge fields obey the classical Yang–Mills equations with vanishing color current, while the fermion field is determined through the Dirac equation in the background $SU(2)$ field:

$$\left(i\gamma^0\partial_0 + i\gamma^i D_i - m\right)\psi(x) = 0\,, \tag{4.33}$$

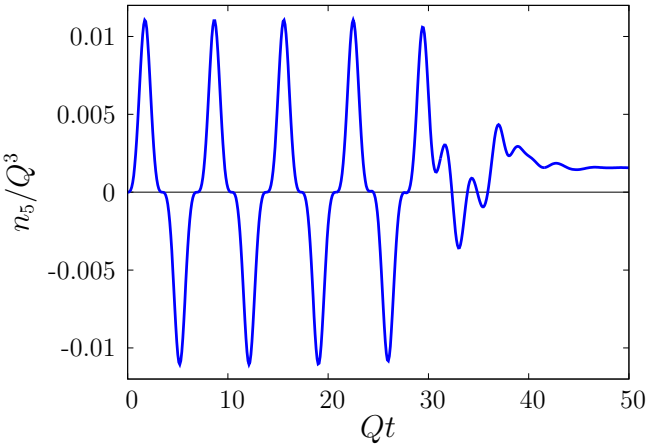

Figure 4.5: Lattice simulation results for the evolution of the axial charge density in the massless limit. The early-time behavior agrees well with the analytic result (4.18) drawn in Fig. 4.3. A nonzero charge density is seen to persists even well beyond the decoherence time of the macroscopic gauge fields. Figure taken from [52].

in temporal gauge with $A_0^a = 0$. Here we denote the spatial components of the covariant derivative by

$$D_i\psi = (\partial_i + igA_i^a T^a)\,\psi\,, \tag{4.34}$$

with the $SU(2)$ generators T^a.

We can expand the field operator in terms of mode functions

$$\psi(x) = \sum_{s,c}\int \frac{d^3p}{(2\pi)^3}\left[\psi^+_{\mathbf{p},s,c}(x)a_{\mathbf{p},s,c} + \psi^-_{\mathbf{p},s,c}(x)b^\dagger_{\mathbf{p},s,c}\right]\,, \tag{4.35}$$

with s being the spin and c denoting the color label. Here $a_{\mathbf{p},s,c}$ and $b_{\mathbf{p},s,c}$ are annihilation operators for particles and antiparticles, respectively. Because the Dirac equation is linear, the mode functions obey the same Dirac equation as the field operator:

$$\left(i\gamma^0\partial_0 + i\gamma^i D_i - m\right)\psi^\pm_{\mathbf{p},s,c}(x) = 0\,. \tag{4.36}$$

We consider for the initial state a perturbative vacuum, so that the initial condition for the mode functions at $t = 0$ reads

$$\psi^+_{\mathbf{p},s,c}(0,\mathbf{x}) = u(\mathbf{p},s)\,\chi_c\,\frac{e^{-ip\cdot x}}{\sqrt{2\omega_p}}\,, \tag{4.37}$$

$$\psi^-_{\mathbf{p},s,c}(0,\mathbf{x}) = v(\mathbf{p},s)\,\chi_c\,\frac{e^{+ip\cdot x}}{\sqrt{2\omega_p}}\,, \tag{4.38}$$

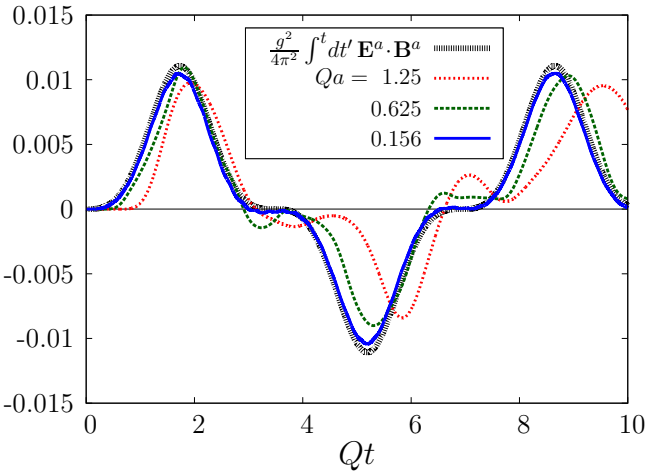

Figure 4.6: Comparison of the Wilson term contribution $2r\int_0^t dt' \mathrm{Re}\langle\overline{\psi} i\gamma_5 W\psi\rangle/Q^3$ and the anomaly term $g^2\int_0^t dt'\langle \mathbf{E}^a\cdot\mathbf{B}^a\rangle/(4\pi^2 Q^3)$ for three different values of the lattice spacing a with fixed Wilson parameter $r=1$. Figure taken from [52].

with χ_c being a unit vector in color space. Once we obtain the mode functions by solving the equation (4.36), we can compute any observables expressed in terms of the field operator ψ.

For the actual computations, we resort to a lattice discretization of the matter and gauge fields. We add the following lattice Hamiltonian for the quark field to the Hamiltonian for the gauge field (4.27):

$$\begin{aligned} H_f = a^3 \sum_{\mathbf{x}} \Big\{ & m\bar{\psi}(x)\gamma^0\psi(x) \\ & - \frac{1}{2a}\sum_i \bar{\psi}(x) i\gamma^i U_i(x)\psi(x+\hat{i}) \\ & + \frac{1}{2a}\sum_i \bar{\psi}(x) i\gamma^i U_i^\dagger(x-\hat{i})\psi(x-\hat{i})\Big\}. \end{aligned} \tag{4.39}$$

The fermion doubling problem is regularized by adding a spatial Wilson term, which we will specify later.

The expectation value of both the axial charge density and the pseudo-scalar condensate are expressed in terms of the mode functions as

$$n_5(t) = \frac{1}{V}\sum_{s,c}\sum_{\mathbf{p}} \psi^{-\,\dagger}_{\mathbf{p},s,c}(x)\gamma_5\psi^-_{\mathbf{p},s,c}(x)\,, \tag{4.40}$$

and

$$\langle\overline{\psi}(x) i\gamma_5\psi(x)\rangle = \frac{1}{V}\sum_{s,c}\sum_{\mathbf{p}} \psi^{-\,\dagger}_{\mathbf{p},s,c}(x) i\gamma^0\gamma_5\psi^-_{\mathbf{p},s,c}(x)\,, \tag{4.41}$$

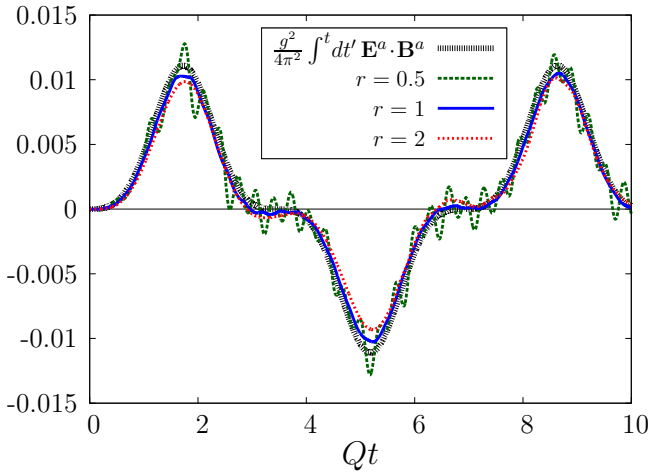

Figure 4.7: Time evolution of the same quantities as in Fig. 4.6, however, now the Wilson term contribution is shown for three different values of the Wilson parameter r with fixed lattice spacing $Qa = 0.208$. Figure taken from [52].

respectively.

The realization of the axial anomaly on a lattice is non-trivial. In fact, it is closely related to the lattice fermion doubling problem and the anomaly is recovered by introducing a regulator term, removing the doubler fermions. As is well known, from the lattice Dirac equation (4.33) one can easily compute the four-divergence of the axial current and obtain an anomaly-free equation. Correspondingly, if we numerically solve the Dirac equation (4.36) with the naive lattice fermions, both $\langle \partial_\mu j_5^\mu \rangle$ and $2m\langle \overline{\psi}(x) i\gamma_5 \psi(x)\rangle$ are zero, and thus the anomalous contributions cancel out. In contrast, if one breaks the chiral symmetry explicitly by introducing a Wilson term, the axial anomaly is recovered by the continuum limit of this regulator, as has been studied in detail in Euclidean field theory [179–181, 211, 227].

In order to recover the anomaly in real-time simulations, typically a combination of a spatial Wilson term together with a suppression of possible temporal doublers using suitable initial conditions are employed [195, 212]. The Dirac equation with the spatial Wilson term reads

$$\left(i\gamma^0\partial_0 + i\gamma^i D_i - m\right)\psi(x) + rW\psi(x) = 0\,, \tag{4.42}$$

where r is a positive constant and we have introduced an abbreviated notation

$$W\psi(x) = \frac{1}{2a}\sum_{i=1}^{3}\Big[U_i(x)\psi(x+\hat{i}) - 2\psi(x) + U_i^\dagger(x-\hat{i})\psi(x-\hat{i})\Big]. \tag{4.43}$$

For the specific case of a homogeneous background gauge field, one could in principle directly restrict the Brillouin zone to remove doublers as well, as long as this is done for the covariant (kinetic) momentum and hence in a gauge invariant way.[2] We comment on this possibility in the appendix.

Analyzing the anomaly on the lattice, it is helpful to point out that the relation (4.17) between the axial charge density, the time-integral of the pseudo-scalar condensate and of the anomaly term $\sim \langle \mathbf{E}^a \cdot \mathbf{B}^a \rangle$ is not realized unless one takes the continuum limit. However, there exists a modified equation that is exactly satisfied on the lattice:

$$n_5(t) = 2m \int_0^t dt' \, \langle \overline{\psi} i\gamma_5 \psi \rangle + 2r \int_0^t dt' \, \mathrm{Re} \langle \overline{\psi} i\gamma_5 W \psi \rangle (t'), \tag{4.44}$$

which can be derived from (4.42). Comparing (4.17) and (4.44), one concludes that for $r \neq 0$ the Wilson term contribution is responsible for the anomaly term:

$$2r \, \mathrm{Re} \langle \overline{\psi} i\gamma_5 W \psi \rangle \simeq \frac{g^2}{4\pi^2} \langle \mathbf{E}^a \cdot \mathbf{B}^a \rangle \, , \tag{4.45}$$

which is expected to be accurate only in the continuum limit.

Fig. 4.6 compares simulation results for the time-integrated left and right hand sides of (4.45) employing different values for the lattice spacing a. One observes that the relation (4.45) emerges for sufficiently small lattice spacing. The employed volume V for these computations is $Q^3V = 20^3$, and we have employed $r = 1$ for $m/Q = 0.1$. In fact, in the continuum limit this result is insensitive to the precise value of $r \neq 0$ although r apparently appears in (4.45) as an overall factor. In Fig. 4.7, we show the same Wilson term contribution for different values of the Wilson parameter r and fixed lattice spacing $Qa = 0.208$, for $m/Q = 0.1$ and $N_{\mathrm{latt}} = 96^3$. For the employed finite lattice spacing, small dependencies on r and deviations from the anomaly term $\sim \int_0^t dt' \langle \mathbf{E}^a \cdot \mathbf{B}^a \rangle$ are still visible, which will also reflect the level of accuracy for the anomaly on the lattice in our calculations.

After this preparatory analysis, we are now in a position to check the anomaly equation (4.17) by separately computing each of its terms. Since the results will depend on the explicit mixing of the different chiral components in the presence of a mass $m \neq 0$, we show in Fig. 4.8 the evolution of the axial charge density, of the time-integral of the pseudo-scalar condensate and of the anomaly term for two different masses $m/Q = 0.1$ and $m/Q = 0.5$. The sum of $2m \int_0^t dt' \, \langle \overline{\psi} i\gamma_5 \psi \rangle$ and of the anomaly term $g^2 \int_0^t dt' \langle \mathbf{E}^a \cdot \mathbf{B}^a \rangle / (4\pi^2)$ is also shown, since it has to agree to n_5 if the anomaly is accurately represented. The parameters used for these computations are $N_{\mathrm{latt}} = 96^3$, $r = 1$ and $Qa = 0.208$ for $m/Q = 0.1$, and $Qa = 0.0625$ for $m/Q = 0.5$.

For $m/Q = 0.1$, one observes from Fig. 4.8 that the anomaly term clearly dominates compared to the contributions from the pseudo-scalar condensate,

[2] In this case, specific non-chiral observables, like the energy-momentum tensor and the charge current, can also be computed with a cutoff to the canonical momentum [49].

while for $m/Q = 0.5$ the pseudo-scalar term gives a larger contribution. In both cases, we find that the anomaly equation (4.17) is satisfied up to the expected accuracy for the employed lattice spacings. This provides an important consistency check for the employed real-time regularization with a spatial Wilson term.

A further verification can be obtained from the comparison of the numerical lattice results for the axial charge density with the analytic solution (4.18). Since the latter is only applicable to the massless case, we perform different lattice simulations with decreasing but nonzero fermion masses in order to be able to study numerically the approach to the massless limit. Fig. 4.9 displays the analytic $m = 0$ curve along with lattice simulation results for three different values of the fermion mass: $m/Q = 0.2$, 0.1 and 0.01. One observes that with lighter fermion masses the numerical results gets closer to the analytic curve (4.18). In fact, Fig. 4.9 exhibits a remarkably good agreement of the massless limit and the massive lattice results already for $m/Q = 0.01$. This comparison represents a powerful demonstration that the axial anomaly is described by our real-time lattice simulations to very good accuracy.

4.3 Conclusions

In this work we have investigated the out-of-equilibrium dynamics of anomalous quark production in two-color QCD. We have shown that the generation of a nonzero axial charge density can be described analytically for a class of initial conditions characterized by large coherent gauge fields motivated from the Glasma picture. Employing real-time lattice simulations, we find that a transient anomalous charge density persists in this case even for times significantly exceeding the decoherence time of the macroscopic color-electric and magnetic fields. These findings can be very interesting for nonequilibrium phenomena such as the chiral magnetic effect during the very early stages of a relativistic heavy-ion collision, where finite-time effects may play a decisive role.

Our combination of analytical and numerical results provides stringent tests of real-time representations of the axial anomaly in lattice QCD. We have investigated in detail the regularization of the fermion doubling problem using a spatial Wilson term. To this end, we considered first a modified anomaly equation that is exactly fulfilled on the lattice, and discussed the impact of a finite lattice spacing for computations of anomalous contributions in the continuum limit. This allowed us to check the anomaly equation by separately computing the different nonequilibrium fermion and gauge correlation functions entering that equation. In particular, we have confirmed the insensitivity of the real-time results to the specific choice of the Wilson parameter approaching the continuum limit.

The present work provides an important basis for more realistic simulations of anomalous nonequilibrium or transport processes in QCD related to heavy-ion collisions. Following along these lines, a wide range of dynamical phenomena can be addressed with ab initio calculations, from the intriguing in-

terplay of non-Abelian and Abelian gauge fields underlying the chiral magnetic effect to possible chiral plasma instabilities [78, 228] followed into the far-from-equilibrium regime.

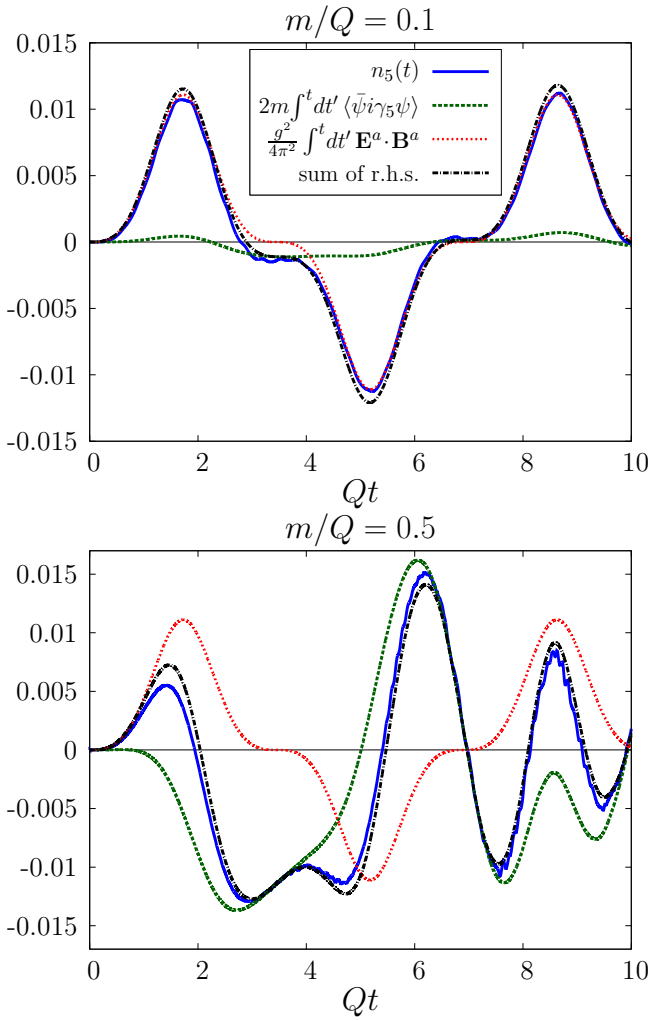

Figure 4.8: Time evolution of the various terms appearing in the anomaly equation (4.17) for two different fermion masses $m/Q = 0.1$ (left) and for $m/Q = 0.5$ (right). The sum of the two terms on the right hand side of (4.17) is plotted as well. Its agreement to n_5 within the expected accuracy for the employed lattice spacing provides a crucial validity check of the employed real-time regularization scheme. Figures taken from [52].

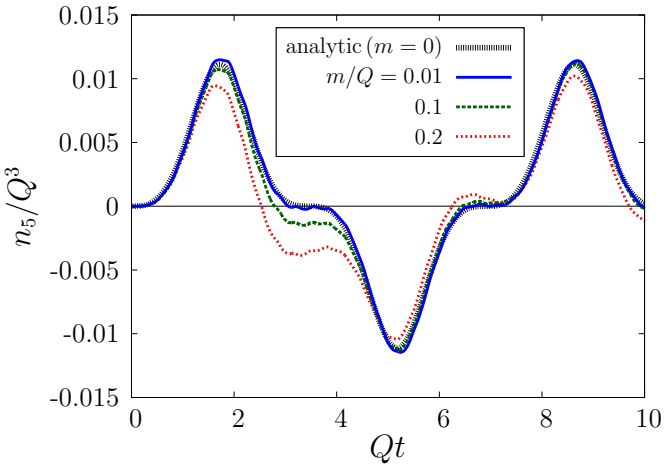

Figure 4.9: Time-dependence of the axial charge density. The analytic result (4.18), which is valid for the massless limit, and the results of the lattice simulations for different values of the quark mass are compared. The parameters used for the numerical computations are $N_{\text{latt}} = 96^3$, $Qa = 0.208$, and $r = 1$. Figure taken from [52].

Chapter 5

Non-equilibrium study of the Chiral Magnetic Effect from real-time simulations with dynamical fermions

The following section is based on the manuscript 'Chiral magnetic effect and anomalous transport from real-time lattice simulations' (N.M., S. Schlichting, S. Sharma), which is published in Phys.Rev.Lett. 117 (2016) no.14, 142301 [arXiv:1606.00342] [229] and 'Non-equilibrium study of the Chiral Magnetic Effect from real-time simulations with dynamical fermions' (M. Mace, N.M., S. Schlichting, S. Sharma), which is published in Phys.Rev. D95 (2017) no.3, 036023 [arXiv:1612.02477] [187]. The results presented here represent the first-ever real-time study of the chiral magnetic effect in the very early time regime of a heavy ion collision using classical-statistical simulations. While our study comprises an ab-initio approach, we note that the set-up that is simulated here, corresponds to a simplified situtations and thus motivates further work.

5.1 Classical-statistical lattice gauge theory with dynamical fermions

We first describe our setup to perform classical-statistical real-time lattice gauge theory simulations with dynamical fermions coupled simultaneously to non-Abelian $SU(N_c)$ and Abelian $U(1)$ gauge fields. Even though we will only consider the $SU(2) \times U(1)$ case in our simulations, the discussion is kept general in anticipation of future applications to the $SU(3) \times U(1)$ case relevant to heavy-ion physics. Our simulations are performed in $3+1$ dimensional Minkowski spacetime ($g^{\mu\nu} = \mathrm{diag}(1, -1, -1, -1)$), and we will denote the spacetime coordinate

x^μ as (t, x, y, z).

We employ temporal axial ($A^t = 0$) gauge and work in the Hamiltonian formalism of lattice gauge theory, first formulated by Kogut and Susskind [176], where time t remains a continuous coordinate while the spatial coordinates $\mathbf{x} = (x, y, z)$ are discretized on a lattice of size $N_x \times N_y \times N_z$ with periodic boundary conditions and lattice spacing a_s along each of the three dimensions. We choose a compact U(1) gauge group, such that both the non-Abelian and Abelian gauge fields are represented in terms of the usual lattice gauge link variables $U_{\mathbf{x},i} \in SU(N)\times U(1)$, where $\mathbf{x} \in \{0, \ldots, N_x-1\}\times\{0, \ldots, N_y-1\}\times\{0, \ldots, N_z-1\}$ denotes the spatial position and $i = x, y, z$ the spatial Lorentz index.

Since the classical-statistical lattice formulation for gauge fields has been extensively discussed in the literature (see e.g. [42]), we will focus on the practical realization of the fermion dynamics, noting that the foundations of the formalism have been laid out in [193, 196]. Since there are various complications with respect to the realization of continuum symmetries of fermions on the lattice, we have implemented two different discretization schemes for fermions in this work. We will first discuss the real-time lattice formulation with Wilson fermions and subsequently describe the real-time lattice formulation with overlap fermions.

5.1.1 Wilson Fermions in real time

Our starting point for the real-time lattice formulation with dynamical Wilson fermions is the lattice Hamiltonian operator, which takes the general form[1] [230]

$$\hat{H}_W = \frac{1}{2}\sum_{\mathbf{x}}[\hat{\psi}^\dagger_{\mathbf{x}}, \gamma^0\Big(-i\not{D}^s_W + m\Big)\hat{\psi}_{\mathbf{x}}]. \tag{5.1}$$

Here the fermion fields obey the usual anti-commutation relations

$$\{\hat{\psi}^\dagger_{\mathbf{x},a}, \hat{\psi}_{\mathbf{y},b}\} = \delta_{\mathbf{x},\mathbf{y}}\delta_{a,b}\ , \tag{5.2}$$

where a, b collectively stand for spin and color indices and $-i\not{D}^s_W$ denotes the tree-level improved Wilson Dirac operator

$$\begin{aligned} -i\not{D}^s_W\hat{\psi}_{\mathbf{x}} &= \frac{1}{2}\sum_{n,i} C_n\Big[\Big(-i\gamma^i - nr_w\Big)U_{\mathbf{x},+ni}\hat{\psi}_{\mathbf{x}+n\mathbf{i}} \\ &+ 2nr_w\hat{\psi}_{\mathbf{x}} - \Big(-i\gamma^i + nr_w\Big)U_{\mathbf{x},-ni}\hat{\psi}_{\mathbf{x}-n\mathbf{i}}\Big]\ . \end{aligned} \tag{5.3}$$

By r_w we denote the Wilson coefficient and we introduced the following short hand notation for the connecting gauge links

$$U_{\mathbf{x},+ni} = \prod_{k=0}^{n-1} U_{\mathbf{x}+k\mathbf{i},i}\ , \qquad U_{\mathbf{x},-ni} = \prod_{k=1}^{n} U^\dagger_{\mathbf{x}-k\mathbf{i},i}. \tag{5.4}$$

[1] We omit explicit factors of the lattice spacing. Hence all definition are given in dimensionless lattice units.

Based on an appropriate choice of the coefficients up to C_n it is possible to explicitly cancel lattice artifacts $\mathcal{O}(a^{2n-1})$ in the lattice Hamiltonian. By choosing only $C_1 = 1$ and all other coefficients to vanish, one recovers the usual (unimproved) Wilson Hamiltonian, which is only accurate to $O(a)$. With the first two terms $C_1 = 4/3$ and $C_2 = -1/6$ we can achieve an $O(a^3)$ (tree level) improvement, and by including also the third term $C_1 = 3/2\ , C_2 = -3/10\ , C_3 = 1/30$ we get an $O(a^5)$ (tree level) improvement.[2]

Operator decomposition and real-time evolution

While the gauge links $U_{\mathbf{x},i}$ are treated as classical variables, it is important to keep track of the quantum mechanical operator nature of the fermion fields. Evolution equations for the fermion operators are derived from the lattice Hamiltonian, as

$$i\gamma^0 \partial_t \hat{\psi}_x = (-i\not{D}^s_W + m)\hat{\psi}_x \ , \tag{5.5}$$

which can be solved on the operator level by performing a mode function expansion [193, 196]. Considering for definiteness an expansion in terms of the eigenstates of the Hamiltonian at initial time ($t = 0$) the mode function decomposition takes the form

$$\hat{\psi}_{\mathbf{x}}(t) = \frac{1}{\sqrt{V}} \sum_{\lambda} \Big(\hat{b}_\lambda(0)\phi^u_\lambda(t,\mathbf{x}) + \hat{d}^\dagger_\lambda(0)\phi^v_\lambda(t,\mathbf{x}) \Big) \ , \tag{5.6}$$

where $\lambda = 1, \cdots, 2N_c N_x N_y N_z$ labels the energy eigenstates and $\hat{b}(0)/\hat{d}^\dagger(0)$ correspond to the (anti) fermion (creation) annihilation operators acting on the initial state ($t = 0$) [193, 196]. By construction the time dependence of the fermion field operator $\hat{\psi}$ is then inherent to the wave-functions $\phi^{u/v}_\lambda(t,\mathbf{x})$, whereas the operator nature of $\hat{\psi}$ only appears through the operators $\hat{b}(0),\ \hat{d}^\dagger(0)$ acting in the initial state.

Since for a classical gauge field configuration the Dirac equation (5.5) is linear in the fermion operator, it follows from the decomposition in Eq.(5.6) that the wave-functions $\phi^{u/v}_\lambda(t,\mathbf{x})$ satisfy the same equation. One can then immediately compute the time evolution of fermion field operator by solving the Dirac equation for each of the $4N_c N_x N_y N_z$ wave functions. We obtain the numerical solutions using a leap-frog discretization scheme with time step $a_t = 0.02 a_s$.

In practice performing the decomposition in Eq.(5.5) amounts to the diagonalization of the matrix

$$\gamma^0 \Big(-i\not{D}^s_W + m \Big) \phi^{u/v}_\lambda(0,\mathbf{x}) = \pm\epsilon_\lambda \phi^{u/v}_\lambda(0,\mathbf{x}) \ , \tag{5.7}$$

at initial time, where $\epsilon_\lambda \geq m$ denotes the energy of single particle states. In the simplest case, where the gauge fields vanish at initial time, the eigenfunctions

[2] Note that our improvement procedure parallels that of Ref. [231]. Alternatively one could follow the procedure detailed in Ref. [232], leading to the appearance of the familiar Clover term.

ϕ^u_λ correspond to plane wave solutions and can be determined analytically as discussed in App. B.1. However, if we introduce a non-vanishing magnetic field B at initial time (c.f. Sec. 5.1.3), this is no longer the case and we instead determine the eigenfunctions ϕ^u_λ numerically using standard matrix diagonalization techniques.[3]

Initial conditions and operator expectation values

When computing any physical observable, one has to evaluate the operator expectation values with respect to the initial state density matrix. We will consider for simplicity an initial vacuum state, characterized by a vanishing single particle occupancy of fermions and anti-fermions $n^{u/v}_\lambda = 0$ yielding the following operator expectation values

$$\langle[\hat{b}^\dagger_\lambda, \hat{b}_{\lambda'}]\rangle = +2(n^u_\lambda - 1/2)\delta_{\lambda,\lambda'} \tag{5.8}$$

$$\langle[\hat{d}_\lambda, \hat{d}^\dagger_{\lambda'}]\rangle = -2(n^v_\lambda - 1/2)\delta_{\lambda,\lambda'} \tag{5.9}$$

whereas all other combinations of commutators vanish identically. Specifically for this choice of the initial state, the expectation values of a local operator $\hat{O}(t, \mathbf{x})$ involving a commutator of two fermion fields can be expressed according to

$$\hat{O}(t, \mathbf{x}) = \sum_{\mathbf{y}} O^{ab}_{\mathbf{xy}} \ \frac{1}{2}[\hat{\psi}^\dagger_{\mathbf{x},a}(t), \hat{\psi}_{\mathbf{y},b}(t)] \tag{5.10}$$

The expectation value of this bilinear form can be expressed according to

$$\begin{aligned}\langle\hat{O}(t, \mathbf{x})\rangle &= \frac{1}{V}\sum_{\lambda,\mathbf{y}}\Big[\phi^{u\dagger}_{\lambda,a}(t, \mathbf{x})O^{ab}_{\mathbf{xy}}\phi^u_{\lambda,b}(t, \mathbf{y})(n^u_\lambda - 1/2) \\ &\quad -\phi^{v\dagger}_{\lambda,a}(t, \mathbf{x})O^{ab}_{\mathbf{xy}}\phi^v_{\lambda,b}(t, \mathbf{y})(n^v_\lambda - 1/2)\Big] .\end{aligned} \tag{5.11}$$

as a weighted sum over the matrix elements of all wave-functions.

Vector and axial currents

We will consider vector j^μ_v and axial currents j^μ_a as our basic observables in this study. Since time remains continuous in the Hamiltonian formalism, vector and axial densities are defined in analogy to the continuum as

$$j^0_v(x) = \frac{1}{2}\langle[\hat{\psi}^\dagger_x, \hat{\psi}_x]\rangle , \qquad j^0_a(x) = \frac{1}{2}\langle[\hat{\psi}^\dagger_x, \gamma_5\hat{\psi}_x]\rangle . \tag{5.12}$$

and no extra terms occur for the time-like components. However, this is different for the spatial components of the currents, where additional terms arise in the

[3] Despite the fact that well known analytic solutions exist in the continuum in the case of a constant homogenous magnetic field, we are not aware of an equivalent analytic solution to Eq.(5.7) on the lattice.

lattice definition. By performing the variation of the Hamiltonian with respect to the Abelian gauge field, we obtain the spatial components of the vector currents according to

$$\begin{aligned} j_v^i(x) = & \\ \sum_{n,k=0}^{n-1} & \frac{C_n}{4}\Big\langle[\hat{\psi}^\dagger_{\mathbf{x}-k\mathbf{i}}, \gamma^0\Big(\gamma^i - inr_w\Big)U_{\mathbf{x}-k\mathbf{i},ni}\ \hat{\psi}_{\mathbf{x}+(n-k)\mathbf{i}}] \\ + & \quad [\hat{\psi}^\dagger_{\mathbf{x}+(n-k)\mathbf{i}}, \gamma^0\Big(\gamma^i + inr_w\Big)U_{\mathbf{x}+(n-k)\mathbf{i},-ni}\ \hat{\psi}_{\mathbf{x}-k\mathbf{i}}]\Big\rangle\ . \end{aligned} \tag{5.13}$$

Since the currents are derived from the improved Hamiltonian, these are by construction improved which is important for reducing discretization effects as we will discuss in more detail in the upcoming section.

Defining the axial currents requires a more careful analysis to recover the correct anomaly relations in the continuum limit. In order to fully appreciate this point, let us first recall that for a naive discretization of the fermion action (obtained e.g. by setting $r_w = 0$) an unphysical cancellation of the anomaly takes place, which can be understood as a consequence of the doubling of fermion modes [179]. Hence the correct realization of the axial anomaly for Wilson fermions relies on lifting the degeneracy between doublers by introducing the Wilson term ($r_w \neq 0$), and achieving an effective decoupling of the fermion doublers in the continuum limit [179]. Defining the spatial components of the axial current as

$$\begin{aligned} j_a^i(x) \quad = \quad & \sum_{n,k=0}^{n-1} \frac{C_n}{4}\Big\langle[\hat{\psi}^\dagger_{\mathbf{x}-k\mathbf{i}}, \gamma^0\gamma^i\gamma_5\ U_{\mathbf{x}-k\mathbf{i},ni}\ \hat{\psi}_{\mathbf{x}+(n-k)\mathbf{i}}] \\ + \quad & [\hat{\psi}^\dagger_{\mathbf{x}+(n-k)\mathbf{i}}, \gamma^0\gamma^i\gamma_5\ U_{\mathbf{x}+(n-k)\mathbf{i},-ni}\ \hat{\psi}_{\mathbf{x}-k\mathbf{i}}]\Big\rangle. \end{aligned} \tag{5.14}$$

it can easily be shown that the axial current for lattice Wilson fermions satisfies the exact relation

$$\partial_\mu j_a^\mu(x) = 2m\eta_a(x) + r_w W(x), \tag{5.15}$$

where $\partial_i j_a^i(x) = j_a^i(x) - j_a^i(x-i)$ and $\eta_a(x)$ denotes the pseudoscalar density

$$\eta_a(x) = \frac{1}{2}\langle[\hat{\psi}^\dagger_x, i\gamma^0\gamma_5\hat{\psi}_x]\rangle \tag{5.16}$$

and $W(x)$ is the explicit contribution from the Wilson term

$$\begin{aligned} W(x) = \sum_{n,i} \frac{n\cdot C_n}{4}\Big\langle[\hat{\psi}^\dagger_{\mathbf{x}}, i\gamma_5\gamma_0\big(U_{\mathbf{x},+ni}\hat{\psi}_{\mathbf{x}+n\mathbf{i}} - 2\hat{\psi}_{\mathbf{x}} \\ + U^\dagger_{\mathbf{x}-n\mathbf{i},+ni}\hat{\psi}_{\mathbf{x}-n\mathbf{i}}\big)] + \text{h.c.}\Big\rangle \end{aligned} \tag{5.17}$$

Even though the lattice anomaly relation in Eq.(5.15) may appear unfamiliar at first sight, it has been shown in the context of Euclidean lattice gauge theory,

that the usual form is recovered in the continuum limit, where the Wilson term gives rise to a non-trivial contribution

$$r_w W(x) \to -\frac{g^2}{8\pi^2}\mathrm{Tr}F_{\mu\nu}(x)\tilde{F}^{\mu\nu}(x), \tag{5.18}$$

$F_{\mu\nu}$ being the field strength tensor and $\tilde{F}^{\mu\nu} = \frac{1}{2}\epsilon^{\mu\nu\rho\sigma}F_{\rho\sigma}$ is it's dual. It can also be shown that the first deviations from the continuum limit appear as an odd function of r_w and improved convergence can be achieved by averaging of positive and negative values of the Wilson parameter [233, 234]. Even though the generalization of these proofs to the non-equilibrium case is non-trivial, explicit numerical verification has been reported in [52] and we will confirm this behavior in Sec. 5.2 based on our own simulations.

5.1.2 Overlap fermions in real time

Constructing the Overlap Hamiltonian

Wilson fermions break the chiral and anomalous $U_A(1)$ symmetries explicitly on the lattice. Explicit chiral symmetry is recovered only in the continuum limit for massless Wilson fermions[4]. With the improvement procedures for the Wilson fermions one can reduce the lattice artifacts responsible for chiral symmetry breaking, however it is still desirable to compare our results with a lattice fermion discretization where the chiral and continuum limits are clearly disentangled. Overlap fermions [183, 185] have exact chiral and flavor symmetries on the lattice and the anomalous $U_A(1)$ symmetry can be realized even for a finite lattice spacing, analogous to the way it happens in the continuum. Even though we will demonstrate that within our simple setup one can obtain comparable results with improved Wilson and Overlap fermions, we point out that the real-time overlap formulation may be important for future real-time simulations that either go beyond classical background fields or involve truly chiral fermions.

We will now employ overlap fermions for real-time simulations of the anomaly induced transport phenomena. As we did for the Wilson fermions, we consider a Hamiltonian formulation which for massless overlap quarks,

$$\hat{H}_{ov} = \frac{1}{2}\sum_{\mathbf{x}}[\hat{\psi}^\dagger_{\mathbf{x}}, \gamma_0\big(-i\not{D}^s_{ov}\big)\hat{\psi}_{\mathbf{x}}] \tag{5.19}$$

Here $-i\not{D}^s_{ov}$ is the 3D spatial overlap Dirac operator given by

$$-i\not{D}^s_{ov} = M\left(\mathbf{1} + \frac{\gamma_0 H_W(M)}{\sqrt{H_W(M)^2}}\right) \tag{5.20}$$

[4]Note that mass renormalization effects can render this issue problematic, as a carful tuning of the Wilson bare mass is required in taking the correct continuum limit. However, since we will only consider the dynamics of fermions in a classical background field, such problems are absent in the simulations present in this work.

and $H_W(M)$ is the original Wilson Hamiltonian kernel, defined in Eq.(5.1) but with $C_n = 0$ for $n \geq 2$, and with the fermion mass m being replaced by the negative of the domain wall height M, namely,

$$H_W(M) = \gamma_0(-i\not{D}^s_W - M). \tag{5.21}$$

The domain wall height takes values $M \in (0, 2]$. In Appendix B.3 we derive the Hamiltonian for the first time in the overlap formalism. We note that it is assuring that this construction is in exact agreement with the ansatz for the overlap Hamiltonian for vector-like gauge theories first discussed in [186]. Furthermore simulating massive overlap quarks is straightforward within this setup, which can be implemented by simply replacing

$$-i\not{D}^s_{ov} \to -i\not{D}^s_{ov}\left(1 - \frac{m}{2M}\right) + m, \tag{5.22}$$

where m is the quark mass we want to simulate.

The overlap Dirac matrix for massless quarks in three spatial dimensions, $\not{D}^s_{ov}$ satisfies the Ginsparg-Wilson relation [190],

$$\{\not{D}^s_{ov}, \gamma_5\} = -i\not{D}^s_{ov}\gamma_5\not{D}^s_{ov} \ . \tag{5.23}$$

Additionally the overlap Dirac operator is γ_0-hermitian, and satisfies a variant of Eq.(5.23),

$$\{\not{D}^s_{ov}, \gamma_0\} = -i\not{D}^s_{ov}\gamma_0\not{D}^s_{ov} \ . \tag{5.24}$$

As a consequence, it was shown in [186] that the Hamiltonian commutes with the operator

$$\hat{Q}_5 = \frac{1}{2}\sum_{\mathbf{x}}\left[\psi^\dagger_{\mathbf{x}}, \gamma_5\left(1 - \frac{-i\not{D}^s_{ov}}{2}\right)\psi_{\mathbf{x}}\right]. \tag{5.25}$$

This allows one to define $\hat{Q}_5$ as the axial charge within the Hamiltonian formalism, whose time evolution is given by the equation,

$$\frac{d\hat{Q}_5}{dt} = i[\hat{H}_{ov}, \hat{Q}_5] + \frac{\partial\hat{Q}_5}{\partial t} \ . \tag{5.26}$$

Since the first term in the right hand side of Eq.(5.26) is identically zero by construction, the time dependence of the axial charge density operator arises from the explicit real-time evolution of the matter fields in the definition of $\hat{Q}_5$. Hence in the real-time overlap formulation, the axial charge is generated exactly in the same way as in the continuum. While in [186] the definition of the axial charge operator, $\hat{Q}_5$, is motivated from the symmetries of the overlap Hamiltonian, we show below how this definition arises naturally from the spatial integral of the time component of the axial current.

Vector and axial currents in the overlap formalism

Since the overlap operator has exact chiral symmetry on the lattice one can define chiral projectors which project onto fermion states with definite handedness. The left and the right-handed fermion fields can be defined in terms of lattice projection operators $\check{P}_{\pm}$ as

$$\psi_{R/L} = \frac{1}{2}(\mathbf{1} \pm \check{\gamma}_5)\psi \equiv \check{P}_{\pm}\psi, \tag{5.27}$$

where $\check{\gamma}_5 \equiv \gamma_5(\mathbf{1} + i\not{D}^s_{ov})$. In order to satisfy the Ginsparg-Wilson relation, the chiral projectors for the conjugate fields are then

$$\psi^{\dagger}_{R/L} = \psi^{\dagger}\frac{1}{2}(\mathbf{1} \pm \gamma_5) \equiv \psi^{\dagger}P_{\pm}. \tag{5.28}$$

Instead of following the approach to define currents from the variation of the Hamiltonian, we can define vector currents in analogy to the continuum by constructing these quantities in terms of the physical left and right-handed fermion modes [191, 192]. Based on this approach, the vector current for overlap fermions in real-time are constructed as

$$\begin{aligned} j^{\mu}_{v} &= \frac{1}{2}\langle[\hat{\psi}^{\dagger}_{R}, \gamma_0\gamma^{\mu}\hat{\psi}_{R}]\rangle + \frac{1}{2}\langle[\hat{\psi}^{\dagger}_{L}, \gamma_0\gamma^{\mu}\hat{\psi}_{L}]\rangle \\ &= \frac{1}{2}\langle[\hat{\psi}^{\dagger}, \gamma_0\gamma^{\mu}\Big(\mathbf{1} - \frac{-i\not{D}^s_{ov}}{2}\Big)\hat{\psi}]\rangle; \end{aligned} \tag{5.29}$$

similarly the axial current are

$$\begin{aligned} j^{\mu}_{a} &= \frac{1}{2}\langle[\hat{\psi}^{\dagger}_{R}, \gamma_0\gamma^{\mu}\hat{\psi}_{R}]\rangle - \frac{1}{2}\langle[\hat{\psi}^{\dagger}_{L}, \gamma_0\gamma^{\mu}\hat{\psi}_{L}]\rangle \\ &= \frac{1}{2}\langle[\hat{\psi}^{\dagger}, \gamma_0\gamma^{\mu}\gamma_5\Big(\mathbf{1} - \frac{-i\not{D}^s_{ov}}{2}\Big)\hat{\psi}]\rangle \ . \end{aligned} \tag{5.30}$$

Numerical Implementation of the overlap operator

The overlap Hamiltonian consists of a matrix sign function of $H_W(M)$, defined in Eq.(5.20). The inverse square root of $H_W(M)^2$ can be expressed as a Zolotarev rational function [235–238],

$$\frac{1}{\sqrt{H_W(M)^2}} = \sum_{l=1}^{N_{\mathcal{O}}} \frac{b_l}{d_l + H_W(M)^2}. \tag{5.31}$$

To compute Eq.(B.23), first we compute the coefficients b_l and d_l from the smallest and largest eigenvalues of $H_W(M)^2$ [237]. Once the Zolotarev expansion coefficients d_l are determined, we implement a multi-shift conjugate gradient solver to calculate the inverse of $d_l + H_W(M)^2$. The lowest and the highest eigenvalues for $H_W(M)^2$ are calculated using the Kalkreuter-Simma Ritz algorithm [239] with 20 restarts and a convergence criterion of 10^{-20}. We find that taking

$N_{\mathcal{O}} = 20$ terms in the Zolotarev polynomial results in $|\text{sign}(H_W)^2 - \mathbf{1}| < 10^{-9}$. We note that the lowest and highest eigenvalues of $H_W(M)^2$ are sensitive to the choice of the domain wall height M. We have chosen M such that we obtain the best approximation to the sign function as well as the Ginsparg-Wilson relation. For the sphaleron configuration we studied in this work the optimal choice was $M \in [1.4, 1.6)$ (see App. B.2 for more details).

For the multi-shift conjugate gradient, the convergence of the conjugate gradient is determined by the smallest d_l, and the convergence criterion is set to $|H_W(M)^2| - 1 < 10^{-16}$. For the largest lattice volumes that we consider in this study and for the single $SU(2)$ sphaleron gauge configuration to be introduced in Sec. 5.1.3, the conjugate gradient algorithm reaches the convergence criterion before the maximum number of steps, which we choose to be 2000. We have also checked that the resultant overlap Dirac operator satisfies the Ginsparg-Wilson relation, and found this is satisfied to a precision of $\mathcal{O}(10^{-9})$. We have also carefully studied the M-dependent cut-off effects for the vector and axial-vector currents which we would illustrate in the subsequent sections as well as in the Appendix B.2. We find that the cut-off effects in the current operators are fairly independent of the choice of M for $M \in [1.4, 1.6)$.

Additionally, we have also implemented the overlap Hamiltonian in the presence an additional static $U(1)$ magnetic field to be introduced in Sec. 5.1.3. For this, we include the $U(1)$ fields in the Wilson Hamiltonian in Eq.(5.20). We find that the sign function is implemented to a precision of 10^{-9} and the overlap Dirac operator in this case satisfies the Ginsparg-Wilson relation to a precision of 10^{-8}.

5.1.3 Non-Abelian and Abelian gauge links

Within the classical-statistical approach, the dynamics of non-Abelian and Abelian fields is usually determined self-consistently by the solution to the classical Yang-Mills and Maxwell equations. In particular, the presence of the fermionic currents in the equations of motion for the gauge fields leads to a back-reaction of fermions, which is naturally included in the approach [193, 240]. Even though it will be desirable to investigate such effects in the long run, in the present study we will limit ourselves to a simpler set-up. Instead of a self-consistent determination of the non-Abelian and Abelian gauge fields, we will treat both of them as classical background fields whose dynamics is a priori prescribed.

$SU(2)$ gauge links

Concerning the $SU(2)$ gauge links, the dynamics is chosen to mimic that of a sphaleron transition by constructing a dynamical transition between topologically distinct classical vacua. Starting from the trivial vacuum solution $U^{SU(2)}_{\mathbf{x},i} = 1$ at initial time $t = 0$, we construct a smooth transition to a topologically non-trivial vacuum $U^{SU(2),G}_{\mathbf{x},i}$ at time $t \geq t_{\text{sph}}$ through a constant chromo-

electric field, corresponding to the shortest path in configuration space,

$$E^a_{\mathbf{x},i} = \begin{cases} \frac{i}{g a_s t_{\rm sph}} \log_{SU(2)}\left(U^{SU(2),G}_{\mathbf{x},i}\right) & , \quad 0 < t < t_{\rm sph} \\ 0 & , \quad t > t_{\rm sph} \end{cases} \tag{5.32}$$

during which the gauge links are constructed according to

$$U^{SU(2)}_{\mathbf{x},i}(t) = \begin{cases} \mathrm{e}^{-\mathrm{i}\mathrm{g}\mathrm{a}_\mathrm{s}\mathrm{t}\mathrm{E}^\mathrm{a}_{\mathbf{x},\mathrm{i}}\frac{\sigma^\mathrm{a}}{2}}\mathrm{U}^{\mathrm{SU}(2)}_{\mathbf{x},\mathrm{i}}(0) & , \quad 0 < t < t_{\rm sph} \\ U^{SU(2),G}_{\mathbf{x},i} & , \quad t > t_{\rm sph} \end{cases} \tag{5.33}$$

Since the different classical vacua are related to each other by a gauge transformation, we can easily construct a topologically non-trivial vacuum solution

$$U^{SU(2),G}_{\mathbf{x},i} = G_{\mathbf{x}} G^\dagger_{\mathbf{x}+\mathbf{i}}. \tag{5.34}$$

by specifying a gauge transformation G_x with a non-zero winding number. Based on the usual parametrization of the $SU(2)$ gauge group,

$$G_{\mathbf{x}} = \alpha_0(\mathbf{x})\mathbf{1} + i\alpha_a(\mathbf{x})\sigma^a \ , \tag{5.35}$$

the coordinates $\alpha_a(\mathbf{x})$ of the gauge transformation on the group manifold are obtained by a distorted stereographic projection of the lattice coordinates $\mathbf{x} = (x, y, z)$, which has a non-zero Brouwer degree. By virtue of our construction detailed in App. **??**, the sphaleron transition profile (i.e all points that map away from the trivial point $G_{\mathbf{x}} = 1$) is localized on a scale $r_{\rm sph}$, which we will refer to as the characteristic size scale of the sphaleron.

$U(1)$ gauge links

With regard to the Abelian gauge links we have chosen to implement a homogenous magnetic field $\vec{B} = B\hat{z}$ along the z-direction. Since on a periodic lattice the magnetic flux $qa_s^2 BN_xN_y$ is quantized in units of 2π [204], a spatially homogenous magnetic field cannot be varied continuously and we have chosen to keep the magnetic field constant as function of time. By choosing the $U(1)$ components of the gauge links according to [205],

$$U^{\mathrm{U}(1)}_{\mathbf{x},x} = \begin{cases} e^{ia_s^2 qBN_x y} & , \quad x = N_x - 1 \\ 1 & , \quad \text{otherwise} \end{cases} \tag{5.36}$$

$$U^{\mathrm{U}(1)}_{\mathbf{x},y} = e^{-ia_s^2 qBn_x} \tag{5.37}$$

with $U_{\mathbf{x},z} = 1$ and $a_s^2 qB = \frac{2\pi n_B}{N_x N_y}$ we can then realize different magnetic field strength by varying the magnetic flux quantum number n_B.

5.2 Sphaleron transition & real-time dynamics of axial charge production in $SU(N)$

We now turn to the results of our simulations and first study the dynamics of axial charges during a sphaleron transition in the absence of electro-magnetic fields ($B = 0$). Since the realization of the axial anomaly on the lattice is non-trivial a first important cross-check is to verify that the continuum version of the anomaly relation

$$\partial_\mu j^\mu_a(x) = 2m\eta_a(x) - 2\partial_\mu K^\mu(x) \,, \tag{5.38}$$

where $\partial_\mu K^\mu(x) = \frac{g^2}{16\pi^2}\mathrm{tr}F_{\mu\nu}\tilde{F}^{\mu\nu}$ denotes the divergence of the Chern-Simons current, is correctly reproduced in our simulations. If we focus on the volume integrated quantities

$$J^0_a(t) = \int d^3\mathbf{x}\; j^0_a(t,\mathbf{x}) \tag{5.39}$$

the net axial charge J^0_a can be directly related to the Chern-Simons number difference, according to

$$\Delta J^0_a(t) = -2\Delta N_{CS}(t) \,, \tag{5.40}$$

which changes by an integer amount over the course of the sphaleron transition. Specifically, for the topological transition constructed in Sec. 5.1.3, $\Delta N_{CS}(t \geq t_{\mathrm{sph}}) = -1$ and one expects $\Delta J^0_a(t) = 2$ units of axial charge to be created during the transition.

Simulation results for the real-time evolution of the net axial charge $J^0_a(t)$ are compactly summarized in Fig.5.1, where we compare results obtained for massless overlap fermions on a 16^3 spatial lattice with the results obtained for light Wilson fermions ($mr_{\mathrm{sph}} = 1.9 \cdot 10^{-2}$). Since the typical size scale of the sphaleron r_{sph} and duration of the sphaleron transition t_{sph} are the only dimensionful parameters in this case, in the following all spatial and temporal coordinates will be normalized in units of r_{sph} and t_{sph} respectively; if not stated otherwise we employ $t_{\mathrm{sph}}/r_{\mathrm{sph}} = 3/2$.

Since we employ a fermionic vacuum as our initial condition, the axial charge is zero initially, as there are no fermions present. As the sphaleron transition takes place fermions are dynamically produced and an axial imbalance is created. By comparing the evolution of $J^0_a(t)$ with that of the Chern-Simons number, extracted independently from the evolution of the gauge fields[5], it can be clearly seen that the global version of the anomaly relation in Eq.(5.40), is satisfied to good accuracy.

Concerning the comparison of different fermion discretizations, we find that the results for improved Wilson fermions (next to leading order) agree nicely with the ones obtained in the overlap formulation. However, we strongly emphasize that the operator improvements for Wilson fermions are essential to achieve

[5] We use an an $O(a^2)$ improved lattice definition described in detail in [125, 178].

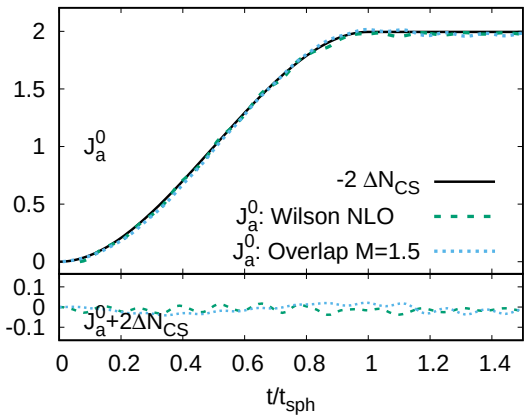

Figure 5.1: A comparison of the net axial charge generated during a sphaleron transition for improved Wilson (NLO) fermions with $mr_{\rm sph} = 1.9 \cdot 10^{-2}$ versus massless overlap fermions on a 16^3 lattice. Top: The net axial charge for both discretizations accurately tracks ΔN_{CS} due to the sphaleron transition. Bottom: Deviations from Eq.(5.40) are shown. Figure taken from [187].

this level of agreement on the relatively small 16^3 lattices. If in contrast one was to consider unimproved Wilson fermions, much finer lattices are needed to correctly reproduce the continuum anomaly and we refer to App. B.2 for further performance and convergence studies.

Even though our present results are obtained for a single smooth gauge field configuration, an important lesson can be inferred for upcoming studies on more realistic gauge fields. Since the computational cost of the simulations scales as $\propto N_x^2 N_y^2 N_z^2$, simulations on fine lattices are often prohibitively expensive and it is therefore of utmost importance to employ improved fermionic operators in real-time lattice simulations with dynamical fermions.

Based on the excellent agreement obtained between different lattice and continuum results for volume integrated quantities, we can now proceed to study the microscopic dynamics of axial charge production in more detail. In Fig. 5.2 we present a breakup of the different contributions, $\partial_t j^0_a, \partial_i j^i_a$ and $-2\partial_\mu K^\mu$, to the local anomaly budget (c.f. Eq.(5.38)) evaluated at the center $(x, y, z) = (N_x/2, N_y/2, N_z/2)$ of the sphaleron transition profile. We have kept the volume fixed in units of $r_{\rm sph}$ and to compare quantities between different lattice spacings and different fermion discretizations we have scaled the observables by appropriate powers of $r_{\rm sph}$. Besides the rate of increase of the axial charge density $\partial_t j^0_a$, a significant fraction of the anomaly budget is compensated by the divergence of the axial current $\partial_i j^i_a$, signaling the outflow of axial charge from the center to the edges of the transition region. Hence, even though an axial charge imbalance is dominantly produced in the center of a sphaleron, axial charge redistributes as a function of time and the axial imbalance at the center again decreases towards later times.

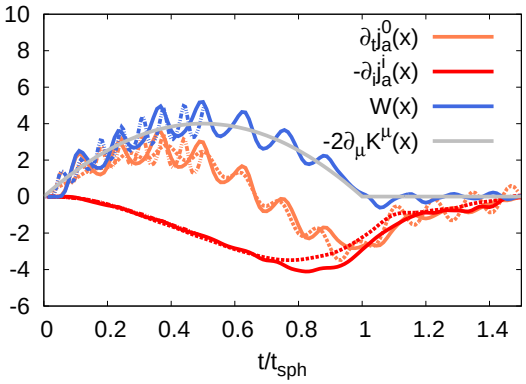

Figure 5.2: The local anomaly budget at the center of the sphaleron transition using improved Wilson (NLO) and overlap fermions. The solid, dash-dotted, and dotted lines represent data for improved Wilson (NLO) on a 16^3 lattice, 32^3 lattice, and overlap fermions on a 16^3 lattice respectively. The gray line represent the local derivative of the Chern Simons current, $-2\partial_\mu K^\mu$. Figure taken from [187].

As discussed in Sec. 5.1.1, the lattice anomaly relation for Wilson fermions is realized through the non-trivial continuum limit of the Wilson term $W(x)$ also depicted in Fig. 5.2. Indeed, the evolution of the Wilson term $W(x)$ follows that of the evolution of divergence of the Chern-Simons current $-2\partial_\mu K^\mu$, albeit superseded by fast oscillations. However, the oscillations average out in both space and time yielding a faster convergence for time and/or volume averaged quantities. It also re-assuring that the comparison of the results for almost massless Wilson and chiral overlap fermions shows good overall agreement, although minor deviations remain on the presently available lattice sizes.

5.2.1 Quark mass dependence

So far we have analyzed the non-equilibrium dynamics of axial charge production for (almost) chiral fermions. We will now vary the quark mass to investigate the effects of explicit chiral symmetry breaking on axial charge production. Before we turn to our physical results a technical remark is in order. Since we find that for Wilson fermions cut-off effects are more pronounced for larger values of the quark mass, we performed r_w averaging of our results, i.e. we performed real-time evolutions with Wilson parameters $r_w = \pm 1$ respectively and calculated observables by averaging the results over each value of r_w. Based on this procedure, a compact summary of our results for massive fermions is compiled in Fig. 5.3, showing freeze-frame profiles of the local anomaly budget for different values of the quark mass. Different panels show profiles of the (four) divergence of the Chern-Simons current $-2\partial_\mu K^\mu$, the pseudoscalar density η,

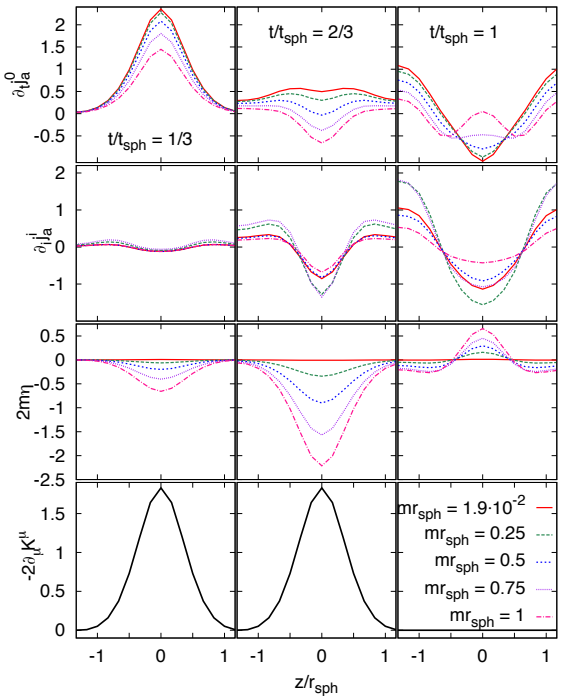

Figure 5.3: One dimensional profiles of the contributions to the anomaly equation for different masses in units of $r_{\rm sph}^{-1}$. As can be seen, the rate of axial charge density production at the center of the sphaleron is reduced due to axial currents carrying charge away and, in the case of a finite quark mass, by the pseudoscalar density, signaling chirality changing fermion-fermion interactions. Figure taken from [187].

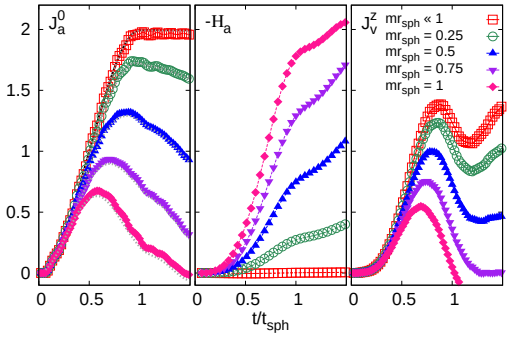

Figure 5.4: Evolution of the axial charge J^0_a (left), pseudo-scalar charge H_a (center) and vector current J^z_v (right) for different values of the fermion mass $mr_{\rm sph} = 3 \cdot 10^{-3}, 0.25, 0.5, 0.75, 1.0$. Comparison with the gray lines in the left panel demonstrates that the axial anomaly relation is satisfied in all cases. Figure taken from [229]

the divergence of the axial current $\partial_i j^i_a$ and the time derivative of the local axial charge density $\partial_t j^0_a$, along one of the spatial directions according to

$$\partial_\mu K^\mu(z,t) = \frac{g^2}{8\pi^2} \int d^2\mathbf{x}_\perp \; E^a_i(x) B^a_i(x) \; , \tag{5.41}$$

and similarly for the other components at three different times $t/t_{\rm sph} = 1/3,\ 2/3,\ 1$ of the sphaleron transition. Different curves in each panel correspond to the results obtained for different values of the fermion mass ranging from almost massless quarks $mr_{\rm sph} = 1.9 \cdot 10^{-2}$ to intermediate values of $mr_{\rm sph} = 1$.

Starting with the dynamics at early times ($t/t_{\rm sph} = 1/3$), the time derivative of the axial charge density shows a clear peak at the center corresponding to the creation of a local imbalance due to the sphaleron transition. While for almost massless quarks $mr_{\rm sph} = 1.9 \cdot 10^{-2}$, the rate of axial charge production $\partial_t j^0_a$ is approximately equal to the divergence of the Chern-Simons current $-2\partial_\mu K^\mu$, for heavier quark masses a significant fraction of the local anomaly budget is balanced by the contribution of the pseudoscalar density $2mn\eta$ resulting in a smaller rate of axial charge production, both locally as well as globally.

Once a local imbalance of axial charge is created at the center, axial currents j^i_a with a negative (positive) divergence $\partial_i j^i_a$ at the center (edges) develop and contribute an outflow of the axial charge density away from the center. Even though the divergence of the Chern-Simons current $-2\partial_\mu K^\mu$ remains positive at times $t/t_{\rm sph} = 2/3$, its contribution to the axial charge production rate j^0_a at the center is largely compensated by the outward flow of axial currents $\partial_i j^i$. In particular, for massive quarks ($mr_{\rm sph} > 1/2$), the combined effects of axial charge dissipation due to a large pseudoscalar density $2mn\eta$ and outflowing currents $\partial_i j^i$ lead to a depletion of axial charge at the center ($\partial_t j^0_a < 0$) even though the sphaleron transition is still in progress.

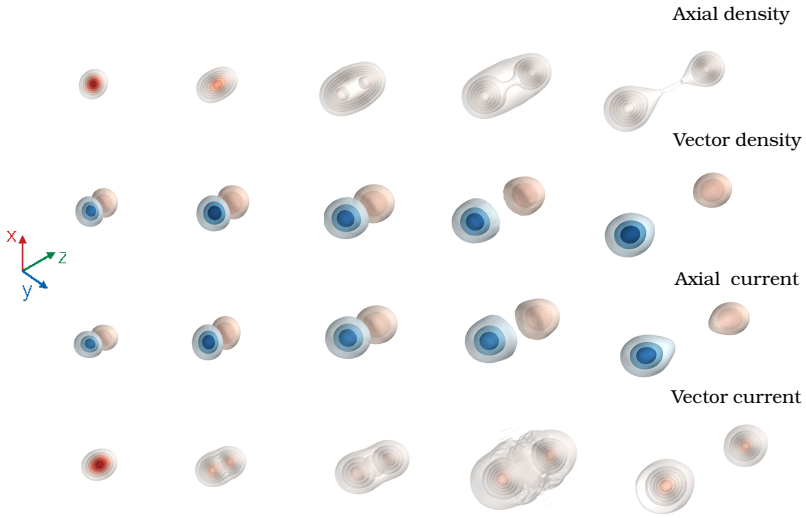

Figure 5.5: Profiles of the axial and vector densities and currents at different times of the real-time evolution for fermions with $mr_{\text{sph}} = 1.9 \cdot 10^{-2}$ for strong magnetic fields $qBr_{\text{sph}}^{-2} = 7.0$ at times $t/t_{\text{sph}} = 0.6, 0.9, 1.1, 1.3, 1.6$. Figure taken from [187].

Subsequently at even later times, axial charge continues to spread across the entire volume leading to a depletion of axial charge at the center and an increase towards the edges. In the case of massive quarks, the pseudoscalar density contributes towards the dissipation of axial charges, and the global imbalance J_a^0 decreases significantly as a function of time. Our simulations clearly point to the importance of including such dissipative effects due to a finite quark masses, and we will further elaborate on their influence on the dynamics of axial and vector charges in Sec. 5.3.2.

5.3 Chiral magnetic effect & Chiral magnetic wave in $SU(N) \times U(1)$

We now turn to investigate the real-time dynamics of fermions during a sphaleron transition in the presence of a strong (Abelian) magnetic field. Simulations are performed on larger $24 \times 24 \times 64$ lattices with improved Wilson fermions. We consider a homogenous magnetic field B in the z direction (c.f. Sec. 5.1.3) and prepare the initial conditions as a fermionic vacuum in the presence of the magnetic field. Since the Abelian magnetic field introduces a non-trivial coupling between the dynamics of vector and axial charges due to the Chiral Magnetic

Effect (CME) and Chiral Separation Effect (CSE) [241], the $SU(N) \times U(1)$ system exhibits interesting dynamics. Below we expand upon the quark mass and magnetic field dependence of the dynamics. Before we address these points in more detail, we will briefly illustrate the general features of the dynamics of vector and axial charges based on simulations for light quarks $mr_{\rm sph} = 1.9 \cdot 10^{-2}$ in a strong magnetic field $qBr_{\rm sph}^{-2} = 7.0$.

The basic features of the dynamics of vector and axial charges are compactly summarized in Fig. 5.5, showing three dimensional profiles of the axial and vector charge ($j^0_{a/v}$) and current ($j^z_{a/v}$) densities at different times ($t/t_{\rm sph} = 0.6, 0.9, 1.1, 1.3, 1.6$) during and after a sphaleron transition. As discussed in the previous section, the $SU(N)$ sphaleron transition leads to the creation of an axial imbalance observed at early times in the top panel of Fig. 5.5. However, in the presence of the $U(1)$ magnetic field, the generation of an axial charge imbalance is now accompanied by the creation of a vector current along the magnetic field direction (CME), which can be observed in the bottom panel of Fig. 5.5. Clearly the spatial profile of the vector current follows that of the axial charge distribution as expected from the constitutive relation $j^z_v \propto j^0_a B^z$ for the Chiral Magnetic Effect.

As seen in the second panel of Fig. 5.5 the vector current leads to a separation of vector charges along the direction of the magnetic field at early times. Over the timescale of the sphaleron transition, positive (red) and negative (blue) charges accumulate at the opposites edges of the sphaleron transition region and give rise to a dipole-like structure of the vector charge distribution. Due to the Chiral Separation Effect (CSE), the presence of a local vector charge imbalance at the edges in turn induces an axial current which is depicted in the third panel of Fig. 5.5 and leads to a separation of axial charge along the direction of the magnetic field. Ultimately the interplay of CME and CSE lead to formation of a Chiral Magnetic Wave, associated with the coupled transport of vector and axial charges along the direction of the magnetic field which can be observed at later times in Fig. 5.5.

Specifically for light fermions in the presence of a strong magnetic field, the emerging wave packets of axial charge and vector current are strongly localized and closely reflect the spacetime profile of the sphaleron. However, as we will see shortly this is no longer necessarily the case for heavier fermions or weaker magnetic fields. We also note that in our present setup, the dynamics at late times is somewhat trivial as the outgoing shock-waves are effectively propagating into the vacuum. While in a more realistic scenario the number of sphaleron transitions at early times is presumably still of $\mathcal{O}(1)$ [125], the chiral shock-waves are created from and move through a hot plasma and it will be interesting to observe how the subsequents dynamics is altered by further interactions with the constituents of the plasma.

Before we analyze the anomalous transport dynamics in more detail, we briefly comment on the comparison of Wilson and Overlap discretizations in the $SU(2) \times U(1)$ case. In order to perform a quantitative comparison of our results with different fermion discretizations, we will focus on the longitudinal

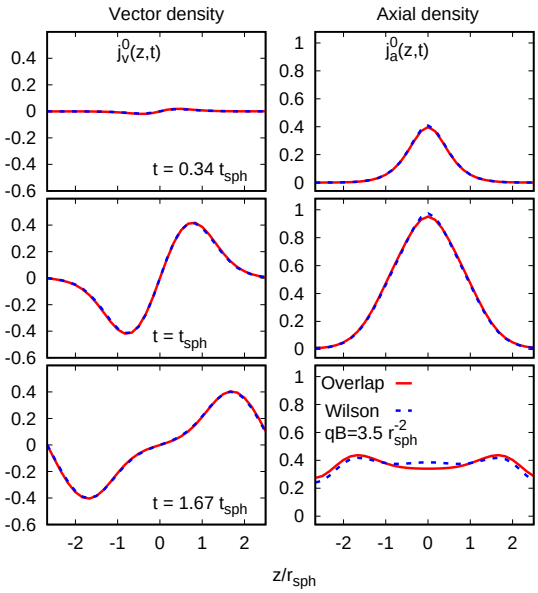

Figure 5.6: Comparison of longitudinal profiles of the vector (left) and axial (right) charge densities for improved Wilson (NLO) fermions and overlap fermions with masses $mr_{\rm sph} = 1.9 \cdot 10^{-2}$ in an external magnetic field $qB = 3.5 r_{\rm sph}^{-2}$ at times $t/t_{\rm sph} = 0.34,\ 1,\ 1.67$ (top to bottom). Figure taken from [187].

profiles of vector and axial charge densities defined as

$$j^0_{a/v}(t,z) = \int d^2\mathbf{x}_\perp \; j^0_{a/v}(t,\mathbf{x}_\perp,z). \tag{5.42}$$

Our results for somewhat smaller magnetic field strength $qB = 3.5 r_{\rm sph}^{-2}$ are compared in Fig. 5.6, showing freeze-frame profiles of the longitudinal vector and axial charge distribution at three different times $t/t_{\rm sph} = 0.34, 1, 1.67$. We observe a striking level of agreement between Wilson and Overlap results. Only at late times minor deviations between different discretizations become visible. However, at this point finite volume effects also start to become significant on the smaller $16 \times 16 \times 32$ lattices employed for this comparison.

5.3.1 Magnetic field dependence & comparison to anomalous hydrodynamics

We will now investigate in more detail the magnetic field strength dependence of these anomalous transport phenomena. Even though the basic features of the dynamics of vector and axial charges observed in Fig. 5.5 in the strong field limit remain the same for all values of the magnetic field considered in our study,

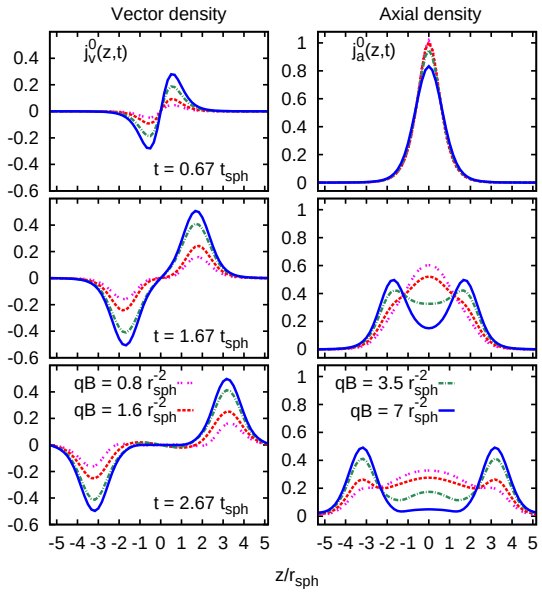

Figure 5.7: Longitudinal profiles of the vector (left) and axial (right) charge density for different magnetic fields qB in units of $r_{\rm sph}^{-2}$ and for $mr_{\rm sph} = 1.9\cdot 10^{-2}$ at times $t/t_{\rm sph} = 0.67,\ 1.67,\ 2.67$ (top to bottom). Figure taken from [187].

some interesting changes occur when the magnitude of the magnetic field, qB, becomes comparable to the size of the inverse sphaleron radius squared, $r_{\rm sph}^{-2}$, which is the other physical scale in our simulations.

Before we turn to the discussion of our simulation results, it is useful to first discuss how the magnetic field dependence enters in a macroscopic description in anomalous hydrodynamics [155]. In anomalous hydrodynamics the dynamics of vector and axial currents (in the chiral limit) is uniquely determined by the (anomalous) conservation of the (axial) vector currents

$$\partial_\mu j_v^\mu = 0\ , \qquad \partial_\mu j_a^\mu = -2\partial_\mu K^\mu\ , \tag{5.43}$$

once the constitutive relations for the currents are enforced. In the ideal limit the constitutive relations take the form [155]

$$j_{v,a}^\mu = n_{v,a} u^\mu + \sigma_{v,a}^B B^\mu\ , \tag{5.44}$$

and the magnetic field dependence enters only via the explicit B dependence of the transport coefficient $\sigma_{v/a}^B$. In the weak field regime ($qB \ll r_{\rm sph}^{-2}$) the conductivity is typically independent of the magnetic field and the CME/CSE currents are linearly proportional to the magnetic field B. In contrast in the strong field limit ($qB \gg r_{\rm sph}^{-2}$), the conductivity of a free fermi gas becomes $\sigma_{v/a}^B = n_{a/v}/B$ [15] for a unit charge and the late time dynamics of vector and

axial currents admits a simple analytic solution [229]

$$j^0_{v,a}(t > t_{\rm sph}, z) = \frac{1}{2}\int_0^{t_{\rm sph}} dt' \left[S\big(t', z - c(t-t')\big) \mp S\big(t', z + c(t-t')\big)\right] \tag{5.45}$$

where $S(t,z) = -\frac{g^2}{8\pi^2}\int d^2x_\perp \mathrm{Tr}\; F^{\mu\nu}\tilde{F}_{\mu\nu}$ reflects the spacetime profile of the sphaleron transition. Most remarkably, the solution in Eq.(5.45) shows explicitly that the anomalous transport dynamics becomes independent of the strength of the magnetic field B in the strong field limit. However, this asymptotic scenario is unlikely to be realized in real-world experiments and it is hence important to understand the real-time dynamics of vector and axial charges beyond such simple asymptotic solutions.

Our simulation results for different magnetic field strength $qBr^2_{\rm sph} = 0.8,\ 1.6,\ 3.5,\ 7.0$ are presented in Fig. 5.7, which shows the longitudinal profile of vector and axial charges densities $j^0_{a/v}(z,t)$ defined in Eq.(5.42) for various times during and after the sphaleron transition. Even though the production of axial charge $j^0_a(z,t)$ during the transition ($t < t_{\rm sph}$) is not altered significantly, the subsequent propagation of the chiral shock-waves is clearly affected by the strength of the magnetic field. While for the largest value of $qBr^2_{\rm sph} = 7.0$, the magnetic field can be interpreted as dominating over all other scales and the late time dynamics is accurately described by the asymptotic solution to anomalous hydrodynamics in Eq.(5.45), significant deviations from the asymptotic behavior occur for smaller values of $qBr^2_{\rm sph} = 0.8,\ 1.6,\ 3.5$. Specifically, one observes from Fig. 5.7 that a smaller CME current is induced for smaller values of the magnetic field, resulting in a reduced height of the vector charge peaks; in contrast the propagation velocities and profiles of the vector charge distribution are unaffected within this range of parameters.

Since a smaller amount of vector charge imbalance in turn leads to a reduction of the induced axial currents related to the CSE, clear differences emerge for the distribution of axial charges at later times. While for strong magnetic fields essentially all of the axial charge is subject to anomalous transport away from the center, a significant fraction of axial charge remains at the center for weaker magnetic field. Considering for instance the curves for $qBr^2_{\rm sph} = 1.6$, the axial charge distribution at later times can be thought of as a superposition of the free ($B = 0$) distribution and the Chiral Magnetic Wave contributing clearly visible peaks at the edges.

One can further quantify the magnetic field dependence by extracting the amount of vector charge separation achieved for different magnetic field strength. More precisely, we compute

$$\Delta J^0_v(t) = \int_{z\geq 0} dz\; j^0_v(t,z)\;, \tag{5.46}$$

corresponding to integrated the amount of vector charge contained in one of the oppositely charged wave-packets in Fig. 5.7. Simulation results for the magnetic

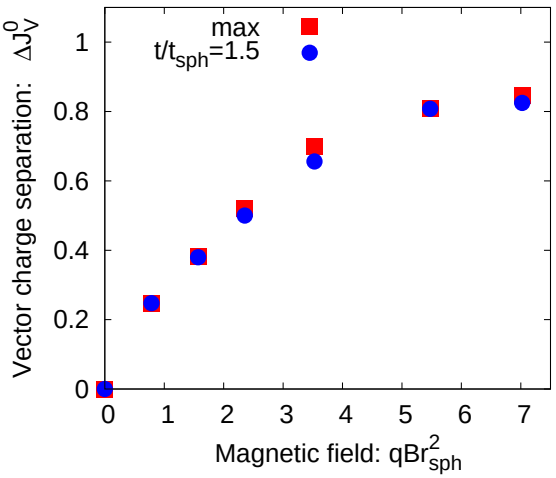

Figure 5.8: Vector charge separation ΔJ_v^0 as a function of the magnetic field strength qB in units of $r_{\rm sph}^{-2}$. Figure taken from [187].

field dependence of the charge separation signal are presented in Fig. (5.8), where different symbols correspond to the value of $\Delta J_v^0(t)$ at $t = 3/2t_{\rm sph}$ and respectively the maximum value of $\Delta J_v^0(t)$ observed over the entire simulation time. In accordance with the expectation that the CME current is linearly proportional to the magnetic field strength in the weak field regime, one observes an approximately linear rise of the charge separation signal at smaller values of the magnetic field strength $qB \lesssim 4/r_{\rm sph}^2$. In contrast for larger magnetic fields, the amount of vector charge separation begins to saturate, asymptotically approaching unity in the strong field limit.

Within our microscopic real-time description we can also attempt to verify directly to what extent the constitutive relations in Eq.(5.44) – assumed in a macroscopic description in anomalous hydrodynamics – are satisfied throughout the dynamical evolution of the system. In order to perform such a comparison, we extract the vector and axial charge $\Delta J_{a/v}^0(t)$ as well as the corresponding current densities $\Delta J_{a/v}^z(t)$ for the left- and right moving wave packets, and investigate the following ratios of net currents to net charges

$$C_{\rm CME}(t) = \frac{\Delta J_v^z(t)}{\Delta J_a^0(t)} \,, \qquad C_{\rm CSE}(t) = \frac{\Delta J_a^z(t)}{\Delta J_v^0(t)} \,. \tag{5.47}$$

If one assumes the validity of the constitutive relations in Eq.(5.44), one can immediately verify that both $C_{\rm CME}$ and $C_{\rm CSE}$ tend towards unity in the strong field limit [15]. In contrast, the weak field regime constitutive relations take the form $\Delta J_{v/a}^z \propto (\Delta J_{a/v}^0)^{1/3} qB$ at low temperatures and $\Delta J_{v/a}^z \propto (\Delta J_{a/v}^0) qB$ at high temperatures. Even though the ratios $C_{\rm CME}$ and $C_{\rm CSE}$ are no longer time independent constants in this limit, their numerical values are significantly

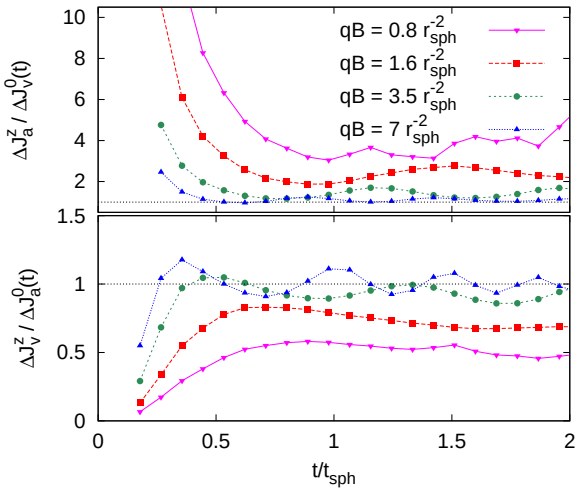

Figure 5.9: Top: Ratio between the axial current along the magnetic field and the electric charge (CSE) as a function of time as a function of the magnetic field strength qB in units of $r_{\rm sph}^{-2}$. Bottom: Ratio between the electric current and the axial charge (CME). Figure taken from [187].

smaller than unity and decrease as a function of axial/vector charge density [15].

Our results for these ratios are presented in Fig. 5.9, where we show the time evolution of $C_{\rm CME}^{\rm eff}$ and $C_{\rm CSE}^{\rm eff}$ for four different values of the magnetic field strength. Irrespective of the strength of the magnetic field one observes the same characteristic behavior of $C_{\rm CME}^{\rm eff}$ characterized by a rapid rise towards an approximately constant behavior at later times. In contrast for $C_{\rm CSE}^{\rm eff}$, the axial current J_a^z also receives a contribution from the outflow of axial charge that is independent of the vector charge density J_v^0. Since the vector charge imbalance J_v^0 is initially small, this contribution dominates over the anomalous transport contribution at early times. Hence the current ratio $C_{\rm CSE}^{\rm eff}$ approaches its asymptotic value from above and can also exhibit asymptotic values larger than unity for small field strength.

Quantitatively the values observed for $C_{\rm CME}^{\rm eff}$ ($C_{\rm CSE}^{\rm eff}$) at later times are close to the strong field limit for $qB = 3.5, 7$ and slightly smaller (larger) for $qB = 0.8, 1.6$ and it is also important to point out that the initial build up of the CME and CSE currents occurs on a shorter time scale for larger magnetic field strength. Oscillations around the constant value are also clearly visible at late times and the oscillation frequency again depends strongly on the strength of the magnetic field. However we can presently not exclude the possibility that the oscillations at late times are due to residual finite volume effects in our simulations and we will therefore not comment further on this behavior.

While the results in Fig. 5.9 nicely confirm the approximate validity of con-

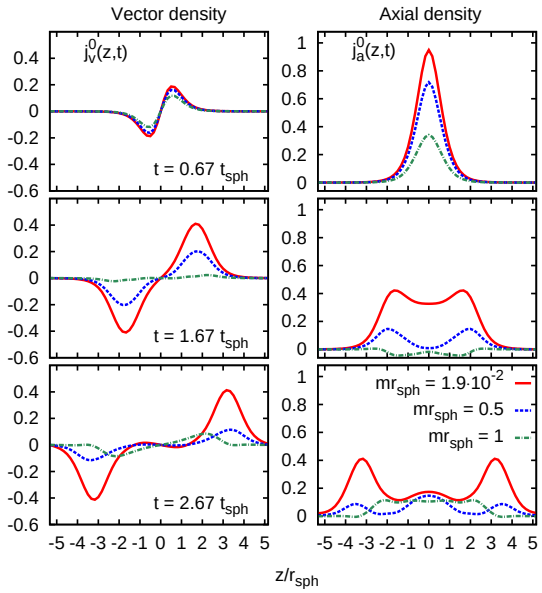

Figure 5.10: Longitudinal profiles of the vector (left) and axial (right) charge densities for different fermion masses in units of $r_{\rm sph}^{-1}$ at times $t/t_{\rm sph} = 0.67,\ 1.67,\ 2.67$ (top to bottom). Figure taken from [187].

stitutive relations at late times, it is also striking to observe that vector (CME) and axial (CSE) currents are not created instantaneously from the local imbalance of axial or vector charges. Conversely the results in Fig. 5.9 serve as a clear illustration of the retarded response and strongly suggest that, in order to describe the dynamics on shorter time scales, macroscopic descriptions should be modified to account for a finite relaxation time of anomalous currents. In the context of anomalous hydrodynamics, a natural way to include such effects is to follow the example of Israel and Stewart [242] by promoting the anomalous contribution to the currents to a dynamical variable $\xi^\mu_{v/a}$ that relaxes to the constitutive value $\sigma^B_{v/a}B^\mu$ on a characteristic time scale $\tau_{v/a}$. Since in high-energy heavy-ion collisions the lifetime of the magnetic field is presumably very short, it appears that the introduction of a finite relaxation time could indeed have quite dramatic effects. Hence it would also be important to understand more precisely which elementary processes determine the relevant time scale for the anomalous relaxation times. However, this question is beyond the scope of the present work.

5.3.2 Effects of finite Quark Masses

We discussed in Sec. 5.2.1 how explicit chiral symmetry breaking due to finite quark masses can significantly alter the production of an axial charge imbalance.

We will now investigate in more detail the effects of explicit chiral symmetry breaking on the subsequent dynamics, characterized by the anomalous transport of axial and vector charges in the presence of a background magnetic field. Our results for different fermion masses are compactly summarized in Fig. 5.10, where we show again the longitudinal profiles of vector and axial charge densities at different times during and after the sphaleron transition. While the simulations are performed with improved Wilson fermions for a relatively large magnetic field strength, $qBr_{\rm sph}^2 = 7.0$, we vary the masses from almost chiral fermions to fermions with large masses of the order of the inverse sphaleron size, $mr_{\rm sph} = 1$, where dissipative effects clearly become important on the time scales of interest.

In accordance with the discussion in Sec. 5.2.1 one observes from Fig. 5.10 that for heavier fermions ($mr_{\rm sph} = 0.5, 1$) the production of an axial charge imbalance at early times ($t/t_{\rm sph} = 0.67$) is suppressed compared to the almost massless case $mr_{\rm sph} = 1.9 \cdot 10^{-2}$. Since the anomalous vector currents are locally proportional to the axial charge imbalance, a similar suppression of the vector charge density of heavier fermions ($mr_{\rm sph} = 0.5, 1$) can also be observed at early times ($t/t_{\rm sph} = 0.67$). Over the course of the evolution, drastic differences in the distribution of vector and axial charges emerge between light and heavy fermions. One clearly observes from Fig. 5.10, how at times $t/t_{\rm sph} = 1.67, 2.67$ the overall amount of axial and vector charge separation is strongly suppressed for larger values of the fermion mass ($mr_{\rm sph} = 0.5, 1$). Moreover, as one would naturally expect for massive charge carriers, it is also evident from Fig. 5.10 that the propagation velocity of the chiral magnetic shock-waves decreases for larger values of the quark mass.

In order to further quantify the quark mass dependence of the anomalous transport effects, we follow the same procedure outlined in Sec. 5.2.1 and extract the vector and axial charge separation. Our results for the amount of vector/axial charge separation $\Delta J^0_{v/a}$ are presented in Fig. 5.11 as a function of the quark mass. Different symbols in Fig. 5.11 correspond to the vector/axial charge separation observed at a fixed time $t/t_{\rm sph} = 1.5$ and respectively the maximum value throughout the simulation ($0 \leq t/t_{\rm sph} \leq 3$). Most strikingly, one observes from Fig. 5.11 that clear deviations from the (almost) massless case emerge already for rather modest values of the quark mass. One finds that, for example for $mr_{\rm sph} = 0.25$, the observed vector charge separation signal is readily reduced by approximately 30%. Considering even heavier quarks up to $mr_{\rm sph} = 1$, the vector charge separation signal almost disappears completely as dissipative effects dominate the dynamics.

In view of the significant mass dependence observed in our simulations it would be interesting to compare our microscopic simulation results at finite quark mass to a macroscopic description of anomalous transport. However, we are presently not a aware of a macroscopic formulation that properly includes the effects of explicit chiral symmetry breaking. Even though mass effects might be small for phenomenological applications [158, 159, 243] in the light (u, d) quark sector, they appear to be highly relevant with regard to the phenomenological

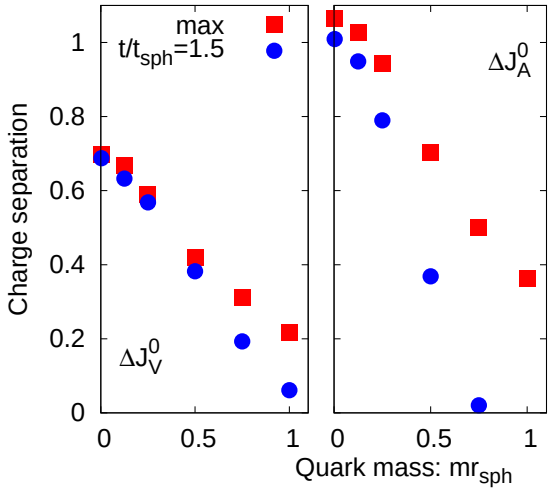

Figure 5.11: Vector (left) and axial (right) charge separation for different quark masses in units of $r_{\rm sph}^{-1}$. The red points denote the maximum amount of charge separation during the entire real-time evolution; the blue points denote the amount of charge separation at a fixed time, $t/t_{\rm sph} = 1.5$, shortly after the sphaleron transition. Figure taken from [187].

description of the CME in the strange quark sector. Based on our results in Fig. 5.11, we expect a significant reduction of the possible CME signals for strange quarks, such that overall the situation may be closer to a two-flavor scenario [244].

5.4 Conclusions & Outlook

We presented a real-time lattice approach to study non-equilibrium dynamics of axial and vector charges in the presence of non-Abelian and Abelian fields. Even though the approach itself is by now well known and established in the literature, we pointed out several improvements related to the choice of the fermion discretization which are important to achieve a reliable description of the dynamics of axial charges in particular. Specifically, we pointed out that the use of tree-level improvements and r-averaging for the Wilson operator are essential to accelerate the convergence to the continuum limit and produce physical results on available lattice sizes. We also discussed the advantages and disadvantages of using overlap fermions in real-time lattice simulations and, to the best of our knowledge, performed the first real-time 3+1D lattice simulations with dynamical fermions with exact chiral symmetry.

Based on our real-time non-equilibrium formulation, we studied the dynamics of axial charge production during an isolated sphaleron transition in $SU(2)$

Yang-Mills theory and explicitly verified that the axial anomaly recovered is satisfied to good accuracy at finite lattice spacing for both improved Wilson and overlap fermions. Beyond the dynamics for light fermions, we also investigated dissipative effects due to finite quark mass and reported how the emergence of a pseudoscalar density leads to a significant reduction of the axial charge imbalance created. Even though at present the sphaleron transition in the background gauge field configuration was constructed by hand and does not satisfy the equations of motion for the non-Abelian gauge fields, we emphasize that approximations of this kind made within our exploratory study can be relaxed in the future without any drawbacks on the applicability of our real-time lattice approach.

By introducing a constant magnetic field, we subsequently expand our simulations to a $SU(2) \times U(1)$ setup to study the real-time dynamics of anomalous transport processes such as the Chiral Magnetic and Chiral Separation Effect. We showed how the interplay of CME and CSE lead to the formation of a chiral magnetic shock-wave and demonstrated explicitly the dynamical separation of vector charges along the magnetic field direction. We also investigated in detail the quark mass and magnetic field dependence of these anomalous transport effects. Most importantly, we showed that the amount of vector charge separation created during this process is linearly proportional to the magnetic field strength (at small qB) and decreases rapidly as a function of the quark mass. Even though for light (u, d) flavors, such quark mass effects are most likely negligible over the typical time scales of a heavy-ion collision, the situation is different with regard to strange quarks, where it appears necessary to take these effects into account in a phenomenological description. Since in contrast to the vector current the axial current is not conserved, it would be extremely important to investigate how creation and dissipation of axial charges, which are accurately described within our microscopic framework, can be accounted for within a macroscopic description. On a similar note, we also studied the onset of the CME and CSE currents and reported first evidence for a finite relaxation time of vector and axial currents. Even though a finite relaxation time may have important phenomenological consequences, given the short lifetime of the magnetic field in high-energy heavy-ion collisions, it is presently unclear which microscopic processes determine the relevant time scale and we intend to return to this issue in a future publication. Our simulations were performed for an isolated sphaleron transition (c.f. Sec. II C 1), allowing us to clearly observe non-perturbative generation and transport of axial charges in a topologically non- trivial background. However, the results presented in this paper can only serve as a qualitative benchmark of the real-time dynamics of anomalous transport effects. In a more realistic scenario one expects the quantitative behavior of anomalous transport to be modified through further interactions with the constituents of the plasma, and it will be in- teresting to explore these effects in more detail in the future by performing analogous studies on more realistic gauge field ensembles.

Despite the fact that our present simulations of anomalous transport phenomena were performed in a drastically simplified setup, our work provides

an important step towards a more quantitative theoretical understanding of the CME and associated phenomena in high-energy heavy-ion collisions. Since the life time of the magnetic field in heavy-ion collisions is short, it is important to understand the dynamics of anomalous transport during the early time non-equilibrium phase. However, as we pointed out, the theoretical techniques developed in this work can be used to the address open questions in this context within a fully microscopic description of the early time dynamics. In the future it will be important to extend these studies to include more realistic gauge configurations and a spacetime dependent magnetic field in order to address important phenomenological issues. Besides the applications to high-energy nuclear physics, the theoretical approach advocated in this chapter has a large variety applications e.g. in the study of cold electroweak baryogenesis [195, 212], strong field QED [76], or cold atomic gases [86]. In this context, the technical developments achieved in this work should also be valuable and we are looking forward to explore further applications of our ideas.

Chapter 6

World-line construction of a covariant chiral kinetic theory

This chapter is based on "The chiral anomaly, Berry's phase and chiral kinetic theory, from world-lines in quantum field theory" (N.M., R. Venugopalan), arXiv:1701.03331 (submitted to Physical Review Letters) [245] and "World-line construction of a covariant chiral kinetic theory" (N.M., R. Venugopalan), arXiv:1702.01233 (submitted to Physical Review D) [246]. In this chapter we discuss a novel world-line framework for computations of the Chiral Magnetic Effect (CME) in ultrarelativistic heavy-ion collisions. Starting from the fermion determinant in the QCD effective action, we show explicitly how its real part can be expressed as a supersymmetric world-line action of spinning, colored, Grassmanian particles in background fields. Restricting ourselves for simplicity to spinning particles, we demonstrate how their constrained Hamiltonian dynamics arises for both massless and massive particles. In a semi-classical limit, this gives rise to the covariant generalization of the Bargmann-Michel-Telegdi equation; the derivation of the corresponding Wong equations for colored particles is straightforward. We outline how Berry's phase arises in a non-relativistic adiabatic limit for massive particles. We extend the discussion here to systems with a finite chemical potential. We discuss a path integral formulation of the relative phase in the fermion determinant that places it on the same footing as the real part. We construct the corresponding anomalous world-line axial vector current and show in detail how the chiral anomaly appears. Our work provides a systematic framework for a relativistic kinetic theory of chiral fermions in the fluctuating topological backgrounds that generate the CME in a deconfined quark-gluon plasma. We outline some further applications of this framework in many-body systems.

6.1 Introduction

The CME has already been observed in condensed matter experiments [19]. Observing its effects in heavy-ion collisions however poses a significant challenge [16, 20]. It requires an understanding of the earliest times in the heavy-ion collision, as the Abelian magnetic fields generated by "spectator" nucleons decrease very rapidly in time [17, 18]. Weak coupling frameworks applicable at high energies indicate that, at these early times, the strongly correlated quark and gluon matter is far off-equilibrium in a highly overoccupied "Glasma" state, which subsequently thermalizes to a quark-gluon plasma (QGP). Recent studies suggest that sphaleron transitions are far more frequent in the Glasma [125], than in the QGP [126]. Classical-statistical real-time simulations that include the dynamics of chiral fermions [52] clearly demonstrate the emergence of the CME in background magnetic fields [187, 229].

However this real-time description of the Glasma breaks down when, due to the spacetime expansion of the Glasma, typical occupation numbers become of order unity. In this dilute regime of the Glasma, classical-statistical methods must be matched to kinetic descriptions that describe the dynamics of the system as a weakly interacting gas of quasi-particles. Real-time simulations studying the thermalization process in the Glasma [41] show that the classical-statistical description matches smoothly on to an effective kinetic theory [247], which in turn can be matched to relativistic viscous hydrodynamics at later times. This description, when extrapolated to realistic values of coupling, gives values for thermalization times that are compatible with hydrodynamic descriptions of heavy-ion data. Phenomenological studies in such a hybrid framework have now been extended to photon production, whose yields are sensitive to all spacetime stages of a heavy-ion collision [248].

Similar considerations apply to the classical-statistical description of the spacetime evolution of the chiral magnetic current through the Glasma. The development of a chiral kinetic theory that interpolates between classical-statistical Glasma dynamics of axial charges at early times and hydrodynamic descriptions of such dynamics in the QGP [137, 155, 157–159] at late times is therefore essential for systematic phenomenological analysis of the CME in heavy-ion collisions. There has been a significant amount of work in developing such a chiral kinetic theory both in the context of condensed matter systems and for a deconfined QGP [142–154]. In several of the treatments, systems with large chemical potential are considered. The dynamics includes a Berry term corresponding to the Berry phase [141] that arises in such systems in an adiabatic limit, valid for excitations near the Fermi surface. While such treatments may be appropriate for systems containing large chemical potentials, they are problematic in relativistic contexts such as heavy-ion collisions where the assumptions of adiabaticity may not apply and where chemical potentials are not a priori large.

A further concern with chiral kinetic treatments is the possible conflation of topological effects due to the chiral anomaly and those arising from geometric phases in adiabatic and non-relativistic limits. Unlike the latter, the topological effects due to anomalies are generic and independent of kinematic limits.

The connection between anomalies and Berry's phase, which has been made frequently in the literature [124, 249, 250] (see [251] for a review), is the subject of a critical series of papers by Fujikawa and collaborators [252–254], where they point to distinctions between the topology of Berry's phase and those of the anomaly [255, 256]).

In this work, we will develop a novel framework towards constructing a consistent Lorentz-covariant chiral kinetic theory that is general valid in relativistic contexts and makes no requirement that the dynamics be adiabatic. To achieve this goal, we will adopt the world-line approach[1] to quantum field theory [258–265]. This world-line framework is closely connected to the Polakov path integral in string theory [266]. These connections were very effectively exploited in the work of Bern, Dixon, Dunbar and Kosower [267, 268] relating string amplitudes to multi-leg Feynman diagrams in QCD. More to point, it is employed in the seminal work on quantum anomalies by Alvarez-Gaume and Witten [269, 270] where it is shown how anomalies arise in the framework from the phase of the fermion determinant – as anticipated in the work of Fujikawa [122, 123].

The principal value of the D'Hoker-Gagné world-line construction is in its treatment of the relative phase in the fermion determinant which, as noted, is responsible for the chiral anomaly. By an ingenious trick, this phase can be rewritten as a path integral, with a point particle "action". This action has an identical structure to the action arising from the real part of the fermion determinant, with the only (and critically important) change being that the gauge fields are multiplied by a regulating parameter which breaks chiral symmetry explicitly. In the letter, we briefly outlined how the chiral anomaly arises in the D'Hoker-Gagné construction.

We will here develop many of the ideas outlined in [245] and provide an explicit derivation, adapted to our QED/QCD framework, of the D'Hoker-Gagné formalism. For the real part of the effective action, we explicitly write down the point particle action, and demonstrate that the equations of motion for QED are the covariant generalization of the Bargmann-Michel-Telegdi [271] equations for spinning particles in external fields. (For colored particles in QCD, the counterparts are the Wong [272] equations.) In particular, we will discuss the constrained Hamiltonian dynamics of spinning particles [273–277] in the world-line approach. This discussion is of considerable importance in deriving the non-relativistic limit for spinning particles.

Another novel feature of this manuscript is an explicit derivation of the chiral anomaly in the D'Hoker-Gagné world-line construction. In their work, they used a perturbative expansion to show how a Wess-Zumino-Witten term arises [255, 256] from the relative phase in the fermion determinant. In our work, in addition to clarifying some subtle points in the D'Hoker-Gagné construction, we will instead employ a non-perturbative variational method to derive the anomaly equation explicitly as the scalar product of electric and magnetic fields. The corresponding world-line anomalous axial current has a structure we will

[1] The original ideas can be traced all the way back to seminal works by Feynman [257] and Schwinger [69].

find useful in constructing a chiral kinetic theory.

This observation provides the segue to note that world-line treatment of the real and imaginary terms in the effective action for the fermion determinant both provide essential ingredients in a kinetic description of relativistic fermions in the background of Abelian or non-Abelian gauge fields. The quasi-particle limit of the theory, and furthermore the Liouville description of phase space, is contained entirely in the *real* part of the fermion effective action (continued to Minkowskian metric), independently of the anomaly. The Hamilton evolution of the corresponding equations of motion, formulated in proper time τ, allow for a Lorentz-covariant kinetic theory. Spin effects related to the definition of a Lorentz frame, such as recently proposed "side-jumps" are natural outcomes of a covariant description of spinning particles [146]. We showed in our letter [245] that for a non-relativistic limit corresponding to massive particles, adiabaticity conditions on the Larmor interaction energy, generate a Berry phase. Since this derivation only involves the real part of the fermion determinant, and the chiral anomaly arises from its imaginary piece, our work is an explicit demonstration of the prior observation by Fujikawa and collaborators [122, 123] regarding the distinction between the topological effects arising from each. For massless relativistic particles, and for situations where the Larmor energy is large, the topology of the anomaly alone is relevant.

An exception is the case of systems with large chemical potential, the original focus of the kinetic theory construction in [142, 144]. We will extend our discussion of non-relativistic limits in [245] to this case. We will show explicitly how the adiabaticity condition for the Larmor energy arises in this case. However even though there is a Berry phase in such situations, it is still distinct from the effects from the anomaly. Our work provides a first principles framework to address the fascinating interplay of these distinct effects. In work in progress[2], the formalism discussed here will be employed to derive the analogous "anomalous" Bödeker theory [279]. The resulting generalization of chiral kinetic theory can then be matched to results from classical-statistical simulations at early times and to anomalous hydrodynamics at late times.

The outline of this manuscript is as follows: In section 6.2, we begin by giving an introduction to the world-line method and we work out its formulation for a Dirac fermion coupled to both vector and axial-vector gauge fields. In particular, we introduce a 16 dimensional matrix formulation of the fermion effective action. As we shall discuss, this formulation is convenient for implementing a coherent state formalism for spinning and colored fields. We will show how the real part of the effective action is expressed in terms of a Grassmanian path integral over a supersymmetric point particle action for such fields. We next discuss the D'Hoker-Gagné path integral construction for the imaginary phase in the fermion determinant and show that it has a similar structure to the path integral formulation of the real part of the effective action. We use this construction to derive expressions for the vector and anomalous axial vector current which fullfil the (anomalous) Ward-identities known from second quantization. We

[2]For another attempt, we refer the reader to [278].

pay particular attention to the anomaly equation, which has novel features, and provide a detailed derivation to expose these features. In section 6.3 we perform a saddle point expansion to obtain the pseudo-classical dynamics of spinning particles. These were studied extensively previously in the literature and we connect our results to this body of work [273–277] in sec. 6.3.1. We note some parallels between our work and those of Stone and collaborators [147, 148, 150] though the derivations are different and employ different techniques.

The pseudo-classical limit of the world-line effective action leads to a Lorentz covariant form of the "anomalous" equations of motions put forward by [142–146, 152], when taking the non-relativistic and adiabatic limit in section 6.3.2. A kinetic theory can be constructed from the world-line framework for half-integer particles; as noted, the equations of motion obtained from the stationarity condition of the world-line path integral constitute characteristic equations for Liouville evolution of the phase space density. We investigate the case of massless particles in the presence of large chemical potential and discuss the corresponding non-relativistic adiabatic limit.

Our findings are supplemented by several appendices: In appendix C.1, we provide details of a derivation that is not discussed in the main text. In appendix C.2, we discuss the symmetry properties of the world-line action for spin-1/2 particles, corresponding to an $N = 1$ supersymmetric quantum mechanics. As our derivations generalize to arbitrary internal symmetry groups, we given an introduction in appendix C.3 to how color degrees of freedom can be treated semi-classically using Grassmanian variables. In appendix C.4, we discuss the difference between covariant and consistent anomalies. Finally in appendix C.5, we discuss in detail the meaning of the pseudo-classical limit in the world-line framework, which is tied to a hidden gauge symmetry and to constraints, which arise upon quantization.

6.2 The world-line framework

6.2.1 Introduction

In this section, we shall derive in the world-line formalism, the one-loop effective action for a Dirac fermion coupling to vector and axial-vector gauge fields. We will show that in Euclidean metric the axial anomaly can be understood as arising from the *imaginary* part of the effective action [269, 270]. This result is transparently related to the violation of chiral symmetry. We begin by introducing the main ideas of the relevant world-line framework. Some parts of our derivation parallel the work of D'Hoker and Gagné [280, 281]. We will however place special emphasis on some of the details in the definition of single particle path integrals. The careful treatment of these is relevant for the realization of the axial anomaly. The expression for the fermionic part of the action in the background of vector (A) and axial-vector (B) fields is

$$S[A,B] = \int d^4x\, \bar{\psi} \left(i\partial\!\!\!/ + A\!\!\!/ + \gamma_5 B\!\!\!/ \right) \psi \,, \tag{6.1}$$

where we allow the fermion fields to carry any internal (gauge) symmetry. We introduced here an auxilliary Abelian axial-vector field B because we are interested in the color singlet axial anomaly. We will treat B as a variational parameter which we will set to zero eventually. In the following, we have absorbed all couplings into the definition of the fields for convenience and they can be easily restored when necessary.

The fermionic part of the full path integral containing the action in Eq.(6.1) is a Grassmanian Gaussian integral and can be performed. This gives the determinant of the bilinear operator, $\det(i\partial\!\!\!/ + A\!\!\!/ + \gamma_5 B\!\!\!/)$, from which the fermion effective action can be defined,

$$-W[A,B] = \log\det(\theta), \qquad \theta \equiv i\partial\!\!\!/ + A\!\!\!/ + \gamma_5 B\!\!\!/\,. \tag{6.2}$$

We can now split Eq.(6.2) in a real and imaginary part,

$$W[A,B] = W_{\mathbb{R}}[A,B] + iW_{\mathbb{I}}[A,B], \tag{6.3}$$

which we discuss in detail below. We will continue with massless quarks; the extension to massive particles is straightforward and for the problems of interest will be discussed explicitly later. Since the imaginary piece above may be unfamiliar to some, we mention for future reference that, albeit in the physical case one has $W[A,B=0]_{\mathbb{I}} = 0$, the *variation* $\delta W[A,B]_{\mathbb{I}}/\delta B_\mu$ is non-zero even if $B = 0$. This variation defines the anomalous axial-vector current. For the sake of illustration, our final results will be given for the QED anomaly, but we will discuss how our findings can be generalized to non-Abelian theories as well. In Appendix C.1 we provide supplementary material and elaborate on some intermediate steps in the calculation.

6.2.2 Real Part

In this section, we will derive an expression for the real part of the fermion determinant, defined in Eq.(6.2) and Eq.(6.3). The real part is related to the modulus of the operator θ and can be expressed as

$$W_{\mathbb{R}} = -\frac{1}{2}\log\det\left(\theta^\dagger\theta\right) = -\frac{1}{2}\mathrm{Tr}\log\left(\theta^\dagger\theta\right)\,. \tag{6.4}$$

The main idea behind the world-line technique is to find an integral representation for the logarithm of the positive definite operator $\theta^\dagger\theta$. As we will shown below, this is equivalent to defining a quantum mechanical path integral for a relativistic particle on a closed loop, which is the world-line. We will require a basis of states for the trace in Eq.(6.4), which is over an infinite-dimensional space and contains both spacetime as well as internal indices. For spinors, this basis is related to the Clifford algebra of fermions, but the basis can include possible further internal symmetry groups such as color.

The spacetime trace can be turned into a quantum mechanical path integral for the bosonic coordinates of a point particle, as was shown in [258]. The trace over the Dirac matrix structure of spinors leads to path integrals using

a Grassmanian coherent state formalism. Such a coherent state formalism is discussed in [280, 281] and requires an artificial enlargment of the dimension of the space, in which the Dirac matrix structure is embedded, from 4×4 to 8×8. Interpreting $\theta^\dagger\theta$ as an eight dimensional matrix and making a similarity transformation as outlined in detail in [281], the fermionic effective action can be written as

$$W_{\mathbb{R}} = -\frac{1}{8}\log\det(\tilde{\Sigma}^2) = -\frac{1}{8}\mathrm{Tr}\log(\tilde{\Sigma}^2), \tag{6.5}$$

where $\tilde{\Sigma}^2$ is given by

$$\tilde{\Sigma}^2 = (p-\mathcal{A})^2\,\mathbb{I}_8 + \frac{i}{2}\Gamma_\mu\Gamma_\nu F_{\mu\nu}[\mathcal{A}],\ . \tag{6.6}$$

Here we have artificially enlarged the representation space of the gauge field to include the left and right handed chiral fields,

$$\mathcal{A} = \begin{pmatrix} A+B & 0 \\ 0 & A-B \end{pmatrix}, \tag{6.7}$$

whereby $\tilde{\Sigma}^2$ is a sixteen dimensional (8×2) matrix. The six 8×8 dimensional gamma matrices Γ_a are defined as

$$\Gamma_\mu = \begin{pmatrix} 0 & \gamma_\mu \\ \gamma_\mu & 0 \end{pmatrix}, \quad \Gamma_5 = \begin{pmatrix} 0 & \gamma_5 \\ \gamma_5 & 0 \end{pmatrix}, \quad \Gamma_6 = \begin{pmatrix} 0 & i\mathbb{I}_4 \\ -i\mathbb{I}_4 & 0 \end{pmatrix}, \tag{6.8}$$

with an additional matrix Γ_7, anti-commuting with all other elements of the algebra,

$$\Gamma_7 = -i\prod_{A=1}^{6}\Gamma_A = \begin{pmatrix} \mathbb{I}_4 & 0 \\ 0 & -\mathbb{I}_4 \end{pmatrix}, \qquad \{\Gamma_7, \Gamma_A\} = 0. \tag{6.9}$$

Here γ_μ and γ_5 are the usual Dirac matrices.

This artificial enlargemment of both the dimensions of the Dirac matrices as well as the representation of gauge fields may seem unmotivated. Indeed the splitting of Eq.(6.7) is strictly speaking not necessary at all, but simplifies our calculations significantly. The dimensional extension of the Dirac matrices, on the other hand, as defined in Eq.(6.8) is a necessity. The elementary idea behind the world-line approach is to express traces, such as those given in Eq.(6.5), in terms of quantum mechanical single particle states. As observed in [280, 282], this is not possible for four-dimensional Dirac matrices; a set of coherent fermion states, representing the corresponding Clifford algebra, exists however for the extension given in Eq.(6.8).

With this path integral formulation in mind, we will adopt Schwinger's integral representation to write Eq.(6.5) as

$$W_{\mathbb{R}} = \frac{1}{8}\int_0^\infty \frac{dT}{T}\ \mathrm{Tr}_{16}\ e^{-\frac{\varepsilon}{2}T\tilde{\Sigma}^2}, \tag{6.10}$$

where, by means of the $T-$integral, we have introduced what is commonly known as a closed world-line of length T. While Eq.(6.10) can be taken as the definition of the world-line, its structure will be discussed in more detail below. We introduced here an arbitrary positive real number $\mathcal{E}$ called the einbein. As is well known, and as we shall discuss explicitly in section 6.3 and in appendix C.2, $\mathcal{E}$ is not a physical quantity but rather a gauge parameter related to reparametrization invariance on the world-line.

The trace in Eq.(6.10) includes the internal (Dirac-)space and it can be evaulated using a coherent state basis that realizes the Clifford algebra of Dirac fermions. More specifically, the spin part of the trace in Eq.(6.10) is turned into a path integral over Grassman variables [280, 281], employing the methods developed first by Berezin and Marinov [273]. Towards this end, we introduce the fermion creation and annihilation operators ($a_r^\pm, r = 1, 2, 3$),

$$a_r^\pm = \frac{1}{2}(\Gamma_r \pm i\Gamma_{r+3}), \qquad \{a_r^+, a_s^-\} = \delta_{rs}, \qquad \{a_r^+, a_s^+\} = \{a_r^-, a_s^-\} = 0. \tag{6.11}$$

These operators $a_r^\pm$ span the space of the Clifford algebra satisfied by the Γ matrices. They define the coherent states $|\theta\rangle, |\bar\theta\rangle$ which satisfy

$$\langle\theta|a_r^- = \langle\theta|\theta_r \qquad a_r^-|\theta\rangle = \theta_r|\theta\rangle \qquad \langle\bar\theta|a_r^+ = \langle\bar\theta|\bar\theta_r \qquad a_r^+|\bar\theta\rangle = \bar\theta_r|\bar\theta\rangle\,, \tag{6.12}$$

with the matrix elements between coherent states defined to be

$$\langle\theta|\bar\theta\rangle = e^{\theta_r\bar\theta_r}, \qquad \langle\bar\theta|\theta\rangle = e^{\bar\theta_r\theta_r}\,. \tag{6.13}$$

These satisfy the completeness relations

$$\int |\theta\rangle\langle\theta|\; d^3\theta = \int d^3\bar\theta\, |\bar\theta\rangle\langle\bar\theta| = \mathbb{I}\,. \tag{6.14}$$

Note that while $\theta_r, \bar\theta_r, d\theta_r, d\bar\theta_r$ anticommute with $\langle\theta|$, $|\bar\theta\rangle$, they commute with $|\theta\rangle$, $\langle\bar\theta|$. All states and variables commute with the vacuum. With these definitions, traces in the coherent state basis can be defined.

The trace over a generic operator has the form

$$\mathrm{Tr}(O) = \int d^3\theta\langle -\theta|O|\theta\rangle\,. \tag{6.15}$$

This expression for the trace is discussed at length in [283]. The negative sign in Eq.(6.15) arises from transforming the coherent state basis to a Fock state basis. As this includes anti-commuting variables, the minus sign in Eq.(6.15) can be interpreted as enforcing anti-periodic boundary conditions for the Grassmann variables on the closed world-line. We can therefore write the trace in Eq.(6.10) as

$$\mathrm{Tr}_{16}\; e^{-\frac{\mathcal{E}}{2}T\tilde\Sigma^2} = \mathrm{tr}\int d^4z\; d^3\theta\; \langle z, -\theta|e^{-\frac{\mathcal{E}}{2}T\tilde\Sigma^2}|z.\theta\rangle\,. \tag{6.16}$$

The remaining trace (tr) on the r.h.s now contains only the trace over the representation space Eq.(6.7) and other internal symmetries such as color. If we proceed with Abelian gauge fields alone, tr is only over the two dimensional representation space Eq.(6.7) and is in fact trivial – it amounts to a simple sum over the two chiral configurations, as we will see below. Non-Abelian gauge fields can be included straigthforwardly. as we show in Appendix C.3. For simplicity, we will discuss only Abelian gauge fields for the rest of the manuscript; the extension to QCD will be discussed in follow-up papers.

We will now express the matrix element on the r.h.s of Eq.(6.16) as a path integral[3], with T playing the role of "time" and the "Hamiltonian" represented by $\mathcal{E}\tilde{\Sigma}^2/2$ [280, 281]. Our derivation, for this real part of the effective action, uses the conventional time-slicing procedure to construct the path integral. Splitting the time interval into N discrete steps of length $\Delta \equiv T/N$ (the continuum limit defined as $N \to \infty$ and $\Delta \to 0$), we define the average position between two time-slices

$$\bar{x}_\mu^k = \frac{x_\mu^k + x_\mu^{k-1}}{2}, \tag{6.17}$$

and for later use combine the three complex Grassman variables $\theta, \bar{\theta}$ into six real ones,

$$\begin{aligned} \psi_a^k &= \frac{1}{\sqrt{2}}(\theta_a^k + \bar{\theta}_a^k) && a = 1,2,3 \\ \psi_a^k &= \frac{i}{\sqrt{2}}(\theta_{a-3}^k - \bar{\theta}_{a-3}^k) && a = 4,5,6\,. \end{aligned} \tag{6.18}$$

Further, with these definitions, matrix elements containing Gamma-matrices Γ are evaluated by making use of Eq.(6.11) and Eq.(6.12) to read

$$\begin{aligned} \langle \theta^k | \Gamma_a \Gamma_b | \theta^{k-1} \rangle &= -\int d\bar{\theta}^k \langle \theta^k | \bar{\theta}^k \rangle \langle \bar{\theta}^k | \theta^{k-1} \rangle \, 2(\psi_a^k \psi_b^{k-1}) \\ &= -\int d\bar{\theta}^k e^{\theta_r^k \bar{\theta}_r^k + \bar{\theta}_r^k \theta_r^{k-1}} \, 2(\psi_a^k \psi_b^{k-1}). \end{aligned} \tag{6.19}$$

Eq.(6.19) can be generalized to higher matrix products using the simple mnemonic $\Gamma_a \to \sqrt{2}\,\psi_a$. After these preliminaries, inserting complete sets of coherent

[3]This strategy highlights the fact that in the world-line approach, contrary to the conventional approaches in quantum field theory, spin is not accounted for by means of a multidimensional wave function (as it is done for fermion spinors) but instead as an independent degree of freedom in the path integral.

states, we obtain,

$$\begin{aligned}
\mathrm{Tr}\Big\{e^{-\frac{\mathcal{E}}{2}T\tilde{\Sigma}^2}\Big\} &= -\mathrm{tr}\int\left(\prod_{l=0}^{N-1}d^4x_l\right)\left(\prod_{l=1}^{N}\frac{d^4p_l}{(2\pi)^4}\right)\left(\prod_{l=0}^{N-1}d^3\theta_l\right)\left(\prod_{l=1}^{N}d^3\bar{\theta}_l\right)\\
&\times\exp\Big\{-\Delta\sum_{k=1}^{N}\big[-ip_\mu^k\frac{(x_\mu^k-x_\mu^{k-1})}{\Delta}+\frac{\mathcal{E}}{2}\left(p_\mu^k-\mathcal{A}_\mu[\bar{x}^k]\right)^2\\
&-\frac{(\theta_r^k-\theta_r^{k-1})}{\Delta}\bar{\theta}_r^k+\frac{i\mathcal{E}}{2}\psi_\mu^kF_{\mu\nu}[\bar{x}^k]\psi_\nu^{k-1}\big]\Big\}\\
&= -\mathrm{tr}\int\left(\prod_{l=0}^{N-1}d^4x_l\right)\left(\prod_{l=1}^{N}\frac{d^4p_l}{(2\pi)^4}\right)\left(\prod_{l=0}^{N-1}d^3\theta_l\right)\left(\prod_{l=1}^{N}d^3\bar{\theta}_l\right)\\
&\times\exp\Big\{-\Delta\sum_{k=1}^{N}\big[-ip_\mu^k\frac{(x_\mu^k-x_\mu^{k-1})}{\Delta}+\frac{\mathcal{E}}{2}\left(p_\mu^k-\mathcal{A}_\mu[\bar{x}^k]\right)^2\\
&+\frac{1}{2}\psi_a^k\frac{(\psi_a^k-\psi_a^{k-1})}{\Delta}+\frac{i\mathcal{E}}{2}\psi_\mu^kF_{\mu\nu}[\bar{x}^k]\psi_\nu^{k-1}\big]\Big\}\\
&\equiv\mathcal{N}\int_P\mathcal{D}x\int_{AP}\mathcal{D}\psi\ \mathrm{tr}\ \exp\Big\{-\int_0^T d\tau\ \mathcal{L}(\tau)\Big\}. \qquad (6.20)
\end{aligned}$$

In obtaining the second equality, we symmetrized the "kinetic term" with respect to the variables $\theta,\bar{\theta}$ in order to replace the complex variables θ with ψ_a^k, using Eq.(6.18), before taking the continuum limit of the path integral [280, 281]. Further, in the last step, we completed the squares and shifted the p integration[4]. Periodic boundary conditions P for bosonic variables and anti-periodic boundary conditions AP for fermion observables are imposed respectively by identifying $x^0=x^N$ and $\psi^0=-\psi^N$. Expressing the Grasssmanian integration measure by the six-dimensional variables $\mathcal{D}\psi=\mathcal{D}\psi_\mu\mathcal{D}\psi_5\mathcal{D}\psi_6$, generates a trivial Jacobian, which can be absorbed in the normalization.

The real part of the effective action can thus be expressed in path integral form as

$$W_{\mathbb{R}}=\frac{1}{8}\int_0^\infty\frac{dT}{T}\mathcal{N}\int_P\mathcal{D}x\int_{AP}\mathcal{D}\psi\ \mathrm{tr}\exp\Big\{-\int_0^T d\tau\ \mathcal{L}(\tau)\Big\}. \qquad (6.21)$$

with the point particle "quantum mechanical" world-line Lagrangian

$$\mathcal{L}(\tau)=\frac{\dot{x}^2}{2\mathcal{E}}+\frac{1}{2}\psi_a\dot{\psi}_a-i\dot{x}_\mu\mathcal{A}_\mu+\frac{i\mathcal{E}}{2}\psi_\mu F_{\mu\nu}[\mathcal{A}]\psi_\nu\,, \qquad (6.22)$$

where

$$\begin{aligned}
\mathcal{L}(\tau)&=\begin{pmatrix}\mathcal{L}_L & 0\\ 0 & \mathcal{L}_R\end{pmatrix},\\
\mathcal{L}_{L/R}(\tau)&=\frac{\dot{x}^2}{2\mathcal{E}}+\frac{1}{2}\psi_a\dot{\psi}_a-i\dot{x}_\mu(A\pm B)_\mu+\frac{i\mathcal{E}}{2}\psi_\mu F_{\mu\nu}[A\pm B]\psi_\nu\,, \qquad (6.23)
\end{aligned}$$

[4]This standard trick replaces $p_\mu^k\to p_\mu^k-A_\mu[\bar{x}^k]-i(x_\mu^k-x_\mu^{k-1})/\mathcal{E}\Delta$.

carries the two-dimensional matrix structure of the helicity representation of the gauge fields Eq.(6.7) and can be trivially split into separate Lagrangians for both chiralities/helicities. The path integral can further be written more explicitly as

$$W_{\mathbb{R}} = \frac{1}{8}\int_0^\infty \frac{dT}{T}\mathcal{N}\int_P \mathcal{D}x \int_{AP}\mathcal{D}\psi \left[\exp\left\{-\int_0^T d\tau\ \mathcal{L}_L(\tau)\right\} + \exp\left\{-\int_0^T d\tau\ \mathcal{L}_R(\tau)\right\}\right]. \tag{6.24}$$

For a vector gauge theory, where $B = 0$, $\mathcal{L}_L = \mathcal{L}_R$, as both left and right handed massless particles couple to vector fields identically. In this case, the the trace in Eq.(6.21) just gives an overall factor of two. For the reasons outlined previously, we will keep $B \neq 0$. The normalization in Eq.(6.21) is

$$\mathcal{N} \equiv \mathcal{N}(T) = \int \mathcal{D}p\ e^{-\frac{\mathcal{E}}{2}\int_0^T d\tau\ p^2(\tau)}. \tag{6.25}$$

With this path integral definition of the real part of fermion effective action, one can begin to define currents (and products thereof). One obtains for instance the vector current $\langle j_\mu^V(y)\rangle$ to be[5]

$$\langle j_\mu^V(y)\rangle = \frac{\delta\Gamma_{\mathbb{R}}}{\delta A_\mu(y)} = -\frac{i}{8}\int_0^\infty \frac{dT}{T}\mathcal{N}\int_P \mathcal{D}x \int_{AP}\mathcal{D}\psi\ j_\mu^{V,cl}\left(e^{-\int_0^T d\tau\ \mathcal{L}_L(\tau)} + e^{-\int_0^T d\tau\ \mathcal{L}_R(\tau)}\right), \tag{6.26}$$

$$j_\mu^{V,cl} \equiv \int_0^T d\tau\ [\mathcal{E}\psi_\nu\psi_\mu\partial_\nu - \dot{x}_\mu]\delta^4\left(x(\tau) - y\right). \tag{6.27}$$

It can be easily shown that

$$\partial_\mu\langle j_\mu^V\rangle = 0 \qquad \Leftrightarrow \qquad \partial_\mu j_\mu^{V,cl} = 0. \tag{6.28}$$

In proving these relations, we first used the definition of the total derivative for the divergence of the first term of Eq.(6.27), employed our knowledge of the boundary terms and used that

$$\int_0^T d\tau\ \dot{x}_\mu\frac{\partial}{\partial y_\mu}\delta^4(x(\tau) - y) = -\int_0^T d\tau\ \frac{d}{d\tau}\delta^4(x(\tau) - y) = 0. \tag{6.29}$$

The second term in the four divergence of Eq.(6.27) vanishes by the anti-symmetry of the Grassmann variables, when interchanging the y and $x(\tau)$ derivatives. We note further that the world-line description provides us with a natural regularization as discussed in [284], whereby $T \to 0$ represents the ultraviolet limit of the effective action and $T \to \infty$ is related to the infrared limit.

[5]Note that this expression is still written in an Euclidean formulation. The continuation of this and like expressions to real-time is straightforward as we will show in section 6.3.

6.2.3 Imaginary Part

World-line representation of the phase of the fermion determinant

In this section, we will derive a path integral representation of the imaginary part of the fermion effective action, as defined in Eq.(6.3). As noted in [269], the absolute value of the phase of the fermion determinant is not well defined (for fermions in a complex representation). On the other hand, *variations* or *relative* phases (variation writh regards to an external parameter), are unambiguous. In the world-line framework, the fact that the absolute value of the phase in the fermion determinant is ill-defined is reflected by the lack of a heat kernel regularization for the imaginary part of the effective action – the latter is only possible when the action breaks axial symmetry explicitly.

We proceed with our discussion by expressing the relation between the phase of the fermion determinant and the corresponding imaginary part of the resulting effective action as

$$W_{\mathbb{I}} = -\arg\det[\theta]\,, \tag{6.30}$$

where θ is defined in Eq.(6.2). Again, extending the dimensionality of θ, we can write the above as

$$W_{\mathbb{I}} = -\frac{1}{2}\arg\det[\Omega], \qquad \Omega = \begin{pmatrix} 0 & \theta \\ \theta & 0 \end{pmatrix}\,, \tag{6.31}$$

where Ω, which is an 8×8 dimensional matrix which reads

$$\Omega = \Gamma_\mu(p_\mu - A_\mu) - i\Gamma_7\Gamma_\mu\Gamma_5\Gamma_6 B_\mu\,. \tag{6.32}$$

The Gamma matrices are those defined previously in Eq.(6.8) and Eq.(6.9). A lengthy derivation, that includes a further doubling of dimensions – discussed in [280, 281] in full detail – results in the expression

$$-iW_{\mathbb{I}} = \frac{1}{4}\mathrm{Tr}\log\tilde{\Omega} - \frac{1}{4}\mathrm{Tr}\log\tilde{\Omega}^\dagger\,, \tag{6.33}$$

where $\tilde{\Omega}$ is given as

$$\tilde{\Omega} = \frac{1}{2}(\tilde{\Sigma} - \tilde{\Sigma}^c)i\Gamma_6\Gamma_7 + \frac{i}{2}\Gamma_5\Gamma_6\Gamma_7\chi(\tilde{\Sigma} - \tilde{\Sigma}^c)i\Gamma_6\Gamma_7\,, \tag{6.34}$$

with

$$\tilde{\Sigma} = \Gamma_\mu(p_\mu - \mathcal{A}_\mu), \qquad \chi = \begin{pmatrix} 1 & 0 \\ 0 & -1 \end{pmatrix}\,. \tag{6.35}$$

We note that $\tilde{\Sigma}^c$ is the chiral conjugate of $\tilde{\Sigma}$, by setting $B \to -B$. This expression allows one to represent the phase of the fermion determinant as the trace of logarithms, as previously. The crucial difference to the real part however is that Eq.(6.34) does not permit a path integral representation analogous to

Eq.(6.10). This is principally because the operator $\tilde{\Omega}$ does not have a positive-definite spectrum, respectively heat kernel expression.

Nevertheless this obstacle is overcome by a trick due to D'Hoker and Gagné [280, 281]. Inserting an auxilliary parameter α, Eq.(6.33) can be written as

$$\begin{aligned} -iW_{\mathbb{I}} &= \frac{1}{4}\int\limits_{-1}^{1} d\alpha\, \frac{\partial}{\partial\alpha}\left(\mathrm{Tr}\log\left[\frac{1}{2}(\tilde{\Omega}+\tilde{\Omega}^{\dagger})+\frac{\alpha}{2}(\tilde{\Omega}-\tilde{\Omega}^{\dagger})\right]\right) \\ &= \frac{1}{4}\int\limits_{-1}^{1} d\alpha\, \mathrm{Tr}\left\{\frac{\tilde{\Omega}-\tilde{\Omega}^{\dagger}}{(\tilde{\Omega}+\tilde{\Omega}^{\dagger})+\alpha(\tilde{\Omega}-\tilde{\Omega}^{\dagger})}\right\}. \end{aligned} \tag{6.36}$$

Symmetrizing this expression with respect to α gives

$$\frac{1}{4}\int\limits_{-1}^{1} d\alpha\, \mathrm{Tr}\left\{\frac{\tilde{\Omega}^2-\tilde{\Omega}^{\dagger 2}}{(\tilde{\Omega}+\tilde{\Omega}^{\dagger})^2+2\alpha[\tilde{\Omega},\tilde{\Omega}^{\dagger}]-\alpha^2(\tilde{\Omega}^2-\tilde{\Omega}^{\dagger 2})}\right\}. \tag{6.37}$$

There is an identity that ensures that the denominator of this expression is positive-definite and admits a heat kernel regularization [280]. Keeping the numerator however separate and defining it as

$$\hat{M} \equiv \tilde{\Omega}^2-\tilde{\Omega}^{\dagger 2}\,, \tag{6.38}$$

in analogy to section 6.2.2, the imaginary part of the effective action can be expressed as

$$W_{\mathbb{I}} = \frac{i\mathcal{E}}{64}\int\limits_{-1}^{1} d\alpha \int\limits_{0}^{\infty} dT\ \mathrm{Tr}\left\{\hat{M}e^{-\frac{\mathcal{E}}{2}T\tilde{\Sigma}^2_{(\alpha)}}\right\}. \tag{6.39}$$

Remarkably the matrix $\tilde{\Sigma}^2_{(\alpha)}$ coincides with $\tilde{\Sigma}^2$ that enters Eq.(6.10), albeit with the replacement of the axial-vector field therein by $B \to \alpha B$. This result permits us to properly interpret α as the parameter regulating chiral symmetry breaking in the effective action. The values $\alpha = \pm 1$ correspond to the coupling of gauge fields to left- (right-) handed particles. Since Eq.(6.39) contains an continuous integral over α, chiral symmetry is necessarily broken for $\alpha \neq \pm 1$. There is a trace insertion Eq.(6.38), in Eq.(6.39) that is absent in the real part of the effective action[6]. This can be split into two contributions,

$$\hat{M} = \Gamma_7\Lambda, \qquad \Lambda = \Lambda^{(1)}+\Lambda^{(2)}, \tag{6.40}$$

which are given as

$$\begin{aligned} \Lambda^{(1)} &\equiv 2\Gamma_5\Gamma_6[\partial_\mu, B_\mu]\,\mathbb{I}_2, \\ \Lambda^{(2)} &\equiv [\Gamma_\mu,\Gamma_\nu]\{\partial_\mu, B_\nu\}\Gamma_5\Gamma_6\,\mathbb{I}_2\,. \end{aligned} \tag{6.41}$$

[6]This contribution is analogous to the γ_5 insertion in "textbook" discussions of the anomaly [266].

Both contributions are linear in the axial-vector field B and further are diagonal in the (two-dimensional) field representation space introduced in Eq.(6.7). Just as in the case for the real part of the effective action, the coherent state basis Eq.(6.11) can be used to present the trace in Eq.(6.39) as follows

$$\mathrm{Tr}\left\{\hat{M}e^{-\frac{\varepsilon}{2}T\tilde{\Sigma}^2_{(\alpha)}}\right\} = \int d^4z\; d^3\theta\; \langle z,-\theta|\hat{M}e^{-\frac{\varepsilon}{2}T\tilde{\Sigma}^2_{(\alpha)}}|z,\theta\rangle. \tag{6.42}$$

Here the (trivial) sub-trace over the two-dimensional field representation space is implicit. From Eq.(6.42), a path integral representation can be found; however the insertion of the operator $\hat{M}$ in the trace requires care in the discretization of the world-line, more so than for the real case discussed in section 6.2.2.

6.2.4 The axial-vector current

Our goal is to derive an expression for the global axial-vector current, defined as

$$\langle j^5_\mu(y)\rangle \equiv \frac{i\delta W_{\mathbb{I}}[A,B]}{\delta B_\mu(y)}\Big|_{B=0}. \tag{6.43}$$

We will subsequently derive the famous anomaly equation in our approach demonstrating that this current is not conserved. Eq.(6.43) can be written as

$$\begin{aligned}\langle j^5_\mu(y)\rangle \equiv \frac{i\delta W_{\mathbb{I}}}{\delta B_\mu(y)}\Big|_{B=0} &= -\frac{\mathcal{E}}{64}\int_0^1 d\alpha \int_0^\infty dT\; \mathrm{Tr}\left\{\frac{\delta\hat{M}}{\delta B_\mu(y)}e^{-\frac{\varepsilon}{2}T\tilde{\Sigma}^2_{(\alpha)}}\right\}_{B=0}\\ &= -\frac{\mathcal{E}}{32}\int_0^\infty dT\; \mathrm{Tr}\left\{\frac{\delta\hat{M}}{\delta B_\mu(y)}e^{-\frac{\varepsilon}{2}T\tilde{\Sigma}^2}\right\}_{B=0}.\end{aligned} \tag{6.44}$$

Note that the variation of the exponential with respect to B^μ does not contribute when B^μ is set to zero. The surviving expression above contains both terms in Eq.(6.40). We will discuss both separately. The trace in Eq.(6.44) is written as

$$\begin{aligned}\mathrm{Tr}\left\{\frac{\delta\hat{M}}{\delta B_\mu(y)}e^{-\frac{\varepsilon}{2}T\tilde{\Sigma}^2}\right\}_{B=0} &= \mathrm{tr}\int d^4x^0\; d^3\theta^0\; \langle x^0,-\theta^0|\;\frac{\delta\hat{M}}{\delta B_\mu(y)}e^{-\frac{\varepsilon}{2}T\tilde{\Sigma}^2}\;|x^0,\theta^0\rangle\\ &= \mathrm{tr}\int d^4x^0\; d^3\theta\; \langle x^0,\theta^0|\;\frac{\delta\Lambda}{\delta B_\mu(y)}\;e^{-\frac{\varepsilon}{2}T\tilde{\Sigma}^2}\;|x^0,\theta^0\rangle\end{aligned} \tag{6.45}$$

Here, in going from the first line to the second, we made use of $\langle-\theta|\Gamma_7 = \langle\theta|$. In particular, Γ_7 can be shown to be the equivalent of $(-1)^F$, where F is the fermion number operator defined from the coherent states in Eq.(6.11) (c.f. [280]).

This has important consequences: due to this world-line insertion, the path integral representation of the imaginary part of the fermion effective action will

contain an integration over Grassmannian variables with *periodic* boundary conditions. Consequently, fermionic zero modes arise, which would not be present otherwise. By insertion of complete sets of states, Eq.(6.44) can be written as

$$\langle j^5_\mu(y)\rangle = -\frac{\mathcal{E}}{32}\int\limits_0^\infty dT\,\mathrm{tr}\int d^4x^0 d^3\theta^0 d^4x^N d^3\theta^N \times\langle x^0,\theta^0|\frac{\delta\Lambda}{\delta B_\mu(y)}|x^N,\theta^N\rangle\langle x^N,\theta^N|\; e^{-\frac{\mathcal{E}}{2}T\tilde{\Sigma}^2}\;|x^0,\theta^0\rangle. \tag{6.46}$$

Both matrix elements in the r.h.s of this expression can be treated separately. We begin with the matrix element containing the exponential. In analogy with previous derivations, we get

$$\langle x^N,\theta^N|\; e^{-\frac{\mathcal{E}}{2}T\tilde{\Sigma}^2}\;|x^0,\theta^0\rangle = -\int\left(\prod_{k=1}^{N-1}d^4x_k\right)\left(\prod_{k=1}^{N}\frac{d^4p_k}{(2\pi)^4}\right)\left(\prod_{k=1}^{N-1}d^3\theta_k\right)\left(\prod_{k=1}^{N}d^3\bar{\theta}_k\right) \times\exp\Big\{-\Delta\sum_{k=1}^{N}\big[-ip^k_\mu\frac{(x^k_\mu-x^{k-1}_\mu)}{\Delta}+\frac{\mathcal{E}}{2}\left(p^k_\mu-A_\mu[\bar{x}^k]\right)^2 -\frac{(\theta^k_r-\theta^{k-1}_r)}{\Delta}\bar{\theta}^k_r+\frac{i\mathcal{E}}{2}\psi^k_\mu F_{\mu\nu}[\bar{x}^k]\psi^{k-1}_\nu\big]\Big\}. \tag{6.47}$$

We now proceed to evaluate the matrix element in Eq.(6.46) that contains the world-line insertion. From Eq.(6.40), the latter can be split into separate parts. We begin our discussion with $\Lambda^{(1)}$, which gives

$$\langle x^0,\theta^0|\frac{\delta\Lambda^{(1)}}{\delta B_\mu(y)}|x^N,\theta^N\rangle = 2\left(\frac{\partial}{\partial x^0_\mu}\delta(x^0-y)\right)\delta(x^0-x^N)\langle\theta^0|\Gamma_5\Gamma_6|\theta^N\rangle\,. \tag{6.48}$$

The second world-line insertion $\propto\Lambda^{(2)}$ is similarly

$$\langle x^0,\theta^0|\frac{\delta\Lambda^{(2)}}{\delta B_\mu(y)}|x^N,\theta^N\rangle =\Big\{\left(\frac{\partial}{\partial x^0_\nu}\delta(x^0-y)\right)\delta(x^0-x^N) +2\left(\frac{\partial}{\partial x^0_\nu}\delta(x^0-x^N)\right)\delta(\bar{x}^0-y)\Big\}\langle\theta^0|[\Gamma_\nu,\Gamma_\mu]\Gamma_5\Gamma_6|\theta^N\rangle\,. \tag{6.49}$$

Adding together Eq.(6.48) and Eq.(6.49), multiplying it with the matrix element in Eq.(6.47), and inserting this expression in the r.h.s of Eq.(6.46), gives us the complete world-line expression for the anomalous axial vector current.

Derivation of the axial anomaly

To determine the anomaly equation, we need to compute $\partial_\mu(\delta iW_{\mathbb{I}}/B_\mu(y))_{B=0}$. We should mention here at the outset that only Eq.(6.48) contributes to the

anomalous non-conservation of the axial-vector current, while Eq.(6.49) does not; this statement is illustrated in appendix C.1. One thus obtains

$$\partial_\mu \langle j^5_\mu(y)\rangle = \partial_\mu \frac{i\delta W_{\mathbb{I}}}{\delta B_\mu(y)}\Big|_{B=0} = -\frac{\mathcal{E}}{32}\int_0^\infty dT\ \partial_\mu \mathrm{Tr}\left(\Gamma_7 \frac{\delta\Lambda^{(1)}}{\delta B_\mu(y)} e^{-\frac{\varepsilon}{2}T\tilde{\Sigma}^2}\right) \tag{6.50}$$

where the trace is now written as

$$\begin{aligned}\partial_\mu \mathrm{Tr}\left(\Gamma_7 \frac{\delta\Lambda^{(1)}}{\delta B_\mu(y)} e^{-\frac{\varepsilon}{2}T\tilde{\Sigma}^2}\right) = -8\int \left(\prod_{l=0}^{N-1} d^4x^l\right)\left(\prod_{i=1}^{N}\frac{d^4p^i}{(2\pi)^4}\right)\left(\prod_{j=0}^{N} d^3\theta^j d^3\bar{\theta}^j\right)\\ \left(\frac{\partial^2}{\partial y_\mu \partial x^0_\mu}\delta(x^0-y)\right)\psi_5^0\psi_6^N \exp\Big\{-\Delta\sum_{k=1}^{N}\Big[-ip^k_\alpha\frac{(x^k_\alpha - x^{k-1}_\alpha)}{\Delta} - \frac{(\theta^k_r-\theta^{k-1}_r)}{\Delta}\\ + \frac{\mathcal{E}}{2}\left(p^k_\alpha - A_\alpha(\bar{x}^k)\right)^2 + \frac{i\mathcal{E}}{2}\psi^k_\alpha\psi^{k-1}_\beta F_{\alpha\beta}(\bar{x}^k)\Big] + (\theta^0_r-\theta^N_r)\bar{\theta}^0_r\Big\}.\end{aligned} \tag{6.51}$$

We have made use of Eq.(6.18) to write this expression in a compact form. We can now follow the same procedure as for the real part and complete the squares for the p_k $(k = 1,\ldots,N)$ integration[7]

$$p^k_\alpha \to p^k_\alpha - A_\alpha[\bar{x}^k] - i\frac{(x^k_\alpha - x^{k-1}_\alpha)}{\Delta\mathcal{E}}\,. \tag{6.52}$$

We then find

$$\begin{aligned}\partial_\mu \mathrm{Tr}\left(\Gamma_7 \frac{\delta\Lambda^{(1)}}{\delta B_\mu(y)} e^{-\frac{\varepsilon}{2}T\tilde{\Sigma}^2}\right) = -8\left\{\int\prod_{l=1}^{N}\frac{d^4p^l}{(2\pi)^4}e^{-\Delta\sum_{k=1}^{N}\frac{\varepsilon}{2}(p^k)^2}\right\}\int\left(\prod_{i=0}^{N-1}d^4x^i\right)\\ \left(\prod_{j=0}^{N}d^3\theta^j d^3\bar{\theta}^j\right)\left(\frac{\partial^2}{\partial y_\mu\partial x^0_\mu}\delta(x^0-y)\right)\psi_5^0\psi_6^N\exp\left\{-\Delta\sum_{k=1}^{N}\mathcal{L}^k\right\}.\end{aligned} \tag{6.53}$$

The exponential factor in the latter expression is

$$\begin{aligned}\exp\left\{-\Delta\sum_{k=1}^{N}\mathcal{L}^k\right\} \equiv \exp\Big\{-\Delta\sum_{k=1}^{N}\Big[\frac{1}{2\mathcal{E}}\frac{(x^k_\alpha - x^{k-1}_\alpha)^2}{\Delta^2} - \frac{(\theta^k_r-\theta^{k-1}_r)}{\Delta}\\ -i\frac{(x^k_\alpha - x^{k-1}_\alpha)}{\Delta}A_\alpha(\bar{x}^k) + \frac{i\mathcal{E}}{2}\psi^k_\alpha\psi^{k-1}_\beta F_{\alpha\beta}(\bar{x}^k)\Big] + (\theta^0_r-\theta^N_r)\bar{\theta}^0_r\Big\}.\end{aligned} \tag{6.54}$$

[7]This of course does not effect the integration variables in the representation of the world-line insertion. We emphasize this point, because in the compact notation in [280], this procedure is unclear and may cause confusion.

By means of partial integration $\frac{\partial^2}{\partial y_\mu \partial x^0_\mu}\delta(x^0-y) = -\delta(x^0-y)\frac{\partial^2}{\partial x^0_\mu \partial x^0_\mu}$, we get

$$\frac{\partial^2}{\partial x^0_\mu \partial x^0_\mu}\exp\left\{-\Delta\sum_{k=1}^{N}\mathcal{L}^k\right\} = \Big[-\frac{8}{\mathcal{E}\Delta} - 2i\left(\frac{\partial}{\partial x^0_\mu}A_\mu(\bar{x}^1) - \frac{\partial}{\partial x^0_\mu}A_\mu(\bar{x}^0)\right)$$
$$-i(x^1_\alpha - x^0_\alpha)\frac{\partial^2}{\partial x^0_\mu \partial x^0_\mu}A_\alpha(\bar{x}^1) - i(x^0_\alpha - x^N_\alpha)\frac{\partial^2}{\partial x^0_\mu \partial x^0_\mu}A_\alpha(\bar{x}^0) + O(\Delta)\Big]e^{-\Delta\sum_{k=1}^{N}\mathcal{L}^k}$$
$$\longrightarrow -\frac{8}{\mathcal{E}\Delta}\exp\left\{-\Delta\sum_{k=1}^{N}\mathcal{L}^k\right\}, \tag{6.55}$$

where the leading terms in the limit of $k \to \tau$, $\Delta \to 0$ are kept. In the continuum limit and setting $B = 0$ we have

$$\partial_\mu \frac{i\delta W_{\mathbb{I}}}{\delta B_\mu(y)} = 2\int_0^\infty dT\mathcal{N}(T)\int_P Dx\int_P D\psi\ (\psi_5\psi_6)(0)\delta(x(0)-y)$$
$$\times\exp\left\{-\int_0^T d\tau\ \frac{1}{2\mathcal{E}}\dot{x}^2 - i\dot{x}_\alpha A_\alpha(x) - \frac{1}{2}\psi_a\dot{\psi}_a + \frac{i\mathcal{E}}{2}\psi_\mu F_{\mu\nu}\psi_\nu\right\}, \tag{6.56}$$

where $(\psi_5\psi_6)(0)$ is an insertion of the respective Grassman variables at world-line "time" $\tau = 0$.

We will now find an analytic solution for Eq.(6.56). To this end, we remark that, as illustrated above, both anti-commuting as well as commuting world-line variables are defined with periodic boundary conditions. We can therefore write both respectively as a sum of a zero mode and a proper time dependent contribution

$$x_\mu(\tau) = \bar{x}_\mu + x'_\mu(\tau)\,, \tag{6.57}$$
$$\psi_a(\tau) = \bar{\psi}_a + \psi'_a(\tau)\,, \tag{6.58}$$

where the zero modes are defined to be

$$\bar{x}_\mu \equiv \int_0^T d\tau\ x_\mu(\tau) \qquad\qquad \bar{x}_\mu = x_\mu(0) = x_\mu(T) \tag{6.59}$$

$$\bar{\psi}_a \equiv \int_0^T d\tau\ \psi_a(\tau) \qquad\qquad \bar{\psi}_a = \psi_a(0) = \psi_a(T) \tag{6.60}$$

and similarly for ψ_5, ψ_6. The latter two fields can be trivially integrated in Eq.(6.56). The result is

$$\int_P d\psi\ \psi\, e^{-\frac{1}{2}\int_0^T d\tau\ \psi\dot{\psi}} = \int d\psi^0 d\psi'\ (\psi^0 + \psi')\, e^{-\frac{1}{2}\int_0^T d\tau\ \psi'\dot{\psi}'} = 1\,, \tag{6.61}$$

where ψ stands for either ψ_5, ψ_6. We will henceforth define the remaining integral measure as $\mathcal{D}\psi \equiv \prod_{\mu=1}^{4} \mathcal{D}\psi_\mu$. The result can be compactly summarized as

$$\partial_\mu \frac{i\delta W_{\mathbb{I}}}{\delta B_\mu(y)}\Big|_{B=0} = 2\int_0^\infty dT\, \mathcal{N}(T) \int D\bar{x}Dx' \int D\bar{\psi}D\psi'\, \delta(\bar{x}-y)$$
$$\times \exp\left\{ -\int_0^T d\tau\, \frac{1}{2\mathcal{E}}\dot{x'}^2 - i\dot{x'}_\alpha A_\alpha(x) - \frac{1}{2}\psi'_\mu\dot{\psi}'_\mu + \frac{i\mathcal{E}}{2}\psi'_\mu F_{\mu\nu}\psi'_\nu + \frac{i\mathcal{E}}{2}\bar{\psi}_\mu F_{\mu\nu}\bar{\psi}_\nu \right\}, \tag{6.62}$$

where the normalization $\mathcal{N}$ is as in Eq.(6.25). Because this normalization has a strong power law dependence on $1/T$ [266], the path integral receives its largest contributions from $T \to 0$. As the non-zero modes in Eq.(6.57) can be expanded in terms of eigenmodes with frequencies T^{-1}, higher modes do not contribute to the $T \to 0$ limit. It is therefore sufficient to expand the integrand around the zero modes, keeping non-zero modes only up to quadratic order. To evaluate this, it is convenient to use Fock-Schwinger gauge[8], centered around $\bar{x}$, which is defined by

$$x'_\mu(\tau) A_\mu(\bar{x} + x'(\tau)) = 0. \tag{6.63}$$

This expression can be formally solved for A, which results in

$$A_\mu(\bar{x}+x') = x'_\nu \int_0^1 d\eta\, \eta\, F_{\nu\mu}(\bar{x}+\eta x') = x'_\nu \int_0^1 d\eta\, \eta\, \exp\left(\eta\, x'_\alpha \partial_\alpha\right) F_{\nu\mu}(\bar{x}) \tag{6.64}$$

As we are expanding around the zero modes, it is sufficient to expand

$$A_\mu(\bar{x}+x') = \frac{1}{2}x'^{\,\nu} F_{\nu\mu}(\bar{x}) + \frac{1}{3}x'^{\,\nu} x'^{\,\rho} \partial_\nu F_{\rho\nu}(\bar{x}) + \dots. \tag{6.65}$$

In fact, we only need to keep

$$A_\mu(x) \approx \frac{1}{2} F_{\mu\nu}(\bar{x}) x'_\nu\,. \tag{6.66}$$

Exploiting Fock-Schwinger gauge thusly, Eq.(6.62) can be brought into the ap-

[8] This procedure was discussed in detail in [269, 270].

pealing form[9],

$$\partial_\mu \frac{i\delta W_{\mathbb{I}}}{\delta B_\mu(y)}\Big|_{B=0} = 2\int_0^\infty dT\mathcal{N}(T)\ \int D\bar{x}Dx' \int D\bar{\psi}D\psi'\ \delta(\bar{x}-y)$$
$$\times \exp\left\{ -\int_0^T d\tau\ \frac{1}{2\mathcal{E}}\dot{x'}^2 - \frac{i}{2}x'_\mu F_{\mu\nu}\dot{x}'_\nu - \frac{1}{2}\psi'_\mu\dot{\psi}'_\mu + \frac{i\mathcal{E}}{2}\psi'_\mu F_{\mu\nu}(\bar{x})\psi'_\nu + \frac{i\mathcal{E}}{2}\bar{\psi}_\mu F_{\mu\nu}(\bar{x})\bar{\psi}_\nu \right\}. \tag{6.67}$$

We proceed by performing the (quadratic) non-zero mode integration in Eq.(6.67). The results of performing these integrals are [262]

$$\int \mathcal{D}x'\ \exp\Big\{ -\int_0^\infty (\frac{\dot{x'}^2}{4} - \frac{i}{2}x'_\mu F_{\mu\nu}\dot{x}'_\nu)\Big\} = \mathrm{Det}'^{-\frac{1}{2}}\left(-\frac{d^2}{d\tau^2} + 2iF\frac{d}{d\tau}\right)$$
$$= \frac{1}{(4\pi T)^2}\mathrm{Det}'^{-\frac{1}{2}}\left(1 - 2iF\left(\frac{d}{d\tau}\right)^{-1}\right) = \frac{1}{(4\pi T)^2}\det{}^{-\frac{1}{2}}\left(\frac{\sin(FT)}{FT}\right) \tag{6.68}$$

and

$$\int \mathcal{D}\psi'\ \exp\Big\{ -\int_0^T (\frac{1}{2}\psi'_\mu\dot{\psi}'_\mu + i\psi'_\mu F_{\mu\nu}\psi'_\nu)\Big\} = \det{}^{\frac{1}{2}}\left(\frac{\sin(FT)}{FT}\right). \tag{6.69}$$

Here Det' indicates the determinant acting on the space of variables *sans* the zero modes, while det is defined on the reduced space on which the gauge field tensor F is defined. Due to the N=1 supersymmetry of Eq.(6.67), the fermionic and bosonic integrals Eq.(6.68) and Eq.(6.69) cancel,

$$\int \mathcal{D}x'\mathcal{D}\psi'\ \exp\Big\{ -\int_0^\tau d\tau\ \frac{\dot{x}'^2}{4} + \frac{1}{2}\psi'_\mu\dot{\psi}'_\mu - \frac{i}{2}x'_\mu F_{\mu\nu}(\bar{x})\dot{x}'_\nu + i\psi'_\mu F_{\mu\nu}(\bar{x})\psi'_\nu\Big\}$$
$$= \frac{1}{4\pi^2}\frac{1}{4T^2}. \tag{6.70}$$

leaving us with the zero mode integration alone:

$$\int D\bar{\psi}\ \exp\Big\{ -\int_0^\infty d\tau\ i\bar{\psi}_\mu F_{\mu\nu}(\bar{x})\bar{\psi}_\nu\Big\} = \int d^4\bar{\psi}\ \exp\Big\{ -iT\bar{\psi}_\mu F_{\mu\nu}(\bar{x})\bar{\psi}_\nu\Big\}$$
$$= -\frac{T^2}{2}\epsilon^{\mu\nu\rho\sigma}F_{\mu\nu}F_{\rho\sigma}. \tag{6.71}$$

[9] As will become clear from our derivation below, Eq.(6.67) carries in fact an $N = 1$ supersymmetry, turning bosonic into fermionic variables and vice-versa. Details are given in appendix C.2.

We therefore obtain

$$\partial_\mu \frac{i\delta W_{\mathbb{I}}}{\delta B_\mu(y)}\Big|_{B=0} = -\frac{1}{16\pi^2}\int_0^\infty dT\mathcal{N}(T)\ \int D\bar{x}\ \delta(\bar{x}-y)\epsilon^{\mu\nu\rho\sigma}F_{\mu\nu}(\bar{x})F_{\rho\sigma}(\bar{x})$$
$$= -\frac{1}{16\pi^2}\left(\int_0^\infty dT\mathcal{N}(T)\right)\ \epsilon^{\mu\nu\rho\sigma}F_{\mu\nu}(y)F_{\rho\sigma}(y)\,. \tag{6.72}$$

The normalization can be set to unity giving us the well known result

$$\partial_\mu\langle j^5_\mu(y)\rangle \equiv \partial_\mu \frac{i\delta W_{\mathbb{I}}}{\delta B_\mu(y)}\Big|_{B=0} = -\frac{1}{16\pi^2}\epsilon^{\mu\nu\rho\sigma}F_{\mu\nu}(y)F_{\rho\sigma}(y). \tag{6.73}$$

This is the central result of this section[10]. It nicely illustrates that the axial anomaly can be understood as arising from the phase of the fermionic determinant. Unlike many derivations in the literature, we employed a a variational technique for the imaginary part of the effective action in an Euclidean formalism. This also confirms that our result for the axial-vector current in Eq.(6.44) is robust. The analytic continuation to Minkowskian metric will be straightforward, albeit the imaginary part of the effective action will have a different interpretation.

In the upcoming section 6.3 we will continue our world-line path integral formulation to real-time and we will make contact with the results of [142–146] containing a Berry connection. Our very general approach allows one to study the origin and role of any geometric phases which arise under certain approximations, such as those corresponding to adiabatic variations in interactions with external fields. We then give an outlook on how a chiral kinetic theory should be constructed, which is equivalent to a saddle point approximation of our world-line path integral. In this context, we argue that Eq.(6.44) in the pseudo-classical limit provides a consistent definition of the axial vector current and can be used in the construction of chiral kinetic extensions of Bödecker's effective theory [287, 288].

For completeness, we note that the corresponding definition of the axial-vector current in the continuum formulation of the world-line path integral is given as

$$\langle j^\mu_5(y)\rangle = \frac{1}{4}\int_0^\infty dT\,\mathcal{N}\int_P \mathcal{D}x\mathcal{D}\psi\,\delta^{(4)}(x(0)-y)\big\{[\dot{x}^\mu+\dot{x}^\nu\psi_\mu\psi_\nu]\psi_5\psi_6\big\}\Big|_{\tau=0}$$
$$\times\exp\left(-\int_0^\infty d\tau\,\mathcal{L}\right), \tag{6.74}$$

where with $B=0$ the Lagrangian $\mathcal{L}=\mathcal{L}_L=\mathcal{L}_R$ is given in Eq.(6.23).

[10] We note that commonly in the literature a distinction is being made between covariant and consistent anomalies [285, 286]. In our situation both definitions agree, as is argued in appendix C.4. However this distinction is of crucial importance, when deriving non-singlet anomalies or anomalies with both physical vector- and axial-vector-background fields present.

6.3 Chiral Kinetic Theory

6.3.1 Pseudo-classical description of spinning particles

The world-line framework provides a consistent Lorentz covariant description of quantum field theory using the language of first quantization. It is therefore well suited for a pseudo-classical kinetic description of quantum many-body systems. We will begin our discussion here with the world-line Lagrangian Eq.(6.22) continued to Minkowskian metric ($g = \mathrm{diag}[-,+,+,+]$). Henceforth we will consider the coupling of fermions to vector gauge fields and set the auxilliary field $B = 0$. We have

$$\mathcal{L} = \frac{\dot{x}^2}{2\mathcal{E}} + \frac{i}{2}\psi^\mu\dot{\psi}_\mu + \frac{i}{2}\psi_5\dot{\psi}_5 + \frac{i}{2}\psi_6\dot{\psi}_6 + \dot{x}_\mu A^\mu(x) - \frac{i\mathcal{E}}{2}\psi^\mu F_{\mu\nu}\psi^\nu, \tag{6.75}$$

and the corresponding world-line effective action, obtained by the continuation of $W_\mathbb{R}$ from Eq.(6.24), is given by

$$W = \int_0^\infty \frac{dT}{T} \int_P \mathcal{D}x \int_{AP} \mathcal{D}\psi \, \exp\Big\{ i \int_0^T d\tau \, \mathcal{L} \Big\}. \tag{6.76}$$

The discussion in section 6.2.3 translates into the Minkowskian formulation directly. The emergence of the anomaly is understood in the Minkowskian formulation as arising from the fact that the path integral measure over the Grassmanian variables in Eq.(6.76) does not contain zero modes.

The path integral is acompanied by an integration over a world-line of length T, which is directly related to the reparametrization invariance of the world-line parameter $\tau \to \tau' = f(\tau)$. In fact, Eq.(6.76) closely resembles Schwinger's proper time method, albeit in this case the world-line manifold is now an interval in proper time rather than a closed loop. Consequently the world-line lenght T and the einbein $\mathcal{E}$, which is the square root of the determinant of the world-line metric, can also be understood to emerge from a BRST construction (see [284]). While reparametrization invariance is a gauge symmetry (a redundancy in our description), it is not related to any symmetry group in the usual sense.

For particles with spin, yet another physicality condition arises, which is not immediately obvious from Eq.(6.76): longitudinal spin components should not be dynamical. This restricts the integral measure $\mathcal{D}\psi$ to a specific physical hypersurface. In practice, this helicity constraint can be implemented by means of introducing a Lagrange multiplier χ in the Lagrangian,

$$\mathcal{L} \to \mathcal{L} - i\frac{\dot{x}_\mu\psi^\mu}{2\mathcal{E}}\chi\,. \tag{6.77}$$

To illustrate its role, we will proceed to the Hamiltonian formulation by defining the conjugate momenta (from Eq.(6.75))

$$p^\mu \equiv \frac{\partial\mathcal{L}}{\partial\dot{x}_\mu} = \pi^\mu + A^\mu\,, \qquad \text{with} \qquad \pi^\mu \equiv \frac{\dot{x}^\mu}{\mathcal{E}} - i\frac{\psi^\mu}{2\mathcal{E}}\chi\,. \tag{6.78}$$

The corresponding world line action, equivalent to Eq.(6.75), can be written as

$$S = \int_0^T d\tau \, \{p_\mu \dot{x}^\mu + \frac{i}{2}[\psi_\mu \dot{\psi}^\mu + \psi_5 \dot{\psi}_5 + \psi_6 \dot{\psi}_6] - \frac{\mathcal{E}}{2}\pi^2 + \frac{i}{2}(\pi_\mu \psi^\mu)\chi - \frac{i\mathcal{E}}{2}\psi^\mu F_{\mu\nu}\psi^\nu\}. \tag{6.79}$$

The role of $\mathcal{E}$ as a Lagrange multiplier is transparent in the above expression. The constraints that are encoded in Eq.(6.79) can be easily understood from their quantized counterparts. Promoting the Grassmanian variables to operators in a Hilbert space,

$$\psi_\mu \to \sqrt{\frac{\hbar}{2}}\gamma_5\gamma_\mu, \qquad \psi_5 \to \sqrt{\frac{\hbar}{2}}\gamma_5\,, \tag{6.80}$$

the mass shell condition and the helicity constraint in Eq.(6.79) correspond to the Klein-Gordon and Dirac operator equations respectively, defining the physical subspace $|\Phi\rangle$ of the theory,

$$\begin{aligned} \pi^2 + i\psi^\mu F_{\mu\nu}\psi^\nu = 0 \qquad &\Leftrightarrow \quad \left(\hat{\pi}^2 + i\sigma^{\mu\nu}F_{\mu\nu}\right)|\Phi\rangle = 0 \qquad \text{(mass-shell constraint)}, \\ \pi_\mu \psi^\mu = 0 \qquad &\Leftrightarrow \qquad \gamma_5\gamma_\mu\hat{\pi}^\mu|\Phi\rangle = 0 \qquad \text{(helicity constraint)}. \end{aligned} \tag{6.81}$$

The generalization of Eq.(6.81) to the massive case is straightforward, as one simply replaces

$$\pi^2 + i\psi^\mu F_{\mu\nu}\psi^\nu + m^2 = 0 \qquad \Leftrightarrow \qquad (\hat{\pi}^2 + i\sigma^{\mu\nu}F_{\mu\nu} + m^2)|\Phi\rangle = 0\,, \tag{6.82}$$

$$\pi_\mu \psi^\mu + m\psi_5 = 0 \qquad \Leftrightarrow \qquad \gamma_5(\gamma_\mu\hat{\pi}^\mu + m)|\Phi\rangle = 0\,, \tag{6.83}$$

as these then reproduce the *massive* Klein-Gordon and Dirac equations.

Eq.(6.82) and Eq.(6.83) are not independent. On the operator level, Eq.(6.82) is the (operator-) squared of Eq.(6.83), whereas, on the level of the world-line phase space variables $p_\mu, x_\mu, \psi_\mu, \psi_5$, the constraints are part of an $N = 1$ SUSY algebra, with the supercharge given by Eq.(6.83). This is discussed further in appendix C.2. In the latter case, both constraints are related by the algebra of Poisson brackets. The action for a spinning massive particle, including both mass-shell and helicity constraints, is then given by

$$\begin{aligned} S &= \int_0^T d\tau \, \Big\{p_\mu \dot{x}^\mu + \frac{i}{2}\left[\psi_\mu \dot{\psi}^\mu + \psi_5 \dot{\psi}_5 + \psi_6 \dot{\psi}_6\right] - \frac{\mathcal{E}}{2}(\pi^2 + m^2) \\ &\qquad\qquad - \frac{i}{2}\left(\pi_\mu \psi^\mu + m\psi_5\right)\chi - \frac{i\mathcal{E}}{2}\psi^\mu F_{\mu\nu}\psi^\nu\Big\} \\ &\equiv \int_0^T d\tau \, \Big\{p_\mu \dot{x}^\mu + \frac{i}{2}\left[\psi_\mu \dot{\psi}^\mu + \psi_5 \dot{\psi}_5 + \psi_6 \dot{\psi}_6\right] - H\Big\}, \end{aligned} \tag{6.84}$$

where the Hamiltonian, being merely a sum of constraints, is

$$H = \frac{\mathcal{E}}{2}(\pi^2 + m^2 + i\psi^\mu F_{\mu\nu}\psi^\nu) + \frac{i}{2}\left(\pi_\mu\psi^\mu + m\psi_5\right)\chi\,. \tag{6.85}$$

Since H does not depend on ψ_6, the dynamics of the latter is trivial, $\psi_6 = const$ and we will drop it from our discussion henceforth. Eq.(6.84) serves as our starting point for the determination of the Hamiltonian dynamics of the world-line theory and ultimately leads to the equations of motion in the pseudo-classical (kinetic) limit of the theory.

The classical limit is not immediately apparent in Eq.(6.76) as the T integration obscures its usual interpretation as the saddle point of a path integral with the variables x, ψ. However, as described above, the T-integration is related to the gauge freedom of the einbein parameter $\mathcal{E}$. We will illustrate how this can be dealt with in practice and refer the reader to appendix C.5 for further detailed discussion.

One approach is to perform the T integral in Eq.(6.76) explictly. In this case, the world-line path integral can be shown to be independent of the value of the einbein parameter $\mathcal{E}$ and the latter can thus can be fixed to any value. The result of the T-integration is a modified single particle action, different from Eq.(6.75). The resulting pseudo-classical dynamics can be derived from this modified action, which now permits [284] only physical degrees of freedom (those satisfying constraint relations) to evolve via the equations of motion. An alternative approach is as follows: instead of performing the T-integral, Eq.(6.75) might be taken as defining the the single-particle action directly, albeit explicitly keeping the T integral in Eq.(6.76). In this case, $\mathcal{E}$ cannot be fixed and must be treated as a variational parameter.

We will here illustrate both approaches, starting with the first. Fixing $\mathcal{E} = 2$ and defining the dimensionless proper time as $u \equiv \tau/T$, Eq.(6.76) can be written as

$$W = \int_0^\infty \frac{dT'}{T'} e^{-iT'} \int \mathcal{D}x\mathcal{D}\psi\, \exp\Big\{\frac{i\bar{m}^2}{T'}\int_0^1 du\,\frac{\dot{x}^2}{4} + i\int_0^1 du\,\big[\frac{i}{2}\left(\psi_\mu\dot{\psi}^\mu + \psi_5\dot{\psi}_5\right) + \dot{x}_\mu A^\mu - \frac{i}{2}\left(\frac{\dot{x}_\mu\psi^\mu}{2} + m\psi_5\right)\chi\big]\Big\}, \tag{6.86}$$

where we further defined $\bar{m}^2 \equiv m^2 + i\int_0^1 du\,\psi^\mu F_{\mu\nu}\psi^\nu$. Provided the kinetic term is large compared to the interactions, the T' integral can be performed by the stationary phase method around the stationary point $T_0' = \bar{m}\sqrt{-\int_0^1 du\,\dot{x}^2}$. The result is

$$W = \int \mathcal{D}x\mathcal{D}\psi\,\tilde{\mathcal{N}}\,\exp iS \tag{6.87}$$

where $\tilde{\mathcal{N}} \equiv \sqrt{i\pi/2\bar{m}}\left(-\int_0^1 du\,\dot{x}^2\right)^{\frac{1}{4}}$, and the corresponding world-line action is

$$S = -\bar{m}\sqrt{-\int_0^1 du\,\dot{x}^2} + i\int_0^1 du\,\Big(\frac{i}{2}\big[\psi_\mu\dot{\psi}^\mu + \psi_5\dot{\psi}_5 + \psi_6\dot{\psi}_6\big] + \dot{x}_\mu A^\mu - \frac{i}{2}\big[\frac{\dot{x}_\mu\psi^\mu}{2} + m\psi_5\big]\chi\Big)\,. \tag{6.88}$$

Using the abbreviation $Y \equiv \sqrt{-\int_0^1 du\,\dot{x}^2}$, the equations of motion are obtained by varying this (non-local) action,

$$-\frac{\bar{m}\ddot{x}^\mu}{Y} + \frac{iY}{2\bar{m}}\psi^\alpha\partial^\mu F_{\alpha\beta}\psi^\beta + F^{\mu\nu}\dot{x}_\nu + \frac{i}{4}\dot{\psi}^\mu\chi = 0\,, \tag{6.89}$$

$$\dot{\psi}^\mu - \frac{Y}{\bar{m}}F_{\mu\nu}\psi^\nu - \frac{\dot{x}_\mu}{4}\chi = 0\,, \tag{6.90}$$

$$\dot{\psi}_5 - \frac{m\chi}{2} = 0\,, \tag{6.91}$$

while, as noted previously, the dynamics of ψ_6 is trivial. These equations of motion, for appropriate choice of χ (as we shall shortly discuss), provide the covariant generalization of the well known Bargmann-Michel-Telegdi equations [271] for spinning particles in external gauge fields. The extension of these equations of motion to include colored degrees of freedom, generalizing thereby the Wong equations [272], was already discussed a long time ago in [289].

As we show in appendix C.5, identical dynamics is obtained in the other approach when $\mathcal{E}$ is treated as a variational parameter and thereby eliminated from the action. This approach will be particularly beneficial when we take the non-relativistic limit of the action. In this variational approach, the Euler-Lagrange equations applied to $\mathcal{E}$, using Eq.(6.75), give the consistency relation

$$\mathcal{E} = m_R^{-1}\left(z - i\frac{\dot{x}_\mu\psi^\mu}{2\,z}\chi\right), \tag{6.92}$$

where $z \equiv \sqrt{-\dot{x}^2}$ and

$$m_R^2 = m^2 + i\psi^\mu F_{\mu\nu}\psi^\nu. \tag{6.93}$$

This consistency relation allows us to eliminate $\mathcal{E}$ by inserting the relation into Eq.(6.75). The resulting equation of motions agree with the dynamics in Eqs. (6.89)-(6.91), provided the constraints are fulfilled.

Therefore a saddle point expansion of Eq.(6.76) – under the proviso that all constraints are respected – provides the correct pseudo-classical limit with the corresponding action given as

$$S = \int_0^T d\tau\;\mathcal{L}, \tag{6.94}$$

where the Lagrangian in Eq.(6.75) can now be expressed as

$$\mathcal{L} \equiv -\frac{m_R z}{2}\left(1+\frac{m^2}{m_R^2}\right)+\frac{i}{2}\left(\psi_\mu\dot{\psi}^\mu+\psi_5\dot{\psi}_5\right) - \frac{im_R}{2}\left(\frac{\dot{x}_\mu\psi^\mu}{z}\left[1-\frac{m^2}{2m_R^2}\right]+\frac{m}{m_R}\psi_5\right)\chi+\dot{x}_\mu A^\mu(x)-\frac{i}{2m_R}z\psi^\mu F_{\mu\nu}\psi^\nu. \tag{6.95}$$

This Lagrangian, explictly implementing the mass-shell constraint, will serve as the starting point for the discussion of the non-relativistic limit in section 6.3.2. We can now use Eq.(6.95) to define the conjugate four-momenta of the constrained phase space; these are

$$p^\mu \equiv \frac{\partial\mathcal{L}}{\partial\dot{x}_\mu}\,, \tag{6.96}$$

where

$$\pi^\mu \equiv p^\mu - A^\mu = m_R u^\mu - \frac{im_R}{2z}\left(1-\frac{m^2}{2m_R^2}\right)\left[\psi^\mu+u_\nu\psi^\nu u^\mu\right]\chi, \tag{6.97}$$

with the four-velocity is defined as

$$u^\mu \equiv \frac{\dot{x}^\mu}{z}\,. \tag{6.98}$$

Eq.(6.96) is easily inverted and gives

$$\dot{x}^\mu = \frac{z}{m_R}\pi^\mu+\frac{i}{2}\left(1-\frac{m^2}{2m_R^2}\right)\left[\psi^\mu+\frac{\pi_\nu\psi^\nu\pi^\mu}{m_R^2}\right]\chi \tag{6.99}$$

The equations of motion in this setup, respecting all constraints, are completely equivalent to Eqs. (6.89)-(6.91). This point is illustrated with a specific example in appendix C.5. We note a few additional points: the Lagrange multiplier χ is an anti-commuting Lorentz scalar, which means that the structure of expressions that can be assigned to it are very restricted [273]. A vanishing $\chi = 0$ is trivially consistent with this requirement; it turns out the only further choice[11] is $\chi \propto \epsilon^{\mu\nu\lambda\sigma}\pi^\mu\psi^\nu\psi^\lambda\psi^\sigma$ [273].

Our considerations here are essential ingredients in deriving a consistent relativistic chiral kinetic theory. The explicit derivation of this kinetic framework is fairly involved and will be left to forthcoming work [279]. In the following subsection, we will discuss the role of χ in more detail and we shall fix it explicitly. Our focus in 6.3.2 will however be on the non-relativistic reduction of Eq.(6.95)–with the helicity constraint imposed. We will comment on some interesting features of the corresponding kinetic theory that are complementary to those discussed in our recent letter [245].

[11] Note that χ cannot be linear in ψ, as this cannot be combined to form a Lorentz invariant. Even powers in ψ result in χ being a *commuting* variable, rather than an anti-commuting one.

6.3.2 The non-relativistic limit

In this subsection, we shall derive the non-relativistic limit of the single particle action defined by Eq.(6.95). We will carefully discuss the role of the mass-shell and helicity constraints and their related Lagrange-multipliers. Based on an adiabatic approximation of our result, we make contact with the geometric action put forward by [142, 143]. As in those works, we showed in our accompanying letter [245] how a Berry term arises in the massive non-relativistic and adiabatic limit. However in [245], we only considered a massive system with a small or vanishing chemical potential. We will extend the discussion here to a system with a large chemical potential.

We will begin by writing Eq.(6.95) with all factors of c specified:

$$\begin{aligned}\mathcal{L} = &- \frac{m_R c\, z}{2}\left(1+\frac{m^2}{m_R^2}\right) + \frac{i}{2}\left(\psi_\mu \dot{\psi}^\mu + \psi_5 \dot{\psi}_5\right) \\ &- \frac{i m_R\, c}{2}\left(\frac{\dot{x}_\mu \psi^\mu}{z}\left[1-\frac{m^2}{2m_R^2}\right] + \frac{m}{m_R}\psi_5\right)\chi + \frac{\dot{x}_\mu A^\mu(x)}{c} - \frac{i}{2m_R c} z \psi^\mu F_{\mu\nu}\psi^\nu .\end{aligned} \tag{6.100}$$

The non-relativistic limit can be derived systematically in an expansion of the particle's velocity over the speed of light. The adiabatic limit corresponds to taking the interaction energy of the particle with the external electromagnetic fields to be small relative to its rest energy. To proceed further in deriving these limits from the relativistic Lagrangian, we choose, without loss of generality, $\chi = 0$. It follows thence from Eq.(6.91) that $\dot{\psi}_5 = 0$ and hence $\psi_5 = const.$

We will next use the supersymmetric properties of the world-line action (discussed in appendix C.2)

$$\psi_\mu \to \psi_\mu + \frac{\dot{x}_\mu}{\sqrt{-\dot{x}^2}}\,\eta\,; \qquad \psi_5 \to \psi_5 + \eta\,; \qquad x_\mu \to x_\mu + i\frac{\psi_\mu \eta}{m}\,, \tag{6.101}$$

where η is an anticommuting parameter generating a $N = 1$ supersymmetric transformation. Since $\psi_5 = const$, we can perform a time-independent transformation such that $\psi_5 = 0$. Thereby eliminating ψ_5 from the dynamics entirely, the Lagrangian can be written as

$$\begin{aligned}\mathcal{L} = -\frac{m_R c\, z}{2}\left(1+\frac{m^2}{m_R^2}\right) + \frac{i}{2}\left(\boldsymbol{\psi}\dot{\boldsymbol{\psi}} - \psi_0\dot{\psi}_0\right) + \frac{\dot{x}_\mu A^\mu(x)}{c} \\ - \frac{i}{m_R c} z\, \psi^0 F_{0i}\psi^i - \frac{i}{2m_R c} z\, \psi^i F_{ij}\psi^j\,,\end{aligned} \tag{6.102}$$

This expression does not contain any approximations yet.

To take the non-relativistic limit, we identify the world line proper time τ of a "particle", with the physical time t as

$$\tau = \frac{ct}{\gamma} = ct\sqrt{1-(d\boldsymbol{x}/dt)^2}, \qquad x^0 = ct\,, \tag{6.103}$$

where $\mathbf{v}$ is the non-relativistic velocity, $\mathbf{v} \equiv d\boldsymbol{x}/dt$. From the spatial components of the Grassmanian variables, the conventional spin vector is defined as $S^i \equiv -\frac{i}{2}\epsilon^{ijk}\psi^j\psi^k$. Using $B^i = \frac{1}{2}\epsilon^{ijk}F^{jk}$ and $E^i = F^{0i}$, we can therefore express

$$-i\psi^0 F_{0i}\psi^i = \frac{\boldsymbol{S}\cdot(\boldsymbol{\pi}\times\boldsymbol{E})}{c\pi^0}\,, \tag{6.104}$$

$$-\frac{i}{2}\psi^i F_{ij}\psi^j = \boldsymbol{S}\cdot\boldsymbol{B}\,. \tag{6.105}$$

Furthermore, in the non-relativistic limit, the electromagnetic "Larmor" energy is small compared to the mass- we can therefore approximate[12]

$$m_R = \sqrt{m^2 + i\psi^\mu F_{\mu\nu}\psi^\nu} \approx m\left(1 + \frac{i}{2}\frac{\psi^\mu F_{\mu\nu}\psi^\nu}{m^2c^2}\right) \equiv m(1+X), \tag{6.106}$$

where we introduced the abreviation

$$X \equiv -\frac{\boldsymbol{S}\cdot(\boldsymbol{\pi}\times\boldsymbol{E})/(c\pi^0) + \boldsymbol{S}\cdot\boldsymbol{B}}{2\,m^2\,c^2} \tag{6.107}$$

The Lagrangian, which is defined by

$$S = \int dt\ \mathcal{L}', \tag{6.108}$$

can be written as

$$\begin{aligned}\mathcal{L}' &= -\frac{m_R c^2}{2\gamma}\left(1+\frac{m^2}{m_R^2}\right) + \frac{i}{2}\left(\boldsymbol{\psi}\dot{\boldsymbol{\psi}} - \psi_0\dot{\psi}_0\right) - A^0 + \frac{\boldsymbol{v}}{c}\cdot\boldsymbol{A} \\ &\qquad + \frac{1}{m_R\gamma}\left(\frac{\boldsymbol{S}\cdot(\boldsymbol{\pi}\times\boldsymbol{E})}{c\pi^0} + \boldsymbol{S}\cdot\boldsymbol{B}\right) \\ &= -\frac{mc^2}{2\gamma}\left(1+X+\frac{1}{1+X}\right) + \frac{i}{2}\left(\boldsymbol{\psi}\dot{\boldsymbol{\psi}} - \psi_0\dot{\psi}_0\right) - A^0 + \frac{\boldsymbol{v}}{c}\cdot\boldsymbol{A} - \frac{2\,mc^2}{\gamma}\frac{X}{1+X}.\end{aligned} \tag{6.109}$$

The non-relativistic limit is found when $x \propto (\boldsymbol{v}/c)^2$ is small. Thus we expand the expression in terms of X and $\boldsymbol{v}/c$ and keep only terms at most quadratic in the latter. This gives

$$\mathcal{L}' \approx -mc^2 + \frac{1}{2}m\boldsymbol{v}^2 + \frac{i}{2}\left(\boldsymbol{\psi}\dot{\boldsymbol{\psi}} - \psi_0\dot{\psi}_0\right) + A^0 - \frac{\boldsymbol{v}}{c}\cdot\boldsymbol{A} + \frac{\boldsymbol{S}\cdot(\boldsymbol{\pi}\times\boldsymbol{E})}{mc\,\pi^0} + \frac{\boldsymbol{S}\cdot\boldsymbol{B}}{m}. \tag{6.110}$$

[12]We note that due the Grassman nature of X there is only one further non-zero term in this expansion $\propto X^2$. Due to the nilpotency of the Grassmanian variables this term is antisymmetric in four Lorentz indices and thus reminicent of the discussion in section 6.2.3. We note however that in section 6.2.3, the emergence of the anomaly was tied to the existence of Grassmannian zero modes and thereby resulted in the well known anomaly relation Eq.(6.73). The order X^2 term here corresponds to a field configuration $\propto \mathbf{E}\cdot\mathbf{B}$; however it is not a sign of the presence of the anomaly and not related to the non-conservation of the axial current. See also [276], where such a term is seen in the equations of motion.

Since in this limit

$$\pi^0 \to p^0 - \frac{A^0}{c}\,, \qquad \text{and} \qquad \boldsymbol{\pi} \to \boldsymbol{p} - \frac{\boldsymbol{A}}{c}\,, \tag{6.111}$$

we obtain our final form for the non-relativistic Lagrangian to be

$$\begin{aligned}\mathcal{L}_{NR} = -mc^2 + \frac{1}{2}m\boldsymbol{v}^2 + \frac{i}{2}\left(\boldsymbol{\psi}\dot{\boldsymbol{\psi}} - \psi_0\dot{\psi}_0\right) - A^0 + \frac{\boldsymbol{v}}{c}\cdot\boldsymbol{A} \\ + \frac{\boldsymbol{S}\cdot\left(\left[\boldsymbol{v}/c - \boldsymbol{A}/(mc^2)\right]\times\boldsymbol{E}\right)}{mc} + \frac{\boldsymbol{S}\cdot\boldsymbol{B}}{m}\,.\end{aligned} \tag{6.112}$$

Here ψ_i, $i = 1, 2, 3$ are the dynamical spin degrees of freedom. Since ψ_0 is not dynamical, we shall drop it from now on. To obtain the corresponding non-relativistic Hamiltonian, we proceed just as we had done in the Lorentz covariant case, by introducing a non-relativistic conjugate momentum

$$p^i = \frac{\partial\mathcal{L}_{NR}}{\partial\dot{x}^i} = m\dot{x}^i + \frac{A^i}{c} + \frac{\epsilon^{ijk}E^jS^k}{mc^2}\,. \tag{6.113}$$

We can then compactly express the non-relativistic action as

$$S = \int dt\left(\boldsymbol{p}\cdot\dot{\boldsymbol{x}} + \frac{i}{2}\boldsymbol{\psi}\cdot\dot{\boldsymbol{\psi}} - H\right)\,, \tag{6.114}$$

where the non-relativistic Hamiltonian (in SI units) is

$$H \equiv mc^2 + \frac{\left(\boldsymbol{p} - \frac{\boldsymbol{A}}{c}\right)^2}{2m} + A^0(x) - \frac{\boldsymbol{S}\cdot\left(\left[\boldsymbol{v}/c - \boldsymbol{A}/(mc^2)\right]\times\boldsymbol{E}\right)}{2mc} - \frac{\boldsymbol{B}\cdot\boldsymbol{S}}{m}\,. \tag{6.115}$$

This expression is of course the well known expression for the Hamiltonian for a fermion in an external electromagnetic field [290]: the penultimate term is the spin-orbit interaction energy from Thomas precession, while the last term is the Larmor interaction energy.

In the accompanying letter [245], we showed in some detail that in an *adiabatic approximation* the system described by Eq.(6.114) and Eq.(6.115) contains a Berry phase with monopole form, also postulated in [142–145].

6.3.3 The emergence of Berry's phase

In the following, we will show how the system described by Eq.(6.115) contains, in an adiabatic approximation, a Berry phase; in this limit, it has the monopole form postulated in [142–145]. To recover the expressions in [142, 143] we re-quantize the spin, by promoting the spin (phase-space) variables ψ to the Hilbert space operators $\psi_i \to \sqrt{\frac{\hbar}{2}}\sigma_i \equiv \hat{\psi}_i$ and $S_i \to \frac{\hbar}{2}\sigma_i \equiv \hat{S}_k$, where σ are the Pauli matrices and hats indicate operators. Further, to describe the finite phase space of Grasmannian variables ψ, we define the two dimensional Hilbert space for a

spin-1/2 particle at every point in phase space $(\boldsymbol{p}, \boldsymbol{x})$ by the eigenstates $|\psi^{\pm}\rangle = |\psi^{\pm}(\boldsymbol{p})\rangle$. Defining $\boldsymbol{n} = \frac{\boldsymbol{p}}{|\boldsymbol{p}|} \equiv (\sin\theta\cos\phi, \sin\theta\sin\phi, \cos\theta)$, one has two choices

$$|\psi_+^{(1)}(\boldsymbol{p})\rangle = \frac{N}{2}\left(1 + \boldsymbol{n}\cdot\boldsymbol{\sigma}\right)\begin{pmatrix}1\\0\end{pmatrix} = \begin{pmatrix}\cos\frac{\theta}{2}\\ e^{i\phi}\sin\frac{\theta}{2}\end{pmatrix} \tag{6.116}$$

$$|\psi_+^{(2)}(\boldsymbol{p})\rangle = \frac{N}{2}\left(1 + \boldsymbol{n}\cdot\boldsymbol{\sigma}\right)\begin{pmatrix}0\\1\end{pmatrix} = \begin{pmatrix}e^{-i\phi}\cos\frac{\theta}{2}\\ \sin\frac{\theta}{2}\end{pmatrix}, \tag{6.117}$$

for the "spin up" + basis vectors (where N is a normalization factor) and similarly for the "spin down" basis vectors (see also [249]). The two choices of basis vectors are not defined globally for all $\boldsymbol{p}$ with Eq.(6.116) (Eq.(6.117)) ill defined for the south (north) pole for $\theta = \pi$ (0). One set can however be used for the northern hemisphere and the other for the southern one, and are related as $|\psi_+^{(1)}(\boldsymbol{p})\rangle = e^{i\phi}|\psi_+^{(2)}(\boldsymbol{p})\rangle$ [249].

These basis states allow us to derive a path integral formulation in the adiabatic limit of the theory defined by Eq.(6.115). The transition amplitude for the Hamiltonian operator corresponding to Eq.(6.115) from an initial state $|\psi^+(\mathbf{p}_i)\rangle$ at time t_i to the state with momentum $\mathbf{p}_f$ at finite time t_f is

$$T(\mathbf{p}_f, \mathbf{p}_i, +) \equiv \langle \mathbf{p}_f, \psi^+(\mathbf{p}_f)|e^{-i\hat{H}(t_f - t_i)}|\mathbf{p}_i, \psi^+(\mathbf{p}_i)\rangle\,. \tag{6.118}$$

The construction of the path integral for this amplitude requires insertions of complete sets of intermediate states satisfying

$$\mathbb{I} = \int d^3x_k\ |\mathbf{x}_k\rangle\langle\mathbf{x}_k| = \int d^3p_k\ |\mathbf{p}_k\rangle\langle\mathbf{p}_k|, \tag{6.119}$$

as well as one for the two dimensional spin-Hilbert space: $\mathbb{I}_2 = |\psi^+\rangle\langle\psi^+| + |\psi^-\rangle\langle\psi^-|$. The adiabatic approximation corresponds to $\frac{\boldsymbol{B}\cdot\boldsymbol{S}}{2m} \approx 0$. Therefore in this limit we can neglect the second term $|\psi^-\rangle\langle\psi^-|$, thereby constraining the dynamical spin degrees of freedom.

The transition matrix element can thus be written as

$$\begin{aligned} T(\mathbf{p}_f, \mathbf{p}_i, +) = &\int \left(\prod_{k=1}^{N-1} d^3p_k\right)\left(\prod_{l=1}^{N} d^3x_l\right) \\ &\times \prod_{j=1}^{N} \frac{1}{(2\pi)^3} e^{-i\mathbf{x}_j\cdot(\mathbf{p}_j - \mathbf{p}_{j-1}) - iH_j\Delta}\langle\psi^+(\mathbf{p}_j)|\psi^+(\mathbf{p}_{j-1})\rangle\,, \end{aligned} \tag{6.120}$$

where $\Delta \equiv (t_f - t_i)/N$ and H_j is Eq.(6.115) evaluated at $(\boldsymbol{x}_j, \boldsymbol{p}_j)$. Taylor expanding $|\psi^+(\mathbf{p}_{j-1})\rangle = \{1 + [\mathbf{p}_j - \mathbf{p}_{j-1}]\cdot\boldsymbol{\nabla}_{\boldsymbol{p}}\}\,|\psi^+(\mathbf{p}_j)\rangle + \cdots$, it is straightforward to show in the continuum limit that one obtains Berry's phase,

$$\prod_{j=1}^{N}\langle\psi^+(\boldsymbol{p}_j)|\psi^+(\boldsymbol{p}_{j-1})\rangle \to \exp\left(i\int dt\ \dot{\mathbf{p}}\cdot\boldsymbol{\mathcal{A}}(\boldsymbol{p})\right). \tag{6.121}$$

where $\boldsymbol{\mathcal{A}}(\boldsymbol{p}) \equiv -i\langle\psi^+(\boldsymbol{p})|\boldsymbol{\nabla}_p|\psi^+(\boldsymbol{p})\rangle$ is the Berry connection. The final expression for the path integral is

$$T(\mathbf{p}_f, \mathbf{p}_i, +) = \int \mathcal{D}x\mathcal{D}p \, \exp\left(i\int dt \left[\dot{\mathbf{x}}\cdot\mathbf{p} - \tilde{H}\right]\right), \tag{6.122}$$

with $\tilde{H} = mc^2 + \frac{(\boldsymbol{p}-\boldsymbol{A}/c)^2}{2m} + A^0(x) - \dot{\mathbf{p}}\cdot\boldsymbol{\mathcal{A}}(\boldsymbol{p})$.

Eq.(6.122) is closely related to a similar formulation in [142–145].

6.3.4 Chemical Potential

The limit that we derived in Eq.(6.115) is different from the one in [142, 143], as the latter contains an effective description for (massless) particles near the Fermi surface, which is well defined for large μ. We will here explore how this limit appears in the world-line framework. As suggested by Eq.(6.81), a chemical potential can be introduced by adding a term to the Dirac operator equation

$$\gamma_5\gamma^\nu\pi_\nu|\Phi\rangle = 0 \qquad \rightarrow \qquad \gamma_5(\gamma^\nu\pi_\nu + \mu\gamma^0)|\Phi\rangle = 0, \tag{6.123}$$

The corresponding world-line expression is

$$\pi_\nu\psi^\nu = 0 \qquad \rightarrow \qquad \pi_\nu\psi^\nu + \mu\psi^0 = 0. \tag{6.124}$$

The mass-shell constraint is modified by the introduction of a chemical potential to read:

$$\pi^2 + i\psi^\alpha F_{\alpha\beta}\psi^\beta + \mu^2 = 0. \tag{6.125}$$

The world-line Lagrangian for massless fermions in the presence of a chemical potential is then[13]

$$\mathcal{L}(\mu) = \frac{\dot{x}^2}{2\mathcal{E}} - \frac{\mathcal{E}}{2}\mu^2 + \frac{i}{2}\psi_\alpha\dot{\psi}^\alpha + \dot{x}_\alpha A^\alpha - \frac{i\mathcal{E}}{2}\psi^\alpha F_{\alpha\beta}\psi^\beta - \frac{i}{2}\left(\frac{\dot{x}_\alpha\psi^\alpha}{\mathcal{E}} + \mu\psi^0\right)\chi\,, \tag{6.126}$$

which we emphasize is a relativistic expression. The path integral we have to evaluate is

$$W(\mu) = \int\frac{dT}{T}\int\mathcal{D}x\int\mathcal{D}\psi\,\exp\big\{i\int_0^T d\tau\,\mathcal{L}(\mu)\big\}. \tag{6.127}$$

As previously for Eq.(6.92), a consistency relation can be derived here as well. In this case, we will proceed by performing the T integration in Eq.(6.127)

[13] For simplicity, we have omitted the kinetic terms for ψ_5 and ψ_6.

directly. The integral in Eq.(6.127) can be performed by the stationary phase method. Fixing $\mathcal{E} = 2$, we obtain

$$\mathcal{L}(\mu) = \int_0^1 du \Big\{ \frac{\dot{x}^2}{4T} - \mu^2\big(1 + \frac{i}{\mu^2}\psi^\alpha F_{\alpha\beta}\psi^\beta\big)T + \dot{x}_\alpha A^\alpha + \frac{i}{2}\psi_\alpha\dot{\psi}^\alpha - \frac{i}{2}\left(\frac{\dot{x}_\alpha\psi^\alpha}{2} + \mu\psi^0\right)\chi\Big\}. \tag{6.128}$$

We further rescale $T \to \int_0^1 du\, \mu^2(1 + \frac{i}{\mu^2}\psi^\mu F_{\mu\nu}\psi^\nu)T \equiv m_{\rm eff}^2 T$ to obtain

$$W(\mu) = \int \frac{dT}{T} e^{-iT} \int \mathcal{D}x \int \mathcal{D}\psi\, \exp\Big\{ i\frac{m_{\rm eff}^2}{T}\int_0^1 du\, \frac{\dot{x}^2}{4} + i\int_0^1 du\, \big\{\dot{x}_\mu A^\mu + \frac{i}{2}\psi_\mu\dot{\psi}^\mu - \frac{i}{2}\big(\frac{\dot{x}_\alpha\psi^\alpha}{2} + \mu\psi^0\big)\chi\big\}\Big\}. \tag{6.129}$$

For large chemical potential the intergral is dominated by the first term in the exponent. Therefore, using the stationary phase method, the T integral can be performed around the stationary point $T_0 = m_{\rm eff}\sqrt{-\int_0^1 du\, \frac{\dot{x}^2}{4}}$. The result is

$$W(\mu) \approx \int \mathcal{D}x \int \mathcal{D}\psi\, \sqrt{\frac{i\pi}{2m_{\rm eff}}}\big(-\int_0^1 du\, \dot{x}^2\big)^{-\frac{1}{4}} \exp\Big\{ - im_{\rm eff}\sqrt{-\int_0^1 du\, \dot{x}^2} + i\int_0^1 du\, \Big(\dot{x}_\alpha A^\alpha + \frac{i}{2}\psi_\alpha\dot{\psi}^\alpha - \frac{i}{2}\left[\frac{\dot{x}_\alpha\psi^\alpha}{2} + \mu\psi^0\right]\chi\Big)\Big\}. \tag{6.130}$$

For a large chemical potential, we can Taylor expand

$$m_{\rm eff} \approx \mu\left(1 + \frac{i}{2\mu^2}\int_0^1 du\, \psi^\alpha F_{\alpha\beta}\psi^\beta\right), \tag{6.131}$$

so that we finally have–using the abreviation $\bar{\mathcal{N}} \equiv \sqrt{\frac{i\pi}{2m_{\rm eff}}}\left(-\int_0^1 du\, \dot{x}^2\right)^{-\frac{1}{4}}$,

$$W(\mu) \approx \int \mathcal{D}x \int \mathcal{D}\psi\, \bar{\mathcal{N}}\, \exp\Big\{ - i\mu\sqrt{-\int_0^1 du\, \dot{x}^2} + i\int_0^1 du\, \left(\frac{-i}{2\mu}\psi^\alpha F_{\alpha\beta}\psi^\beta + \dot{x}_\alpha A^\alpha + \frac{i}{2}\psi_\alpha\dot{\psi}^\alpha\right)\Big\}. \tag{6.132}$$

This effective action describes excitations near the fermion surface for a massless theory with a large chemical potential. In obtaining this form for the action, in

analogy with the previous section, we chose $\chi = 0$. Eq.(6.132) can be directly compared with the result in section 6.3.2: as might have been anticipated, the role of the mass parameter is effectively taken over by the chemical potential. The non-relativistic limit is thus identical upon this identification, as is the adiabatic limit in [245]. It was shown there how a Berry monopole is found when level crossings between spin states are suppressed.

A closer look at the individual terms in the action of $W(\mu)$ illustrates these points nicely. While the first square root term is the conventional kinetic term for a particle with effective mass μ, the second term is a Larmor-interaction energy, with the effective mass μ. For large chemical potentials, excitations around the Fermi surface behave non-relativistically. Further, the adiabatic limit corresponds to $\psi^\alpha F_{\alpha\beta}\psi^\beta/\mu \approx 0$. The effective description of [142, 143] is thus straightforwardly understood by taking the appropriate limits in the world-line framework.

The aforementioned non-relativistic and the adiabatic approximation may not be applicable to ultra-relativistic heavy-ion collisions. Instead, the general Lorentz-covariant world-line framework, which we have established in Eqs. (6.89-6.91) is ideally suited for the description of the anomalous transport of axial charges in the hot fireball created in a heavy-ion collision.

6.4 Conclusions

In this chapter we developed a world line framework in quantum field theory to construct a Lorentz-covariant chiral kinetic theory for fermions. In the first part of the paper, we obtained a world-line path integral representation of the (Euclidean) fermion determinant in the background of vector and axial-vector gauge fields. This was achieved by using a heat-kernel representation of the (infinite-dimensional) operator logarithm. We exploited a fermionic coherent state formalism whereby spin is not treated as part of a wave function but rather as an independent degree of freedom in the path integral. This powerful construction can be extended to include other internal degrees of freedom such as color.

We then investigated how the axial anomaly arises in world line quantization. As is well known [269], the axial anomaly is related to the phase of the fermion determinant, which is ill-defined for fermions in a complex representation. The fermion effective action is thus understood to contain both a real as well as an imaginary part, the latter being related to the violation of chiral symmetry. Using a path integral construction due to D'Hoker and Gagné [280, 281], we obtained a representation of the real part of the effective action in terms of a Grassmanian path integral over spinning variables. Remarkably, there is a very similar path integral representation for the imaginary part, wherein an integral over a regulating parameter represents the loss of chiral symmetry. This path integral representation includes an operator insertion, which in this framework is responsible for the fermion zero modes in the spectrum of the theory. Following the discussion by Alvarez-Gaume and Witten [269], we demonstrated in our

framework how these modes are responsible for the axial anomaly. In particular, we employed a variational method to obtain a non-perturbative expression for the axial-vector current in first-quantization and thence derived the anomaly equation. The emergence of the axial anomaly in first quantization crucially depends on a hidden supersymmetry between bosonic and fermionic degrees of freedom induced by periodic boundary conditions for the fermion variables on the closed world-line.

Motivated by our findings in section 6.3, we derived the pseudo-classical kinetic limit of the world-line effective action. Continuing our prior discussion from Euclidean to Minkowski metric, we established that the Liouville dynamics of spinning particles arises from the real part (in the original Euclidean formulation) of the fermion determinant alone. This contribution to the kinetic dynamics is independent of those arising from the piece in the path integral containing the fermionic zero modes that are responsible for the anomaly. However in a chiral kinetic theory, anomalous contributions to the dynamics, in a covariant formulation, will be manifest through the axial vector current.

A part of the impetus of our work was to understand the origins of the Berry term in kinetic descriptions from first principles in quantum field theory and to establish thereby its relation, if any, to the chiral anomaly. In our accompanying letter [245], we showed how such a term arises from the world-line action for massive spinning particles in external background gauge fields. We demonstrated explicitly that we needed to take the non-relativistic limit of large masses, as well as an adiabatic limit wherein the Larmor interaction energy of the spinning particles was much smaller than the rest energy. In this paper, we addressed the problem in the case where the spinning particles are massless but the system possesses a large chemical potential. This is the case for quasi-particle excitations near the Fermi surface in a number of condensed matter systems. We showed explicitly in the world-line framework that the chemical potential replaces the role of the mass and the rest energy in a manner that is exactly the same as was the case for massive spinning particles. An anaologous non-relativistic and adiabatic limit for these excitations can therefore be taken, and it can be similarly be demonstrated how the Berry term arises upon taking these limits.

This exercise also suggests that away from the adiabatic non-relativistic limit, the Berry phase is not robust and its effects are implicit in the relativistic dynamics of spinning particles. As such, we have arrived at the same conclusion as the previous observation by Fujikawa and collaborators [252–254]. In contrast to the Berry phase, the effects of the anomaly are robust and manifest in a relativistic kinetic description. More generally, the semi-classical world-line construction we obtained here can be incorporated in a real-time Schwinger-Keldysh framework to describe the evolution of a chiral current in a gauge field background. A similar such construction was performed in [261] for spinless colored particles. It was shown in that case how one recovers in the world-line framework the non-Abelian Boltzmann Langevin "Bödeker kinetic theory" [287, 288, 291] of hot QCD. This framework can be extended to construct an "anomalous Bödeker theory" which can then be matched to classical-statistical simulations at early

times in heavy-ion collisions and to anomalous hydrodynamics at late times. This work is in progress [279]. We note that there has been a recent discussion of the anomalous Bödeker kinetic theory in the literature [228, 278] in a different approach and it will be useful in future to compare and contrast results in the two approaches.

The framework presented here is not only applicable in the QCD framework of heavy-ion collisions but is potentially applicable to a number of many-body contexts where topology is important and the dynamics is relativistic. One such example is that of the transport of chiral fermions in an astrophysical situations [77, 78, 78–80]. In this context, our framework provides a first principles perspective that can be used to address situations where masses and chemical potentials are not large and non-relativistic and adiabatic assumptions are no longer valid. Another intriguing possibility is to apply this framework to helicity evolution in QCD at small x [292]. In QCD at small x, semi-classical concepts provide fertile ground[33, 34]; a semi-classical world-line description was previously employed [293] to derive the well known BFKL equation for unpolarized parton distributions [97, 294]. The world-line construction developed here for spinning particles therefore shows great promise for a wide of many-body problems and will be pursued in future work.

Chapter 7

Magnetic catalysis and inverse magnetic catalysis in QCD

This section is based on the publication "Magnetic catalysis and inverse magnetic catalysis in QCD" (N.M. J. Pawlowski), published in Phys.Rev. D91 (2015) no.11, 116010 (arXiv:1502.08011) [295] and represents a somewhat different aspect of matter under extreme conditions as was presented in the previous chapters. In this section we will focus on the *strongly-coupled* regime of QCD and moreover we will describe an equilibrium situation here. As such the work that we will present here aims at extending our knowledge of the QCD phase diagram and thus the later stages in a heavy ion collision, which are described by hydrodynamics. Apart from this experimental application, the study presented here can be understood as an important attempt of extending our knowledge of Quantum-Chromodynamics at finite temperature, chemical potential and magnetic fields. The motivation for this study was a fundamental tension between lattice and model studies in the understanding of the QCD phase diagram in the $T - B$ plane, as we shall outline below.

We investigate the effects of strong magnetic fields on the QCD phase structure at vanishing density by solving the gluon and quark gap equations, and by studying the dynamics of the quark scattering with the four-fermi coupling. The chiral crossover temperature as well as the chiral condensate are computed. For asymptotically large magnetic fields we find magnetic catalysis, while we find inverse magnetic catalysis for intermediate magnetic fields. Moreover, for large magnetic fields the chiral phase transition for massless quarks turns into a crossover.

The underlying mechanisms are then investigated analytically within a few simplifications of the full numerical analysis. We find that a combination of gluon screening effects and the weakening of the strong coupling is responsible for the phenomenon of inverse catalysis. In turn, the magnetic catalysis at large

magnetic field is already indicated by simple arguments based on dimensionality.

7.1 Introduction

In recent years there has been a growing interest in the QCD phase structure in the presence of strong magnetic fields, see e.g. [296–301]. Such fields may play an important role for the physics of the early universe, in compact stars, and in non-central heavy ion collisions [300, 302, 303].

Despite the rich phenomenology, theoretical predictions are challenging. Starting from QED, e.g. [304–307] the influence of magnetic fields onto QCD was investigated in both model calculations, e.g. [308–322], such as quark-meson, Nambu-Jona-Lasinio models and AdS/QCD, e.g. [323–329], with functional renormalisation group methods, e.g. [330–336], Dyson-Schwinger equations, e.g. [299, 337–339] and in lattice calculations, e.g. [205, 340–345].

The importance of magnetic fields for chiral symmetry breaking has been pointed out in [304]. It has been argued that chiral symmetry breaking is enhanced due to an effective dimensional reduction, the *magnetic catalysis*. This effect has been linked to an increase of the chiral condensate as well as that of the critical temperature T_c in model studies. Recent lattice results, [205, 340, 341, 345], have shown that while the chiral condensate indeed is increased, the critical temperature is decreasing with an increasing magnetic field, at least for small enough magnetic field strength. This effect has been called *inverse magnetic catalysis* or *magnetic inhibition*, [346].

Continuum studies have mainly been performed in low energy fermionic models, such as the (Polyakov loop enhanced) quark-meson– or NJL–model. Hence the reason for the discrepancy has to relate to the full dynamics of QCD, and in particular the back-reaction of the matter sector to the gluonic fluctuations. There have been a number of improvements to these model studies to include QCD dynamics [317–321, 347, 348]. Input parameters of low energy effective models, such as the four-fermi coupling, should be determined from the QCD dynamics at larger scales. At these scales they are sensitive to sufficiently large external parameters such as temperature, density, or magnetic fields. This has been emphasized and used in functional renormalisation group (FRG) studies, see [349–352]. The dependence of the four-fermi coupling on temperature and magnetic field effects including gluon screening has been investigated in the recent FRG-work [336] of QCD in strong magnetic fields, where inverse magnetic catalysis at small magnetic fields and a *delayed magnetic catalysis* at large fields was found, see also [329] for an AdS/QCD computation.

In the present work we investigate (inverse) magnetic catalysis by solving the coupled quark and gluon gap equations within the Dyson-Schwinger (DSE) approach to QCD, and within a FRG study of the four-fermi coupling based on QCD flows and low energy effective models. We find magnetic catalysis at large magnetic fields, while inverse magnetic catalysis takes place at small magnetic fields.

The present work is organized as follows: The gap equations for quark and

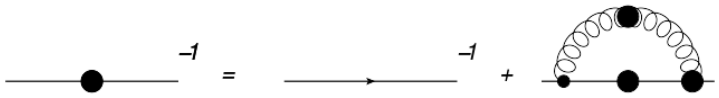

Figure 7.1: Quark Dyson-Schwinger equation. Lines with blobs stand for fully dressed propagators, vertices with large blobs stand for fully dressed vertices. Lines without blobs stand for classical propagators, vertices with small blobs stand for classical vertices. Figure taken from [295]

gluon propagators at finite temperature and magnetic field in two flavor QCD are discussed in Section 7.2. We discuss the dependence of the chiral transition temperature T_c on the magnetic field as well as the magnetic field dependence of the chiral condensate. In Section 7.3 the mechanisms behind the phenomena of magnetic and inverse magnetic catalysis are evaluated within analytically accessible approximations to the gap equations as well as to the dynamics of the four-fermi coupling. In this set-up we are also able to reproduce the lattice results at $eB < 1$ GeV^2. In summary this provides a complete picture of chiral symmetry breaking in the presence of magnetic fields in QCD.

7.2 Chiral symmetry breaking in large magnetic fields

We investigate chiral symmetry breaking in the presence of large magnetic fields within a functional continuum approach. To this end we calculate the chiral condensate for the two lightest quark flavors and obtain the critical temperature T_c at finite magnetic field. This is done by solving the gap equations for the quark and gluon propagator in the presence of a magnetic field using the Ritus method [353–359]. The computations are performed in the Landau gauge.

7.2.1 Quark and gluon gap equations

The gap equation for the quark propagator, see Fig. (7.1), depends on the gluon propagator and the quark-gluon vertex. The former is expanded about the quenched propagator. This expansion has been successfully used at vanishing temperature, e.g. [360, 361], and at finite temperature in e.g. [362–365], the reliability of this expansion has been discussed in [366]. The quark-gluon vertex is estimated with the help of Slavnov-Taylor identities (STIs) from the quark and gluon propagators. The systematic error of the latter estimate gives rise to the dominating systematic error, at vanishing temperature this has been investigated in [367], a related upgrade of the vertex will be used in a subsequent work.

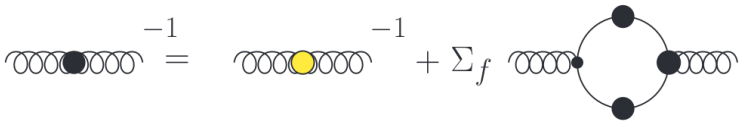

Figure 7.2: Gluon Dyson-Schwinger equation. The gluon line with the yellow dot represents the pure glue loops. Figure taken from [295]

The inverse quark and gluon propagators, $G_q(q)$ and $G_A(q)$ respectively, read in a tensor decomposition at finite eB and T

$$G_q^{-1}(q) = Z_q(q)\left(i\gamma_3 q_3 + i\gamma_0 q_0 Z_0 + i\gamma_\perp q_\perp Z_\perp + M\right) ,$$

$$G_A^{-1\,\mu\nu}(q) = \left(Z_\parallel P_\parallel^{\mu\nu} + Z_\perp P_\perp^{\mu\nu}\right) q^2 + \frac{1}{\xi}\frac{q^\mu q^\nu}{q^2} , \tag{7.1}$$

with $P_\parallel^{\mu\nu} = (g_\parallel^{\mu\nu} - p_\parallel^\mu p_\parallel^\nu / p_\parallel^2)$ and $P_\perp = P - P_\parallel$, where $P_{\mu\nu}$ is the transverse projector. The projection operator $g_\parallel^{\mu\nu}$ has the property $g_\parallel^{\mu\nu} p_\parallel^\mu = p_\parallel^\nu$. The Ritus representation Eq. (7.1) for the quark propagator is equivalent to the Schwinger proper time method, see e.g. [368]. In the following we will denote $Z_A \equiv Z_\parallel$ and concentrate on the Landau gauge, $\xi = 0$. The STIs-induced parametrisation of the quark-gluon vertex is introduced as

$$\Gamma^\mu(q,p) = \gamma^\mu z_{\bar{q}Aq}^{\mathrm{DSE}}(q,p) , \tag{7.2}$$

with $z_{\bar{q}Aq}^{\mathrm{DSE}}(q,p)$ discussed in Appendix D.1. The quark gap equation can be written in a compact notation as

$$G_q^{-1}(p) = G_{q,0}^{-1}(p) + C_f \sum\!\!\!\!\!\!\int_q (g\gamma^\mu) G_q(q) \Gamma^\nu(q,p) G_A^{\mu\nu}(q') , \tag{7.3}$$

with $q' = q - p$ and $G_{q,0}$ as the bare propagator. The integration $\sum\!\!\!\!\!\!\int_q$ stands for an integration over momenta, as well as sums over Matsubara frequencies and Landau levels. The gluon propagator can be expanded about its pure glue part,

$$G_A^{-1\,\mu\nu}(p) = G_{\mathrm{glue}}^{-1\,\mu\nu}(p) + \Pi_f^{\mu\nu}(p) , \tag{7.4}$$

where we have written the fermionic part of the gluon self energy explicitly, while the gluon and ghost loop contributions are contained in G_{glue}. The corresponding DSE for the gluon propagator within this expansion is depicted Fig. (7.2). In the following we consider the back-reaction of the vacuum polarisation on the pure glue part as small, and approximate

$$G_{\mathrm{glue}}^{-1\,\mu\nu}(p) \approx G_{\mathrm{YM}}^{-1\,\mu\nu}(p) . \tag{7.5}$$

At vanishing temperature this has been shown to hold quantitatively for momenta $q \gtrsim 4$ GeV, while for smaller momenta this approximation still holds

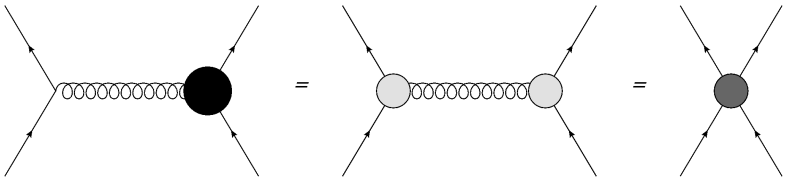

Figure 7.3: Relation of the quark DSE interaction kernel to a 1PI skeleton expansion, which in effect induces an effective momentum dependent four-fermi vertex. Figure taken from [295]

qualitatively with an error of less than 20%, see Fig. 6 in [366]. Note that for momenta $q \gtrsim 4$ GeV the dominant effect of the unquenching is the modification of the scales ($\Lambda_{\rm YM} \to \Lambda_{\rm QCD}$) and the momentum dependence induced by the different β-functions. This is well-captured with the above procedure. In turn, at lower momentum scale the non-perturbative mass-gap related to confinement comes into play. The magnetic field leads to a shift in the momentum dependence such as that of the running coupling, as well as (additional) mass-gaps in propagators. For both asymptotic regimes ($eB \to 0$ and $eB \to \infty$) these effects are well-captured semi-perturbatively and we expect that the approximation (7.5) holds well. For the intermediate regime we rely on the error estimate at zero temperature of about 20% deduced from [366].

The fermionic vacuum polarisation part $\Pi_f^{\mu\nu}(P)$ reads

$$\Pi_f^{\mu\nu}(p) = \frac{1}{2}\mathrm{tr}\sum\!\!\!\!\!\!\int_q (g\gamma^\mu) G_q(q) \Gamma^\nu(q,p) G_q(q')\,, \tag{7.6}$$

where the trace includes a sum over the quark flavors. Details of this expansion can be found in [299]. Here we proceed in the lowest Landau level approximation, where we write down the most general tensor decomposition for gluon and quark propagators. Projecting onto different tensor compositions, we obtain a coupled set of equations for the dressing functions of the different tensor components. In the next section we will comment on the relation of the Dyson-Schwinger equations to other functional expansions and discuss the numerical solutions to these equations.

7.2.2 Skeleton expansion

Before proceeding to the numerical analysis, we discuss the standard approximation schemes for the quark-gluon vertex used in the Dyson-Schwinger framework from a more general point of view. This allows us to connect the present ansätze to the approximations used in gap equations derived within other functional approaches, such as functional renormalisation group (FRG) or nPI-approaches.

DSE studies have made extensively use of the specific input for the quark-gluon vertex and the YM-gluon propagator in (D.2) and (D.4) and similar truncations with great success. Since the quark and gluon self energy diagrams,

depicted in Fig. (7.1) and Fig. (7.2), contain one bare vertex, the correct renormalisation group behavior and momentum dependence of the equations must be discussed carefully. The truncations to the gap equations (7.3) and (7.4) can actually be very well motivated from a skeleton expansion of the 1PI effective action, which would yield similar diagrams as in Fig. (7.1) and Fig. (7.2), but with both vertices dressed. Fig. (7.3) serves to strengthen this motivation as it becomes clear that all approximations should encode the correct behavior of the four-fermi interaction, which is at the heart of chiral symmetry breaking. This allows to consistently reshuffle functional dependencies in the interaction kernels of the above equations.

In turn, the FRG-approach (or nPI effective action) can be used to systematically derive gap equations in terms of full propagators and vertices respectively, see e.g. [171]. Here, we simply note that the 1PI effective action can be written as

$$\Gamma[\phi] = \frac{1}{2}\mathrm{Tr}\ln\Gamma[\phi] + \int_t \partial_t \Gamma_k[\phi] - \text{terms}\,, \tag{7.7}$$

where ϕ encodes all species of fields, the trace in (7.7) sums over momenta, internal indices and all species of fields including relative minus signs for fermions (ψ and $\psi^\dagger$ are counted separately), and a logarithmic RG-scale $t = \ln k$. The RG-scale in (7.7) is an infrared scale. Momenta $p^2 \lesssim k^2$ are suppressed in $\Gamma_k[\phi]$, and $\Gamma[\phi] = \Gamma_{k=0}[\phi]$. The second term on the right hand side of (7.7) is a RG-improvement term which only contains diagrams with two loops and more in full propagators and vertices. To see this we discuss the gap equation derived from (7.7). It follows by taking the second derivative of (7.7) w.r.t. to the fields. The first term of the right hand side gives the diagrams as in Fig. (7.1) and Fig. (7.2) with only full vertices (and additional tadpole diagrams). These diagrams can be iteratively re-inserted into the RG-improvement term, systematically leading to higher loop diagrams in full propagators and vertices. Due to its sole dependence on dressed correlation functions such a diagrammatics naturally encodes the momentum- as well as the RG-running on an equal footing. This also facilitates the consistent renormalisation. Note however that it comes at the price of an infinite series of loops diagrams which can be computed systematically. Here we take the simplest non-trivial approximation which boils down to Fig. (7.1) and Fig. (7.2) with only full vertices. In terms of the original gap equation this leads to the relation

$$z^{\mathrm{DSE}}_{\bar{q}Aq} \approx \left(z^{\mathrm{1PI}}_{\bar{q}Aq}\right)^2, \tag{7.8}$$

where $z^{\mathrm{1PI}}_{\bar{q}Aq}$ is the dressing function of the 1PI-quark gluon vertex. This immediately leads to the standard DSE-dressing in (D.2). Moreover, in our numerical study the vertices are evaluated at their symmetric momentum point.

Note that, while the ansatz for $z^{\mathrm{DSE}}_{\bar{q}gq}$ is indeed consistent when used in the quark and gluon gap equations, it cannot be used in functional equations for higher vertices such as the four-fermi vertex. It is already clear from the discussion above that a consistent evaluation of renormalisation group running and momentum dependence must be considered separately for each vertex equation.

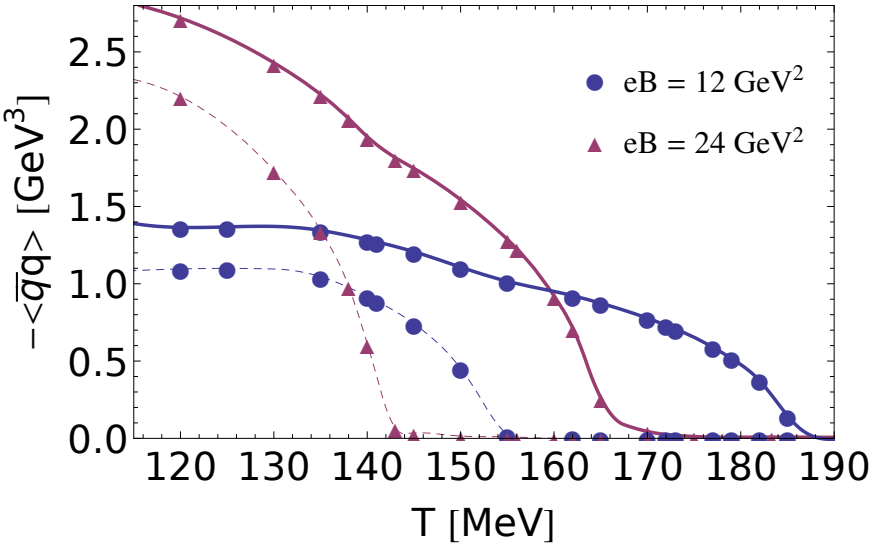

Figure 7.4: Comparison of the chiral condensate (scenario 1) for up (continuous lines) and down quark (dashed lines) at $eB = 12$ GeV^2 and $eB = 24$ GeV^2. Figure taken from [295].

7.2.3 Results

We numerically solve the coupled system of quark and gluon functional equations in the lowest Landau level approximation at finite temperature. This approximation is valid in the presence of a clear scale hierarchy with $eB \gg \Lambda_{\rm QCD}$. We use an ansatz for Γ^μ similar to that used in Dyson-Schwinger studies, e.g. [299, 369], discussed in appendix D.1, but adapted for temperature and magnetic field effects.

While at large momentum the influence of temperature and magnetic fields is very small, at large temperatures and magnetic fields the system is effectively dimensionally reduced and hence the momentum dependencies corresponding to the absent dimensions vanish. This can be accounted for if we replace $Q_\perp^2$ by $2|eB|$ once $Q_\perp^2 < 2|eB|$ and Q_0 by $2\pi T$ for $Q_0 < 2\pi T$ as the relevant scale in the quark gluon vertex, which is consistent with renormalisation group arguments. Within this parametrisation we are still left to decide what exact momentum scale to choose, at which the influence of the external scales T and eB is small already. We investigate this question in detail in section 7.3.1.

The gluon propagator deserves some additional attention. It is decomposed in different polarisation components in the presence of an external magnetic field, see e.g. [299]. Apart from the splitting into longitudinal and transverse components with respect to the heat bath, there is an additional splitting transverse and longitudinal to the magnetic field. In the lowest Landau level approximation only the polarisation subspace projected onto by $P_\parallel^{\mu\nu} = (g_\parallel^{\mu\nu} - p_\parallel^\mu p_\parallel^\nu / p_\parallel^2)$

receives contributions from the quark loop in the self energy, see [299]. Note that in analogy to temperature effects, also the other gluon components must receive contributions from the interaction with the magnetic field, as gluon and ghost loops mix different polarisation components. This is an important difference between QCD and QED. From dimensionality these contributions are linear in eB at least for asymptotically large magnetic fields, leaving aside implicit B-dependencies via the vertices. Their full computation is beyond the scope of the present work. Here we investigate the following two limiting cases.

1. **Scenario 1** We simply neglect the screening effect of the magnetic field onto those polarisation components that feel magnetic effects only through the Yang-Mills sector in a QED-type approximation. This leads to underestimating the effects leading to inverse magnetic catalysis and hence an upper limit for T_c.

2. **Scenario 2** For the large magnetic fields discussed here, the gluon and ghost loops contributions to the self energy must have a similar dependence on eB as the fermionic part. Since this sector does not directly contain charged particles, the effect of the magnetic field onto the YM-sector is suppressed by powers of the involved couplings. Hence, most likely the B-dependence is much smaller than that from the fermionic sector. As a limiting case we will assume the same magnitude of the self energy for all gluon components, which is given by the fermionic contributions. With that we overestimate the gluon screening effect and obtain a lower limit for T_c.

Both scenarios give consistent limiting cases for the truncation used here.

As an order parameter for chiral symmetry breaking we calculate the chiral condensate as a function of temperature and magnetic field in two flavor QCD in the limit of vanishing bare quark masses $m_u \approx m_d \approx 0$. The Ritus method is not reliable for rather small values of $q_f eB$, with $q_f + 2/3$ and $-1/3$ for up and down quark respectively. We expect the lowest Landau level approximation to be a good estimate once $eB \gtrsim 4$ GeV^2 (see [299]) which is also the regime where the approximation (7.5) works well for vanishing temperature.

The numerical computation is very demanding in the vicinity of the phase transition due to the diverging correlation length. This translates into a numerical error in the critical temperature indicated by the error bars in the plots. Fig. (7.4) and Fig. (7.5) show the up- and down-quark condensate for different values of eB. The inverse magnetic catalysis effect described in [340, 341] is evident. While the chiral condensate still rises with the external field in the low temperature limit, the transition between chiral broken and symmetric phase drops. This signals inverse magnetic catalysis as observed on the lattice, [205, 340]. Furthermore the phase transition, which is second order at zero magnetic field turns into a crossover with growing eB, even for vanishing bare quark masses. This can be understood as magnetic screening: the magnetic field effectively serves as an infrared cutoff, which inhibits an infinite correlation length.

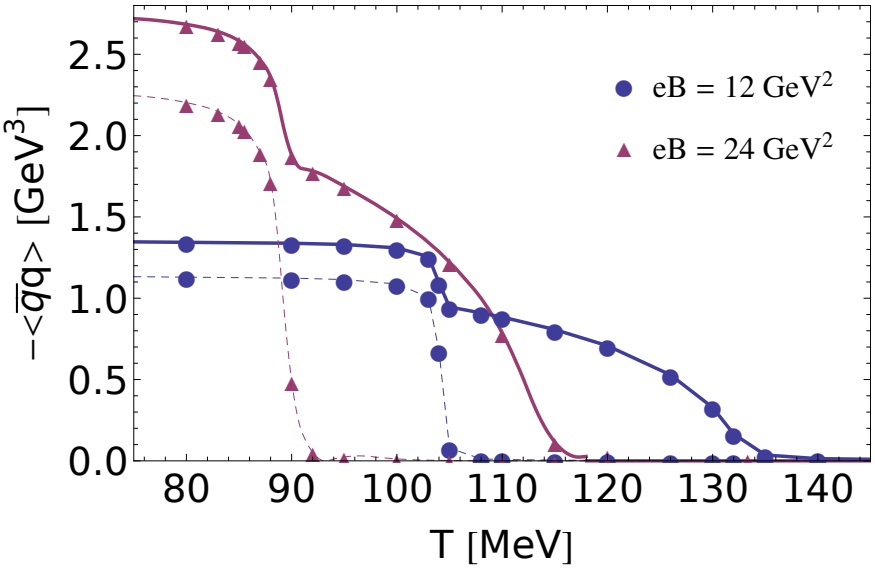

Figure 7.5: Comparison of the chiral condensate for scenario 2 at $eB = 12$ GeV^2 and $eB = 24$ GeV^2. Figure taken from [295].

In the present computation in two-flavor QCD, an even more intricate effect is observed. Up and down quarks come with different electric charges, therefore the presence of a strong electromagnetic field breaks isospin explicitly. This results in a non-degenerate chiral phase transition for the two flavors. Because gluons travel through a medium filled with both virtual up and down quarks, isospin breaking effects the self interactions of the quarks, which leads to interference between the chiral transitions of the two flavors as seen in Fig. (7.4) and Fig. (7.5).

This interference can be interpreted as follows. Virtual quark fluctuations contributing to the gluon screening are suppressed in the chiral broken phase by the quark mass. Since the down quark undergoes the chiral phase transition already at lower scales, its fluctuations are suddenly enhanced due to the vanishing mass in the symmetric phase. The up quark, while still in its chirally broken phase, is drastically effected by these enhanced fluctuations, which lead to reduction of the up quark condensate even below the real phase transition.

It can be seen from Fig. (7.4) and Fig. (7.5) that this effect is more prominent in scenario 2, which should come as no surprise, as the coupling of the magnetic field to the gauge sector is probably overestimated here. Nevertheless the isospin induced chiral transition substructure is observable in the limiting scenario 1 as well, which is a strong indication of its validity. Therefore this important physical effect might be observable in lattice calculations, as well. In [340, 341] the averaged chiral condensate was investigated at finite quark mass. However when we investigate the chiral transition at a bare quark mass

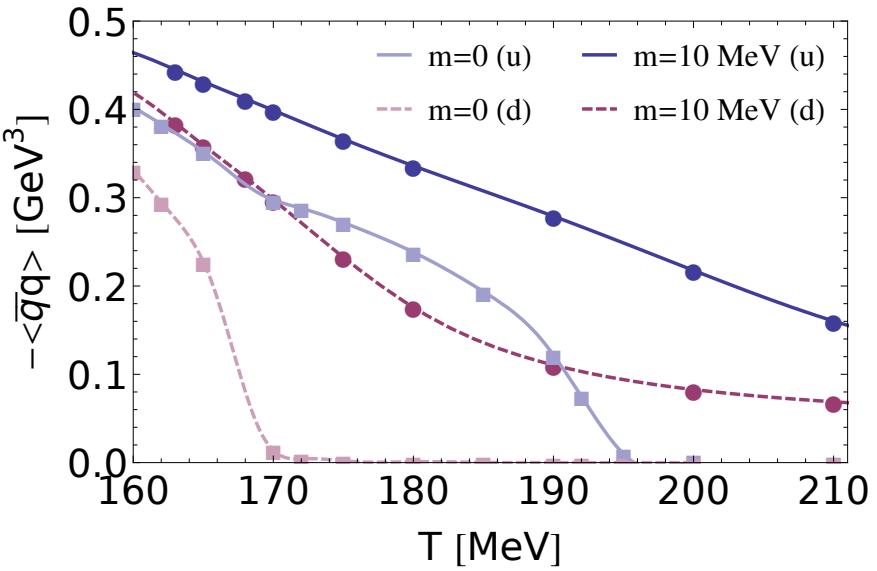

Figure 7.6: Comparison of the chiral condensate at zero bare mass and at a finite bare quark mass of $m_u = m_d = 10$ MeV at $eB = 4$ GeV^2 in scenario 1. Figure taken from [295].

of 10 MeV we find that the interference effect is completely masked by the crossover behavior as can be seen in Fig. (7.6). Note that here the unregularized condensate at finite bare mass is plotted, hence the offset between the curves.

In analogy with lattice calculation we define T_c at the inflection points of the curves shown. In Fig. (7.7) and Fig. (7.8) the obtained values for T_c for the limiting cases described by scenario 1 and 2 are shown. The two curves give lower and upper limits for T_c, as discussed before. The chiral transition temperature is decreasing for a large range in eB before it seems to saturate for intermediate values in both scenarios. At very large fields it rises again.

In accordance with our previous discussions we see that the up and down quark chiral transitions do not coincide. The transition temperature from the flavor averaged quark condensate is given in Fig. (7.7) and Fig. (7.8) as well. As can be seen from Fig. (7.4) and Fig. (7.5) the transition temperature of the flavor averaged condensate is essentially determined by the up quark.

Both scenarios give estimates for the chiral transition temperature, which differ only quantitatively. Scenario 1, which underestimates the magnetic field effects in the gluon sector extrapolates to a critical temperature at $eB = 0$ between $170 - 210$ MeV with a turning point between catalysis and inverse catalysis of about $eB \approx 30$ GeV^2. On the other hand scenario 2 gives T_c at zero magnetic field of about $140 - 165$ MeV with a turning point slightly higher than in scenario 1. This is in accordance with the fact that scenario 2 overes-

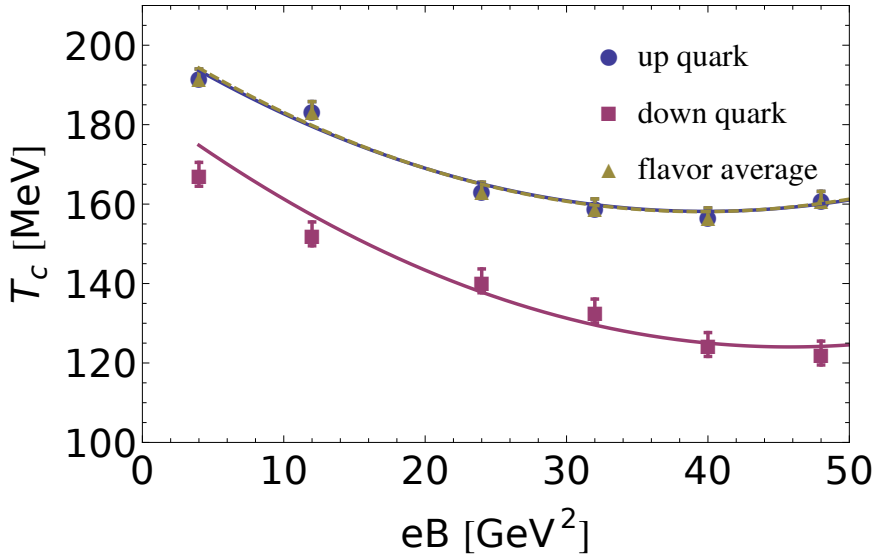

Figure 7.7: Critical temperature obtained from scenario 1 for up quark, down quark and from the flavor averaged condensate. Figure taken from [295].

timates the gluonic sector, which is the source of the inverse catalysis effects. At $B = 0$ the chiral phase transitions for up and down quark coincide. While the continuous lines in Fig. (7.7) and Fig. (7.8) are obtained from a fit with a simple quadratic polynomial, reflecting the turnover behavior at large fields, these should not be mistaken as extrapolations towards zero. Furthermore the computations have been performed in the lowest landau level approximation. This leads to an uncertainty of about 10% for B smaller than 10 GeV^2, while the qualitative behavior is not effected, as discussed in [299, 301]. In the following section we will see that the behavior of T_c at small B is steeper than just quadratic.

It is well known that within approximation schemes such as the one discussed here, relative fluctuation scales are usually well accounted for, whereas absolute scales have to be fixed. The position of T_c at $eB = 0$ gives us the possibility of identifying absolute scales and allows to adjust our truncation. We will not be concerned about matching the exact scale of T_c at zero magnetic field with the lattice, moreover we will investigate the mechanisms behind the $B - T$ phase structure in greater detail. We will discuss the issue of scales in the following sections.

7.3 Analytic approaches

In the present Section we are specifically interested in the mechanisms at work in magnetic and inverse magnetic catalysis. To that end we discuss approximations

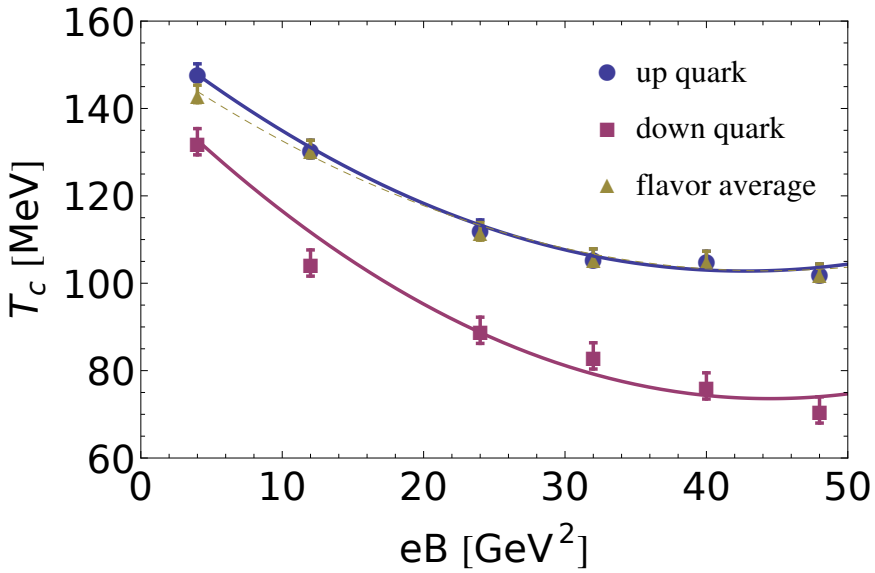

Figure 7.8: Critical temperature obtained from scenario 2. Figure taken from [295].

to the quark gap equation in Section 7.3.1, as well as to the dynamics of the four-fermi coupling or quark scattering kernel in Section 7.3.2, that allow for an analytic approach to chiral symmetry breaking. While the quark gap equation can be straightforwardly reduced to an analytic form from that used for the numerical study, the four-fermi coupling is studied in a renormalisation group approach to QCD, that reduces to an NJL-type model for low momentum scales.

7.3.1 Quark gap equation

The mechanisms behind the phenomena observed in our numerical study can be analyzed within approximations detailed below, that allow for an analytic access. These approximations to the gap equation have been introduced in [306] for QED, and can be extended to QCD at finite temperature. The self-consistent Dyson-Schwinger equation for the mass functions reads in lowest Landau level approximation with zero bare mass

$$M(p_\parallel) = 4\pi C_F \sum\!\!\!\!\!\!\int_{q_\parallel} \frac{M(q_\parallel)\mathrm{Tr}(\Delta(\mathrm{sgn}(eB))\gamma_\parallel^\mu\gamma_\parallel^\nu)}{M^2(q_\parallel)+q_\parallel^2}$$

$$\int_{k_\perp} \alpha_s \exp\left(-\frac{k_\perp^2}{2|eB|}\right)\frac{P_{\mu\nu}(k)}{k^2+\Pi(k^2)}\,. \tag{7.9}$$

Here $\not{\sum} = T\sum_n \int \mathrm{d}q_\parallel/(2\pi)^3$ and $\Delta(s) = (1 + s\sigma^3)/2$. The quark gap equation (7.9) is obtained from a skeleton expansion of the effective action, e.g. [370], and is nothing but a manifestly renormalisation group invariant approximation of the above Dyson-Schwinger equations, see the discussion in Section 7.2.2. It includes only dressed vertices. In appendix D.1 we discuss how the interaction kernels can be related in both pictures. The 1PI quark-gluon vertex is parametrized as

$$\Gamma^\mu_{\bar{q}Aq}(q^2) = Z_A^{1/2}(q^2)\sqrt{4\pi\alpha_s(q^2)}\gamma^\mu_\parallel \,, \tag{7.10}$$

The gluon propagator is transversal due to the Landau gauge, and we allow for a gluonic mass via thermal and magnetic effects. $M(p_\parallel)$ is a function that is approximately constant in the IR but falls of rapidly for $p_\parallel^2 \geq 2|eB|$. Hence, if we are interested in $M(0) = M_{\rm IR}$ we can write, dividing the equation by its trivial solution,

$$1 - 4\pi^2 C_F T \sum_{q_\parallel}^{2eB} \frac{1}{M_{\rm IR}^2 + q_{\parallel,f}^2} \times \int \mathrm{d}x \frac{\alpha_s \exp\left(-x/2|eB|\right)}{q_{\parallel,b}^2 + x + \Pi(x, q_{\parallel,b})} \left(2 - \frac{q_{\parallel,b}^2}{q_{\parallel,b}^2 + x}\right) = 0 \,. \tag{7.11}$$

In (7.11) we have introduced $q_{\parallel,b} \equiv (q_3, 2n\pi T)$ and $q_{\parallel,f} \equiv (q_3, 2\pi T(n + 1/2))$. Chiral symmetry breaking is realized once a solution $M_{\rm IR}^2 > 0$ exists. Due to the shape of $M(q)$ and the exponential factor in (7.11), the integrand only has support for $x \lesssim 2|eB|$. In the following we carefully investigate the ingredients to this self consistent equation and the physical mechanisms, which are responsible for the intriguing behavior seen in the previous section.

Due to the finite support of the integrand, the momenta running through the vertices are comparable or smaller than the relevant dimensionful quantities eB and T^2. Note that in our numerical study we have used an ansatz for the quark gluon vertex, that includes generic eB and T dependencies. Here we utilize the fact that the running of α_s is dominated by the temperature and magnetic field scales. We resort to a simple ansatz for $\alpha_s(Q^2/\Lambda_{\rm QCD}^2)$ based on the analytic coupling $\alpha_{s,\rm HQ}$ suggested in [371, 372], see [373] for an investigation within the present context. This coupling yields a linear potential such as seen in the heavy quark limit.

$$\alpha_s(z) = \alpha_{s,\rm HQ}(z)\, r_{\rm IR}(z) \,, \tag{7.12}$$

where

$$\alpha_{s,\rm HQ}(z) = \frac{1}{\beta_0}\frac{z^2 - 1}{z^2 \log(z^2)} \,, \tag{7.13}$$

with $\beta_0 = (33 - 2N_f)/12\pi$ and

$$z^2 = \frac{\lambda_B 2eB + \lambda_T (2\pi T)^2}{\Lambda_{\rm QCD}^2} \,, \tag{7.14}$$

with coefficients λ_T, λ_B, which are of order one. These coefficients determine the point at which eB or T dominate momentum scales. For the relevant magnetic fields and temperatures the running of the coupling with temperature is very small compared to the running with eB. We use an ansatz for the infrared behavior of the vertex, which is parametrized in $r_{\rm IR}$. Here we use

$$r_{\rm IR}(z^2) = \frac{z^4}{(z^2+b^2)^2}\left(1+\frac{c^2}{z^2+b^2}\right), \tag{7.15}$$

which scales with $\propto z^4$ for $z \to 0$, and approaches unity in the perturbative regime. Eq. (7.12) reproduces the correct behavior of the full quark gluon vertex in (7.10). We leave b and c as parameters which allow us to model the infrared behavior of the quark gluon vertex. Our ansatz for (7.15) is motivated from the quantitative renormalisation group study of quenched QCD in [367], which we use to determine b and c. We get

$$b = 1.50\,, \quad c = 7.68\,, \tag{7.16}$$

from the fit to Fig. 4 in [367].

Furthermore we discuss the gluon self energy in the presence of magnetic fields at finite temperature in this simplified setup. It is important to notice that we can facilitate our calculations by the following argument. The function on the right hand side of (7.11) is a continuous real function of $M_{\rm IR}$ and approaches $+1$ as $M_{\rm IR} \to \infty$. Hence it is sufficient to check whether the expression is negative for $M_{\rm IR} = 0$, because then it had to pass through zero at some point, which means that a solution exists.

The gluon self energy receives two important contributions. The first is through the appearance of fermion loops, which are also present in an abelian calculation. The fermionic self energy part in lowest Landau level approximation with $M_{\rm IR} = 0$ factorizes

$$\Pi_f^{\mu\nu}(p) = \alpha eB \exp\left(-p_\perp^2/2eB\right)\Pi^{\mu\nu}(p_\parallel, T)\,. \tag{7.17}$$

Contracting with $P^{\mu\nu}$ in the Landau gauge, we can write the second term as

$$\Pi_f(p_\parallel, T) = -8\pi^2\left[3-2(1-p_\parallel^2/p^2)\right]\frac{1}{\tau^2}$$
$$\times \int_0^1 {\rm d}x \sum\!\!\!\!\!\!\int_{\tilde{q}_\parallel} \frac{x(x-1)}{\left(\tilde{q}_3^2 + (2\pi)^2(n+1/2)^2 + x(1-x)/\tau^2\right)^2}\,, \tag{7.18}$$

where we defined $\tau^2 \equiv T^2/p_\parallel^2$. The function can be evaluated numerically and is very well described by the simple function

$$\Pi_f(p_\parallel, T) = (1/2\pi)\left[3-2(1-p_\parallel^2/p^2)\right]\frac{1}{1+(4\pi^2/3)\tau^2}\,. \tag{7.19}$$

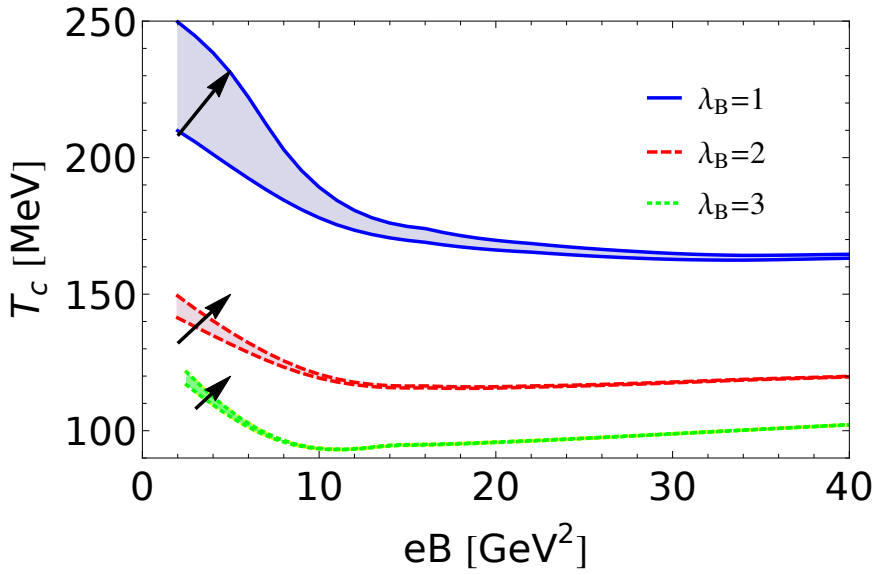

Figure 7.9: Analytic calculation of the critical temperature for the chiral phase transition. The bands indicated correspond to $\lambda_T = 1$ and $\lambda_T = 0$. Arrows indicate the direction from $\lambda_T = 1$ to $\lambda_T = 0$. Figure taken from [295].

Eq. (7.17) and Eq. (7.19) state that the relevant contributions to the self energy stem from $p_\perp^2 \approx 2eB$ and $p_\parallel^2 \approx T^2$. Similar as before, the influence of the magnetic field onto the Yang-Mills sector is not easily accounted for. Here we focus on the abelian-like part of the gluon self energy. As we have investigated before numerically, this is qualitatively correct and we will use Eq. (7.14) to account for the correct scales. It is well known from Dyson-Schwinger studies [374], that approximations similar to this semi-bare vertex ansatz underestimate the strength of chiral symmetry breaking, due to the negligience of important tensor structures in the vertex, especially those structures that break chiral symmetry explicitly [367]. In order to compensate the overall weakness of the interaction, we allow for a phenomenological parameter κ in front of the integral in Eq. (7.11).

Using our simple ansatz we can investigate chiral symmetry. In Fig. (7.9) a family of solutions to Eq. (7.11) is shown for various values of λ_B and λ_T, using the ansatz described above with $\kappa = 1.2$ for the two upper curves and $\kappa = 1.4$ for the lower curves. The choice of κ is for better visualisation only, as the curves can be shifted up and down using this parameter.

The observed behavior agrees with that in our numerical study. It can be seen from Fig. (7.9), that for small eB inverse magnetic catalysis is present, while at large eB the the critical temperature rises again with the magnetic

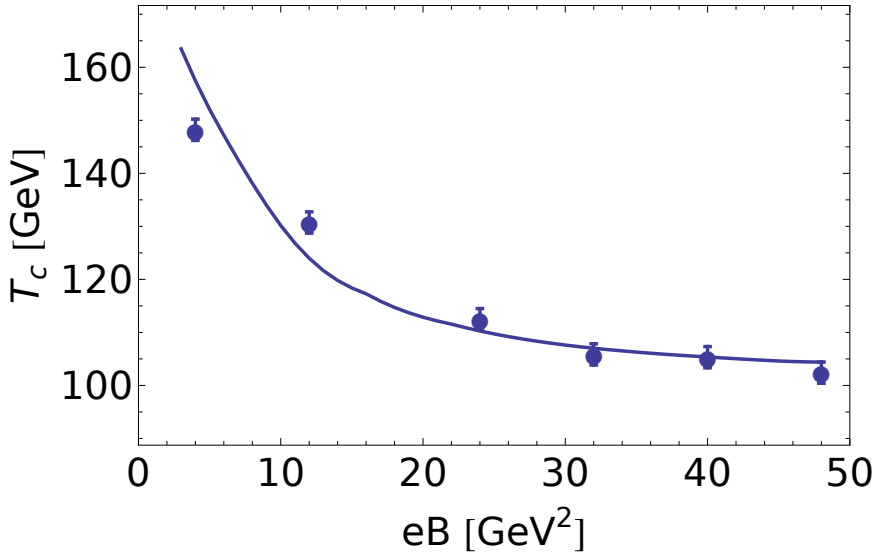

Figure 7.10: Comparison of the critical temperature obtained with our full numerical procedure to the simple analytic estimate for $\lambda_B = 1.1$, $\lambda_T = 1$ and $\kappa = 1.19$. Figure taken from [295].

field, with

$$T_c(B/\Lambda^2_{\rm QCD} \to \infty) \propto \sqrt{e\,B}\,, \tag{7.20}$$

as one would anticipate from dimensional considerations. This behavior is universal for all λ_B and λ_T. We see that the choice of λ_B effects the position of the turning point of the chiral phase boundary.

With the present analytical considerations the numerical results in Fig. (7.7) and Fig. (7.8) are readily explained: they roughly correspond to $\lambda_B \approx 1$, which explains the relatively large value of eB at the turning point. We see that already small changes in λ_B have a huge effect on this quantity, see Fig. (7.9).

In Fig. (7.10) we have plotted the analytic result with $\lambda_B = 1.1$, $\lambda_T = 1$ and $\kappa = 1.19$, which agrees well with the numerical results from scenario 2. Based on the present work we estimate that $\lambda_B \approx 2 - 3$ is a realistic choice for the B-dependence of the running coupling, as in our numerical study quark and gluon propagator turn into their corresponding $B = 0$-propagators at this momentum scale.

The present analysis reveals the following mechanism: The gauge sector acquires a B-dependence through the feedback of the fermionic sector. This dependence is responsible for the phenomena called inverse magnetic catalysis, as has been also observed recently in a FRG-study within QCD, [336]. This also explains why it cannot be seen in model calculation without explicit QCD input. From Eq. (7.11), Eq. (7.12) and Eq. (7.19) we see that the gluon screening and the running of the strong coupling (both by thermal and magnetic effects) are

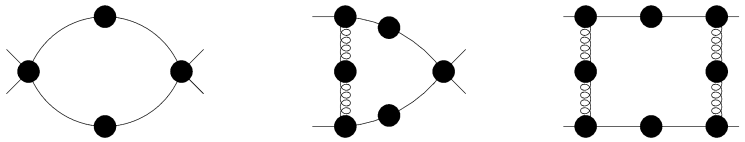

Figure 7.11: Diagrams contributing to the renormalisation group flow of the four-fermi coupling. Figure taken from [295].

competing with the generic fermionic enhancement of chiral symmetry breaking in a dimensionally reduced system. We see from Fig. (7.9) that at small magnetic field screening effects dominate the behavior of the fermionic self energy, while at asymptotically large fields, thermal fluctuations are negligible and hence eB, as the dominating scale, drives the phase transition towards higher T_c (magnetic catalysis).

7.3.2 Four-fermi coupling

For a further analytical grip we also resort to a low energy effective theory point of view: integrating-out the gapped gluons leads to an effective four-fermi theory, that is initialized at about the decoupling scale of the glue sector of $\Lambda \approx 1$ GeV. Previously there have been phenomenological approaches in low energy effective models to include QCD dynamics as the source of the inverse magnetic catalysis effect [317, 318, 347]. From the point of view of the FRG for QCD this can be seen as follows [352, 362, 366, 367, 375–377]: At a large momentum scale k QCD is perturbative, and the 1PI effective action Γ_k in (7.7) is well-described perturbatively. A four-fermi coupling is generated from the one-loop diagrams (in full propagators and vertices) encoded in (7.7), the related diagrams are depicted in Fig. (7.11). In the present discussion we have dropped diagrams that depend on the $q\bar{q} - AA$ vertex, $qq\bar{q}\bar{q} - AA$-vertex and the $qqq\bar{q}\bar{q}\bar{q}$-vertex. Furthermore we assume a classical tensor structure for the $\bar{q}Aq$-vertex with a coupling $\sqrt{4\pi\alpha_{s,k}}$, and only consider the scalar–pseudo-scalar four-fermi vertex

$$\Gamma_{\text{four-fermi}}[q,\bar{q},B] = \frac{1}{2}\,\bar{q}_i^{a\alpha} q_j^{b\alpha}\;\Gamma^{abcd}_{k,ijlm}\;\bar{q}_l^{c\beta} q_m^{d\beta}\,, \tag{7.21}$$

with the scalar–pseudo-scalar tensor structure

$$\Gamma^{abcd}_{k,ijlm} = \lambda_k\big[\delta_{ij}\delta_{lm}\delta^{ab}\delta^{cd} + (\mathrm{i}\gamma_5)_{ij}(\mathrm{i}\gamma_5)_{lm}(\tau^n)^{ab}(\tau^n)^{cd}\big]\,. \tag{7.22}$$

The four-fermi term in (7.21) can be viewed as the interaction term of a NJL-type model. Within the approximation to QCD outlined above the flow of the four-fermi coupling, $\partial_t\lambda_k$, has the form

$$\begin{aligned}\partial_t\lambda_k =& -k^2\lambda_k^2 F_\lambda(G_q) - \lambda_k\alpha_{s,k}F_{\lambda\alpha_s}(G_q,G_A)\\ &- \frac{\alpha_{s,k}^2}{k^2}F_{\alpha_s^2}(G_q,G_A)\,,\end{aligned} \tag{7.23}$$

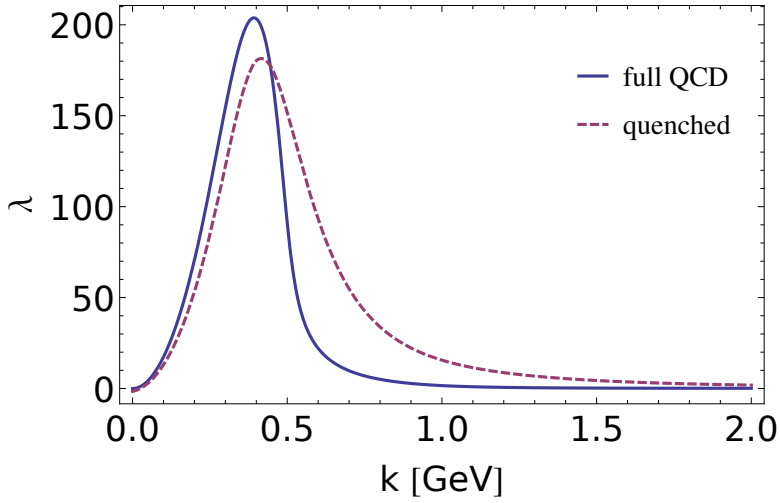

Figure 7.12: Scalar–pseudo-scalar four-fermi coupling in the vacuum, $T = 0$, $B = 0$, computed with quantitatively reliable QCD-flows in quenched QCD, [367], and with qualitative full QCD flows, [366]. Figure taken from [295].

with positive coefficients $F_\lambda, F_{\lambda\alpha_s}, F_{\alpha_s}$. The respective diagrams are depicted in Fig. (7.11). The different classes of diagrams in Fig. (7.11) depend on combinations of gluon and quark propagators, G_A and G_q respectively.

The four-fermi coupling λ_k in two-flavor QCD at $T = 0$ has been quantitatively computed (including its momentum-dependence) in quenched QCD with the FRG in [367], and in a more qualitative approximation (without its momentum-dependence) in fully dynamical QCD in [366]. The respective results are depicted in Fig. (7.12). As expected, the couplings have a similar dependence and maximal strength. However, the slope of the coupling in the qualitative computation in the peak regime relevant for chiral symmetry breaking is bigger for the qualitative computation. This can be traced back to the missing momentum-dependencies, whose lack artificially increases the locality in momentum space and in the cutoff scale. Hence, guided by the experience gained in the DSE-computations we expect the slope to play a large rôle and we shall use the quantitative quenched results for λ_k and α_s in our present computations. We shall further comment on the differences in the next Section.

For large cutoff scales k the propagators approach the classical propagators. The current quark mass at these scales is negligible and only the cutoff scale is present, if temperature and magnetic field are considered small relative to the cutoff scale. Then the dimensionless Fs are simple combinatorial factors. For optimized regulators, [378], they are given as

$$F_\lambda = 4N_c\,, \quad F_{\lambda\alpha_s} = 12\frac{N_c^2-1}{2N_c}\,, \quad F_{\alpha_s^2} = \frac{3}{16}\frac{9N_c^2-24}{N_c}\,, \tag{7.24}$$

in the vacuum, see e.g. [366, 367, 377] for more details. For small enough cutoff scales k the gluonic diagrams decouple due to the QCD mass gap. In the Landau gauge this can be directly seen with the gapping of the gluon propagator. For $T = 0$, $B = 0$ this entails

$$p^2 G_A(p^2 \lesssim \Lambda^2) \propto p^2/m_{\rm gap}^2 \,. \tag{7.25}$$

with $\Lambda \approx 1$ GeV. We emphasize that (7.25) only reflects the mass gap present in the Landau gauge gluon propagator, the gluon propagator is not that of a massive particle, see e.g. [379]. For momentum scales $p^2 \lesssim \Lambda^2$ this approximately leaves us with an NJL-type model with the action

$$\Gamma_{\rm NJL}[q,\bar{q},B] = \int_x \bar{q}\,\mathrm{i}\partial\!\!\!/ q + \Gamma_{\text{four-fermi}}[q,\bar{q},B]\,, \tag{7.26}$$

with the scalar–pseudo-scalar four-fermi interaction defined in (7.21). In the presence of a magnetic field this model including fermionic fluctuations has been investigated in [331] within the FRG. Here we shall use the respective results within the lowest Landau level approximation. Then T_c shows an exponential dependence on the dimensionful parameter eB

$$T_c = 0.42\Lambda \exp\left(-\frac{2\pi^2}{N_c \lambda_\Lambda \sum\limits_f |q_f eB|}\right). \tag{7.27}$$

The well-known exponential dependence of T_c on the four-fermi coupling λ_Λ already explains the large sensitivity of the scales of magnetic calatysis and inverse magnetic catalysis to details of the computation. Eq. (7.27) is valid for large magnetic field and for $\Lambda \ll m_{\rm gap}^2$, that is deep in the decoupling regime of the gluons. An estimate that also interpolates to small magnetic fields is given by

$$T_c = 0.42\Lambda \exp\left(-\frac{1}{c_\Lambda \lambda_\Lambda}\right), \tag{7.28}$$

with

$$c_k(B) = \frac{N_c}{2\pi^2}\left(\sum_f |q_f e\, B| + c_1\, k^2\right), \quad \text{with} \quad c_1 = 3\,, \tag{7.29}$$

where c_1 has been adjusted to reproduce $T_c(B=0) \approx 158$ MeV. While Eq. (7.29) resembles a lowest Landau level approximation, it is actually an expansion in B. Using this ansatz we can describe the behavior of the phase transition on scales below 1 GeV^2 qualitatively, while the $B = 0$ limit is fixed.

It is also well-known that for $k \gg m_{\rm gap}$ the flow of the four-fermi coupling is driven by the gluonic diagrams summed-up in F_{α_s}: for large scales we can set $\lambda_{k\gg m_{\rm gap}} \approx 0$. The gauge coupling is small, $\alpha_{s,k\gg m_{\rm gap}} \ll 1$ and the flow

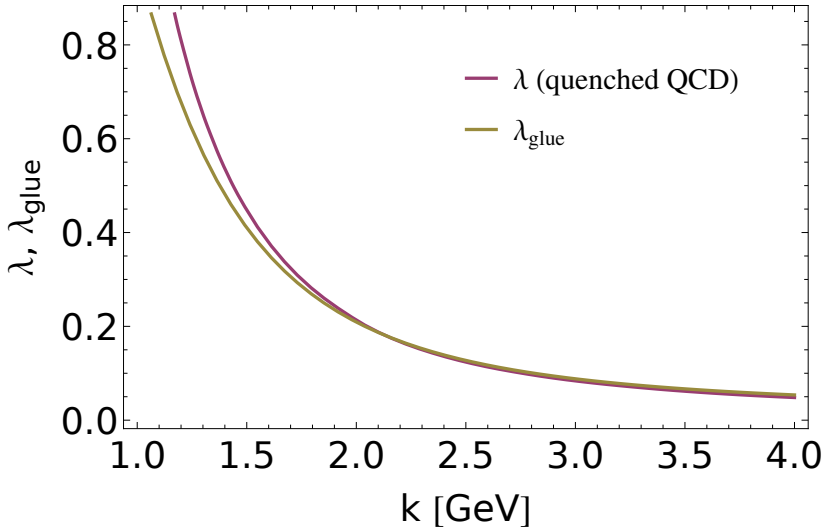

Figure 7.13: Scalar–pseudo-scalar four-fermi coupling at $T = 0$, $B = 0$ computed with quantitatively reliable QCD-flows in quenched QCD, [367], in comparison to $\lambda_{\rm glue}$ computed from (7.31). Figure taken from [295].

gives $\lambda_k \propto \alpha_s^2$. This entails that the diagrams with four-fermi couplings are suppressed by additional powers of α_s, and the four-fermi coupling obeys

$$\partial_t \lambda_{{\rm glue},k} = -\frac{\alpha_{s,k}^2}{k^2} F_{\alpha_s}(G_q, G_A)\,, \tag{7.30}$$

where the subscript 'glue' indicates that the flow is driven by glue fluctuations. As discussed before, for $k \gg m_{\rm gap}$ we have classical dispersions for quark and gluon, and the diagrammatic factor F_{α_s} is a constant, see (7.24). The strong coupling $\alpha_{s,k}$ has the form (7.12) with $z \propto k$. Integrating (7.30) with (7.12) gives

$$\lambda_{{\rm glue},k} \propto \frac{\alpha_{s,k}^2}{2k^2} F_{\alpha_s}(G_q, G_A)\,. \tag{7.31}$$

where an estimate for the B-dependence of the gluonic diagram in F_{α_s} is given in Appendix D.2.

At vanishing magnetic field $\lambda_{{\rm glue},k}$ agrees well with the full result for the four-fermi coupling in [367] for $k \gtrsim 2$ GeV, see Fig. (7.13). Below $k \approx 2$ GeV, $\lambda_{{\rm glue},k}$ is increasingly smaller than the full scalar–pseudo-scalar four-fermi coupling in quenched QCD. In this intermediate range, where all diagrams contribute, we write the resulting coupling within a resummed form that captures already the fermionic diagram proportional to F_λ,

$$\lambda_k = \frac{\bar\lambda_k}{1 - \bar c_k \bar\lambda_k}\,, \quad \text{with} \quad \bar c_k = \int_k^\Lambda dk'\, k' F_\lambda(G_q)\,. \tag{7.32}$$

The resummed form in (7.32) already reflects the matter part of the flow in (7.23) which is the term proportional to $\partial_t \lambda_k$. The other terms add up to

$$\partial_t \bar{\lambda}_k = -(1 - \bar{c}_k \bar{\lambda}_k)^2 \left(\lambda_k \alpha_{s,k} F_{\lambda \alpha_s} + \frac{\alpha_{s,k}^2}{k^2} \right) . \tag{7.33}$$

For $\bar{c}_k \bar{\lambda}_k \ll 1$ the flow of $\bar{\lambda}_k$ boils down to (7.30). For $\bar{c}_k \bar{\lambda} \to 1$ the flow in (7.33) tends towards zero. In this regime the four-fermi coupling grows large and the matter flow dominates. Hence, for the present qualitative analysis we simply identify $\bar{\lambda}$ with the glue $\lambda_{\rm glue}$, (7.31), up to a prefactor,

$$\bar{\lambda}_k = Z_\lambda \lambda_{{\rm glue},k} . \tag{7.34}$$

The prefactor Z_λ accounts for the fact that we have used results of quantitative QCD-flows [367] for the strong coupling which also includes wave function renormalisations for the quarks. In the current model considerations without wave function renormalisation and further simplifications this has to be accounted for. For the same reason the normalisation $0.42\,\Lambda$ related to a four-fermi flow with an optimised regulator has to be generalised. Moreover, the prefactor $\bar{c}_{\lambda,k}$ is the integrated four-fermi flow already present in (7.28) up to an overall normalisation accounting for the model simplifications. We choose

$$\bar{c}_k(B) = c_3\, c_k(B) , \quad \text{and} \quad 0.42\,\Lambda \to 0.42\,\Lambda \exp(c_2 - c_3) , \tag{7.35}$$

and arrive at

$$T_c = 0.42 \Lambda \exp\left(-\frac{1}{c_\Lambda \bar{\lambda}_\Lambda} + c_2 \right) , \tag{7.36}$$

with c_Λ as given in (7.29) and $\bar{\lambda}$ in (7.34) and (7.31). Note that the parameter c_3 has dropped out. Its value can be adjusted to achieve a quantitative agreement of (7.31) with the QCD result in [367] with

$$c_3 = \frac{1}{2 Z_\lambda} , \tag{7.37}$$

where the factor $1/Z_\lambda$ simply removes the mapping factor adjusting for the missing wave function renormalisations in the model computation. This quantitative agreement strongly supports the reliability of the approximate solution to the flow equation given by (7.32) in the intermediate momentum regime that is of importance for the current considerations. The remaining parameters are fixed as follows,

$$Z_\lambda = 2.2 , \quad c_1 = 3 , \quad c_2 = 1.4 . \tag{7.38}$$

The parameter c_1 has already been adjusted to meet $T_c(B = 0) \approx 158$ MeV, see (7.28) and (7.29). The parameter c_2 re-adjusts the overall scale $0.42\,\Lambda \to 0.42\,\Lambda \exp c_2 = 1.7\Lambda$. As already discussed above, it depends on the regulator

and the approximation at hand. It reflects the dependence on the renormalisation group scheme. Similarly to c_1 it is fixed with $T_c(B=0) \approx 158$ MeV, and is a function of the overall normalisation of the four-fermi coupling Z_λ. The latter is the only free parameter left. In (7.38) we use the value that reproduces the lattice results, see Fig. (7.14). We emphasise that no other parameter is present that allows to shift the minimum in T_c, the latter being a prediction.

Obviously, the effect seen in our numerical and analytic DSE-study, is also present in the analytic approach to the dynamics of the four-fermi coupling, including a direct grip on the underlying mechanisms. We see that the non-monotonous behavior, i.e. the delayed magnetic catalysis, [336, 344], is already present at smaller scales compared to Fig. (7.7) and Fig. (7.8), while the lattice results are reproduced.

In turn, for asymptotically large magnetic field, the critical temperature runs logarithmically with B,

$$T_c(B/\Lambda_{\rm QCD}^2 \to \infty) \propto \ln B/\Lambda_{\rm QCD}\,, \tag{7.39}$$

related to a double-log–dependence on B of the exponent. Due to the qualitative nature of the approximation of the B-dependence of the gluon propagator it cannot be trusted for asymptotically large B. Indeed, (7.39) has to be compared to (7.20) within the analytic DSE-approach predicting a square root dependence. Note that in the latter computation the quark vaccum polarisation is included selfconsistently at large B even though the backreaction on the pure glue loops in Fig. (7.2) is neglected. Still this indicates the validity of the square root dependence, even though a definite answer to this question requires more work.

7.3.3 Discussion of scales & mechanisms

With the findings of the last two sections we have achieved an analytic understanding of the mechanisms at work. The decrease of T_c for small magnetic fields, the increase of T_c for larger fields, as well as the related magnetic field regimes can now be understood. In particular this concerns the magnetic field $B_{\rm min}$, where $T_c(B_{\rm min})$ is at its minimum. This is the turning point between increasing and decreasing $T_c(B)$.

Magnetic catalysis relates to the dimensional reduction due to the magnetic field in diagrams with quark correlation functions leading to an increase of the condensate. At finite temperature the catalysis due to the dimensional reduction is accompanied by a thermal gapping of the quarks that counteracts against the magnetic catalysis effects. In total this leads to a rise of both, the chiral condensate and the critical temperature, if the magnetic field dependence of the involved couplings is sufficiently small. As the magnetic field also sets a momentum scale of the physics involved, this scenario holds true for sufficiently large magnetic field strength $eB/\Lambda_{\rm QCD}^2 \gg 1$, where the B-dependence of the couplings can be computed (semi-)-perturbatively. This explains the regime of delayed magnetic catalysis.

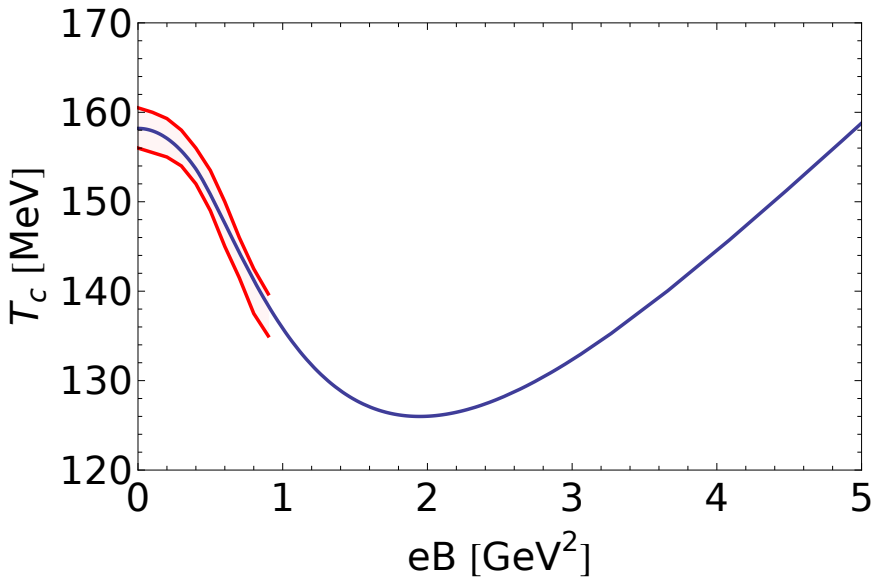

Figure 7.14: Comparison of the chiral transition temperature obtained within the simple mean field NJL estimate Eq. (7.14) to the lattice results of [205] (see their Fig. 10). Figure taken from [295].

The above discussion of the standard scenario already entails that rapidly changing couplings are required for a decreasing T_c. The couplings involved are the scalar–pseudo-scalar four-fermi coupling λ_k and the strong coupling $\alpha_{s,k}$, where k sets the momentum scale. Both are rising rapidly towards the infrared for momentum scales $k \lesssim 4 - 10$ GeV, for λ_k see Fig. (7.13). In this regime chiral symmetry breaking and confinement is triggered and takes place in QCD at vanishing magnetic field. Switching on the magnetic field increases the relevant momentum scale $k^2 \propto e\,B$ and hence decreases λ and α_s. The condensate still grows with B as the B-enhancement in the broken phase is still present, only T_c decreases.

Our results from the analytic approach to the quark gap equation, presented in Fig. (7.9), support these findings. The position of the turning point $B_{\min}$ in both the full numerical as well as the analytic analysis of the gap equation depends crucially on the magnetic field and temperature dependence of the quark gluon vertex, see Fig. (7.9). When contrasted with the quantitative FRG results of α_s in [367], the strong coupling in (D.2) decays considerably slower towards the UV. In turn, the couplings in the qualitative FRG study for full QCD, [366] have a steeper decay, for the four-fermi coupling see Fig. (7.13). Seemingly, this already explains the large value of $B_{\min}$ in the current DSE-study as well as the small value of $B_{\min}$ in [336], which uses approximations similar to [366]. Note however, that we have used the quenched quantitative α_s in the analytic DSE-study which agrees well with the numerical DSE result for

$\lambda_B \approx 1$.

In summary we have identified the physics mechanisms behind the $T - B$ phase diagram from our full QCD calculations. Moreover, Fig. (7.14) suggests a turning point for $e\,B_{\rm min} \approx 1.5{-}10$ GeV^2, the large regime for $e\,B_{\rm min}$ being related to the exponential dependence on the couplings. Evidently, the effects observed depend on a sensitive balance of different scales and parameters. Hence, further studies are required to fully uncover the intricate underlying dynamics. Very recent findings in AdS/QCD models, [329], indicate an inverse magnetic catalysis behavior up to $eB \approx 4$ GeV^2, which supports our findings.

7.4 Conclusions

We have investigated the chiral phase structure of QCD at finite temperature in the presence of an external magnetic field. Our study resolves the discrepancy between recent lattice and continuum calculations at magnetic fields below 1 GeV^2, see also [336]. We confirm the inverse magnetic catalysis effect seen in lattice studies at small B. At larger B we see that magnetic catalysis is restored, with $T_c \propto \sqrt{eB}$. Indications for the turnover behavior have already been found in [336], and in [344] within two-color lattice-QCD. We hope that further lattice calculations in full QCD at the scales discussed here will become feasible soon.

The reason for this non-monotonous behavior are screening effects of the gauge sector, i.e. modifications of the gluon self energy, as well as the strong coupling α_s in the presence of magnetic fields. Moreover we have investigated the nature of the chiral transition at finite magnetic field.

Apart from the B-dependence of the critical temperature, we observe that the phase transition in the chiral limit turns smoothly into a crossover with rising B. Notably, we find a non-degeneracy in the phase transition which is due to the explicit isospin breaking caused by the different electric charges of up and down quark. This non-degeneracy might lead to phenomenological consequences in experimental studies of the QCD phase diagram with non-central heavy-ion collisions, as there might be a mixed phase between the up and down quark transitions. Recent lattice calculations [380] support the possibility of a non-degenerate chiral phase transition.

In addition, our calculations show that, due to this isospin breaking, there is a step-like behavior in the up quark condensate triggered by the chiral transition of the down quark. While this is an significant effect in the chiral limit it smoothens out rapidly with increasing current quark mass. Physical current quark masses are in the transition regime, and this effect might have phenomenological consequences. To our knowledge, this is a novel effect in the QCD phase diagram and it certainly deserves further investigation.

We have used analytic studies of the quark gap equation and the dynamics of the four-fermi coupling for an investigation of the physics mechanisms behind (inverse) magnetic catalysis. The results are discussed at length in the previous Section 7.3.3, leading to a rough prediction of the turning point at $e\,B_{\rm min} \approx 1.5 - 10$ GeV. Our investigations highlight the rich phenomenology of

QCD matter in external magnetic fields, which motivates further studies, e.g. at finite chemical potential, towards more realistic descriptions of matter under extreme conditions. Recent studies [381] have suggested even richer QCD phase structures in the presence of magnetic fields.

Chapter 8

Summary and outlook

In this chapter we summarize our main results and provide an outlook onto future research directions. The main motive of this manuscript has been the out-of-equilibrium nature of anomalous and topological effects in both Abelian as well as non-Abelian gauge theories, which comprise a central aspect of current experimental efforts in high-energy QCD.

Given the many challenges and limitations that are still hindering theoretical interpretation of experimental studies (see our detailed account in chapter 1.3), we were strongly persuaded to find simpler and cleaner experimental set-ups for the study of the Chiral Magnetic and other related effects, whose understanding are the main objectives of this work. To this end, we have devoted our efforts to the field of high-intensity laser physics, an fascinating and rapidly progressing field, which in the near future will provide novel perspectives onto particle physics: as the famous Schwinger intensity limit is within striking distance of planned experimental facilities, the non-linear regime of QED and Schwinger pair production is becoming an almost imminent reality.

This exciting new research field has only been addressed with rather conventional techniques and the intriguing consequences of the out-of-equilibrium and quantum field theoretical nature of the non-linear regime of QED has not been appreciated fully. Consequently by applying advanced real-time simulation techniques, which have been developed originally in the context of high energy QCD and cosmology, we were able to uncover some of the fascinating consequences of the Chiral Magnetic Effect in QED and we have predicted novel and compelling phenomena that result directly from the axial anomaly. Moreover, we have outlined how these effects can be measured in experiment: by studying non-trivial gauge field configurations $\mathbf{E} \cdot \mathbf{B}$ beyond the Schwinger intensity limit, we have observed that the combination of the anomaly and the presence of magnetic fields lead to the creation of anomalous electric currents $\mathbf{j} \propto \sigma_5 \mathbf{B}$. A consequence of this dynamics is the phenomenon of *anomaly induced dynamical refringence*: we found fermionic backcoupling to be responsible for an anomalous rotation of the polarization of the electric field, observable using spectroscopic measurements. We studied the emergence of chiral plasma oscil-

lations and found an intriguing tracking behavior in the non-linear interplay of fermions and gauge fields, which tends to maximize the effects of the anomaly. In this context we have explicitly verified the anomaly realization in the continuum limit of real-time lattice QED and we have investigated the effects of the fermion mass. We found that the explicit violation due to the finite fermion mass counteracts the creation of axial charge and we have estimated that it will ultimately dampen the dynamical transfer between fermionic chirality and magnetic helicity. Our results are presented in chapter 3.

Our findings in chapter 3 have clarified the role of the axial anomaly in out-of-equilibrium situations and have unambiguously shown that its relevance in experiment is beyond its topological content, contrary to thermal or vacuum situations. Consequently the out-of-equilibrium nature of anomalous and topological dynamics is of crucial importance in high energy QCD experiments and should be investigated carefully. Accordingly in chapter 4 we have studied the effect of typical out-of-equilibrium gauge field configurations, which can be understood from the Color-Glass-Condensate/Glasma high energy limit of QCD at small parton momentum fraction x and anomalous fermion production. Starting from typical 'flux-tube' initial conditions, which do not carry any non-trivial topology, we observed that net axial charge is produced for a given configuration. We subsequently found that fluctuations are responsible for the break-up of these coherent field configurations on time scales of the order of the inverse saturation scale Q_s^{-1}. Accordingly we studied the dependence of the axial charge generation in the regime of instabilities and we observed that net axial charge might survive until much later times. This highlights the significance of glasma initial conditions for hydrodynamic simulations. From a technical point of view we have carefully studied the realization of the axial anomaly using Wilson lattice fermions and found that the anomaly term is recovered from the continuum limit of the Wilson regulator.

Chapter 5 is devoted to the study of the Chiral Magnetic Effect in the early stage of an ultra-relativistic heavy ion collision using classical-statistical real-time lattice simulations. In a simplified set-up we have investigated the dynamics of anomalous fermion production during an isolated sphaleron transition. We have studied the dynamics of anomalous transport, and investigated the fermion mass and magnetic field dependence of the Chiral Magnetic and the Chiral Separation Effect. Moreover we observed the emergence of chiral density waves (Chiral Magnetic Wave) and our study is the first ever field-theoretical ab-initio approach to do so. Our most important observation are significant deviations from the idealized topological "dissipation-less" transport of axial and vector charges that was predicted in the literature. Our microscopic approach has enabled us to study anomalous transport properties that are crucial input for hydrodynamic simulations. Our studies revealed a finite relaxation time for both the CME and CSE, which must be taken into account in future studies. This might be accomplished by promoting the static transport coefficients used in hydrodynamic set-ups to dynamical variables, that relax to their asymptotic value on a characteristic time scale, which can be estimated from our studies. We also observed that for weak and intermediate magnetic fields the ratios

between vector (axial) densities and axial (vector) currents differ clearly from unity. Dissipation effects play an important role for massive fermions and by studying the quark mass dependence we can rule out contributions to the CME from heavy quark flavors.

While our study was performed in a simplified and not yet realistic situation, we have shown that classical-statistical simulations allow to address the two largest uncertainties hindering experimental observations of the Chiral Magnetic Effect. First, our simulations enable us to determine axial and vector charge distributions at earliest times, that provide the initial conditions for hydrodynamics and our work has shown that the dynamics of these microscopic quantities differs significantly from simple estimates. Moreover our microscopic approach enables us to study the electromagnetic response of the medium created in ultra-relativistic heavy ion collisions. While the lifetime of the external magnetic field is presumably very short, the medium might sustain magnetic fields on much longer timescales and we can address this aspect quantitatively by including fermionic backcoupling, as we had done in chapter 3.

Our ab-initio study represents significant progress in the understanding of real-time fermion dynamics: in our study we have for the first time demonstrated the use of algorithmic improvements such as operator improvements and r_W-averaging in real-time for lattice Wilson fermions. Moreover we have presented the first-ever real-time simulation of chiral (overlap) lattice fermions in 3+1D.

The understanding of chiral transport is tied to the dynamics of chiral fermions in topological non-trivial backgrounds. While real-time lattice simulations prove powerful when occupation numbers are large and the dynamics is quasi-classical, the classical-statistical approximations breaks down when the occupancies of the gauge fields become of order one. The fire-ball expands typically on time scales of only a few fm/c and the dynamics becomes that of a dilute plasma – well described using kinetic approximations. Only very recently has the question of chirality transport and anomalous fermionic dynamics been approached using kinetic approximations. In the framework of *Chiral Kinetic Theory* it is conjectured that the anomaly-related dynamics of fermions is realized by a *Berry monopole*, which arises in the non-relativistic and adiabatic limit of the theory. This proposal has raised our doubts and motivated us to pursue a closer examination. Inspired by observations of Fujikawa, we identified a number of weak points in the construction of chiral kinetic theory: First, the connection between the topology of the anomaly and that of Berry's phase is unclear – most importantly because the latter is shown to arise only in a very specific limit, while the presence of the anomaly is generic and should not depend on approximations. Moreover present approaches rely on the existence of a large chemical potential (and thus implicitly on the non-relativistic limit) and clearly such approximations are unjustified in the context of heavy ion collisions. The absence of Lorentz covariance in current proposals has been counteracted by including relativistic corrections – the results however not being very convincing.

Using the string-inspired framework of world-lines we show in chapter 6 that the emergence of a Berry monopole and the axial anomaly are in fact

unrelated. In a quasi-particle description of particles with spin, Berry's phase merely accounts for the effects of spin transport (in the adiabatic limit). In the absence of approximations, Berry's phase is not robust (not geometric) and spin transport is part of the relativistic formulation of the dynamics of the system. On the contrary, the emergence of the anomaly is related to the phase of the fermion determinant. By means of the world-line method, this phase can be expressed in single-particle language: in an euclidean formulation the effects of the anomaly are tied to the emergence of fermionic zero modes in the heat-kernel representation of the imaginary part of the fermion effective action. A kinetic theory can be derived from the real part. The framework that we have put forward, thus allows for a Lorentz-covariant description of the quasi-particle description of spinning and colored particles. Our framework permits to derive a covariant kinetic theory, with scattering terms being motivated from a microscopic origin.

As a next step we aim to systematically derive the anomalous equivalent of Bodecker's theory and we aim to provide an ab-initio derivation of anomalous hydrodynamics from quantum field theory. Our findings have wide applications, such as the anomalous transport of chiral fermions in astrophysical systems or helicity evolution in QCD of partons at small momentum fraction x.

Our last chapter 7 provides a complimentary view on the effects of large Abelian magnetic fields onto QCD. In this chapter we studied the strong coupling regime of QCD matter and the aspect of spontanous chiral symmetry breaking, including the generation of large constituent masses for the light quark flavors in the presence of magnetic fields. Our study is an important contribution to the understanding of the QCD phase diagram at finite temperature and magnetic field. In chapter 7 we investigated the recent discrepancy between model and lattice computation in regards to magnetic catalysis: while lattice computations suggest that the critical temperature for the chiral phase transition is reduced with increasing magnetic field strength (inverse catalysis), model studies predict the opposite effect. In our study we found that the intriguing interplay between magnetic catalysis and inverse magnetic catalysis is due to screening effects in the gauge sector that have not been included in model studies. To this end, we observed that, while at small and intermediate (in units of the temperature) magnetic fields *inverse magnetic catalysis* is prevalent, at asymptotically large magnetic fields *magnetic catalysis* is restored. We gave a first prediction of the critical magnetic field necessary for this intriguing turnover behavior, however we found large systematic uncertainties. Moreover, we observed that the (iso-spin-)degeneracy of the chiral phase transition of up and down quarks is lifted for large magnetic fields and we we studied the emergence of a semi-chiral phase, where only the down-quark is chiral. Additionally, the nature of the phase transition becomes crossover-like even for massless bare quarks in the presence of magnetic fields.

The central results of this work are the advanced non-equilibrium techniques that allow to investigate the dynamics of anomalous and topological effects in QCD. The ultimate goal of the efforts that we have presented in the preced-

ing chapters is of course a more complete and quantitative understanding of the space-time dynamics of an ultra-relativistic heavy ion collision. Despite the success of the weak-coupling techniques presented in this thesis, a comprehensive understanding of QCD out-of-equilibrium is a remarkably difficult challenge and will require much more effort: the classical-statistical simulation techniques of gauge field and fermion dynamics should be extended towards realistic initial conditions and expanding space-time geometries, before concrete predictions for experiments can be obtained. While we have outlined some of the necessary tools for this goal, going beyond the set-ups that were presented here is computationally very demanding. While the results that were illustrated here were obtained through the collaboration of a handful of researchers and using rather 'modest' computational resources of a few million CPU hours, future studies will require substantially more effort. To this end, the development of novel algorithmic techniques is of crucial importance and is currently investigated.

Building upon the significant progress that is illustrated in this thesis, a future research objective should be the simulation of the early time dynamics of the CME using *realistic* configurations of the initial state of a collision, described by the Color-Glass Condensate. The methods that have been developed and presented here, make this goal achievable within the next one or two years, provided the continued existence of sufficient computational resources. Typical computational demands are estimated to be in the tens of million core hour regime. Moreover it should be a central goal to understand the electromagnetic response of matter created in the high-energy regime of QCD out-of-equilibrium. As the lifetime of the external magnetic field represents an important uncertainty for CME predictions, the effect of fermionic back-reaction and the electromagnetic properties of the out-of-equilibrium medium created in the earliest stages of a heavy ion collision should be investigated using the techniques described herein.

Moreover the dynamics of the anomalous transport of axial and vector charges must be understood more thoroughly and connected with hydrodynamic descriptions. The subsequent evolution of axial and vector charges during the expansion of the fire-ball created in a collision, can be systematically described by the combination of real-time lattice simulation techniques and the string-inspired fermionic transport framework, which was first introduced here. This will allow a characterization of out-of-equilibrium anomalous transport; initial conditions for hydrodynamic simulations can be derived and a precise prediction of experimental outcome is possible.

Moreover, the presented simulation techniques are an excellent tool to study non-thermal production of direct photons. Therefore they should be used to investigate the origins of the *photon puzzle*, which is the discrepancy between theoretical predictions and experiments with regard to the spectrum of photons and their azimuthaml flow at small transverse energies both at RHIC and LHC experiments. Using real-time lattice simulations we aim to calculate photon production directly and substantial efforts are underway.

Apart from their striking relevance in high-energy QCD, the real-time lattice simulation techniques of gauge field and fermion dynamics have a wide range of applications across different fields: classical-statistical simulations have been

employed in a cosmological context to investigate electroweak phase transitions. A further objective of current studies are chiral instabilities, which are conjectured to arise from the interplay between fermionic chirality and magnetic helicity on suitable out-of-equilibrium conditions. The instabilities are speculated to play an important role in astrophysical situations such as neutron stars and supernovae. Moreover, they could be responsible for large primordial magnetic fields, observable in todays galactic background. The simulation techniques that have been established here allow a precise examination of chiral instabilities and the conditions under which they might arise. To this end, we will put special attention to study of the effect of a finite fermion mass.

The string-inspired world-line framework is a powerful tool for the study of the dynamics of the axial anomaly and will allow detailed predictions, when applied in the kinetic regime of an ultra-relativistic heavy ion collision. Inspired by the universality of the approach, we have identified yet another exciting prospect of application: the spin structure of high-energy QCD. This interest is motivated by the commitment of the US nuclear physics community to construct an Electron-Ion Collider within the near future. This fascinating experimental possibility allows the test of the helicity structure of QCD at small parton momentum fraction x. The presented world-line framework allows to derive an effective action formalism, which is a natural continuation of the Color-Glass-Condensate description. First studies in this context are in progress.

Acknowledgments

In this section I will come to the hardest part of all: thanking all the wonderful people that have contributed to the success of this thesis and to my steep learning curve on how things work in life. The difficulties arises (a) because this section is limited in space and (b) listing names sometimes indicates the importance of contributions. Since it is impossible to sort people according to the latter, I ask you to please ignore the order of names that is given here. You all are great!

First of all I would like to thank my two supervisors Jan M. Pawlowski and Juergen Berges, who I am deeply indepted to for having guided me through the last three years so well. I am grateful for them putting so much confidence in me and for the unlimited support. Thanks also for tolerating my rampant use of institute's money. I would like to express my gratitude to Raju Venugopalan, who's one-year stay in Heidelberg offered me so many unique chances. Thanks for all the insights you shared with me and for everything I learned in the past year.

I would like to thank Valentin Kasper, who is one of the greatest persons I have ever met and who's knowledge in physics, as well as in the things that actually matter, I envy a lot. Valentin, thank you for teaching me so many things and for making all the difference.

Moreover I would like to Soeren Schlichting for having such a tremendous impact on my way of life and for putting so much faith in my ideas and work. Thank you Mark Mace and Sayantan Sharma for being wonderful colleagues and adding to my perspective in life.

I would like to thank my wonderful group (past and present members) in Heidelberg for being such a fine bunch of human beings: Thank you Aleksandr for being such a pleasant and caring office mate. Many thanks go to Carlos for many things, among them sharing an appartment in the boonies on Long Island and for being the best coffee – really the best – I mean there is other coffee, but I have talked to people and they tell me this coffee is the best. Love the coffee, really love it. Its great. I thank Alexander L. and hope that you will have a fun time in Heidelberg. Moreover I am indebted to Asier, who is a wonderful colleague and who cares a lot about the well-being of his colleagues. Also I am working hard on my babaric approach towards food, trust me. I would like to thank Alexander R. for sharing his experiences with me and for supporting me, when things looked gloomy. I wish you and your wife all the best for the

comming years! I thank Niels for being a great office mate and for the climbing lessons, hopefully I did not scare you too much. I thank Alexander S. for being such a great guy and for his professional handling of hostage crisises in general. Many thanks go to Linda, who it was a pleasure to share an office with, for being so motivational and bringing a lot of drive to the group. Thanks also for not killing my plants while I was away. Thank you Naoto for being such a great person and I believe that you are incredible smart and talented. I wish you all the best for your future road in life. Non fare il modesto, sei il migliore. I would like to thank Torsten for always willing to tolerate my annoying physics discussions. Thank you Roland for being my favourite Franke.

Furthermore I would like to thank the past members of my group who I had the pleasure of interacting with. First of foremost I thank Florian Hebenstreit for all his support and for being such a great example, illustrating that one can manage a successful co-existence of physics and life. I would like to thank Kiril and Daniil for all the fun we had. My gratitude to the travel reimbursment office, for their your indisputably magnificent assistance and for the remarkable degree of financial security, which their lightning-fast, always correct and hard work has enabled, is almost infinite. Thanks to Benjamin, who always payed careful attention to my progress and who I should write to more often. Thanks also to Andreas for being a great office mate. I know you will be super successful in Austria given how smart you are! I would like to thank Tina Kuka for taking care of everything. They should give you a raise for the excellent work you do. Thanks also to everyone who helped me writing this thesis by proofreading and constructive comments. I thank Sebastian Erne in particular for all the effort he made providing me with feeback from 'outside my field' and for being such a nice person in general.

Moreover I am indebted to Steve Ellis, who had a very important impact on the way I think about physics and who in some ineffable way is responsible for a lot of my achievements. Also I would like to thank the wonderful people that I have met during my stay in Seattle and with whom I will always be connected: Larry and Jerry for having understood what being a good person means, and for knowing what happiness is; Deb and Dean for being the most caring and tolerant people I know.

I am indebt to the Studienstiftung des Deutschen Volkes for the great support not only during my Bachelor and Master studies but also for the generous scholarship they have offered me during my PhD. I am grateful for all the support and for making many things possible. I would like to thank the Heidelberg Graduate School of Fundamental Physics and everyone involved in its management for providing all the support and for financing some of my travels. My doctoral studies were supported in part by the DFG Sonderforschungsbereich 1225 (ISOQUANT).

Ich danke meiner Familie für die bedingungslose Unterstützung und für alles was ich lernen durfte. Besonders möchte ich meinen Eltern danken dafür, dass sie mir beigbracht haben, die richtigen Dinge im Leben wert zu schätzen und dafür, dass sie versucht haben mich zu einem vernünftigen Menschen zu erziehen. Ich hoffe, dass das zumindest in einigen Ansätzen gelungen ist.

Zuletzt und an wichtigster Stelle möchte ich meiner Verlobten Svende danken, dafür, dass du mein Leben verändert und mir einen tiefen Sinn gegeben hast. Worte genügen nicht zu beschreiben was du mir bedeutest und darum verzeihe mir, dass dieser Absatz so kurz ausfällt. Ich hoffe, dass ich noch viel Gelegenheit haben werden, alles was du für mich getan hast, dir auch zurückgeben zu können.

Appendix A

Chiral anomaly and cutoff regularization

In this part of the appendix we willll illustrate the emergence of the lattice anomaly from the issue of gauge invariance and regularization. The calculations presented here are taken from [52]

For the specific case of fermion dynamics in the presence of homogeneous background gauge fields considered in section 4.2, there is in principle an efficient alternative procedure to implement the anomaly on the lattice by restricting the Brillouin zone to remove doublers [382]. In this appendix, by using analytic solutions of the Dirac equation for the example of quantum electrodynamics (QED), we will demonstrate that it is crucial for such a procedure to implement the corresponding momentum cutoff to preserve gauge invariance in order to describe the anomaly correctly.

For QED in a uniform system with background electric field $\mathbf{E}$ and magnetic field $\mathbf{B}$, the anomaly equation reads

$$\partial_t n_5(t) = \langle \overline{\psi} i\gamma_5 \psi \rangle + \frac{e^2}{2\pi^2} \mathbf{E} \cdot \mathbf{B}\,, \tag{A.1}$$

where e denotes the electromagnetic coupling. In the following, we will verify this equation by using analytic solutions of the Dirac equation in the presence of a homogeneous background field that carries nonzero $\mathbf{E}\cdot\mathbf{B}$. As an example of field configurations with nonzero $\mathbf{E}\cdot\mathbf{B}$ that are simple enough to access analytical solutions of the Dirac equation, we consider a Sauter-type pulsed electric field superposed by a constant magnetic field:

$$\mathbf{E}(t) = \frac{E}{\cosh^2(t/\tau)} \mathbf{e}_z, \quad \mathbf{B} = B\mathbf{e}_z, \tag{A.2}$$

where E, B, and the characteristic pulse time τ are constant, with $\mathbf{e}_z$ denoting a unit vector in the z-direction. In the following, we assume $eE > 0$ and $eB > 0$.

A.1 Analytic solutions of the Dirac equation

The electromagnetic fields (A.2) are described by the gauge potential

$$A^\mu = (0, -By, 0, -E\tau\left[\tanh(t/\tau) + 1\right]). \tag{A.3}$$

Under this gauge field, the mode functions are labeled by momenta p_x and p_z, Landau level n $(= 0, 1, 2, \cdots)$, and spin s $(=\uparrow, \downarrow)$ as well as labels $+$ and $-$ that distinguish positive and negative energy solutions. We employ the Dirac representation for the gamma matrices, and use the following basis to expand spinors:

$$\begin{aligned} \Gamma_1 &= \frac{1}{\sqrt{2}}\begin{pmatrix}1\\0\\1\\0\end{pmatrix},\ \Gamma_2 = \frac{1}{\sqrt{2}}\begin{pmatrix}0\\1\\0\\-1\end{pmatrix}, \\ \Gamma_3 &= \frac{1}{\sqrt{2}}\begin{pmatrix}1\\0\\-1\\0\end{pmatrix},\ \Gamma_4 = \frac{1}{\sqrt{2}}\begin{pmatrix}0\\1\\0\\1\end{pmatrix}. \end{aligned} \tag{A.4}$$

The mode functions are conveniently described by the following dimensionless parameters

$$\xi = \frac{1}{2}\left[1 + \tanh(t/\tau)\right], \tag{A.5}$$

$$\eta = \sqrt{\frac{2}{eB}}\left(eBy + p_x\right), \tag{A.6}$$

$$\lambda = eE\tau^2, \tag{A.7}$$

$$\mu = \frac{\tau}{2}\sqrt{m^2 + eB(2n + 1 - s) + p_z^2}, \tag{A.8}$$

$$\nu = \frac{\tau}{2}\sqrt{m^2 + eB(2n + 1 - s) + (p_z + 2eE\tau)^2}, \tag{A.9}$$

where $s = 1$ for spin-up and $s = -1$ for spin-down. The mode functions are expressed in terms of these quantities as follows:

$$\begin{aligned} \psi^+_{p_x,p_z,n,\uparrow}(x) = &\left(\frac{eB}{\pi}\right)^{1/4}\sqrt{\frac{L}{n!}}\frac{1}{\sqrt{4\mu(2\mu - p_z\tau)}}\xi^{-i\mu}(1-\xi)^{-i\nu} \\ &\times\left[2i\tilde{\varphi}^+(\xi)D_n(\eta)\Gamma_3 - \sqrt{2eB}\tau\varphi^+(\xi)nD_{n-1}(\eta)\Gamma_2\right. \\ &\left. + m\tau\varphi^+(\xi)D_n(\eta)\Gamma_1\right]e^{i(p_x x + p_z z)}, \end{aligned}$$

$$\begin{aligned} \psi^+_{p_x,p_z,n,\downarrow}(x) = &\left(\frac{eB}{\pi}\right)^{1/4}\sqrt{\frac{L}{n!}}\frac{1}{\sqrt{4\mu(2\mu - p_z\tau)}}\xi^{-i\mu}(1-\xi)^{-i\nu} \\ &\times\left[2i\tilde{\varphi}^+(\xi)D_n(\eta)\Gamma_4 + \sqrt{2eB}\tau\varphi^+(\xi)D_{n+1}(\eta)\Gamma_1\right. \\ &\left. + m\tau\varphi^+(\xi)D_n(\eta)\Gamma_2\right]e^{i(p_x x + p_z z)}, \end{aligned}$$

$$\psi^-_{p_x,p_z,n,\uparrow}(x) = \left(\frac{eB}{\pi}\right)^{1/4} \sqrt{\frac{L}{n!}} \frac{1}{\sqrt{4\mu(2\mu+p_z\tau)}} \xi^{+i\mu}(1-\xi)^{-i\nu} \times \big[-2i\tilde{\varphi}^-(\xi) D_n(\eta)\Gamma_3 + \sqrt{2eB}\tau\varphi^-(\xi) n D_{n-1}(\eta)\Gamma_2 - m\tau\varphi^-(\xi) D_n(\eta)\Gamma_1\big] e^{i(p_x x + p_z z)},$$

$$\psi^-_{p_x,p_z,n,\downarrow}(x) = \left(\frac{eB}{\pi}\right)^{1/4} \sqrt{\frac{L}{n!}} \frac{1}{\sqrt{4\mu(2\mu+p_z\tau)}} \xi^{+i\mu}(1-\xi)^{-i\nu} \times \big[-2i\tilde{\varphi}^-(\xi) D_n(\eta)\Gamma_4 - \sqrt{2eB}\tau\varphi^-(\xi) D_{n+1}(\eta)\Gamma_1 - m\tau\varphi^-(\xi) D_n(\eta)\Gamma_2\big] e^{i(p_x x + p_z z)},$$

where L is the linear size of the system with volume $V = L^3$, and $D_n(z)$ is the parabolic cylinder function. The functions $\varphi^\pm(\xi)$ and $\tilde{\varphi}^\pm(\xi)$ are represented by the hypergeometric function ${}_2F_1(a,b;c;z)$ as follows:

$$\varphi^\pm(\xi) = {}_2F_1(\mp i\mu - i\nu - i\lambda, \mp i\mu - i\nu + i\lambda + 1; 1 \mp 2i\mu; \xi), \tag{A.10}$$

$$\begin{aligned}\tilde{\varphi}^\pm(\xi) &= \xi^{\pm i\mu}(1-\xi)^{i\nu}\left[\xi(1-\xi)\frac{d}{d\xi} + i\lambda\xi + \frac{i}{2}p_z\tau\right] \\ &\quad \times \xi^{\mp i\mu}(1-\xi)^{-i\nu}\,{}_2F_1(\mp i\mu - i\nu - i\lambda, \mp i\mu - i\nu + i\lambda + 1; 1 \mp 2i\mu; \xi) \\ &= (1 \mp i\mu + i\nu + i\lambda)\,{}_2F_1(\mp i\mu - i\nu - i\lambda - 1, \mp i\mu - i\nu + i\lambda + 1; 1 \mp 2i\mu; \xi) \\ &\quad + \left[(1+2i\lambda)\,\xi - \left(1 + i\nu + i\lambda - \frac{i}{2}p_z\tau\right)\right] \\ &\qquad \times {}_2F_1(\mp i\mu - i\nu - i\lambda, \mp i\mu - i\nu + i\lambda + 1; 1 \mp 2i\mu; \xi).\end{aligned}$$

We note that the limits $t \to -\infty$ and $t \to +\infty$ correspond to $\xi \to 0$ and $\xi \to 1$, respectively. The mode functions $\psi^+_{p_x,p_z,n,s}(x)$ and $\psi^-_{p_x,p_z,n,s}(x)$ satisfy the boundary condition such that at $t \to -\infty$ they approach the positive and negative energy solutions, respectively, in a constant magnetic field. The mode functions are normalized by the inner product

$$(\psi_1|\psi_2) = \int d^3x\, \psi_1^\dagger(t,\mathbf{x})\psi_2(t,\mathbf{x}), \tag{A.11}$$

such that

$$\left(\psi^+_{p_x,p_z,n,s}\middle|\psi^+_{p'_x,p'_z,n',s'}\right) = \delta_{s,s'} L \delta_{n,n'} (2\pi)^2 \delta(p_x - p'_x)\delta(p_z - p'_z), \tag{A.12}$$

$$\left(\psi^-_{p_x,p_z,n,s}\middle|\psi^-_{p'_x,p'_z,n',s'}\right) = \delta_{s,s'} L \delta_{n,n'} (2\pi)^2 \delta(p_x - p'_x)\delta(p_z - p'_z), \tag{A.13}$$

$$\left(\psi^+_{p_x,p_z,n,s}\middle|\psi^-_{p'_x,p'_z,n',s'}\right) = \left(\psi^-_{p_x,p_z,n,s}\middle|\psi^+_{p'_x,p'_z,n',s'}\right) = 0. \tag{A.14}$$

In terms of the mode functions, the fermion field operator ψ is expanded as

$$\psi(x) = \sum_s \frac{1}{L}\sum_{n=0}^{\infty} \int \frac{dp_x}{2\pi} \int \frac{dp_z}{2\pi} \left[\psi^+_{p_x,p_z,n,s}(x) a_{p_x,p_z,n,s} + \psi^-_{p_x,p_z,n,s}(x) b^\dagger_{p_x,p_z,n,s}\right]. \tag{A.15}$$

The creation and annihilation operators satisfy

$$\left\{a_{p_x,p_z,n,s}, a^\dagger_{p'_x,p'_z,n',s'}\right\} = \left\{b_{p_x,p_z,n,s}, b^\dagger_{p'_x,p'_z,n',s'}\right\} = \delta_{s,s'} L \delta_{n,n'} (2\pi)^2 \delta(p_x - p'_x)\delta(p_z - p'_z).$$

A.2 Verification of the anomaly equation

The vacuum expectation of the chiral charge density, $n_5(t)$, is expressed by the mode functions as

$$n_5(t) = \sum_s \frac{1}{L} \sum_{n=0}^{\infty} \int \frac{dp_x}{2\pi} \int \frac{dp_z}{2\pi} \psi^{-\,\dagger}_{p_x,p_z,n,s}(x)\gamma_5 \psi^-_{p_x,p_z,n,s}(x). \tag{A.16}$$

After substituting the explicit forms of the mode functions (A.10-A.10), we can first execute the p_x-integral by using

$$\int_{-\infty}^{\infty} dx \left[D_n(x)\right]^2 = \sqrt{2\pi} n!. \tag{A.17}$$

We note that the p_x-integration is finite without a cutoff. After the integration, it turns out that the contribution of the mode with $(n+1, \uparrow)$ and that with $(n, \downarrow)$ cancel each other. As a consequence, only the lowest mode $(n = 0, s = \uparrow)$ contributes to the chiral charge, and one obtains:

$$n_5(t) = \frac{eB}{4\pi^2} \int dp_z \frac{1}{2\sqrt{m^2 + p_z^2}(\sqrt{m^2 + p_z^2} + p_z)} \times \left[-\frac{4}{\tau^2} \left|\tilde{\varphi}^-(\xi)\right|^2 + m^2 \left|\varphi^-(\xi)\right|^2 \right]_{n=0,s=\uparrow}. \tag{A.18}$$

In a similar way, we can compute the pseudo-scalar condensate:

$$\langle \overline{\psi} i\gamma_5 \psi \rangle = \frac{eB}{4\pi^2} \int dp_z \frac{1}{2\sqrt{m^2 + p_z^2}(\sqrt{m^2 + p_z^2} + p_z)} \times \frac{4m}{\tau} \mathrm{Re}\left[\varphi^{-\,*}(\xi)\tilde{\varphi}^-(\xi)\right]_{n=0,s=\uparrow}. \tag{A.19}$$

The right hand side of (A.18) depends on time only through ξ. After some algebra, one finds that

$$\frac{\partial}{\partial t}\left|\varphi^-(\xi)\right|^2 = \frac{4}{\tau}\mathrm{Re}\left[\varphi^{-\,*}(\xi)\tilde{\varphi}^-(\xi)\right], \tag{A.20}$$

and

$$\frac{\partial}{\partial t}\left|\tilde{\varphi}^-(\xi)\right|^2 = -\tau m^2 \mathrm{Re}\left[\varphi^{-\,*}(\xi)\tilde{\varphi}^-(\xi)\right]. \tag{A.21}$$

Collecting all these results, we finally arrive at

$$\partial_t n_5 = 2m\langle \overline{\psi} i\gamma_5 \psi \rangle, \tag{A.22}$$

which so far does not contain the anomaly term.

In the diagrammatic derivation of the axial anomaly, it is crucial to regularize a divergent integral in a gauge-invariant way. Also in our calculation, we need to regularize the integral in (A.18) to obtain the anomaly term. In fact, the integrand of (A.18) does not fall off at $p_z \to \pm\infty$. By using the asymptotic expansion of the hypergeometric function ${}_2F_1(a,b;c;z)$ for large $|c|$ [222], one finds that

$$\{\text{integrand of (A.18)}\} \approx \begin{cases} -1 & (p_z \to +\infty) \\ +1 & (p_z \to -\infty). \end{cases} \tag{A.23}$$

To regularize this divergent integral, one may naively introduce a cutoff for p_z as

$$\int_{-\infty}^{+\infty} dp_z \longrightarrow \int_{-\Lambda}^{+\Lambda} dp_z \tag{A.24}$$

to see that this does not alter the result (A.22). The reason why the anomaly term is not obtained is that it introduces the cutoff for the canonical momentum. The canonical momentum $\mathbf{p}_{\rm can}$ is related to the kinetic momentum $\mathbf{p}_{\rm kin}$ as

$$\mathbf{p}_{\rm can} = \mathbf{p}_{\rm kin} + e\mathbf{A}\,. \tag{A.25}$$

While here the kinetic momentum is a gauge-invariant quantity, the canonical momentum is gauge-dependent. In a translational-invariant system, the canonical momentum is a constant of motion, and thus it is associated with a plane wave factor $e^{i\mathbf{p}\cdot\mathbf{x}}$. Therefore, the momentum p_z appearing in (A.18) is a canonical momentum. Since the canonical momentum is not a gauge-invariant quantity, putting a cutoff breaks gauge invariance. In order to regularize the integral keeping the gauge invariance, we need to introduce a cutoff for the kinetic momentum. Because of the relation (A.25), putting a cutoff $\pm\Lambda$ to the kinetic momentum amounts to putting a time-dependent cutoff $\pm\Lambda + eA^3(t)$ to the canonical momentum:

$$\int_{-\infty}^{+\infty} dp_z \longrightarrow \int_{-\Lambda+eA^3(t)}^{+\Lambda+eA^3(t)} dp_z\,. \tag{A.26}$$

Thanks to this time-dependent cutoff, $\partial_t n_5(t)$ acquires the anomaly term:

$$\begin{aligned} \partial_t n_5 &= \frac{eB}{4\pi^2}\partial_t \int_{-\Lambda+eA^3(t)}^{+\Lambda+eA^3(t)} dp_z \Big\{ \cdots \Big\} \\ &= 2m\langle\overline{\psi} i\gamma_5 \psi\rangle + \frac{e^2 B}{4\pi^2}\frac{dA^3}{dt}\Big[\cdots\Big]_{p_z=-\Lambda+eA^3(t)}^{p_z=\Lambda+eA^3(t)} \\ &= 2m\langle\overline{\psi} i\gamma_5 \psi\rangle + \frac{e^2}{2\pi^2}\mathbf{E}\cdot\mathbf{B}\,, \end{aligned} \tag{A.27}$$

where we have used $E_z = -dA^3/dt$ and (A.23).

In the massless case the gauge invariant regularization of (A.26) can also be seen in context of spectral flow (see e.g. [383]). The use of the covariant

momentum corresponds to a time dependent rearrangement of the eigenvalues of the Hamiltonian. In the case of nonzero $\mathbf{E} \cdot \mathbf{B}$, the dispersion relation of the fermions is altered in such a way, that the rearrangement is different for left and right handed particles and thus a net chiral charge is generated.

We have demonstrated how the anomaly term appears from the gauge-invariant cutoff regularization. However, such a computation applies only to the specific case of an abelian and uniform background gauge field. For non-abelian and/or inhomogeneous gauge fields, the relation between kinetic and canonical momentum becomes ambiguous. In that case, the lattice regularization with the Wilson term method provides a powerful way to describe the axial anomaly, as discussed in the main text. Here we note that the derivative appearing in the Wilson term is the covariant derivative, and the covariant derivative corresponds to the kinetic momentum, $\boldsymbol{D} e^{i\mathbf{p}_{\mathrm{can}}\cdot\mathbf{x}} = i\mathbf{p}_{\mathrm{kin}} e^{i\mathbf{p}_{\mathrm{can}}\cdot\mathbf{x}}$.

Appendix B

Real-time lattice simulations with dynamical Wilson and overlap-fermions

This part of the appendix is based on the pubilcations 'Chiral magnetic effect and anomalous transport from real-time lattice simulations' (N.M., S. Schlichting, S. Sharma), which is published in Phys.Rev.Lett. 117 (2016) no.14, 142301 [arXiv:1606.00342] [229] and 'Non-equilibrium study of the Chiral Magnetic Effect from real-time simulations with dynamical fermions' (M. Mace, N.M., S. Schlichting, S. Sharma), which is published in Phys.Rev. D95 (2017) no.3, 036023 [arXiv:1612.02477] [187].

B.1 Eigenmodes of the Dirac Hamiltonian in the helicity basis

In this appendix (c.f. [187]) we derive the eigenmodes for non-interacting fermions in the helicity basis by diagonalizing the Dirac Hamiltonian for Wilson and overlap fermions.

We begin by taking the gamma matrices in the Dirac representation. In the absence of gauge fields ($U = \mathbf{1}$) the eigenfunctions of the Wilson and overlap Dirac equation can be written in the plane wave basis. The spatial momenta

and effective mass term for the improved Wilson fermions in this basis are

$$\begin{aligned} p_i^w &= \sum_n \frac{C_n}{a_s}\sin(na_s q_i) \\ m_{\text{eff}}^w &= m + \sum_{n,i} \frac{2nC_n}{a_s} r_w \sin^2(\frac{naq_i}{2}) \end{aligned} \tag{B.1}$$

and similarly for massless overlap fermions[1]

$$\begin{aligned} p_i^{ov} &= M\frac{p_i^w}{s} \\ m_{\text{eff}}^{ov} &= M\left(1+\frac{p_5}{s}\right) \end{aligned} \tag{B.2}$$

where

$$\begin{aligned} q_i &= \frac{2\pi n_i}{N_i}, \quad n_i \in 1, ..., N_i - 1 \\ p_5 &= -M + \sum_i \frac{2}{a_s}\sin^2(\frac{aq_i}{2}) \\ s &= \sqrt{\sum_i p_i^2 + p_5^2}. \end{aligned} \tag{B.3}$$

With this notation, the eigenvalue problem takes the same form for either discretization; we will we drop the superscript differentiating the two since everything that follows applies equally to both cases. The Hamiltonian in this basis is then

$$H = \begin{pmatrix} m_{\text{eff}}\mathbf{1}_2 & \vec{\sigma}\cdot\vec{p} \\ \vec{\sigma}\cdot\vec{p} & -m_{\text{eff}}\mathbf{1}_2 \end{pmatrix}, \tag{B.4}$$

which has eigenvalues $E_\pm = \pm\sqrt{m_{\text{eff}}^2 + \vec{p}^2}$, where the positive (negative) eigenvalues corresponds to (anti) particles. The corresponding eigenvectors are given as

$$\begin{aligned} u^h(p) &= \sqrt{\frac{2E_+(E_+ - m_{\text{eff}})}{p^2}} \begin{pmatrix} \phi^{(h)}(p) \\ h\frac{|E|-m_{\text{eff}}}{|p|}\phi^{(h)}(p) \end{pmatrix} \\ v^h(p) &= \sqrt{\frac{2E_-(E_- - m_{\text{eff}})}{p^2}} \begin{pmatrix} \phi^{(h)}(-p) \\ -h\frac{|E|+m_{\text{eff}}}{|p|}\phi^{(h)}(-p). \end{pmatrix}, \end{aligned} \tag{B.5}$$

Since the Hamiltonian, Eq.(B.4), commutes the helicity operator, the eigenvectors of the Hamiltonian are simultaneously eigenvectors of the helicity operator. We then choose ϕ to be normalized with respect to helicity $\frac{\vec{p}\cdot\vec{\sigma}}{|\vec{p}|}$, so the index

[1] For overlap, we always take $r_w = 1$ and the Wilson improvement coefficients $C_1 = 1$,$C_n = 0$ for $n > 1$

h is the helicity and takes values $h = \pm 1$. Now we solve for the ϕ. First, if $(p_x, p_y) \in \{0, N_x/2\} \times \{0, N_y/2\}$, then

$$\phi^+(p) = (1,0)^T \tag{B.6}$$

$$\phi^-(p) = (0,1)^T \tag{B.7}$$

otherwise

$$\phi^h(p) = \frac{1}{\sqrt{1 + \frac{(p_z - h|\vec{p}|)^2}{p_x^2+p_y^2}}} \begin{pmatrix} 1 \\ -\frac{p_z - h\sqrt{p_x^2+p_y^2+p_z^2}}{p_x - ip_y} \end{pmatrix} \tag{B.8}$$

For the case $(p_x, p_y, p_z) \in \{0, N_x/2\} \times \{0, N_y/2\} \times \{0, N_z/2\}$, where the linear momentum term vanishes, for $m_{\text{eff}} > 0$

$$u^h(p) = \begin{pmatrix} \phi^h(0) \\ 0 \end{pmatrix}, \quad v^h(p) = \begin{pmatrix} 0 \\ \phi^h(0) \end{pmatrix}, \tag{B.9}$$

while for $m_{\text{eff}} < 0$ we have

$$u^h(p) = \begin{pmatrix} 0 \\ \phi^h(0) \end{pmatrix}, \quad v^h(p) = \begin{pmatrix} \phi^h(0) \\ 0 \end{pmatrix}. \tag{B.10}$$

While this is most obvious in the last case, the orthogonality conditions

$$u^\dagger_{q,\lambda} u_{q,\lambda'} = \delta_{\lambda,\lambda'} \tag{B.11}$$

$$v^\dagger_{q,\lambda} v_{q,\lambda'} = \delta_{\lambda,\lambda'} \tag{B.12}$$

$$u^\dagger_{q,\lambda} v_{q,\lambda'} = v^\dagger_{q,\lambda} u_{q,\lambda'} = 0. \tag{B.13}$$

are held for all eigenvectors. We have now constructed the helicity eigenmodes for the free Wilson and overlap Dirac Hamiltonian.

B.2 Convergence study of net axial charge for Wilson and Overlap fermions

In this appendix (c.f. [187]) we will discuss finite size effects and convergence of our Wilson (see Sec. 5.1.1) and overlap (see Sec. 5.1.2) lattice fermions, and we will compare the properties of two fermion discretizations. In order to be able to concentrate on the chiral properties of the fermions as a function of volume, improvement, and discretization, we will only consider the single sphaleron transition introduced in Sec. 5.1.3. We keep $r_{\text{sph}}/a = 6$ fixed for all simulations and consider only isotropic lattices in this section, and will keep the Wilson r-parameter fixed at $r_w = 1$ for all comparisons. In this section we work in the nearly massless limit for the Wilson fermions ($mr_{\text{sph}} = 1.9 \cdot 10^{-2}$) and the massless limit for overlap fermions, so the integrated anomaly equation reduces

to Eq.(5.40). We have previously shown for Wilson fermions how both the unintegrated (see Fig. 5.3) and integrated (Figure 3 in [229]) anomaly equation are maintained as a function of mass. For the Wilson fermions, we first pick a volume, $N^3 = 16^3$, and study the total axial charge created as a function of time for various levels of operator improvement, as was discussed in Sec. 5.1.1. This is plotted in Fig. B.1. We can clearly see that at Leading Order (LO), the standard unimproved Wilson fermion formulation, there is significant deviation, at the 25% level, from the Chern Simons term $-2\Delta N_{CS}$, which is quantified in the lower panel of Fig. B.1. However, upon going to one level of improvement, Next to Leading Order improvement (NLO), we see that this disagreement disappears. At Next to Next to Leading Order (NNLO) improvement, we see no noticeable difference from NLO, and thus see that our improvement scheme has converged. In practice, we find that in all cases in our current study, NLO is sufficient and nothing additional is gained by going to NNLO.

Now we need to understand how important finite volume effects are in our study. This is shown in Fig. B.2. Here we look at the axial charge generated by NLO improved Wilson fermions for three volumes. It is clear from the lower panel of Fig. B.2 that for $N = 12 = 2r_{\rm sph}/a$, there are clear finite volume effects that lead to large oscillations of the J_a^0 around the sphaleron transition from Eq.(5.40). This is then subsequently improved by going to a volume $N = 16 = 2.67r_{\rm sph}/a$, where we can see noticeable improvement. To test this convergence, we further look at $N = 32 = 5.34r_{\rm sph}/a$; here we see that there is no difference in the average deviations from the Chern-Simons term as compared to the $N = 16 = 2.67r_{\rm sph}/a$.

However, we should note that this is only for resolving the creation of axial charge from a single localized sphaleron transition. To look at charge transport as a function of time, like we studied in Sec 5, we need even larger volumes, especially in the magnetic field direction. Typically we choose a spatially anisotropic lattice, where the transverse length is $N_{trans} \geq 2r_{\rm sph}/a$, while along the direction of the magnetic field $N_z \gg 2r_{\rm sph}/a$ (a typical choice is $N^3 = 16^2 \times 32 - 24^2 \times 64$). Moreover, the transverse size of the lattice has to be large enough to accommodate the cyclotron orbits of charged particles. In practice this constraint limits the available magnetic field strength to larger magnetic flux quanta.

Next, for the overlap fermions, we proceed in the same manner. Instead of improving the Wilson kernel, we vary the domain wall height M for a fixed isotropic lattice $N = 16$. As we see in Fig. B.3, values in the range of $M \in [1.4, 1.6)$ give the best results. They are the best results, really. Other results are loosers [384]. We choose $M = 1.5$. We have verified that the volume dependence of the currents for the overlap is similar to the Wilson fermions with NLO improvement, which is evident from Fig. (5.1).

In summary, for Wilson fermions, NLO improvement is necessary and sufficient to accurately reproduce the anomaly. At this level, we find that it gives comparable results to the overlap fermions, which we find that for a well tuned domain wall mass M we can reproduce the anomaly relation even on reasonably small lattices. Additionally, we find that for spatial lattice sizes of $N = 2\ r_{\rm sph}/a$,

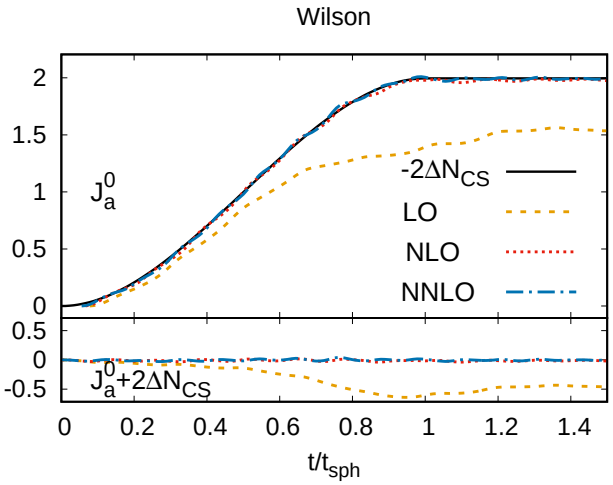

Figure B.1: A comparison of the net axial charge generated during a sphaleron transition for a fixed volume of $N = 16$ using $mr_{\rm sph} = 1.9 \cdot 10^{-2}$ Wilson fermions with different operator improvements. Top: Already at NLO we see that the net axial charge tracks ΔN_{CS} due to the sphaleron transition. Bottom: Deviations from Eq.(5.40) are shown. Figure taken from [187].

finite volume effects are somewhat noticeable, but seem to be completely under control for lattice size $N > 2r_{\rm sph}/a$. This will serve also as crucial input for how fine to make one's lattice for future studies with more realistic gauge field configurations, where the size sphalerons is set by physical scales of the problem.

B.3 Details of the Hamiltonian overlap construction

In this appendix we illustrate the Hamiltonian formualtion of overlap fermions in 3+1 dimensions with Minkowskian matric (see [187]). The spatial overlap operator is

$$-i\not{D}_{ov} \quad = \quad M\Big(\mathbf{1} + \gamma_5 \frac{Q}{\sqrt{Q^2}}\Big), \tag{B.14}$$

where Q is the overlap kernel that can be chosen as follows

$$Q \equiv \gamma_5 \not{D}_W(M), \tag{B.15}$$

where $-i\not{D}_W(M)$ is the massless Wilson Dirac operator. The parameter $M \in [0, 2)$ the height of the defect that localizes the chiral fermions on 4D Euclidean spacetime starting from a 5D domain wall formalism [188].

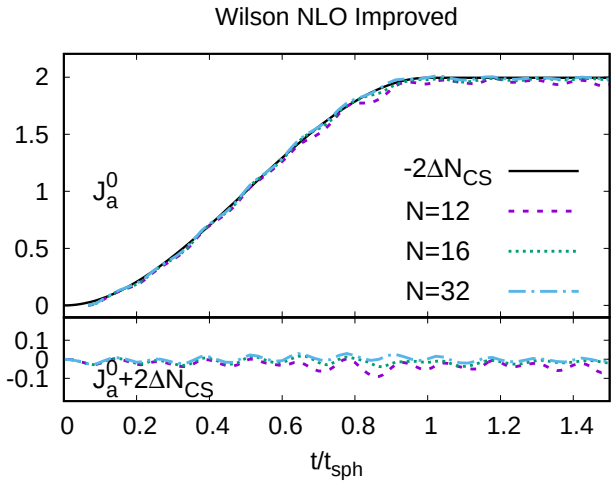

Figure B.2: A comparison of the net axial charge generated during a sphaleron transition using $mr_{\rm sph} = 1.9{\cdot}10^{-2}$ improved Wilson (NLO) fermions for different lattice volumes. Top: At N=16 and beyond the net axial charge tracks ΔN_{CS} due to the sphaleron transition. Bottom: Deviations from Eq.(5.40) are shown. Figure taken from [187].

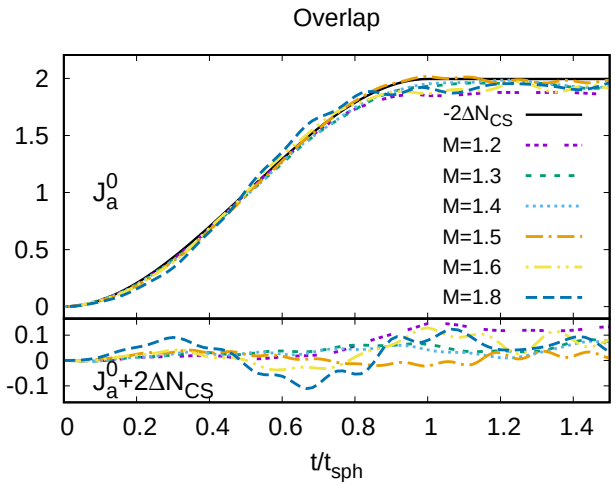

Figure B.3: A comparison of the net axial charge generated during a sphaleron transition using massless overlap fermions for different domain wall heights M at a fixed lattice volume $N = 16$. Top: For $M \in [1.4, 1.6)$, the net axial charge tracks ΔN_{CS} due to the sphaleron transition. Bottom: Deviations from Eq.(5.40) are shown. Figure taken from [187].

Our aim is to utilize the Dirac equation $-i\not{D}_{ov}\psi = 0$ to evolve the overlap fermions, defined on a fixed time slice, forward in time,

$$-i\not{D}_{ov}\psi \quad = \quad M\Big[\mathbf{1} + \frac{-i\not{D}_W(M)}{\sqrt{\gamma_5(-i\not{D}_W(M))\gamma_5(-i\not{D}_W(M))}}\Big]\psi \tag{B.16}$$

In agreement with our procedure for Wilson fermions, we utilize axial-temporal gauge and we assume the time direction to be contiuous in principle. In practice we use a very fine temporal 'lattice' spacing along temporal, finer than the other relevant scales in the operator, such that $a_t \ll M, a_s$. In this case the overlap operator is

$$-i\not{D}_{ov} = M\Big[\mathbf{1} + \frac{-i\not{D}^s_W - ia_t\not{\partial}_t - M}{\sqrt{\not{D}^s_W \not{D}^{s\dagger}_W + a_t^2\partial_t^2 + M^2}}\Big]\,. \tag{B.17}$$

Since a_t is very small, we can proceed by expanding in this quantity, keeping only terms which are leading order in a_t. Thus we get for Eq.(B.17)

$$M\Big[\mathbf{1} + \frac{-i\not{D}^s_W - M}{\sqrt{\not{D}^s_W \not{D}^{s\dagger}_W + M^2}} + \frac{-ia_t\not{\partial}_t}{\sqrt{\not{D}^s_W \not{D}^{s\dagger}_W + M^2}}\Big]\,. \tag{B.18}$$

The domain well height, which is in the denominator of the second term of Eq.(B.18) scales as $1/a_s$, whereas the spatial Wilson-Dirac operator scales as linear power in a_s. Therefore the overlap operator in Eq.(B.18) simply reduces to

$$-i\not{D}_{ov} = -ia_t\not{\partial}_t + M\Big[\mathbf{1} + \frac{-i\not{D}^s_W - M}{\sqrt{\not{D}^s_W \not{D}^{s\dagger}_W + M^2}}\Big] \tag{B.19}$$

This expression allows to express the overlap Dirac equation in very appealing for suitable for evolution in time. We can rewrite Eq.(B.16) to give

$$i\gamma^0\partial_t\psi = -i\not{D}^s_{ov}\psi \tag{B.20}$$

where $-i\not{D}^s_{ov}$ is the spatial overlap operator given by

$$-i\not{D}^s_{ov} \quad = \quad M\Big[\mathbf{1} + \frac{-i\not{D}^s_W(M)}{\sqrt{\gamma_5(-i\not{D}^s_W(M))\gamma_5(-i\not{D}^s_W(M))}}\Big]. \tag{B.21}$$

Eq.(B.20) is the analogue of the corresponding evolution equation with Wilson fermion discretization discussed in the main text. Using the γ_5 and γ_0 hermiticity of $-i\not{D}^s_W$, we can recast Eq.(B.20) as a Hamiltonian equation with the overlap Hamiltonian in 3D Minkowski space for massless fermions defined as,

$$H_{ov} = -i\gamma_0\not{D}^s_{ov} \quad = \quad M\Big(\gamma^0 + \frac{H_W(M)}{\sqrt{H_W(M)^2}}\Big), \tag{B.22}$$

where H_W is the Wilson Hamiltonian defined in Eq.(5.1) but with $C_n = 0$ for $n \geq 2$ and the mass m being replaced by the negative of the domain wall height M.

The numerical procedures treating the framework outlined here and in section 2.2 is quite involved. The implementation of overlap fermions however is by now a standard procedure. In the rest of this section we outline some of the details of an explicit implementation. For all practical purposes we have used algorithms and codes developed by the Bielefeld-BNL collaboration. We note that the details of this numerical implementation have been worked out by others. In our simulations we have made use of these advanced developments. The overlap Hamiltonian consists of a matrix sign function of $H_W(M)$, defined in Eq.(5.20). The inverse square root of $H_W(M)^2$ might be expressed as a Zolotarev rational function [235–238],

$$\frac{1}{\sqrt{H_W(M)^2}} = \sum_{l=1}^{N_\mathcal{O}} \frac{b_l}{d_l + H_W(M)^2}. \tag{B.23}$$

To compute Eq.(B.23), the coefficients b_l and d_l have to be determined from the smallest and largest eigenvalues of $H_W(M)^2$ [237]. Subsequently we employ a multi-shift conjugate gradient solver to calculate the inverse of $d_l + H_W(M)^2$. The lowest and the highest eigenvalues of $H_W(M)^2$ are found using the Kalkreuter-Simma Ritz algorithm [239] with 20 restarts and a convergence criterion of 10^{-20}. Using $N_\mathcal{O} = 20$ terms in the Zolotarev polynomial results in an error of $|\mathrm{sign}(H_W)^2 - \mathbf{1}| < 10^{-9}$. Our results here do dependent on the choice of the domain wall height M and thus we have chosen M such that we obtain the best approximation to the sign function as well as the Ginsparg-Wilson relation. For the sphaleron configuration we studied in this work the optimal choice was $M \in [1.4, 1.6)$ (see App. B.2 for more details).

For the multi-shift conjugate gradient solver, the quality of convergence is judged by the smallest d_l, and the convergence criterion is set to $|H_W(M)^2| - 1 < 10^{-16}$. For all studies presented in this work we have made sure that the conjugate gradient algorithm reaches the convergence criterion with less than 2000 steps. An important crosscheck of our method is whether the resultant overlap Dirac operator satisfies the Ginsparg-Wilson relation, which we have found to be satisfied to a precision of $\mathcal{O}(10^{-9})$.

Appendix C

Details of the World-line construction

This part of the appendix is based on the publication "The chiral anomaly, Berry's phase and chiral kinetic theory, from world-lines in quantum field theory" (N.M., R. Venugopalan), arXiv:1701.03331 (submitted to Physical Review Letters) [245] and "World-line construction of a covariant chiral kinetic theory" (N.M., R. Venugopalan), arXiv:1702.01233 (submitted to Physical Review D) [246].

C.1 Details of the calculation of the imaginary part of the effective action

In this Appendix, as promised, we will show that the second term in the world-line insertion, does not contribute to the non-conservation of the axial vector current. Writing out the relevant expression,

$$
\begin{aligned}
&\partial_\mu \mathrm{Tr}\left(\Gamma_7 \frac{\delta\Lambda^{(2)}}{\delta B_\mu(y)} e^{-\frac{\mathcal{E}}{2}T\tilde{\Sigma}^2}\right) = -\int\left(\prod_{l=0}^{N} d^4x^l d^3\theta^l d^3\bar{\theta}^l\right)\left(\prod_{l=1}^{N}\frac{d^4p^l}{(2\pi)^2}\right)\\
&\langle\theta^0|[\Gamma_\mu,\Gamma_\nu]\Gamma_5\Gamma_6|\theta^N\rangle\Big[\left(\frac{\partial^2}{\partial y_\mu \partial x^0_\mu}\delta(x^0-y)\right)\delta(x^0-x^N) + 2\left(\frac{\partial}{\partial x_\nu}\delta(x^0-x^N)\right)\left(\frac{\partial}{\partial y_\mu}\delta(\bar{x}^0-y)\right)\Big]\\
&\exp\Big\{-\Delta\sum_{k=1}^{N}\Big[-ip^k_\alpha\frac{(x^k_\alpha-x^{k-1}_\alpha)}{\Delta} + \frac{\mathcal{E}}{2}\left(p^k_\alpha - A_\alpha(\bar{x}^k)\right)^2 - \frac{(\theta^k_r-\theta^{k-1}_r)}{\Delta}\bar{\theta}^k_r + \frac{i\mathcal{E}}{2}\psi^k_\alpha\psi^{k-1}_\beta F_{\alpha\beta}(\bar{x}^k)\Big]\Big\}\\
&= -\int\left(\prod_{l=0}^{N-1} d^4x^l\right)\left(\prod_{l=0}^{N} d^3\theta^l d^3\bar{\theta}^l\right)\left(\prod_{l=1}^{N}\frac{d^4p^l}{(2\pi)^2}\right)\langle\theta^0|[\Gamma_\mu,\Gamma_\nu]\Gamma_5\Gamma_6|\theta^N\rangle\Big[-\frac{\partial^2}{\partial x^0_\mu\partial x^0_\nu}\Big]\\
&\times\exp\Big\{-\Delta\sum_{k=1}^{N}\Big[-ip^k_\alpha\frac{(x^k_\alpha-x^{k-1}_\alpha)}{\Delta} + \frac{\mathcal{E}}{2}\left(p^k_\alpha - A_\alpha(\bar{x}^k)\right)^2 - \frac{(\theta^k_r-\theta^{k-1}_r)}{\Delta}\bar{\theta}^k_r + \frac{i\mathcal{E}}{2}\psi^k_\alpha\psi^{k-1}_\beta F_{\alpha\beta}(\bar{x}^k)\Big]\Big\}
\end{aligned}
\tag{C.1}
$$

In the final expression above, we observe that while the expression containing the commutator of Gamma matrices is anti-symmetric under the exchange of μ

and ν, the derivative of the exponent is clearly symmetric under this exchange. Therefore

$$\partial_\mu \mathrm{Tr}\left(\Gamma_7 \frac{\delta\Lambda^{(2)}}{\delta B_\mu(y)} e^{-\frac{\xi}{2}T\tilde{\Sigma}^2}\right) = 0\,, \tag{C.2}$$

which completes our proof of the statement following Eq.(6.40) in the main text of the paper.

C.2 Supersymmetry and gauge freedom of the relativistic spinning particle

The Lorentz-covariant formulation of the spinning particle action given by Eq.(6.75) posses two important symmetries respected by the world-line path integral. Firstly, the physical content of the theory is invariant under reparametrizations of the world line parameter τ,

$$\tau \to \tau' = f(\tau) \tag{C.3}$$

This gauge symmetry corresponds to the mass-shell constraint or "charge"

$$\mathcal{H} \equiv \frac{1}{2}\left(\pi_\mu \pi^\mu + m^2 + i\psi^\mu F_{\mu\nu}\psi^\nu\right)\,, \tag{C.4}$$

(with π^μ defined as in Eq.(6.78)) which upon quantization is a constraint on the physical states in the Hilbert space–equivalent to the Klein-Gordon equation. It is also closely connected to another invariance of the action in terms of proper time dependent quantum mechanical supersymmetric transformations. Assuming $\eta(\tau)$ to be an anti-commuting parameter, these supersymmetric transformations are

$$\begin{aligned}
&\psi_\mu \to \psi_\mu + \frac{\dot{x}_\mu}{\sqrt{-\dot{x}^2}}\,\eta\,,\\
&\psi_5 \to \psi_5 + \eta\,,\\
&x_\mu \to x_\mu + i\frac{\psi_\mu \eta}{m}\,.
\end{aligned} \tag{C.5}$$

These transformations correspond to the supersymmetric charge,

$$\mathcal{Q} \equiv \pi_\mu \psi^\mu + m\psi_5\,. \tag{C.6}$$

This charge, along with the constraints Eq.(C.4) and Eq.(C.6), generates an $N = 1$ SUSY algebra,

$$\{\mathcal{Q}, \mathcal{Q}\} = -2i\,\mathcal{H}. \tag{C.7}$$

In generating this algebra, one employs the fundamental Possion brackets:

$$\{x^\mu, p_\nu\} = \delta^\mu_{\ \nu}\,, \tag{C.8}$$
$$\{\psi^\mu, \psi_\nu\} = -i\delta^\mu_{\ \nu}\,, \tag{C.9}$$
$$\{\psi_5, \psi_5\} = -i\,, \tag{C.10}$$
$$\{\psi^\mu, \psi_5\} = 0\,. \tag{C.11}$$

We refer the reader to [269, 284] for more details on the use of SUSY models in the context of path integrals and index theorems, as they are used, most prominently, in gravity. A discussion of a covariant of a covariant fixing of the gauge freedom (reparamentrization invariance under $\tau \to \tau'$) in terms of a BRST construction can be found in [284] and gives a nice illustration of the structure of the world-line path integral. These techniques will be particularly helpful in implementing the phase space constraints satisfied by the relativistic dynamics of spinning and colored particles.

C.3 Internal Symmetries

Internal symmetries, such as color, can be represented via Grassmaniann path integrals in the same manner as we have done for the spin degrees of freedom. These were discussed in [273–277] and their path integral formulation was worked out in [280, 281]. The essential elements are anti-commuting color degrees of freedom that combine to give the color charges, which in classical representations satisfy the Wong equations [272]. It was shown in [280, 281] that path ordered exponentials of the form

$$\mathrm{tr}\,\mathcal{P}e^{-\int_0^T d\tau\,\mathcal{L}(\tau)}\,, \tag{C.12}$$

where $\mathcal{L}(\tau)$ is a $N \times N$ Hermitian traceless matrix, can be written as

$$\int \mathcal{D}\lambda^\dagger \mathcal{D}\lambda\, \mathcal{J}(\lambda^\dagger\lambda)\, \exp\left\{-\int_0^T d\tau\, \left(\frac{\dot{x}^2}{2\mathcal{E}} + \frac{1}{2}\psi_a\dot{\psi}_a + \lambda^\dagger\dot{\lambda} - \lambda^\dagger\mathcal{L}_{\rm int}\lambda\right)\right\}, \tag{C.13}$$

where $\mathcal{L}_{\rm int}$ is the interaction part of the Lagrangian and

$$\mathcal{J}(\lambda^\dagger\lambda) = (\frac{\pi}{T})^N \sum_\phi \exp[i\phi(\lambda^\dagger\lambda + N/2 - 1)]\,. \tag{C.14}$$

If the matrix structure of $\mathcal{L}$ is that of fermions in the fundamental representation of $SU(N_c)$, then simply $N = N_c$. In a similar fashion, an insertion ω into the trace gives

$$\mathrm{tr}\mathcal{P}\,\omega\, e^{-\int_0^T d\tau\,\mathcal{L}(\tau)} = \int \mathcal{D}\lambda^\dagger\mathcal{D}\lambda\, \mathcal{J}(\lambda^\dagger\lambda)\,\{\lambda^\dagger\omega\lambda\}\, e^{-\int_0^T d\tau\,\left(\frac{\dot{x}^2}{2\mathcal{E}} + \frac{1}{2}\psi_a\dot{\psi}_a + \lambda^\dagger\dot{\lambda} - \lambda^\dagger\mathcal{L}_{\rm int}\lambda\right)}\,. \tag{C.15}$$

It can be shown that defining the world-line path integral for colored, albeit spinless, particles reproduces Wong's equations in the pseudo-classicial limit [261]. The equations of motion for spinning colored particles were already written down 40 years ago in [289].

C.4 Consistent vs. Covariant Anomalies

It has long been known that the definition of axial-vector currents is ambiguous in some cases, allowing for two anomaly types, termed consistent and covariant respectively. It was pointed out [285] that this difference arises when one derives the non-singlet anomaly either from the variation of an effective action (which yields the consistent anomaly) or from Fujikawa's method via variation of the measure (which gives the covariant anomaly). The first type was called the consistent anomaly, as it fullfils the Wess-Zumino consistency conditions thereby predicting the correct anomalous physics of effective hadronic theories. The second type is obtained from the first type by adding a local counterterm, which makes the non-singlet anomaly transform covariantly under group transformations.

For the singlet anomaly, and in QED, this issue is much simpler, as in this case one has manifestly gauge *invariant* expressions for both vector and axial-vector currents. Therefore the possibility that a current is not covariant never arises. However as was discussed by Bardeen [286], care has to be taken when deriving currents, when there are both non-zero vector- as well as axial-vector fields. In this case, there is an ambiguity whether the anomaly should be contained in the vector- or the axial-vector-currents (or even both). Physics dictates that the vector current is related to the baryon number and so it better be conserved. Hence by the introduction of local Bardeen-counterterms this physicality condition can be enforced. We note however that if there are no physical axial-vector gauge fields present, as it is in our case, this ambiguity does not exist. The vector current is conserved by construction and hence the only possible form of the anomaly is given by Eq.(6.73).

C.5 Saddle Point Expansion in the World Line framework and Gauge Invariance

We will discuss here two different appraoches to the fixing of the gauge symmetry determining $\mathcal{E}$. Our derivation is based on the fact that $\mathcal{E}$ is related to the reparametrization invariance of the proper time

$$\tau \to \tau' = f(\tau), \tag{C.16}$$

where f is an arbitrary continuous function. For the sake of simplicity, we will neglect here spin dependent pieces of our action and write down the world-line path integral for a scalar particle. We will then subsequently generalize the

discussion to particles with spin. The world-line path integral for the spinless case is

$$W_{\rm scalar} = \int_0^\infty \frac{dT}{T} \int \mathcal{D}x \ \exp\left(i \int_0^T d\tau \ \left[\frac{\dot{x}^2}{2\mathcal{E}} + \dot{x}_\mu A^\mu(x) - \frac{\mathcal{E}}{2} m^2 \right] \right)$$
$$= \int_0^\infty \frac{dT}{T} \int \mathcal{D}x \ \exp\left(i \int_0^1 du \ \left[\frac{(dx/du)^2}{2\mathcal{E}T} + \frac{dx_\mu}{du} A^\mu(x) - \frac{\mathcal{E}T}{2} m^2 \right] \right), \tag{C.17}$$

where in the second line we have replaced $u = \tau/T$. From Eq.(C.17) it is clear that T and $\mathcal{E}$ are not independent. Setting $\mathcal{E}$ to a constant value does not affect the result of the T integration. Therefore we can simply set $\mathcal{E} = 2$ and rescale $m^2 T \to T$. The path integral is then given as

$$W_{\rm scalar} = \int_0^\infty \frac{dT}{T} \int \mathcal{D}x \ \exp\left(i \int_0^1 du \ \left[m^2 \frac{(dx/du)^2}{4T} + \frac{dx_\mu}{du} A^\mu(x) - T \right] \right), \tag{C.18}$$

The T integration can now either be performed explicitly (see [385, 386]) or via the method of stationary phase around the expansion point

$$T_0 = \frac{m}{2} \left(- \int_0^1 du \ \left[\frac{dx_\mu}{du} \right]^2 \right)^{\frac{1}{2}} . \tag{C.19}$$

We obtain

$$W_{\rm scalar} \approx \sqrt{\frac{i\pi}{2m}} \int \mathcal{D}x \ \left(- \int_0^1 du \ \left[\frac{dx_\mu}{du} \right]^2 \right)^{-\frac{1}{4}}$$
$$\times \exp i \left\{ m \left(- \int_0^1 du \ \left[\frac{dx_\mu}{du} \right]^2 \right)^{\frac{1}{2}} + \int_0^1 du \ \frac{dx_\mu}{du} A^\mu(x) \right\} . \tag{C.20}$$

We now derive the equations of motion from requiring the invariance of this action under variation. The result is

$$\left(- \int_0^1 du \ \dot{x}^2 \right)^{-\frac{1}{2}} \ m \ddot{x}_\mu = \dot{x}_\nu F^{\mu\nu} . \tag{C.21}$$

We can write this, defining $z = \sqrt{-\dot{x}^2}$, as[1]

$$\frac{m \ddot{x}_\mu}{z} = \dot{x}_\nu F^{\mu\nu} . \tag{C.22}$$

[1] Multiplying this equation through by $\dot{x}^\mu$, one observes that $\dot{x}^2 =$ constant.

One can alternately start from the Lagrangian in Eq.(C.17). Instead of fixing $\mathcal{E}$ and leaving the T integral explicit, we can work with the single particle action

$$S = \int_0^T d\tau \left[\frac{\dot{x}^2}{2\mathcal{E}} + \dot{x}_\mu A^\mu(x) - \frac{\mathcal{E}}{2}m^2\right] \tag{C.23}$$

directly. Since $\mathcal{E}$ is kept explicit, there are two variations to perform – one for $\mathcal{E}$ and one with respect to x. Variation with respect to $\mathcal{E}$ gives

$$\frac{\dot{x}^2}{\mathcal{E}^2} - m^2 = 0\,. \tag{C.24}$$

Solving this equation for $\mathcal{E}$, one obtains the consistency relation

$$\mathcal{E} = \frac{\sqrt{-\dot{x}^2}}{m} = \frac{z}{m}\,. \tag{C.25}$$

Note that Eq.(C.25) does not fix the gauge, as z has yet to be determined. It rather is an equation that allows us to implement the constraint in the action directly. Plugging Eq.(C.25) into Eq.(C.23) eliminates the dependence on the einbein parameter and yields

$$S = \int_0^T d\tau \left[mz + \dot{x}_\mu A^\mu(x)\right], \tag{C.26}$$

from which the equations of motion follow directly. Not surprisingly, they coincide with Eq.(C.22). This derivation shows that Eq.(C.23) can be interpreted as a single-particle action, under the premise that all constraints are implemented correctly and the consistency condition Eq.(C.25) is fulfilled. The latter is satisfied if the einbein $\mathcal{E}$ is treated as a variational parameter. This equivalence generalizes easily to the case of spinning particles as discussed in the main text.

Appendix D

Details of the functional approaches

This part of the appendix contains details that are relevant to chapter 7, which is based on "Magnetic catalysis and inverse magnetic catalysis in QCD" (N.M. J. Pawlowski), published in Phys.Rev. D91 (2015) no.11, 116010 (arXiv:1502.08011) [295]. Below we discuss the truncation scheme that is employed in the Dyson-Schwinger approach in chapter 7 and we outline the emergence of magnetic catalysis and inverse catalysis from a four-fermion perspective.

D.1 Gluon Propagator and Quark Gluon vertex from Dyson Schwinger studies

Here we discuss the truncation scheme for the quark gap equation and the gluon propagator, based on [363, 369]. The quark gluon vertex is taken as $\Gamma^\mu = z_{qgq}\gamma^\mu$, with

$$z_{qgq}(Q^2) = \frac{d_1}{d_2 + Q^2} \tag{D.1}$$

$$+ \frac{Q^2}{\Lambda^2 + Q^2}\left(\frac{\beta_0 \alpha(\mu) \log Q^2/\Lambda^2 + 1}{4\pi}\right)^{2\delta}, \tag{D.2}$$

containing the parameters

$$d_1 = 7.9 \text{ GeV}^2 \qquad d_2 = 0.5 \text{ GeV}^2\,,$$

$$\delta = -18/88\,, \qquad \Lambda = 1.4 \text{ GeV}\,. \tag{D.3}$$

Here the scales must be identified correctly in order to capture the correct dependence with T and eB. We take Q to be the symmetric momentum $Q^2 = (q^2 + p^2 + (q-p)^2)/3$ at the vertex with $Q^2 = Q_3^2 + Q_0^2 + Q_\perp^2$, where

$Q_0^2 = (2\pi T)^2$ if $Q_0^2 < (2\pi T)^2$ and $Q_\perp^2 = 2|eB|$ if $Q_\perp^2 < 2|eB|$. We note that this roughly corresponds to an identification of scales as in section 7.3.1 with $\lambda_B \approx 1$, although the present vertex is clearly more sophisticated as it includes momentum dependencies and thereby generic eB effects. For a current overview of the quark gluon vertex in Dyson-Schwinger truncations see [387, 388]. Furthermore in order to be able to solve the gluon Dyson-Schwinger equation we rely on lattice input for the Yang-Mills part, which we then "dress" with magnetic field effects, as described above. The reliability of this truncation was already discussed in detail at finite temperature [363] and utilized in the presence of magnetic fields before [299]. The lattice fit is given by

$$Z_{\rm YM}^{-1}(Q^2) = \frac{Q^2\Lambda^2}{(Q^2+\Lambda^2)^2}\Big[\left(\frac{c}{Q^2+a\Lambda^2}\right)^b + \frac{Q^2}{\Lambda^2}\left(\frac{\beta_0\alpha(\mu)\log Q^2/\Lambda^2+1}{4\pi}\right)^\gamma\Big], \tag{D.4}$$

with

$$\Lambda = 1.4\ \text{GeV}\,, \quad c = 11.5\ \text{GeV}^2\,,$$
$$\beta_0 = 11N_c/3\,, \quad \gamma = -13/22\,, \tag{D.5}$$

where $\alpha(\mu) = 0.3$ and a and b are temperature dependent parameters, which can be found in [369]. As discussed before the Dyson-Schwinger truncation scheme can be related to the skeleton expansion done in our analytic estimate, which was motivated by renormalisation group invariance

$$4\pi\alpha_s(Q^2)r_{\rm IR}(Q^2)\frac{P_{\mu\nu}}{Q'^2+\Pi} \equiv \frac{P_{\mu\nu}}{Z_{\rm YM}Q'^2+\Pi_f}z_{qgq}\,, \tag{D.6}$$

where the sum over different polarisation tensor components is implied. The right hand side actually serves as the input to our numerical study, while the different components of Π are determined dynamically from solving the gluon Dyson-Schwinger equation.

D.2 Magnetic field dependence of the four-fermi coupling from QCD

As we have discussed in Section 7.3.2 the value of the NJL coupling λ at the intrinsic cutoff scale of the model is determined by QCD dynamics. At large scales the dynamics of λ is driven by the rightmost diagram shown in Fig. (7.11). Within simplifications we will motivate the functional dependence of this diagram on temperature and the magnetic field. In the lowest Landau level approximation the quarks are constraint to the t-z plane denoted by ($\|$),

whereas the gluons propagate in all four dimensions ($\parallel, \perp$). We write the gluon box diagram in Fig. (7.11) at zero external momentum as

$$F_{\alpha_s}(e\,B \geq 0.3\,\mathrm{GeV}) \simeq 4.5\,e\,B \int_0^\infty dq_\parallel \, \frac{q_\parallel}{q_\parallel^2 + m_q^2 + \alpha_s e B c_q} \times \int_0^\infty dq_\perp \, \frac{q_\perp}{[q_\perp^2 + q_\parallel^2 + m_A^2 + eB\alpha_s c_A]^2}\,, \tag{D.7}$$

where α_s is given as Eq.(7.12).

For $e\,B < 0.3$ (D.7) is smoothly (quadratic fit) extrapolated to $e\,B = 0$ with minimising the $e\,B$-dependence. The flavor, color and Dirac tensor indices have been contracted, and the comparison with the results for λ in quenched QCD shown in Fig. (7.13) shows that the prefactor resulting from the tensor contract is approximately 4.5. We have written the propagators in a semi-perturbative form with medium dependent mass terms. Further we have taken $m_A \approx 1$ GeV as the decoupling scale, $m_q \approx 300$ MeV in the chiral broken phase and $c_A = c_q = 1$. Strictly speaking both masses are larger than 1 GeV as we have to add the cutoff masses $\propto \Lambda^2$. We have chosen smaller masses in order to also potentially have access to the infrared domain $k \to 0$, where the constituent quark mass is of the order 0.3 GeV and the gluonic mass gap is of the order 1 GeV. Furthermore we have approximated the Matsubara sum by an integration, due to the small level spacing compared to the magnetic field. This approximation does not hold small eB, but (D.7) is only used for $e\,B \geq 0.3$ GeV. Eq.(D.7) includes the correct dependence on α_s as well and thus captures eB and T effects qualitatively. The model parameters in Section 7.3.2 allow us to reproduce the quantitative behavior of the chiral transition temperature and a more elaborate version of Eq.(D.7) does not give much greater insight. Apart from the agreement with the T_c results from lattice calculation, Fig. (7.13) shows that quantitatively reliable results from QCD-flows in quenched QCD [367] are reproduced.

Bibliography

[1] Frans R. Klinkhamer and N. S. Manton. A Saddle Point Solution in the Weinberg-Salam Theory. *Phys. Rev.*, D30:2212, 1984.

[2] Roger F. Dashen, Brosl Hasslacher, and Andre Neveu. Nonperturbative Methods and Extended Hadron Models in Field Theory. 3. Four-Dimensional Nonabelian Models. *Phys. Rev.*, D10:4138, 1974.

[3] V. Soni. POSSIBLE CLASSICAL SOLUTIONS IN THE WEINBERG-SALAM MODEL. *Phys. Lett.*, B93:101–106, 1980.

[4] J. Boguta. CAN NUCLEAR INTERACTIONS BE LONG RANGED? *Phys. Rev. Lett.*, 50:148–152, 1983.

[5] P. Forgacs and Z. Horvath. Topology and Saddle Points in Field Theories. *Phys. Lett.*, B138:397–401, 1984.

[6] Stephen L. Adler. Axial vector vertex in spinor electrodynamics. *Phys. Rev.*, 177:2426–2438, 1969.

[7] J. S. Bell and R. Jackiw. A PCAC puzzle: pi0 –¿ gamma gamma in the sigma model. *Nuovo Cim.*, A60:47–61, 1969.

[8] N. H. Christ. Conservation Law Violation at High-Energy by Anomalies. *Phys. Rev.*, D21:1591, 1980.

[9] A. D. Sakharov. Violation of CP Invariance, c Asymmetry, and Baryon Asymmetry of the Universe. *Pisma Zh. Eksp. Teor. Fiz.*, 5:32–35, 1967. [Usp. Fiz. Nauk161,61(1991)].

[10] Antonio Riotto and Mark Trodden. Recent progress in baryogenesis. *Ann. Rev. Nucl. Part. Sci.*, 49:35–75, 1999.

[11] Andrew G. Cohen, D. B. Kaplan, and A. E. Nelson. Progress in electroweak baryogenesis. *Ann. Rev. Nucl. Part. Sci.*, 43:27–70, 1993.

[12] V. A. Rubakov and M. E. Shaposhnikov. Electroweak baryon number nonconservation in the early universe and in high-energy collisions. *Usp. Fiz. Nauk*, 166:493–537, 1996. [Phys. Usp.39,461(1996)].

[13] M. Gradhand, D. V. Fedorov, F. Pientka, P. Zahn, I Mertig, and B. L. Gyorffy. *J. Phys. Condens. Matter*, 2012.

[14] Dmitri E. Kharzeev, Larry D. McLerran, and Harmen J. Warringa. The Effects of topological charge change in heavy ion collisions: 'Event by event P and CP violation'. *Nucl. Phys.*, A803:227–253, 2008.

[15] Kenji Fukushima, Dmitri E. Kharzeev, and Harmen J. Warringa. The Chiral Magnetic Effect. *Phys. Rev.*, D78:074033, 2008.

[16] D. E. Kharzeev, J. Liao, S. A. Voloshin, and G. Wang. Chiral magnetic and vortical effects in high-energy nuclear collisionsA status report. *Prog. Part. Nucl. Phys.*, 88:1–28, 2016.

[17] V. Skokov, A. Yu. Illarionov, and V. Toneev. Estimate of the magnetic field strength in heavy-ion collisions. *Int. J. Mod. Phys.*, A24:5925–5932, 2009.

[18] Wei-Tian Deng and Xu-Guang Huang. Event-by-event generation of electromagnetic fields in heavy-ion collisions. *Phys. Rev.*, C85:044907, 2012.

[19] Qiang Li, Dmitri E. Kharzeev, Cheng Zhang, Yuan Huang, I. Pletikosic, A. V. Fedorov, R. D. Zhong, J. A. Schneeloch, G. D. Gu, and T. Valla. Observation of the chiral magnetic effect in ZrTe5. *Nature Phys.*, 12:550–554, 2016.

[20] Vladimir Skokov, Paul Sorensen, Volker Koch, Soeren Schlichting, Jim Thomas, Sergei Voloshin, Gang Wang, and Ho-Ung Yee. Chiral Magnetic Effect Task Force Report. 2016.

[21] Soren Schlichting and Scott Pratt. Effects of Charge Conservation and Flow on Fluctuations of parity-odd Observables ar RHIC. 2010.

[22] Soren Schlichting and Scott Pratt. Charge conservation at energies available at the BNL Relativistic Heavy Ion Collider and contributions to local parity violation observables. *Phys. Rev.*, C83:014913, 2011.

[23] Scott Pratt, Soeren Schlichting, and Sean Gavin. Effects of Momentum Conservation and Flow on Angular Correlations at RHIC. *Phys. Rev.*, C84:024909, 2011.

[24] Adam Bzdak, Volker Koch, and Jinfeng Liao. Azimuthal correlations from transverse momentum conservation and possible local parity violation. *Phys. Rev.*, C83:014905, 2011.

[25] Yoshitaka Hatta, Akihiko Monnai, and Bo-Wen Xiao. Elliptic flow difference of charged pions in heavy-ion collisions. *Nucl. Phys.*, A947:155–160, 2016.

[26] Xu-Guang Huang, Yi Yin, and Jinfeng Liao. In search of chiral magnetic effect: separating flow-driven background effects and quantifying anomaly-induced charge separations. *Nucl. Phys.*, A956:661–664, 2016.

[27] Vardan Khachatryan et al. Observation of charge-dependent azimuthal correlations in pPb collisions and its implication for the search for the chiral magnetic effect. *Phys. Rev. Lett*, 2016. [Phys. Rev. Lett.118,122301(2017)].

[28] B. I. Abelev et al. Azimuthal Charged-Particle Correlations and Possible Local Strong Parity Violation. *Phys. Rev. Lett.*, 103:251601, 2009.

[29] Betty Abelev et al. Charge separation relative to the reaction plane in Pb-Pb collisions at $\sqrt{s_{NN}} = 2.76$ TeV. *Phys. Rev. Lett.*, 110(1):012301, 2013.

[30] L. Adamczyk et al. Observation of charge asymmetry dependence of pion elliptic flow and the possible chiral magnetic wave in heavy-ion collisions. *Phys. Rev. Lett.*, 114(25):252302, 2015.

[31] Gang Wang. Experimental Overview of the Search for Chiral Effects at RHIC. *J. Phys. Conf. Ser.*, 779(1):012013, 2017.

[32] Liwen Wen. Systematic Searches for the Chiral Magnetic Effect and the Chiral Vortical Effect Using Identi ed Particles at RHIC/STAR. *J. Phys. Conf. Ser.*, 779(1):012067, 2017.

[33] Larry D. McLerran and Raju Venugopalan. Computing quark and gluon distribution functions for very large nuclei. *Phys. Rev.*, D49:2233–2241, 1994.

[34] Larry D. McLerran and Raju Venugopalan. Gluon distribution functions for very large nuclei at small transverse momentum. *Phys. Rev.*, D49:3352–3355, 1994.

[35] Francois Gelis, Edmond Iancu, Jamal Jalilian-Marian, and Raju Venugopalan. The Color Glass Condensate. *Ann. Rev. Nucl. Part. Sci.*, 60:463–489, 2010.

[36] Paul Romatschke. Do nuclear collisions create a locally equilibrated quarkgluon plasma? *Eur. Phys. J.*, C77(1):21, 2017.

[37] Alex Krasnitz and Raju Venugopalan. Nonperturbative computation of gluon minijet production in nuclear collisions at very high-energies. *Nucl. Phys.*, B557:237, 1999.

[38] T. Lappi. Production of gluons in the classical field model for heavy ion collisions. *Phys. Rev.*, C67:054903, 2003.

[39] Bjoern Schenke, Prithwish Tribedy, and Raju Venugopalan. Event-by-event gluon multiplicity, energy density, and eccentricities in ultrarelativistic heavy-ion collisions. *Phys. Rev.*, C86:034908, 2012.

[40] Bjrn Schenke, Sren Schlichting, and Raju Venugopalan. Azimuthal anisotropies in p+Pb collisions from classical YangMills dynamics. *Phys. Lett.*, B747:76–82, 2015.

[41] J. Berges, K. Boguslavski, S. Schlichting, and R. Venugopalan. Turbulent thermalization process in heavy-ion collisions at ultrarelativistic energies. *Phys. Rev.*, D89(7):074011, 2014.

[42] Jurgen Berges, Soren Schlichting, and Denes Sexty. Over-populated gauge fields on the lattice. *Phys. Rev.*, D86:074006, 2012.

[43] Thomas Epelbaum and Francois Gelis. Pressure isotropization in high energy heavy ion collisions. *Phys. Rev. Lett.*, 111:232301, 2013.

[44] Aleksi Kurkela and Guy D. Moore. UV Cascade in Classical Yang-Mills Theory. *Phys. Rev.*, D86:056008, 2012.

[45] R. Baier, Alfred H. Mueller, D. Schiff, and D. T. Son. 'Bottom up' thermalization in heavy ion collisions. *Phys. Lett.*, B502:51–58, 2001.

[46] Juergen Berges, Kirill Boguslavski, Soeren Schlichting, and Raju Venugopalan. Universal attractor in a highly occupied non-Abelian plasma. *Phys. Rev.*, D89(11):114007, 2014.

[47] F. Gelis, K. Kajantie, and T. Lappi. Chemical thermalization in relativistic heavy ion collisions. *Phys. Rev. Lett.*, 96:032304, 2006.

[48] Florian Hebenstreit, Jrgen Berges, and Daniil Gelfand. Simulating fermion production in 1+1 dimensional QED. *Phys. Rev.*, D87(10):105006, 2013.

[49] Naoto Tanji. Electromagnetic currents induced by color fields. *Phys. Rev.*, D92(12):125012, 2015.

[50] Francois Gelis and Naoto Tanji. Schwinger mechanism revisited. *Prog. Part. Nucl. Phys.*, 87:1–49, 2016.

[51] D. Gelfand, F. Hebenstreit, and J. Berges. Early quark production and approach to chemical equilibrium. *Phys. Rev.*, D93(8):085001, 2016.

[52] Naoto Tanji, Niklas Mueller, and Jrgen Berges. Transient anomalous charge production in strong-field QCD. *Phys. Rev.*, D93(7):074507, 2016.

[53] Francois Gelis and Jamal Jalilian-Marian. Photon production in high-energy proton nucleus collisions. *Phys. Rev.*, D66:014021, 2002.

[54] Boris Z. Kopeliovich, Alexander V. Tarasov, and Andreas Schafer. Bremsstrahlung of a quark propagating through a nucleus. *Phys. Rev.*, C59:1609–1619, 1999.

[55] Jamal Jalilian-Marian. Production of forward rapidity photons in high energy heavy ion collisions. *Nucl. Phys.*, A753:307–315, 2005.

[56] Jamal Jalilian-Marian and Amir H. Rezaeian. Prompt photon production and photon-hadron correlations at RHIC and the LHC from the Color Glass Condensate. *Phys. Rev.*, D86:034016, 2012.

[57] Amir H. Rezaeian. Semi-inclusive photon-hadron production in pp and pA collisions at RHIC and LHC. *Phys. Rev.*, D86:094016, 2012.

[58] Sanjin Benic, Kenji Fukushima, Oscar Garcia-Montero, and Raju Venugopalan. Probing gluon saturation with next-to-leading order photon production at central rapidities in proton-nucleus collisions. *JHEP*, 01:115, 2017.

[59] Peter Brockway Arnold, Guy D. Moore, and Laurence G. Yaffe. Photon emission from quark gluon plasma: Complete leading order results. *JHEP*, 12:009, 2001.

[60] A. Adare et al. Trends in Yield and Azimuthal Shape Modification in Dihadron Correlations in Relativistic Heavy Ion Collisions. *Phys. Rev. Lett.*, 104:252301, 2010.

[61] Chun Shen. Electromagnetic Radiation from QCD Matter: Theory Overview. *Nucl. Phys.*, A956:184–191, 2016.

[62] Christian Klein-Bsing and Larry McLerran. Geometrical Scaling of Direct-Photon Production in Hadron Collisions from RHIC to the LHC. *Phys. Lett.*, B734:282–285, 2014.

[63] Yves Schutz and Urs Achim Wiedemann. Quark matter. Proceedings, 22nd International Conference on Ultra-Relativistic Nucleus-Nucleus Collisions, Quark Matter 2011, Annecy, France, May 23-28, 2011. *J. Phys.*, G38:120301, 2011.

[64] J Berges, O. Garcia-Montero, N. Mueller, and N. Tanji. *in progress.*

[65] Mattias Marklund and Joakim Lundin. Quantum Vacuum Experiments Using High Intensity Lasers. *Eur. Phys. J.*, D55:319–326, 2009.

[66] A. Di Piazza, C. Muller, K. Z. Hatsagortsyan, and C. H. Keitel. Extremely high-intensity laser interactions with fundamental quantum systems. *Rev. Mod. Phys.*, 84:1177, 2012.

[67] Fritz Sauter. Uber das Verhalten eines Elektrons im homogenen elektrischen Feld nach der relativistischen Theorie Diracs. *Z. Phys.*, 69:742–764, 1931.

[68] W. Heisenberg and H. Euler. Consequences of Dirac's theory of positrons. *Z. Phys.*, 98:714–732, 1936.

[69] Julian S. Schwinger. On gauge invariance and vacuum polarization. *Phys. Rev.*, 82:664–679, 1951.

[70] D. B. Blaschke, A. V. Prozorkevich, C. D. Roberts, S. M. Schmidt, and S. A. Smolyansky. Pair production and optical lasers. *Phys. Rev. Lett.*, 96:140402, 2006.

[71] Florian Hebenstreit, Reinhard Alkofer, Gerald V. Dunne, and Holger Gies. Momentum signatures for Schwinger pair production in short laser pulses with sub-cycle structure. *Phys. Rev. Lett.*, 102:150404, 2009.

[72] Thomas Heinzl, Anton Ilderton, and Mattias Marklund. Finite size effects in stimulated laser pair production. *Phys. Lett.*, B692:250–256, 2010.

[73] Christian Kohlfrst, Holger Gies, and Reinhard Alkofer. Effective mass signatures in multiphoton pair production. *Phys. Rev. Lett.*, 112:050402, 2014.

[74] Florian Hebenstreit and Franois Fillion-Gourdeau. Optimization of Schwinger pair production in colliding laser pulses. *Phys. Lett.*, B739:189–195, 2014.

[75] A. Otto, Daniel Seipt, David Blaschke, Burkhard Kmpfer, and S. A. Smolyansky. Lifting shell structures in the dynamically assisted Schwinger effect in periodic fields. *Phys. Lett.*, B740:335–340, 2015.

[76] Niklas Mueller, Florian Hebenstreit, and Jrgen Berges. Anomaly-induced dynamical refringence in strong-field QED. *Phys. Rev. Lett.*, 117(6):061601, 2016.

[77] James Charbonneau and Ariel Zhitnitsky. Topological Currents in Neutron Stars: Kicks, Precession, Toroidal Fields, and Magnetic Helicity. *JCAP*, 1008:010, 2010.

[78] Yukinao Akamatsu and Naoki Yamamoto. Chiral Plasma Instabilities. *Phys. Rev. Lett.*, 111:052002, 2013.

[79] Maxim Dvornikov and Victor B. Semikoz. Non-conservation of the neutrino current in a hot plasma of the early universe. 2016.

[80] David B. Kaplan, Sanjay Reddy, and Srimoyee Sen. Energy Conservation and the Chiral Magnetic Effect. 2016.

[81] Dorota Grabowska, David B. Kaplan, and Sanjay Reddy. Role of the electron mass in damping chiral plasma instability in Supernovae and neutron stars. *Phys. Rev.*, D91(8):085035, 2015.

[82] Er-dong Guo and Shu Lin. Quark mass effect on axial charge dynamics. *Phys. Rev.*, D93(10):105001, 2016.

[83] D. Banerjee, M. Dalmonte, M. Muller, E. Rico, P. Stebler, U. J. Wiese, and P. Zoller. Atomic Quantum Simulation of Dynamical Gauge Fields coupled to Fermionic Matter: From String Breaking to Evolution after a Quench. *Phys. Rev. Lett.*, 109:175302, 2012.

[84] Erez Zohar, J. Ignacio Cirac, and Benni Reznik. Quantum simulations of gauge theories with ultracold atoms: local gauge invariance from angular momentum conservation. *Phys. Rev.*, A88:023617, 2013.

[85] L. Tagliacozzo, A. Celi, A. Zamora, and M. Lewenstein. Optical Abelian Lattice Gauge Theories. *Annals Phys.*, 330:160–191, 2013.

[86] V. Kasper, F. Hebenstreit, M. Oberthaler, and J. Berges. Schwinger pair production with ultracold atoms. *Phys. Lett.*, B760:742–746, 2016.

[87] J. Schmiedmayer and J. Berges. Cold Atom Cosmology. *Science*, 341(6151):1188–1189, 2013.

[88] Larry D. McLerran. The Color glass condensate and small x physics: Four lectures. *Lect. Notes Phys.*, 583:291–334, 2002.

[89] Larry McLerran. RHIC physics: The Quark gluon plasma and the color glass condensate: Four lectures. 2003.

[90] Elliott D. Bloom et al. High-Energy Inelastic e p Scattering at 6-Degrees and 10-Degrees. *Phys. Rev. Lett.*, 23:930–934, 1969.

[91] Martin Breidenbach, Jerome I. Friedman, Henry W. Kendall, Elliott D. Bloom, D. H. Coward, H. C. DeStaebler, J. Drees, Luke W. Mo, and Richard E. Taylor. Observed Behavior of Highly Inelastic electron-Proton Scattering. *Phys. Rev. Lett.*, 23:935–939, 1969.

[92] Guido Altarelli and G. Parisi. Asymptotic Freedom in Parton Language. *Nucl. Phys.*, B126:298–318, 1977.

[93] Yuri L. Dokshitzer. Calculation of the Structure Functions for Deep Inelastic Scattering and e+ e- Annihilation by Perturbation Theory in Quantum Chromodynamics. *Sov. Phys. JETP*, 46:641–653, 1977. [Zh. Eksp. Teor. Fiz.73,1216(1977)].

[94] V. N. Gribov and L. N. Lipatov. Deep inelastic e p scattering in perturbation theory. *Sov. J. Nucl. Phys.*, 15:438–450, 1972. [Yad. Fiz.15,781(1972)].

[95] L. N. Lipatov. Reggeization of the Vector Meson and the Vacuum Singularity in Nonabelian Gauge Theories. *Sov. J. Nucl. Phys.*, 23:338–345, 1976. [Yad. Fiz.23,642(1976)].

[96] E. A. Kuraev, L. N. Lipatov, and Victor S. Fadin. Multi - Reggeon Processes in the Yang-Mills Theory. *Sov. Phys. JETP*, 44:443–450, 1976. [Zh. Eksp. Teor. Fiz.71,840(1976)].

[97] E. A. Kuraev, L. N. Lipatov, and Victor S. Fadin. The Pomeranchuk Singularity in Nonabelian Gauge Theories. *Sov. Phys. JETP*, 45:199–204, 1977. [Zh. Eksp. Teor. Fiz.72,377(1977)].

[98] J. Breitweg et. al. *Eur. Phys. J.*, 67:609, 1999.

[99] Raju Venugopalan. The Color glass condensate: An Overview. *Eur. Phys. J.*, C43:337–344, 2005.

[100] Jamal Jalilian-Marian, Alex Kovner, Andrei Leonidov, and Heribert Weigert. The BFKL equation from the Wilson renormalization group. *Nucl. Phys.*, B504:415–431, 1997.

[101] Jamal Jalilian-Marian, Alex Kovner, Andrei Leonidov, and Heribert Weigert. The Wilson renormalization group for low x physics: Towards the high density regime. *Phys. Rev.*, D59:014014, 1998.

[102] Alex Kovner, J. Guilherme Milhano, and Heribert Weigert. Relating different approaches to nonlinear QCD evolution at finite gluon density. *Phys. Rev.*, D62:114005, 2000.

[103] Jamal Jalilian-Marian, Alex Kovner, Larry D. McLerran, and Heribert Weigert. The Intrinsic glue distribution at very small x. *Phys. Rev.*, D55:5414–5428, 1997.

[104] Edmond Iancu, Andrei Leonidov, and Larry D. McLerran. Nonlinear gluon evolution in the color glass condensate. 1. *Nucl. Phys.*, A692:583–645, 2001.

[105] Edmond Iancu, Andrei Leonidov, and Larry D. McLerran. The Renormalization group equation for the color glass condensate. *Phys. Lett.*, B510:133–144, 2001.

[106] Elena Ferreiro, Edmond Iancu, Andrei Leonidov, and Larry McLerran. Nonlinear gluon evolution in the color glass condensate. 2. *Nucl. Phys.*, A703:489–538, 2002.

[107] Alex Kovner, Larry D. McLerran, and Heribert Weigert. Gluon production at high transverse momentum in the McLerran-Venugopalan model of nuclear structure functions. *Phys. Rev.*, D52:3809–3814, 1995.

[108] Alex Kovner, Larry D. McLerran, and Heribert Weigert. Gluon production from nonAbelian Weizsacker-Williams fields in nucleus-nucleus collisions. *Phys. Rev.*, D52:6231–6237, 1995.

[109] M. Gyulassy and Larry D. McLerran. Yang-Mills radiation in ultrarelativistic nuclear collisions. *Phys. Rev.*, C56:2219–2228, 1997.

[110] Kenji Fukushima, Francois Gelis, and Larry McLerran. Initial Singularity of the Little Bang. *Nucl. Phys.*, A786:107–130, 2007.

[111] Hirotsugu Fujii and Kazunori Itakura. Expanding color flux tubes and instabilities. *Nucl. Phys.*, A809:88–109, 2008.

[112] S. Mrowczynski. Plasma instability at the initial stage of ultrarelativistic heavy ion collisions. *Phys. Lett.*, B314:118–121, 1993.

[113] Peter Brockway Arnold, Jonathan Lenaghan, Guy D. Moore, and Laurence G. Yaffe. Apparent thermalization due to plasma instabilities in quark-gluon plasma. *Phys. Rev. Lett.*, 94:072302, 2005.

[114] Erich S. Weibel. Spontaneously Growing Transverse Waves in a Plasma Due to an Anisotropic Veloc ity Distribution. *Phys. Rev. Lett.*, 2:83–84, 1959.

[115] Jurgen Berges, Kirill Boguslavski, and Soren Schlichting. Nonlinear amplification of instabilities with longitudinal expansion. *Phys. Rev.*, D85:076005, 2012.

[116] Paul Romatschke and Raju Venugopalan. Collective non-Abelian instabilities in a melting color glass condensate. *Phys. Rev. Lett.*, 96:062302, 2006.

[117] Paul Romatschke and Raju Venugopalan. A Weibel instability in the melting color glass condensate. *Eur. Phys. J.*, A29:71–75, 2006.

[118] Paul Romatschke and Raju Venugopalan. The Unstable Glasma. *Phys. Rev.*, D74:045011, 2006.

[119] J. Berges, K. Boguslavski, S. Schlichting, and R. Venugopalan. Basin of attraction for turbulent thermalization and the range of validity of classical-statistical simulations. *JHEP*, 05:054, 2014.

[120] J. Berges, K. Boguslavski, S. Schlichting, and R. Venugopalan. Universality far from equilibrium: From superfluid Bose gases to heavy-ion collisions. *Phys. Rev. Lett.*, 114(6):061601, 2015.

[121] Liam Keegan, Aleksi Kurkela, Paul Romatschke, Wilke van der Schee, and Yan Zhu. Weak and strong coupling equilibration in nonabelian gauge theories. *JHEP*, 04:031, 2016.

[122] Kazuo Fujikawa. Path Integral Measure for Gauge Invariant Fermion Theories. *Phys. Rev. Lett.*, 42:1195–1198, 1979.

[123] Kazuo Fujikawa. Path Integral for Gauge Theories with Fermions. *Phys. Rev.*, D21:2848, 1980. [Erratum: Phys. Rev.D22,1499(1980)].

[124] Philip C. Nelson and Luis Alvarez-Gaume. Hamiltonian Interpretation of Anomalies. *Commun. Math. Phys.*, 99:103, 1985.

[125] M. Mace, S. Schlichting, and R. Venugopalan. Off-equilibrium sphaleron transitions in the Glasma. *Phys. Rev.*, D93(7):074036, 2016.

[126] Guy D. Moore and Marcus Tassler. The Sphaleron Rate in SU(N) Gauge Theory. *JHEP*, 02:105, 2011.

[127] B. I. Abelev et al. Observation of charge-dependent azimuthal correlations and possible local strong parity violation in heavy ion collisions. *Phys. Rev.*, C81:054908, 2010.

[128] Panos Christakoglou. Charge separation measurements in Pb-Pb collisions at LHC energies. *J. Phys. Conf. Ser.*, 381:012041, 2012.

[129] Adam Bzdak, Volker Koch, and Jinfeng Liao. Charge-Dependent Correlations in Relativistic Heavy Ion Collisions and the Chiral Magnetic Effect. *Lect. Notes Phys.*, 871:503–536, 2013.

[130] Adam Bzdak and Vladimir Skokov. Event-by-event fluctuations of magnetic and electric fields in heavy ion collisions. *Phys. Lett.*, B710:171–174, 2012.

[131] Xu-Guang Huang. Electromagnetic fields and anomalous transports in heavy-ion collisions — A pedagogical review. *Rept. Prog. Phys.*, 79(7):076302, 2016.

[132] John Bloczynski, Xu-Guang Huang, Xilin Zhang, and Jinfeng Liao. Azimuthally fluctuating magnetic field and its impacts on observables in heavy-ion collisions. *Phys. Lett.*, B718:1529–1535, 2013.

[133] G. Wang V. Skokov. Magnetic field in heavy ion collisions, physics insights from isobaric running, workshop on chirality, vorticity and magnetic field in heavy ion collisions. 2016.

[134] L. McLerran and V. Skokov. Comments About the Electromagnetic Field in Heavy-Ion Collisions. *Nucl. Phys.*, A929:184–190, 2014.

[135] B. G. Zakharov. Electromagnetic response of quarkgluon plasma in heavy-ion collisions. *Phys. Lett.*, B737:262–266, 2014.

[136] Kirill Tuchin. Electromagnetic field and the chiral magnetic effect in the quark-gluon plasma. *Phys. Rev.*, C91(6):064902, 2015.

[137] Umut Gursoy, Dmitri Kharzeev, and Krishna Rajagopal. Magnetohydrodynamics, charged currents and directed flow in heavy ion collisions. *Phys. Rev.*, C89(5):054905, 2014.

[138] H. T. Ding, A. Francis, O. Kaczmarek, F. Karsch, E. Laermann, and W. Soeldner. Thermal dilepton rate and electrical conductivity: An analysis of vector current correlation functions in quenched lattice QCD. *Phys. Rev.*, D83:034504, 2011.

[139] Alessandro Amato, Gert Aarts, Chris Allton, Pietro Giudice, Simon Hands, and Jon-Ivar Skullerud. Electrical conductivity of the quark-gluon plasma across the deconfinement transition. *Phys. Rev. Lett.*, 111(17):172001, 2013.

[140] Gert Aarts, Chris Allton, Alessandro Amato, Pietro Giudice, Simon Hands, and Jon-Ivar Skullerud. Electrical conductivity and charge diffusion in thermal QCD from the lattice. *JHEP*, 02:186, 2015.

[141] Michael V. Berry. Quantal phase factors accompanying adiabatic changes. *Proc. Roy. Soc. Lond.*, A392:45–57, 1984.

[142] Dam Thanh Son and Naoki Yamamoto. Berry Curvature, Triangle Anomalies, and the Chiral Magnetic Effect in Fermi Liquids. *Phys. Rev. Lett.*, 109:181602, 2012.

[143] M. A. Stephanov and Y. Yin. Chiral Kinetic Theory. *Phys. Rev. Lett.*, 109:162001, 2012.

[144] Dam Thanh Son and Naoki Yamamoto. Kinetic theory with Berry curvature from quantum field theories. *Phys. Rev.*, D87(8):085016, 2013.

[145] Jiunn-Wei Chen, Jin-yi Pang, Shi Pu, and Qun Wang. Kinetic equations for massive Dirac fermions in electromagnetic field with non-Abelian Berry phase. *Phys. Rev.*, D89(9):094003, 2014.

[146] Jing-Yuan Chen, Dam T. Son, Mikhail A. Stephanov, Ho-Ung Yee, and Yi Yin. Lorentz Invariance in Chiral Kinetic Theory. *Phys. Rev. Lett.*, 113(18):182302, 2014.

[147] Michael Stone and Vatsal Dwivedi. Classical version of the non-Abelian gauge anomaly. *Phys. Rev.*, D88(4):045012, 2013.

[148] Vatsal Dwivedi and Michael Stone. Classical chiral kinetic theory and anomalies in even space-time dimensions. *J. Phys.*, A47:025401, 2013.

[149] Cristina Manuel and Juan M. Torres-Rincon. Chiral transport equation from the quantum Dirac Hamiltonian and the on-shell effective field theory. *Phys. Rev.*, D90(7):076007, 2014.

[150] Michael Stone, Vatsal Dwivedi, and Tianci Zhou. Berry Phase, Lorentz Covariance, and Anomalous Velocity for Dirac and Weyl Particles. *Phys. Rev.*, D91(2):025004, 2015.

[151] Cristina Manuel and Juan M. Torres-Rincon. Dynamical evolution of the chiral magnetic effect: Applications to the quark-gluon plasma. *Phys. Rev.*, D92(7):074018, 2015.

[152] Jing-Yuan Chen, Dam T. Son, and Mikhail A. Stephanov. Collisions in Chiral Kinetic Theory. *Phys. Rev. Lett.*, 115(2):021601, 2015.

[153] Yifeng Sun, Che Ming Ko, and Feng Li. Anomalous transport model study of chiral magnetic effects in heavy ion collisions. *Phys. Rev.*, C94(4):045204, 2016.

[154] Yoshimasa Hidaka, Shi Pu, and Di-Lun Yang. Relativistic Chiral Kinetic Theory from Quantum Field Theories. 2016.

[155] Dam T. Son and Piotr Surowka. Hydrodynamics with Triangle Anomalies. *Phys. Rev. Lett.*, 103:191601, 2009.

[156] A. V. Sadofyev and M. V. Isachenkov. The Chiral magnetic effect in hydrodynamical approach. *Phys. Lett.*, B697:404–406, 2011.

[157] Masaru Hongo, Yuji Hirono, and Tetsufumi Hirano. First Numerical Simulations of Anomalous Hydrodynamics. 2013.

[158] Yuji Hirono, Tetsufumi Hirano, and Dmitri E. Kharzeev. The chiral magnetic effect in heavy-ion collisions from event-by-event anomalous hydrodynamics. 2014.

[159] Yi Yin and Jinfeng Liao. Hydrodynamics with chiral anomaly and charge separation in relativistic heavy ion collisions. *Phys. Lett.*, B756:42–46, 2016.

[160] L. V. Keldysh. Diagram technique for nonequilibrium processes. *Zh. Eksp. Teor. Fiz.*, 47:1515–1527, 1964. [Sov. Phys. JETP20,1018(1965)].

[161] Julian S. Schwinger. Brownian motion of a quantum oscillator. *J. Math. Phys.*, 2:407–432, 1961.

[162] Gordon Baym and Leo P. Kadanoff. Conservation Laws and Correlation Functions. *Phys. Rev.*, 124:287–299, 1961.

[163] R. P. Feynman and F. L. Vernon, Jr. The Theory of a general quantum system interacting with a linear dissipative system. *Annals Phys.*, 24:118–173, 1963. [Annals Phys.281,547(2000)].

[164] Juergen Berges. Introduction to nonequilibrium quantum field theory. *AIP Conf. Proc.*, 739:3–62, 2005. [,3(2004)].

[165] Jurgen Berges. Nonequilibrium Quantum Fields: From Cold Atoms to Cosmology. 2015.

[166] A. Kamenev. Field Theory of Non-Equilibrium Systems. *Cambridge University Press 2011.*

[167] Esteban A. Calzetta and Bei-Lok B. Hu. *Nonequilibrium Quantum Field Theory.* Cambridge University Press, 2008.

[168] Kenneth G. Wilson. The Renormalization Group and Strong Interactions. *Phys. Rev.*, D3:1818, 1971.

[169] Christof Wetterich. Exact evolution equation for the effective potential. *Phys. Lett.*, B301:90–94, 1993.

[170] M. Reuter and C. Wetterich. Effective average action for gauge theories and exact evolution equations. *Nucl. Phys.*, B417:181–214, 1994.

[171] Jan M. Pawlowski. Aspects of the functional renormalisation group. *Annals Phys.*, 322:2831–2915, 2007.

[172] Kenneth G. Wilson. Confinement of Quarks. *Phys. Rev.*, D10:2445–2459, 1974. [,45(1974)].

[173] H. J. Rothe. Lattice gauge theories: An Introduction. *World Sci. Lect. Notes Phys.*, 43:1–381, 1992. [World Sci. Lect. Notes Phys.82,1(2012)].

[174] I. Montvay and G. Munster. *Quantum fields on a lattice*. Cambridge University Press, 1997.

[175] Christof Gattringer and Christian B. Lang. Quantum chromodynamics on the lattice. *Lect. Notes Phys.*, 788:1–343, 2010.

[176] John B. Kogut and Leonard Susskind. Hamiltonian Formulation of Wilson's Lattice Gauge Theories. *Phys. Rev.*, D11:395–408, 1975.

[177] S. Coleman. *Aspects of Symmetries*.

[178] Guy D. Moore. Improved Hamiltonian for Minkowski Yang-Mills theory. *Nucl. Phys.*, B480:689–728, 1996.

[179] Luuk H. Karsten and Jan Smit. Lattice Fermions: Species Doubling, Chiral Invariance, and the Triangle Anomaly. *Nucl. Phys.*, B183:103, 1981. [,495(1980)].

[180] Holger Bech Nielsen and M. Ninomiya. Absence of Neutrinos on a Lattice. 1. Proof by Homotopy Theory. *Nucl. Phys.*, B185:20, 1981. [,533(1980)].

[181] D. Friedan. A PROOF OF THE NIELSEN-NINOMIYA THEOREM. *Commun. Math. Phys.*, 85:481–490, 1982.

[182] T. Reisz and H. J. Rothe. Chiral symmetry restoration and axial vector renormalization for Wilson fermions. *Phys. Rev.*, D62:014504, 2000.

[183] Rajamani Narayanan and Herbert Neuberger. Chiral fermions on the lattice. *Phys. Rev. Lett.*, 71(20):3251, 1993.

[184] Rajamani Narayanan and Herbert Neuberger. A Construction of lattice chiral gauge theories. *Nucl. Phys.*, B443:305–385, 1995.

[185] Herbert Neuberger. Exactly massless quarks on the lattice. *Phys. Lett.*, B417:141–144, 1998.

[186] Michael Creutz, Ivan Horvath, and Herbert Neuberger. A New fermion Hamiltonian for lattice gauge theory. *Nucl. Phys. Proc. Suppl.*, 106:760–762, 2002.

[187] Mark Mace, Niklas Mueller, Sren Schlichting, and Sayantan Sharma. Non-equilibrium study of the Chiral Magnetic Effect from real-time simulations with dynamical fermions. *Phys. Rev.*, D95(3):036023, 2017.

[188] David B. Kaplan. A Method for simulating chiral fermions on the lattice. *Phys. Lett.*, B288:342–347, 1992.

[189] R. Narayanan. Tata lectures on overlap fermions. 2011.

[190] Paul H. Ginsparg and Kenneth G. Wilson. A Remnant of Chiral Symmetry on the Lattice. *Phys. Rev.*, D25:2649, 1982.

[191] R. V. Gavai and Sayantan Sharma. Exact chiral invariance at finite density on the lattice. *Phys. Lett.*, B716:446–449, 2012.

[192] R. Narayanan and Sayantan Sharma. Introduction of the chemical potential in the overlap formalism. *JHEP*, 10:151, 2011.

[193] Gert Aarts and Jan Smit. Real time dynamics with fermions on a lattice. *Nucl. Phys.*, B555:355–394, 1999.

[194] J. Berges, D. Gelfand, and J. Pruschke. Quantum theory of fermion production after inflation. *Phys. Rev. Lett.*, 107:061301, 2011.

[195] Paul M. Saffin and Anders Tranberg. Real-time Fermions for Baryogenesis Simulations. *JHEP*, 07:066, 2011.

[196] Valentin Kasper, Florian Hebenstreit, and Jrgen Berges. Fermion production from real-time lattice gauge theory in the classical-statistical regime. *Phys. Rev.*, D90(2):025016, 2014.

[197] P. V. Buividovich and M. V. Ulybyshev. Numerical study of chiral plasma instability within the classical statistical field theory approach. *Phys. Rev.*, D94(2):025009, 2016.

[198] Gerard A. Mourou, Toshiki Tajima, and Sergei V. Bulanov. Optics in the relativistic regime. *Rev. Mod. Phys.*, 78:309–371, 2006.

[199] A. Ringwald. Fundamental physics at an x-ray free electron laser. In *Electromagnetic probes of fundamental physics. Proceedings, Workshop, Erice, Italy, October 16-21, 2001*, pages 63–74, 2001.

[200] Extreme Light Infrastructure `https://eli-laser.eu/`.

[201] James J. Klein and B. P. Nigam. Dichroism of the Vacuum. *Phys. Rev.*, 136:B1540–B1542, 1964.

[202] Thomas Heinzl, Ben Liesfeld, Kay-Uwe Amthor, Heinrich Schwoerer, Roland Sauerbrey, and Andreas Wipf. On the observation of vacuum birefringence. *Opt. Commun.*, 267:318–321, 2006.

[203] Kenji Fukushima, Dmitri E. Kharzeev, and Harmen J. Warringa. Real-time dynamics of the Chiral Magnetic Effect. *Phys. Rev. Lett.*, 104:212001, 2010.

[204] M. H. Al-Hashimi and U. J. Wiese. Discrete Accidental Symmetry for a Particle in a Constant Magnetic Field on a Torus. *Annals Phys.*, 324:343–360, 2009.

[205] G. S. Bali, F. Bruckmann, G. Endrodi, Z. Fodor, S. D. Katz, S. Krieg, A. Schafer, and K. K. Szabo. The QCD phase diagram for external magnetic fields. *JHEP*, 02:044, 2012.

[206] J. K. Daugherty and I. Lerche. Theory of Pair Production in Strong Electric and Magnetic Fields and Its Applicability to Pulsars. *Phys. Rev.*, D14:340–355, 1976.

[207] Sang Pyo Kim and Don N. Page. Schwinger pair production in electric and magnetic fields. *Phys. Rev.*, D73:065020, 2006.

[208] Naoto Tanji. Dynamical view of pair creation in uniform electric and magnetic fields. *Annals Phys.*, 324:1691–1736, 2009.

[209] Harmen J. Warringa. Dynamics of the Chiral Magnetic Effect in a weak magnetic field. *Phys. Rev.*, D86:085029, 2012.

[210] Y. Kluger, J. M. Eisenberg, B. Svetitsky, F. Cooper, and E. Mottola. Fermion pair production in a strong electric field. *Phys. Rev.*, D45:4659–4671, 1992.

[211] Heinz J. Rothe and Neda Sadooghi. A New look at the axial anomaly in lattice QED with Wilson fermions. *Phys. Rev.*, D58:074502, 1998.

[212] Paul M. Saffin and Anders Tranberg. Dynamical simulations of electroweak baryogenesis with fermions. *JHEP*, 02:102, 2012.

[213] G. Sansone et al. Isolated Single-Cycle Attosecond Pulses. *Science*, 314:443, 2006.

[214] Jun Xiong, Satya K. Kushwaha, Tian Liang, Jason W. Krizan, Wudi Wang, R. J. Cava, and N. P. Ong. Signature of the chiral anomaly in a Dirac semimetal: a current plume steered by a magnetic field. In *APS March Meeting 2015 San Antonio, Texas, March 2-6, 2015*, 2015.

[215] D. Kharzeev, A. Krasnitz, and R. Venugopalan. Anomalous chirality fluctuations in the initial stage of heavy ion collisions and parity odd bubbles. *Phys. Lett.*, B545:298–306, 2002.

[216] Jurgen Berges, Sebastian Scheffler, Soren Schlichting, and Denes Sexty. Out of equilibrium dynamics of coherent non-abelian gauge fields. *Phys. Rev.*, D85:034507, 2012.

[217] T. Lappi and L. McLerran. Some features of the glasma. *Nucl. Phys.*, A772:200–212, 2006.

[218] G. Z. Baseian, Sergei G. Matinyan, and G. K. Savvidy. NONLINEAR PLANE WAVES IN MASSLESS YANG-MILLS THEORY. (IN RUSSIAN). *Pisma Zh. Eksp. Teor. Fiz.*, 29:641–644, 1979.

[219] Sergei G. Matinyan, G. K. Savvidy, and N. G. Ter-Arutunian Savvidy. CLASSICAL YANG-MILLS MECHANICS. NONLINEAR COLOR OSCILLATIONS. *Sov. Phys. JETP*, 53:421–425, 1981. [Zh. Eksp. Teor. Fiz.80,830(1981)].

[220] T. S. Biro, Sergei G. Matinyan, and Berndt Muller. Chaos driven by soft - hard mode coupling in thermal Yang-Mills theory. *Phys. Lett.*, B362:29–33, 1995.

[221] Thomas N. Tudron. Instability of Constant Yang-Mills Fields Generated by Constant Gauge Potentials. *Phys. Rev.*, D22:2566, 1980.

[222] M. Abramowitz and I. Stegun. Handbook of Mathematical Functions. *Dover Publications*, 1964.

[223] N. K. Nielsen and P. Olesen. An Unstable Yang-Mills Field Mode. *Nucl. Phys.*, B144:376–396, 1978.

[224] Shau-Jin Chang and Nathan Weiss. Instability of Constant Yang-Mills Fields. *Phys. Rev.*, D20:869, 1979.

[225] Juergen Berges, Sebastian Scheffler, and Denes Sexty. Bottom-up isotropization in classical-statistical lattice gauge theory. *Phys. Rev.*, D77:034504, 2008.

[226] Guy D. Moore. Motion of Chern-Simons number at high temperatures under a chemical potential. *Nucl. Phys.*, B480:657–688, 1996.

[227] T. Reisz and H. J. Rothe. The Axial anomaly in lattice QED: A Universal point of view. *Phys. Lett.*, B455:246–250, 1999.

[228] Yukinao Akamatsu, Alexander Rothkopf, and Naoki Yamamoto. Non-Abelian chiral instabilities at high temperature on the lattice. *JHEP*, 03:210, 2016.

[229] Niklas Mller, Sren Schlichting, and Sayantan Sharma. Chiral magnetic effect and anomalous transport from real-time lattice simulations. *Phys. Rev. Lett.*, 117(14):142301, 2016.

[230] W. Greiner, Berndt Muller, and Johann Rafelski. *QUANTUM ELECTRODYNAMICS OF STRONG FIELDS*. 1985.

[231] Tohru Eguchi and Noboru Kawamoto. Improved Lattice Action for Wilson Fermion. *Nucl. Phys.*, B237:609–625, 1984.

[232] B. Sheikholeslami and R. Wohlert. Improved Continuum Limit Lattice Action for QCD with Wilson Fermions. *Nucl. Phys.*, B259:572, 1985.

[233] Sinya Aoki. New Phase Structure for Lattice QCD with Wilson Fermions. *Phys. Rev.*, D30:2653, 1984.

[234] Asit K. De, A. Harindranath, and Santanu Mondal. Effect of r averaging on Chiral Anomaly in Lattice QCD with Wilson Fermion: Finite volume and cutoff effects. *JHEP*, 07:117, 2011.

[235] Robert G. Edwards, Urs M. Heller, and Rajamani Narayanan. A Study of practical implementations of the overlap Dirac operator in four-dimensions. *Nucl. Phys.*, B540:457–471, 1999.

[236] J. van den Eshof, A. Frommer, T. Lippert, K. Schilling, and H. A. van der Vorst. Numerical methods for the QCD overlap operator. I. Sign function and error bounds. *Comput. Phys. Commun.*, 146:203–224, 2002.

[237] Ting-Wai Chiu, Tung-Han Hsieh, Chao-Hsi Huang, and Tsung-Ren Huang. A Note on the Zolotarev optimal rational approximation for the overlap Dirac operator. *Phys. Rev.*, D66:114502, 2002.

[238] Rajiv V. Gavai, Sourendu Gupta, and Robert Lacaze. Speed and adaptability of overlap fermion algorithms. *Comput. Phys. Commun.*, 154:143–158, 2003.

[239] Thomas Kalkreuter and Hubert Simma. An Accelerated conjugate gradient algorithm to compute low lying eigenvalues: A Study for the Dirac operator in SU(2) lattice QCD. *Comput. Phys. Commun.*, 93:33–47, 1996.

[240] Gert Aarts and Jan Smit. Particle production and effective thermalization in inhomogeneous mean field theory. *Phys. Rev.*, D61:025002, 2000.

[241] Dmitri E. Kharzeev and Ho-Ung Yee. Chiral Magnetic Wave. *Phys. Rev.*, D83:085007, 2011.

[242] W. Israel and J. M. Stewart. Transient relativistic thermodynamics and kinetic theory. *Annals Phys.*, 118:341–372, 1979.

[243] Yin Jiang, Shuzhe Shi, Yi Yin, and Jinfeng Liao. Quantifying Chiral Magnetic Effect from Anomalous-Viscous Fluid Dynamics. 2016.

[244] Dmitri E. Kharzeev and Dam T. Son. Testing the chiral magnetic and chiral vortical effects in heavy ion collisions. *Phys. Rev. Lett.*, 106:062301, 2011.

[245] Niklas Mueller and Raju Venugopalan. The chiral anomaly, Berry's phase and chiral kinetic theory, from world-lines in quantum field theory. 2017.

[246] Niklas Mueller and Raju Venugopalan. World-line construction of a covariant chiral kinetic theory. 2017.

[247] Aleksi Kurkela and Yan Zhu. Isotropization and hydrodynamization in weakly coupled heavy-ion collisions. *Phys. Rev. Lett.*, 115(18):182301, 2015.

[248] Jurgen Berges, Klaus Reygers, Naoto Tanji, and Raju Venugopalan. What shines brighter, Glasma or Quark-Gluon Plasma: a parametric estimate of photon production at early times in heavy-ion collisions. 2017.

[249] Michael Stone. The Born-oppenheimer Approximation and the Origin of Wess-Zumino Terms: Some Quantum Mechanical Examples. *Phys. Rev.*, D33:1191, 1986.

[250] I. J. R. Aitchison. Berry Phases, Magnetic Monopoles and Wess-Zumino Terms or How the Skyrmion Got Its Spin. *Acta Phys. Polon.*, B18:207, 1987.

[251] Alfred D. Shapere and Frank Wilczek. Geometric Phases in Physics. *Adv. Ser. Math. Phys.*, 5:1–509, 1989.

[252] Shinichi Deguchi and Kazuo Fujikawa. Second quantized formulation of geometric phases. *Phys. Rev.*, A72:012111, 2005.

[253] Kazuo Fujikawa. Geometric phases and hidden local gauge symmetry. *Phys. Rev.*, D72:025009, 2005.

[254] Kazuo Fujikawa. Quantum anomaly and geometric phase: Their basic differences. *Phys. Rev.*, D73:025017, 2006.

[255] J. Wess and B. Zumino. Consequences of anomalous Ward identities. *Phys. Lett.*, 37B:95–97, 1971.

[256] Edward Witten. Global Aspects of Current Algebra. *Nucl. Phys.*, B223:422–432, 1983.

[257] R. P. Feynman. Mathematical formulation of the quantum theory of electromagnetic interaction. *Phys. Rev.*, 80:440–457, 1950.

[258] Matthew J. Strassler. Field theory without Feynman diagrams: One loop effective actions. *Nucl. Phys.*, B385:145–184, 1992.

[259] Myriam Mondragon, Lukas Nellen, Michael G. Schmidt, and Christian Schubert. Yukawa couplings for the spinning particle and the worldline formalism. *Phys. Lett.*, B351:200–205, 1995.

[260] Myriam Mondragon, Lukas Nellen, Michael G. Schmidt, and Christian Schubert. Axial couplings on the worldline. *Phys. Lett.*, B366:212–219, 1996.

[261] Jamal Jalilian-Marian, Sangyong Jeon, Raju Venugopalan, and Jens Wirstam. Minding one's P's and Q's: From the one loop effective action in quantum field theory to classical transport theory. *Phys. Rev.*, D62:045020, 2000.

[262] Christian Schubert. Perturbative quantum field theory in the string inspired formalism. *Phys. Rept.*, 355:73–234, 2001.

[263] F. Bastianelli and P. van Nieuwenhuizen. *Path integrals and anomalies in curved space*. Cambridge University Press, 2006.

[264] Andres Hernandez, Thomas Konstandin, and Michael G. Schmidt. Sizable CP Violation in the Bosonized Standard Model. *Nucl. Phys.*, B812:290–300, 2009.

[265] Olindo Corradini and Christian Schubert. Spinning Particles in Quantum Mechanics and Quantum Field Theory. 2015.

[266] Alexander M. Polyakov. Gauge Fields and Strings. *Contemp. Concepts Phys.*, 3:1–301, 1987.

[267] Zvi Bern and David A. Kosower. The Computation of loop amplitudes in gauge theories. *Nucl. Phys.*, B379:451–561, 1992.

[268] Zvi Bern, Lance J. Dixon, David C. Dunbar, and David A. Kosower. One loop n point gauge theory amplitudes, unitarity and collinear limits. *Nucl. Phys.*, B425:217–260, 1994.

[269] Luis Alvarez-Gaume and Edward Witten. Gravitational Anomalies. *Nucl. Phys.*, B234:269, 1984.

[270] Luis Alvarez-Gaume. Supersymmetry and the Atiyah-Singer Index Theorem. *Commun. Math. Phys.*, 90:161, 1983.

[271] V. Bargmann, Louis Michel, and V. L. Telegdi. Precession of the polarization of particles moving in a homogeneous electromagnetic field. *Phys. Rev. Lett.*, 2:435–436, 1959. [,92(1959)].

[272] S. K. Wong. Field and particle equations for the classical Yang-Mills field and particles with isotopic spin. *Nuovo Cim.*, A65:689–694, 1970.

[273] F. A. Berezin and M. S. Marinov. Particle Spin Dynamics as the Grassmann Variant of Classical Mechanics. *Annals Phys.*, 104:336, 1977.

[274] A. P. Balachandran, Per Salomonson, Bo-Sture Skagerstam, and Jan-Olof Winnberg. Classical Description of Particle Interacting with Nonabelian Gauge Field. *Phys. Rev.*, D15:2308–2317, 1977.

[275] A. P. Balachandran, S. Borchardt, and A. Stern. Lagrangian and Hamiltonian Descriptions of Yang-Mills Particles. *Phys. Rev.*, D17:3247, 1978.

[276] A. Barducci. Pseudoclassical Description of Relativistic Spinning Particles With Anomalous Magnetic Moment. *Phys. Lett.*, B118:112–114, 1982.

[277] L. Brink, P. Di Vecchia, and Paul S. Howe. A Lagrangian Formulation of the Classical and Quantum Dynamics of Spinning Particles. *Nucl. Phys.*, B118:76–94, 1977.

[278] Yukinao Akamatsu and Naoki Yamamoto. Chiral Langevin theory for non-Abelian plasmas. *Phys. Rev.*, D90(12):125031, 2014.

[279] R. Venugopalan N. Mueller and Y. Yin. in progress.

[280] Eric D'Hoker and Darius G. Gagne. Worldline path integrals for fermions with scalar, pseudoscalar and vector couplings. *Nucl. Phys.*, B467:272–296, 1996.

[281] Eric D'Hoker and Darius G. Gagne. Worldline path integrals for fermions with general couplings. *Nucl. Phys.*, B467:297–312, 1996.

[282] Mayank R. Mehta. Euclidean Continuation of the Dirac Fermion. *Phys. Rev. Lett.*, 65:1983–1986, 1990. [Erratum: Phys. Rev. Lett.66,522(1991)].

[283] Y. Ohnuki and T. Kashiwa. Coherent States of Fermi Operators and the Path Integral. *Prog. Theor. Phys.*, 60:548, 1978.

[284] F. Bastianelli and C. Schubert. book in preparation (Cambridge University Press) and F. Bastianelli, *Constrained hamiltonian systems and relativistic particles*, lecture notes INFN Bologna 2012.

[285] William A. Bardeen and Bruno Zumino. Consistent and Covariant Anomalies in Gauge and Gravitational Theories. *Nucl. Phys.*, B244:421–453, 1984.

[286] William A. Bardeen. Anomalous Ward identities in spinor field theories. *Phys. Rev.*, 184:1848–1857, 1969.

[287] Dietrich Bodeker. On the effective dynamics of soft nonAbelian gauge fields at finite temperature. *Phys. Lett.*, B426:351–360, 1998.

[288] Dietrich Bodeker. From hard thermal loops to Langevin dynamics. *Nucl. Phys.*, B559:502–538, 1999.

[289] A. Barducci, R. Casalbuoni, and L. Lusanna. Classical Scalar and Spinning Particles Interacting with External Yang-Mills Fields. *Nucl. Phys.*, B124:93–108, 1977.

[290] J. J. Sakurai. Advanced Quantum Mechanics.

[291] Daniel F. Litim and Cristina Manuel. Effective transport equations for nonAbelian plasmas. *Nucl. Phys.*, B562:237–274, 1999.

[292] Yuri V. Kovchegov, Daniel Pitonyak, and Matthew D. Sievert. Small-x asymptotics of the quark helicity distribution. *Phys. Rev. Lett.*, 118(5):052001, 2017.

[293] Jamal Jalilian-Marian, Sangyong Jeon, and Raju Venugopalan. Wong's equations and the small x effective action in QCD. *Phys. Rev.*, D63:036004, 2001.

[294] I. I. Balitsky and L. N. Lipatov. The Pomeranchuk Singularity in Quantum Chromodynamics. *Sov. J. Nucl. Phys.*, 28:822–829, 1978. [Yad. Fiz.28,1597(1978)].

[295] Niklas Mueller and Jan M. Pawlowski. Magnetic catalysis and inverse magnetic catalysis in QCD. *Phys. Rev.*, D91(11):116010, 2015.

[296] Igor A. Shovkovy. Magnetic Catalysis: A Review. *Lect. Notes Phys.*, 871:13–49, 2013.

[297] Massimo D'Elia. Lattice QCD Simulations in External Background Fields. *Lect. Notes Phys.*, 871:181–208, 2013.

[298] Kenji Fukushima. Views of the Chiral Magnetic Effect. *Lect. Notes Phys.*, 871:241–259, 2013.

[299] Niklas Mueller, Jacqueline A. Bonnet, and Christian S. Fischer. Dynamical quark mass generation in a strong external magnetic field. *Phys. Rev.*, D89(9):094023, 2014.

[300] Jens O. Andersen, William R. Naylor, and Anders Tranberg. Phase diagram of QCD in a magnetic field: A review. *Rev. Mod. Phys.*, 88:025001, 2016.

[301] Vladimir A. Miransky and Igor A. Shovkovy. Quantum field theory in a magnetic field: From quantum chromodynamics to graphene and Dirac semimetals. *Phys. Rept.*, 576:1–209, 2015.

[302] Gokce Basar, Dmitri Kharzeev, Dmitri Kharzeev, and Vladimir Skokov. Conformal anomaly as a source of soft photons in heavy ion collisions. *Phys. Rev. Lett.*, 109:202303, 2012.

[303] Gkce Basar, Dmitri E. Kharzeev, and Edward V. Shuryak. Magneto-sonoluminescence and its signatures in photon and dilepton production in relativistic heavy ion collisions. *Phys. Rev.*, C90(1):014905, 2014.

[304] V. P. Gusynin, V. A. Miransky, and I. A. Shovkovy. Dimensional reduction and catalysis of dynamical symmetry breaking by a magnetic field. *Nucl. Phys.*, B462:249–290, 1996.

[305] V. P. Gusynin, V. A. Miransky, and I. A. Shovkovy. Dynamical chiral symmetry breaking in QED in a magnetic field: Toward exact results. *Phys. Rev. Lett.*, 83:1291–1294, 1999.

[306] V. P. Gusynin, V. A. Miransky, and I. A. Shovkovy. Theory of the magnetic catalysis of chiral symmetry breaking in QED. *Nucl. Phys.*, B563:361–389, 1999.

[307] V. P. Gusynin, V. A. Miransky, and I. A. Shovkovy. Dynamical chiral symmetry breaking by a magnetic field in QED. *Phys. Rev.*, D52:4747–4751, 1995.

[308] Tomohiro Inagaki, Daiji Kimura, and Tsukasa Murata. Four fermion interaction model in a constant magnetic field at finite temperature and chemical potential. *Prog. Theor. Phys.*, 111:371–386, 2004.

[309] Jorn K. Boomsma and Daniel Boer. The Influence of strong magnetic fields and instantons on the phase structure of the two-flavor NJL model. *Phys. Rev.*, D81:074005, 2010.

[310] Massimo D'Elia, Swagato Mukherjee, and Francesco Sanfilippo. QCD Phase Transition in a Strong Magnetic Background. *Phys. Rev.*, D82:051501, 2010.

[311] Ana Julia Mizher, M. N. Chernodub, and Eduardo S. Fraga. Phase diagram of hot QCD in an external magnetic field: possible splitting of deconfinement and chiral transitions. *Phys. Rev.*, D82:105016, 2010.

[312] Raoul Gatto and Marco Ruggieri. Dressed Polyakov loop and phase diagram of hot quark matter under magnetic field. *Phys. Rev.*, D82:054027, 2010.

[313] Raoul Gatto and Marco Ruggieri. Deconfinement and Chiral Symmetry Restoration in a Strong Magnetic Background. *Phys. Rev.*, D83:034016, 2011.

[314] Bhaswar Chatterjee, Hiranmaya Mishra, and Amruta Mishra. Vacuum structure and chiral symmetry breaking in strong magnetic fields for hot and dense quark matter. *Phys. Rev.*, D84:014016, 2011.

[315] Raoul Gatto and Marco Ruggieri. Quark Matter in a Strong Magnetic Background. *Lect. Notes Phys.*, 871:87–119, 2013.

[316] Marco Frasca and Marco Ruggieri. Magnetic Susceptibility of the Quark Condensate and Polarization from Chiral Models. *Phys. Rev.*, D83:094024, 2011.

[317] M. Ferreira, P. Costa, O. Loureno, T. Frederico, and C. Providncia. Inverse magnetic catalysis in the (2+1)-flavor Nambu-Jona-Lasinio and Polyakov-Nambu-Jona-Lasinio models. *Phys. Rev.*, D89(11):116011, 2014.

[318] E. J. Ferrer, V. de la Incera, and X. J. Wen. Quark Antiscreening at Strong Magnetic Field and Inverse Magnetic Catalysis. *Phys. Rev.*, D91(5):054006, 2015.

[319] R. L. S. Farias, K. P. Gomes, G. I. Krein, and M. B. Pinto. Importance of asymptotic freedom for the pseudocritical temperature in magnetized quark matter. *Phys. Rev.*, C90(2):025203, 2014.

[320] Alejandro Ayala, M. Loewe, Ana Julia Mizher, and R. Zamora. Inverse magnetic catalysis for the chiral transition induced by thermo-magnetic effects on the coupling constant. *Phys. Rev.*, D90(3):036001, 2014.

[321] Alejandro Ayala, M. Loewe, and R. Zamora. Inverse magnetic catalysis in the linear sigma model with quarks. *Phys. Rev.*, D91(1):016002, 2015.

[322] Lang Yu, Jos Van Doorsselaere, and Mei Huang. Inverse Magnetic Catalysis in the three-flavor NJL model with axial-vector interaction. *Phys. Rev.*, D91(7):074011, 2015.

[323] Oren Bergman, Gilad Lifschytz, and Matthew Lippert. Response of Holographic QCD to Electric and Magnetic Fields. *JHEP*, 05:007, 2008.

[324] Clifford V. Johnson and Arnab Kundu. External Fields and Chiral Symmetry Breaking in the Sakai-Sugimoto Model. *JHEP*, 12:053, 2008.

[325] Veselin G. Filev, Clifford V. Johnson, and Jonathan P. Shock. Universal Holographic Chiral Dynamics in an External Magnetic Field. *JHEP*, 08:013, 2009.

[326] Florian Preis, Anton Rebhan, and Andreas Schmitt. Inverse magnetic catalysis in dense holographic matter. *JHEP*, 03:033, 2011.

[327] Florian Preis, Anton Rebhan, and Andreas Schmitt. Inverse magnetic catalysis in field theory and gauge-gravity duality. *Lect. Notes Phys.*, 871:51–86, 2013.

[328] Alfonso Ballon-Bayona. Holographic deconfinement transition in the presence of a magnetic field. *JHEP*, 11:168, 2013.

[329] Kiminad A. Mamo. Inverse magnetic catalysis in holographic models of QCD. *JHEP*, 05:121, 2015.

[330] V. Skokov. Phase diagram in an external magnetic field beyond a mean-field approximation. *Phys. Rev.*, D85:034026, 2012.

[331] Kenji Fukushima and Jan M. Pawlowski. Magnetic catalysis in hot and dense quark matter and quantum fluctuations. *Phys. Rev.*, D86:076013, 2012.

[332] Kazuhiko Kamikado and Takuya Kanazawa. Chiral dynamics in a magnetic field from the functional renormalization group. *JHEP*, 03:009, 2014.

[333] Kazuhiko Kamikado and Takuya Kanazawa. Magnetic susceptibility of a strongly interacting thermal medium with 2+1 quark flavors. *JHEP*, 01:129, 2015.

[334] Jens O. Andersen and Anders Tranberg. The Chiral transition in a magnetic background: Finite density effects and the functional renormalization group. *JHEP*, 08:002, 2012.

[335] Jens O. Andersen, William R. Naylor, and Anders Tranberg. Chiral and deconfinement transitions in a magnetic background using the functional renormalization group with the Polyakov loop. *JHEP*, 04:187, 2014.

[336] Jens Braun, Walid Ahmed Mian, and Stefan Rechenberger. Delayed Magnetic Catalysis. *Phys. Lett.*, B755:265–269, 2016.

[337] Toru Kojo and Nan Su. The quark mass gap in a magnetic field. *Phys. Lett.*, B720:192–197, 2013.

[338] Toru Kojo and Nan Su. A renormalization group approach for QCD in a strong magnetic field. *Phys. Lett.*, B726:839–845, 2013.

[339] Peter Watson and Hugo Reinhardt. Quark gap equation in an external magnetic field. *Phys. Rev.*, D89(4):045008, 2014.

[340] G. S. Bali, F. Bruckmann, G. Endrodi, Z. Fodor, S. D. Katz, and A. Schafer. QCD quark condensate in external magnetic fields. *Phys. Rev.*, D86:071502, 2012.

[341] G. S. Bali, F. Bruckmann, G. Endrodi, F. Gruber, and A. Schaefer. Magnetic field-induced gluonic (inverse) catalysis and pressure (an)isotropy in QCD. *JHEP*, 04:130, 2013.

[342] Falk Bruckmann, Gergely Endrodi, and Tamas G. Kovacs. Inverse magnetic catalysis and the Polyakov loop. *JHEP*, 04:112, 2013.

[343] G. S. Bali, F. Bruckmann, G. Endrdi, S. D. Katz, and A. Schfer. The QCD equation of state in background magnetic fields. *JHEP*, 08:177, 2014.

[344] E. M. Ilgenfritz, M. Muller-Preussker, B. Petersson, and A. Schreiber. Magnetic catalysis (and inverse catalysis) at finite temperature in two-color lattice QCD. *Phys. Rev.*, D89(5):054512, 2014.

[345] V. G. Bornyakov, P. V. Buividovich, N. Cundy, O. A. Kochetkov, and A. Schfer. Deconfinement transition in two-flavor lattice QCD with dynamical overlap fermions in an external magnetic field. *Phys. Rev.*, D90(3):034501, 2014.

[346] Kenji Fukushima and Yoshimasa Hidaka. Magnetic Catalysis Versus Magnetic Inhibition. *Phys. Rev. Lett.*, 110(3):031601, 2013.

[347] E. S. Fraga, B. W. Mintz, and J. Schaffner-Bielich. A search for inverse magnetic catalysis in thermal quark-meson models. *Phys. Lett.*, B731:154–158, 2014.

[348] Jens O. Andersen, William R. Naylor, and Anders Tranberg. Inverse magnetic catalysis and regularization in the quark-meson model. *JHEP*, 02:042, 2015.

[349] Jan M. Pawlowski. The QCD phase diagram: Results and challenges. *AIP Conf. Proc.*, 1343:75–80, 2011.

[350] Lisa M. Haas, Rainer Stiele, Jens Braun, Jan M. Pawlowski, and Jrgen Schaffner-Bielich. Improved Polyakov-loop potential for effective models from functional calculations. *Phys. Rev.*, D87(7):076004, 2013.

[351] Tina Katharina Herbst, Mario Mitter, Jan M. Pawlowski, Bernd-Jochen Schaefer, and Rainer Stiele. Thermodynamics of QCD at vanishing density. *Phys. Lett.*, B731:248–256, 2014.

[352] Jan M. Pawlowski. Equation of state and phase diagram of strongly interacting matter. *Nucl. Phys.*, A931:113–124, 2014.

[353] D. S. Lee, Chung Ngoc Leung, and Y. J. Ng. Chiral symmetry breaking in a uniform external magnetic field. *Phys. Rev.*, D55:6504–6513, 1997.

[354] V. A. Miransky and I. A. Shovkovy. Magnetic catalysis and anisotropic confinement in QCD. *Phys. Rev.*, D66:045006, 2002.

[355] Chung Ngoc Leung and Shang-Yung Wang. Gauge independence and chiral symmetry breaking in a strong magnetic field. *Annals Phys.*, 322:701–708, 2007.

[356] Alejandro Ayala, Adnan Bashir, Alfredo Raya, and Eduardo Rojas. Dynamical mass generation in strongly coupled quantum electrodynamics with weak magnetic fields. *Phys. Rev.*, D73:105009, 2006.

[357] Eduardo Rojas, Alejandro Ayala, Adnan Bashir, and Alfredo Raya. Dynamical mass generation in QED with magnetic fields: Arbitrary field strength and coupling constant. *Phys. Rev.*, D77:093004, 2008.

[358] V. I. Ritus. Radiative corrections in quantum electrodynamics with intense field and their analytical properties. *Annals Phys.*, 69:555–582, 1972.

[359] V. I. Ritus. METHOD OF EIGENFUNCTIONS AND MASS OPERATOR IN QUANTUM ELECTRODYNAMICS OF A CONSTANT FIELD. *Sov. Phys. JETP*, 48:788, 1978. [Zh. Eksp. Teor. Fiz.75,1560(1978)].

[360] C. S. Fischer, P. Watson, and W. Cassing. Probing unquenching effects in the gluon polarisation in light mesons. *Phys. Rev.*, D72:094025, 2005.

[361] Dominik Nickel, Reinhard Alkofer, and Jochen Wambach. On the unlocking of color and flavor in color-superconducting quark matter. *Phys. Rev.*, D74:114015, 2006.

[362] Jens Braun, Lisa M. Haas, Florian Marhauser, and Jan M. Pawlowski. Phase Structure of Two-Flavor QCD at Finite Chemical Potential. *Phys. Rev. Lett.*, 106:022002, 2011.

[363] Christian S. Fischer and Jan Luecker. Propagators and phase structure of Nf=2 and Nf=2+1 QCD. *Phys. Lett.*, B718:1036–1043, 2013.

[364] Christian S. Fischer, Leonard Fister, Jan Luecker, and Jan M. Pawlowski. Polyakov loop potential at finite density. *Phys. Lett.*, B732:273–277, 2014.

[365] Christian S. Fischer, Jan Luecker, and Christian A. Welzbacher. Phase structure of three and four flavor QCD. *Phys. Rev.*, D90(3):034022, 2014.

[366] Jens Braun, Leonard Fister, Jan M. Pawlowski, and Fabian Rennecke. From Quarks and Gluons to Hadrons: Chiral Symmetry Breaking in Dynamical QCD. *Phys. Rev.*, D94(3):034016, 2016.

[367] Mario Mitter, Jan M. Pawlowski, and Nils Strodthoff. Chiral symmetry breaking in continuum QCD. *Phys. Rev.*, D91:054035, 2015.

[368] Tzuu-Kang Chyi, Chien-Wen Hwang, W. F. Kao, Guey-Lin Lin, Kin-Wang Ng, and Jie-Jun Tseng. The weak field expansion for processes in a homogeneous background magnetic field. *Phys. Rev.*, D62:105014, 2000.

[369] Christian S. Fischer, Axel Maas, and Jens A. Muller. Chiral and deconfinement transition from correlation functions: SU(2) vs. SU(3). *Eur. Phys. J.*, C68:165–181, 2010.

[370] Christian S. Fischer and Jan M. Pawlowski. Uniqueness of infrared asymptotics in Landau gauge Yang-Mills theory II. *Phys. Rev.*, D80:025023, 2009.

[371] A. V. Nesterenko. Quark - anti-quark potential in the analytic approach to QCD. *Phys. Rev.*, D62:094028, 2000.

[372] A. V. Nesterenko. New analytic running coupling in space - like and time - like regions. *Phys. Rev.*, D64:116009, 2001.

[373] Nicolai Christiansen, Michael Haas, Jan M. Pawlowski, and Nils Strodthoff. Transport Coefficients in Yang–Mills Theory and QCD. *Phys. Rev. Lett.*, 115(11):112002, 2015.

[374] Reinhard Alkofer, Christian S. Fischer, Felipe J. Llanes-Estrada, and Kai Schwenzer. The Quark-gluon vertex in Landau gauge QCD: Its role in dynamical chiral symmetry breaking and quark confinement. *Annals Phys.*, 324:106–172, 2009.

[375] Jens Braun and Holger Gies. Chiral phase boundary of QCD at finite temperature. *JHEP*, 06:024, 2006.

[376] Jens Braun and Holger Gies. Running coupling at finite temperature and chiral symmetry restoration in QCD. *Phys. Lett.*, B645:53–58, 2007.

[377] Jens Braun. Fermion Interactions and Universal Behavior in Strongly Interacting Theories. *J. Phys.*, G39:033001, 2012.

[378] Daniel F. Litim. Optimization of the exact renormalization group. *Phys. Lett.*, B486:92–99, 2000.

[379] Christian S. Fischer, Axel Maas, and Jan M. Pawlowski. On the infrared behavior of Landau gauge Yang-Mills theory. *Annals Phys.*, 324:2408–2437, 2009.

[380] Gergely Endrodi. Critical point in the QCD phase diagram for extremely strong background magnetic fields. *JHEP*, 07:173, 2015.

[381] Kazuya Nishiyama, Shintaro Karasawa, and Toshitaka Tatsumi. Hybrid chiral condensate in the external magnetic field. *Phys. Rev.*, D92:036008, 2015.

[382] Kenji Fukushima. Simulating net particle production and chiral magnetic current in a CP-odd domain. *Phys. Rev.*, D92(5):054009, 2015.

[383] Frans R. Klinkhamer and Christian Rupp. Sphalerons, spectral flow, and anomalies. *J. Math. Phys.*, 44:3619–3639, 2003.

[384] D. Trump and T. Schwartz. *The Art of the deal.* Ballantine Books, 1987.

[385] Gerald V. Dunne and Christian Schubert. Worldline instantons and pair production in inhomogeneous fields. *Phys. Rev.*, D72:105004, 2005.

[386] Gerald V. Dunne, Qing-hai Wang, Holger Gies, and Christian Schubert. Worldline instantons. II. The Fluctuation prefactor. *Phys. Rev.*, D73:065028, 2006.

[387] Reinhard Alkofer, Gernot Eichmann, Christian S. Fischer, Markus Hopfer, Milan Vujinovic, Richard Williams, and Andreas Windisch. On propagators and three-point functions in Landau gauge QCD and QCD-like theories. *PoS*, QCD-TNT-III:003, 2013.

[388] Richard Williams. The quark-gluon vertex in Landau gauge bound-state studies. *Eur. Phys. J.*, A51(5):57, 2015.